Forschungsbericht 2023-08

Numerical Modelling of the Acoustic Response of Cryogenic Oxygen-Hydrogen Rocket Flames

Federica Tonti

Deutsches Zentrum für Luft- und Raumfahrt
Institut für Raumfahrtantriebe
Lampoldshausen

Deutsches Zentrum
DLR für Luft- und Raumfahrt

Forschungsbericht 2023-08

Numerical Modelling of the Acoustic Response of Cryogenic Oxygen-Hydrogen Rocket Flames

Federica Tonti

Deutsches Zentrum für Luft- und Raumfahrt
Institut für Raumfahrtantriebe
Lampoldshausen

215 Seiten
100 Bilder
16 Tabellen
246 Literaturstellen

Deutsches Zentrum
DLR für Luft- und Raumfahrt

Herausgeber:

Deutsches Zentrum
für Luft- und Raumfahrt e. V.
Wissenschaftliche Information
Linder Höhe
D-51147 Köln

ISSN 1434-8454
ISRN DLR-FB-2023-08
Erscheinungsjahr 2023

DOI: https://doi.org/10.57676/ns5k-2t91

D 82 (Diss. RWTH Aachen University, [2023])

Raketenflammen, Verbrennung, Verbrennungsinstabilitäten, akustische Moden, Flammenantwort, Flammenspektren, OH Strahlungsintensität, Ray-tracing Algorithmus*

Federica TONTI
DLR, Institut für Raumfahrtantriebe, Lampoldshausen

Numerische Modellierung der akustischen Antwort von kryogenen Wasserstoff-Sauerstoff-Raketenflammen
RWTH Aachen, Dissertation

Hochfrequente Verbrennungsinstabilitäten bestehen aus Druckschwankungen, die an instationären Verbrennungsprozessen koppeln. Wenn es die richtigen Bedingungen gibt, können die instationären Schwankungen unkontrolliert ansteigen, die Betriebsbedingungen der Brennkammer beeinträchtigen und im schlimmsten Fall zum Ausfall des Triebwerks führen. Das Ziel dieser Arbeit ist es, Methoden zu entwickeln, um die Flammenantwort auf hochfrequente akustische Anregungen, die den Rahmenbedingungen beim Auftreten von Verbrennungsinstabilitäten entsprechen, zu untersuchen. Ein Einzelinjektormodell der BKH wird verwendet, um die Flammenantwort auf longitudinale und transversale Anregung sowie den Einfluss der Randbedingungen auf die Resultate der numerischen Simulationen zu untersuchen und diese mit vorherigen Simulationen und experimentellen Daten zu vergleichen.

Eine Randbedingung für die Beschreibung des physikalischen Verhaltens des externen Anregungssystems von BKH wird implementiert und getestet mit einer Kaltgas-Simulation getestet. Die Resultate werden mit vorherigen numerischen Simulationen verglichen, die das Verhalten des Anregungssystems in einer vereinfachten Form beschrieben hatten.

Ein Algorithmus wird entwickelt, der einen besseren Vergleich von Bildern der von Hochgeschwindigkeitskameras erfassten OH*-Strahlungsintensität und mit Ergebnissen der CFD Simulationen in einem post-processing-Schritt ermöglicht. Die Spektren von OH* werden zuerst modelliert. Danach werden mit Hilfe eines Ray-Tracing Algorithmus aus der CFD-Lösung pseudo-OH* Strahlungsbilder erzeugt, die dann mit den Bildern der Hochgeschwindigkeitskameras verglichen werden können. Die numerischen Resultate zeigen eine gute qualitative Übereinstimmung mit den experimentellen Daten. Selbstabsorption und Lichtbrechung, die in vorherigen Arbeiten nicht berücksichtigt wurden, sind hier beachtet.

Eine stationäre Simulation der BKH wird unter Verwendung von im Vergleich zu früheren Arbeiten veränderten Geometrie, Netz und Randbedingungen durchgeführt. Die Resultate werden mit vorherigen Simulationen und experimentellen Daten verglichen und der Ray-tracing-Algorithmus wird auf die Lösung angewendet. Die akustische Analyse wird mit einem LNS Solver auf Grundlage der stationären Lösung durchgeführt, um die Hauptresonanzmoden der Brennkammer zu ermitteln. Die Resultate werden mit vorherigen Helmholtz-Simulationen und mit Experimenten verglichen. Der LNS Solver ergibt für die Moden Werte, die trotz der Vereinfachungen vergleichbar mit Experimenten sind.

Rocket flames, combustion, combustion instabilities, acoustic modes, flame response, flame spectra, OH emission intensity, ray-tracing algorithms*

(Published in English)

Federica TONTI
German Aerospace Center (DLR), Institute of Space Propulsion, Lampoldshausen

Numerical Modelling of the Acoustic Response of Cryogenic Oxygen-Hydrogen Rocket Flames

RWTH Aachen, thesis

High frequency combustion instabilities in liquid propellant rocket engines are a phenomenon which is not yet completely understood. They consist in pressure fluctuations which couple with unsteady combustion processes. When the right conditions are present, the unsteady fluctuations can grow uncontrolled and affect the operation conditions of the chamber and in the most extreme cases lead to the failure of the engine. When designing a new combustion chamber, understanding and predicting combustion instabilities becomes crucial in order to prevent their occurrence and reduce the risk of failure.
The goal of this work is to develop methods for investigating the flame response to high frequency acoustic forcing which represents the conditions of occurrence of combustion instabilities.
A single injector model of BKH is employed to investigate the flame response to longitudinal and transverse excitation and the influence of the boundary conditions on the simulation results, comparing them also with previous simulations and experimental data. A boundary condition for the description of the physical behavior of the external excitation system of BKH is implemented and tested on a cold flow run. The results are compared with previous numerical simulation describing the behavior of the excitation system in a simplified way. n algorithm is developed to allow a better comparison of images form high-speed cameras and CFD simulation results using OH* radiation intensity in a post-processing step. The spectra of OH* are first modelled and then a ray-tracing algorithm is applied on the CFD solution in order to obtain pseudo-OH* radiation images comparable with high-speed camera images. The results show a good qualitative agreement with experimental data taking into account self-absorption and refraction phenomena which have been not considered in past works.

A steady-state simulation of BKH is performed considering a different geometry, mesh and boundary conditions with respect to previous work. The results are compared with former simulation results and experimental data and the ray tracing algorithm is applied on the solution. The acoustic analysis using a LNS solver is performed on the steady-state solution in order to identify the main resonant modes of the chamber. The results are compared with previous results using a Helmholtz solver and with experimental data, showing that the LNS solver gives values comparable with experiments despite the number of simplifications introduced.

Numerical Modelling of the Acoustic Response of Cryogenic Oxygen-Hydrogen Rocket Flames

Numerische Modellierung der akustischen Antwort von kryogenen Wasserstoff-Sauerstoff Raketenflammen

Von der Fakultät für Maschinenwesen der Rheinisch-Westfälischen Technischen Hochschule Aachen zur Erlangung des akademischen Grades einer Doktorin der Ingenieurwissenschaften genehmigte Dissertation

vorgelegt von

Federica Tonti

Berichter/in: Univ.-Prof. Dr. rer. nat. Michael Oschwald
Univ.-Prof. Dr.-Ing. Peter Jeschke
Prof. Dr.-Ing. Chiara Manfletti

Tag der mündlichen Prüfung: 08. März 2023

I hereby declare that I have created this work completely on my own and used no other sources or tools than the ones listed, and that I have marked any citations accordingly.
Hiermit versichere ich, dass ich die vorliegende Arbeit selbständig verfasst und keine anderen als die angegebenen Quellen und Hilfsmittel benutzt sowie Zitate kenntlich gemacht habe.

Aachen, March 2023
Federica Tonti

Abstract

High frequency combustion instabilities in liquid propellant rocket engines are a phenomenon which is not yet completely understood. They consist in pressure fluctuations which couple with unsteady combustion processes. When the right conditions are present, the unsteady fluctuations can grow uncontrolled and affect the operation conditions of the chamber and in the most extreme cases lead to the failure of the engine. When designing a new combustion chamber, understanding and predicting combustion instabilities becomes crucial in order to prevent their occurrence and reduce the risk of failure.
The goal of this work is to develop methods for investigating the flame response to high frequency acoustic forcing which represents the conditions of occurrence of combustion instabilities.
A single injector model of BKH is employed to investigate the flame response to longitudinal and transverse excitation and the influence of the boundary conditions on the simulation results, comparing them also with previous simulations and experimental data.
A boundary condition for the description of the physical behavior of the external excitation system of BKH is implemented and tested on a cold flow run. The results are compared with previous numerical simulation describing the behavior of the excitation system in a simplified way.
An algorithm is developed to allow a better comparison of images form high-speed cameras and CFD simulation results using OH* radiation intensity in a post-processing step. The spectra of OH* are first modelled and then a ray-tracing algorithm is applied on the CFD solution in order to obtain pseudo-OH* radiation images comparable with high-speed camera images. The results show a good qualitative agreement with experimental data taking into account self-absorption and refraction phenomena which have been not considered in past works.
A steady-state simulation of BKH is performed considering a different geometry, mesh and boundary conditions with respect to previous work. The results are compared with former simulation results and experimental data and the ray tracing algorithm is applied on the solution. The acoustic analysis using a LNS solver is performed on the steady-state solution in order to identify the main resonant modes of the chamber. The results are compared with previous results using a Helmholtz solver and with experimental data, showing that the LNS solver gives values comparable with experiments despite the number of simplifications introduced.

Zusammenfassung

Hochfrequente Verbrennungsinstabilitäten bestehen aus Drückschwankungen, die an instationären Verbrennungsprozessen koppeln. Wenn es die richtigen Bedingungen gibt, können die instationären Schwankungen unkontrolliert ansteigen, die Betriebsbedingungen der Brennkammer beeinträchtigen und im schlimmsten Fall zum Ausfall des Triebwerks führen. Das Ziel dieser Arbeit ist es, Methoden zu entwickeln, um die Flammenantwort auf hochfrequente akustische Anregungen, die den Rahmenbedingungen beim Auftreten von Verbrennungsinstabilitäten entsprechen, zu untersuchen. Ein Einzelinjektormodell der BKH wird verwendet, um die Flammenantwort auf longitudinale und transversale Anregung sowie den Einfluss der Randbedingungen auf die Resultate der numerischen Simulationen zu untersuchen und diese mit vorherigen Simulationen und experimentellen Daten zu vergleichen. Eine Randbedingung für die Beschreibung des physikalischen Verhaltens des externen Anregungssystems von BKH wird implementiert und getestet mit einer Kaltgas-Simulation getestet. Die Resultate werden mit vorherigen numerischen Simulationen verglichen, die das Verhalten des Anregungssystems in einer vereinfachten Form beschrieben hatten. Ein Algorithmus wird entwickelt, der einen besseren Vergleich von Bildern der von Hochgeschwindigkeitskameras erfassten OH*-Strahlungsintensität und mit Ergebnissen der CFD Simulationen in einem post-processing-Schritt ermöglicht. Die Spektren von OH* werden zuerst modelliert. Danach werden mit Hilfe eines Ray-Tracing Algorithmus aus der CFD-Lösung pseudo-OH* Strahlungsbilder erzeugt, die dann mit den Bildern der Hochgeschwindigkeitskameras verglichen werden können. Die numerischen Resultate zeigen eine gute qualitative Übereinstimmung mit den experimentellen Daten. Selbstabsorption und Lichtbrechung, die in vorherigen Arbeiten nicht berücksichtigt wurden, sind hier beachtet. Eine stationäre Simulation der BKH wird unter Verwendung von im Vergleich zu früheren Arbeiten veränderten Geometrie, Netz und Randbedingungen durchgeführt. Die Resultate werden mit vorherigen Simulationen und experimentellen Daten verglichen und der Ray-tracing-Algorithmus wird auf die Lösung angewendet. Die akustische Analyse wird mit einem LNS Solver auf Grundlage der stationären Lösung durchgeführt, um die Hauptresonanzmoden der Brennkammer zu ermitteln. Die Resultate werden mit vorherigen Helmholtz-Simulationen und mit Experimenten verglichen. Der LNS Solver ergibt für die Moden Werte, die trotz der Vereinfachungen vergleichbar mit Experimenten sind.

Se la vita non ha sogni, io li ho e te li do.

(Lucio Dalla)

I'm not the man they think I am at home, I'm a rocket man.

(Elton John)

E quindi uscimmo a riveder le stelle.

(Dante Alighieri)

Acknowledgements

First of all, I would like to thank my supervisor, prof. Michael Oschwald and Dr. Justin Hardi, who allowed me to pursue my PhD and gave me the opportunity to study such a complex and fascinating topic as combustion instabilities in liquid propellant rocket engines. I thank you for the experience, guidance and support given thoughout all the duration of the project. You also understood all the difficulties arose over time and always trusted that I could find solutions to solve the issues in the best possible way.
I would like to thank the DLR Institute of Space Propulsion and all the people working there, because I never felt as a stranger but rather as the member of a family. I would also like to acknowledge the invaluable assistance from Joachim Sender, Stefan General, Dirk Schneider, Michaela Hanke, Melanie Schmidt and Isabell Böhringer that allowed me to navigate the many technical and bureaucratic hurdles during my time at the DLR.
My gratitude goes also to the DLR Institute of Aerodynamics and Flow Technology, in particular to Sebastian Karl, who helped me a lot in understanding the OH* radiation aspect and provided the fundamentals for developing the spectra of OH*. Tim Hörchler and Stefan Fechter are probably the two persons I have to thank the most for the continuous support with my CFD simulations. They always helped me solving the problems I had with the code and they played an important part in the completion of this work.
This work has been developed and financed in the frame of the TAUROS and AMADEUS projects and I would like to thank also all the members.
Thanks to all the REST community, the French-German collaboration in combustion instabilities. The work done in this frame is invaluable and helped me to gain a deeper knowledge on many aspects of combustion instabilities in liquid propellant rocket engines, from experimental to numerical aspects.
I would like also to thank the colleagues who shared with me the office during my PhD, not only for all the support provided for my work but also for the friendly environment I found and we built toghether: Wolfgang Armbruster, Jan Martin and Min Son. Although he was not in the office with us, I would like to thank also Michael Börner, who is now leading the VDY Group at DLR.
I must especially thank Dr. Justin Hardi, not only because he is a great leader of the RAT Department at DLR, but above all for the person that he is. He was not only a guide for my work, but also a person which is capable of listening and always supporting his team and motivating everyone everyday.
Finally, my deepest gratitudes goes to my mother and my grandmother, who supported me in all the possible ways a person can be supported. Thanks also to my grandfather Enrico, who is not here with me, but whose presence I feel everyday. I know your are watching me from above and I hope you will be proud of me.

Contents

List of Figures **xiii**

List of Tables **xvii**

Nomenclature **xviii**

1 Introduction **1**
1.1 Motivation and goals . . . 2
1.1.1 Logical flow and thesis structure . . . 2

2 Theoretical and experimental background **5**
2.1 Oxygen-Hydrogen Combustion . . . 5
2.1.1 Supercritical conditions and injection . . . 7
2.2 Fundamental equations . . . 11
2.2.1 Main processes in a LPRE combustion chamber . . . 11
2.2.2 Non-dimensional numbers . . . 13
2.2.3 Acoustics . . . 16
2.2.4 Basic concepts of turbulence . . . 20
2.2.5 The Rayleigh criterion . . . 23
2.3 Combustion instabilities . . . 24
2.3.1 Modelling high pressure combustion . . . 27
2.3.2 Modelling combustion instabilities . . . 31
2.3.3 Modelling OH* radiation . . . 34
2.3.4 Experimental and Numerical Test Cases . . . 38

3 CFD solver: the TAU code **49**
3.1 Governing equations . . . 49
3.2 Finite rate chemistry model . . . 50
3.3 Supercritical combustion . . . 51
3.4 Turbulence models . . . 52
3.4.1 One equation turbulence models . . . 54
3.4.2 Two equation turbulence models . . . 56

4 BKH Single Injector Modelling **59**
4.1 The BKH experimental combustor . . . 59
4.2 Numerical approach . . . 64
4.3 Modelling excitation profiles . . . 69
4.4 Steady state results . . . 71
4.4.1 2D steady-state field . . . 71
4.4.2 3D steady state field . . . 72

4.5 1L mode excitation results . . . 76
4.5.1 Comparison with experimental data . . . 87
4.6 1T mode excitation . . . 89
4.7 Influence of the numerical setup . . . 92
4.7.1 Numerical setup: domain and mesh . . . 92
4.7.2 Steady state results . . . 95
4.7.3 Excitation results . . . 98
4.8 Summary . . . 107

5 BKH Cold Flow Modelling 109
5.1 Experimental data and numerical setup . . . 109
5.2 Numerical results . . . 112
5.3 Summary . . . 118

6 OH* Radiation Modelling and Ray-tracing 121
6.1 OH* radiation spectrum . . . 121
6.1.1 Excitation mechanisms . . . 124
6.2 BKH optical diagnostics . . . 125
6.3 The SMART algorithm . . . 127
6.4 Application to the BKH combustor . . . 131
6.5 Summary . . . 136

7 BKH Full chamber analysis 139
7.1 Numerical setup . . . 140
7.1.1 Mesh . . . 143
7.2 Numerical results . . . 145
7.2.1 Flow field . . . 145
7.2.2 Acoustic analysis . . . 153
7.3 Summary . . . 157

8 Conclusions and Outlook 161

Bibliography 170

List of Figures

2.1 Equilibrium vacuum I_{sp} for different propellants' combination [181] . 7
2.2 Generic phase diagram of a pure substance [146]. 8
2.3 Features of supercritical injection. TP and CP indicates the triple point and critical point, respectively [8]. 9
2.4 Subcritical and supercritical injection characteristics [10]. 10
2.5 First tangential (a) and first radial (b) mode of a cylinder calculated with an impedance boundary condition to model the nozzle. 20
2.6 Length of a turbulent diffusion flame L_f as a function of Re [163]. . 22
2.7 Representation of the extended Rayleigh criterion [39] 25
2.8 Thermoacoustic instabilities description [161]. 25
2.9 Sketch of the level of details of the different CFD solvers in terms of computational costs and modelling complexity. 30
2.10 Energy spectrum as a function of the wave number in logarithmic scale [163]. 31
2.11 Cross section of the CRC [155] 41
2.12 Section of CVRC [195] 42
2.13 BKD thrust chamber (a) and optical measurement ring (b) [7]. . . . 45

4.1 BKH [15] 60
4.2 BKH section and injection plane with relevant dimensions[86] 60
4.3 BKH section and injection plane with relevant dimensions[86] 61
4.4 BKH cut with manifolds. Oxygen is displayed in blue, primary and secondary hydrogen in red and window cooling in purple. The chamber volume is in orange.[15] 62
4.5 Position of dynamic pressure sensors in BKH.[15] 63
4.6 BKH optical diagnostics setup concept.[86] 63
4.7 Line-of-sight optical data from a test run without acoustic excitation [86] 64
4.8 Spectrogram and pressure signal registered by PCCDYN2 during a test run at ROF=6 p_{cc}=60 bar[15] 65
4.9 Domain and boundaries of the 2D axisymmetric configuration. . . . 66
4.10 Domain of 3D single injector configuration for the investigation of the acoustic velocity disturbance [15]. 68
4.11 Distribution of the disturbance profiles along the 2D domain. 69
4.12 Steady-state pressure field in the 2D domain. 72
4.13 Steady-state distribution of density (a), temperature (b), OH mass fraction (c) and heat release (d) in the 2D domain. 73
4.14 OH mass fraction (a) and heat release rate (b) closeup. 74
4.15 Density (a), and OH mass fraction (b) and temperature (c) distribution in the 3D axisymmetric configuration. 75

4.16 Isodensity surfaces at ρ =100 kg/m^3 and ρ = 10 kg/m^3 for Sc_t =0.2 and Sc_t =0.3 76
4.17 Pressure signal in the chamber axis at different locations for the entire calculation time at f=3400 Hz. 77
4.18 Pressure signal in the chamber axis at different locations for 3 bar amplitude at steady-state fluctuations for f=3400 Hz. 78
4.19 Volumetric integrated heat release rate at different amplitudes for 3300 Hz excitation frequency. 80
4.20 Density distribution in the chamber volume for different amplitudes at 3200 Hz. 82
4.21 Density distribution in the chamber volume for different amplitudes at 3400 Hz. 83
4.22 Comparison of OH mass fraction distribution at 6 bar 3200 Hz excitation (top) and steady state solution (bottom) 85
4.23 Comparison of OH mass fraction distribution at 3 bar 3400 Hz excitation with representative pressure disturbance including axial velocity (top) and with uniform pressure disturbance (bottom) [15] 86
4.24 Distribution of properties along the axis at the maximum of acoustic pressure oscillation amplitudes at 3 bar 3400 Hz. 86
4.25 Distribution of properties along the axis at the minimum of acoustic pressure oscillation amplitudes at 3 bar 3400 Hz. 87
4.26 Reconstructed DMD images at different phases of the acoustic cycle. LOx core in blue [15]. 88
4.27 Density distribution at the same location of the shadowgraph images at different phases of the acoustic cycle for 1.5 bar pressure excitation amplitude. 88
4.28 Density isosurfaces at 10 and 100 kg/m^3 after ten acoustic cycles . . 90
4.29 Pressure and transverse velocity profiles at various locations over time at steady-state fluctuations. 91
4.30 Integrated heat release rate for the 1T mode excitation. 91
4.31 3D domain for 1L mode (a) and 1T mode (b) simulation. 93
4.32 Hybrid meshes for 1L mode (a) and 1T mode (b) simulation. 94
4.33 Density isosurfaces at ρ= 10 and 100 kg/m^3. The 2D solution is interpolated on a 3D domain to make the results immediately comparable. 96
4.34 Shear layer close up for the three meshes downstream of the injection plane. OH mass fraction is used to identify the shear layer zone. . . 97
4.35 Density isosurfaces at ρ= 10 and 100 kg/m^3 for the box configuration. 99
4.36 Pressure signal at steady-state fluctuations for the three configurations at the tip of the flame, x=50 mm (Amplitude 3 bar, frequency 3200 Hz). 100
4.37 Pressure signal at steady-state fluctuations for the 2D and 3D unstructured configuration at the tip of the flame, x=50 mm (Amplitude 3 bar, frequency 3400 Hz). 101

4.38 Comparison of the density field after 16 acoustic cycles for the three configurations. . . . 102
4.39 Comparison of the volumetric heat release rate for three different configurations at steady-state fluctuations. . . . 103
4.40 Comparison of density isosurfaces at ρ=100 and 10 kg/m^3 after ten acoustic cycles. . . . 105
4.41 OH partial density integrated over the domain for the half and the full domain. . . . 106
4.42 Volumetric heat release rate for the half and the full domain. . . . 106

5.1 Spectrogram of dynamic pressure data from BKH cold flow test and dynamic pressure data. . . . 110
5.2 Dynamic pressure oscillations at secondary nozzle location from experimental data during 1T mode excitation. . . . 111
5.3 Simplified BKH geometry used for preliminary testing of the siren boundary condition. . . . 112
5.4 Pressure signal at the top and bottom wall sensors during 1T mode excitation. . . . 113
5.5 Comparison of dynamic pressure signals at top and bottom wall sensors. 114
5.6 Comparison of dynamic pressure signals at secondary nozzle sensor. . 115
5.7 Normalized dynamic pressure distribution at different phases of the cycle. . . . 116
5.8 FFT of the dynamic pressure signal of the bottom wall sensor. . . . 117
5.9 FFT of the dynamic pressure signal of the secondary nozzle sensor. . 117

6.1 OH* emission spectrum at p=62 bar and T=3000 K [107] 122
6.2 Flame emission spectra of BKD for different pressure levels. The impact of self-absorption becomes more important with increasing pressure [58]. . . . 123
6.3 Spectrum of pure OH at T = 3000 K and p = 1 bar. The pure emission spectrum (e) and radiance spectrum (L) which takes into account self-absorption are compared [56]. . . . 124
6.4 BKH optical diagnostics setup [15]. . . . 126
6.5 Line-of-sight access and images recorded during a BKH test without acoustic excitation [15]. . . . 126
6.6 Sketch of the ray tracing algorithm. [219]. . . . 130
6.7 Mesh and domain used for the application of SMART [15] 132
6.8 Temperature (a), pressure (b) and OH mass fraction distribution (c) in BKH. The load point refers to 60 bar chamber pressure and ROF 6 [15]. These distributions are used as an input for the ray tracing algorithm which generates the pseudo-OH* images 132
6.9 Ray path visualization through refractive index gradient. The gradients correspond to the increase in the LOx jet density at different locations. . . . 133

6.10 Comparison between the time averaged OH* radiation measurements (a), the LOS integrated image [15] (b) and the image obtained with SMART (c). [219] 134
6.11 Integrated radiance along the ray path. 135
6.12 Difference in total radiance prediction with and without self-absorption 137
6.13 Relative difference in simulated total radiance between fully ray traced and 1D integrated image. 138

7.1 BKH geometry used for the RANS simulation. 141
7.2 Mesh of the steady state chamber model. 144
7.3 Density (a), OH mass fraction (b) and pressure field (c) at steady state. 146
7.4 Heat release field and OH isosurfaces inside the BKH chamber at centerplane and outer plane. 147
7.5 Comparison of the density field as seen from the window between the new simulation and the previous simulation by Beinke [15]. 148
7.6 Comparison of the OH mass fraction distribution between the new setup (top) and the simulation by Beinke (bottom) [15] 149
7.7 Temperature distribution and OH mass fraction isosurface. 150
7.8 Comparison of experimental data and the application of SMART on the new solution and previous simulation by Beinke [15]. 151
7.9 Comparison of the 1D integrated radiance and the SMART image. . 152
7.10 Speed of sound distribution at the centerplane. The regions with further refinement are highlighted. 154
7.11 Variation of the mass fractions of the species along the domain. . . . 154
7.12 Radial average of the needed properties. 155
7.13 Domain and mesh used in the acoustic solver. 155
7.14 Mode shapes 156
7.15 1T mode with impedance boundary condition at the secondary nozzle. 158

8.1 Comparison of the OH mass fraction distribution in the window region of the LES simulation and the application of SMART in the same area. 165
8.2 OH mass fraction distribution and ray paths at different phase angles of the cycle 167
8.3 Density distribution and ray paths at different phase angles of the cycle 168

List of Tables

2.1 Critical properties of oxygen and hydrogen 9

4.1 Values for the single injector configuration simulated operating point. Mass flow rates are calculated for the single element. 66
4.2 Deviation from the mean p_{cc} at X = -100 mm and X = -50 mm inside the LOx post at steady-state fluctuations for the different amplitudes and frequencies of the applied disturbance. 79
4.3 Mean volumetric heat release at steady state fluctuations. 80
4.4 Ratio between gain of volumetric heat release rate and pressure signals. 81
4.5 Mean difference between the length of the LOx core at steady state and for the different excitation conditions 84
4.6 LOx core length measured at different densities and L/D ratio for the cylindrical configuration. 95
4.7 LOx core length measured at different densities and L/D ratio for the box configuration. 98
4.8 Heat relase rate fluctuations at p'=3 bar f=3200 Hz. 102
4.9 Heat release rate fluctuations for the half and full domain during 1T mode excitation. 105

5.1 Operating conditions for the cold flow load point. 111

6.1 Operating conditions 131

7.1 Experimental data for the considered load point. 142
7.2 Calculated values for the considered load point 142
7.3 Results of the acoustic analysis LNS 157
7.4 Results of the acoustic analysis Helmholtz by Beinke [15] 157

Nomenclature

Acronims

BKD	Brennkammer D, Combustion chamber D
BKH	Brennkammer H, Combustion chamber H
CAA	Computational Aero-Acoustics
CFD	Computational Fluid Dynamics
CRC	Common Research Chamber
CVRC	Continuously Variable Resonant Combustor
DC	Detailed Chemistry
DDES	Delayed Detached Eddy Simulations
DES	Detached Eddy Simulations
DLR	Deutsches Zentrum für Luft- und Raumfahrt, German Aerospace Center
DMD	Dynamic Mode Decomposition
DNS	Direct Numerical Simulations
EFRM	Equilibrium Filtered Radiation Model
EOS	Equation of State
FDF	Flame Describing Function
FTF	Flame Transfer Function
HF	High Frequency
LES	Large Eddy Simulations
LF	Low Frequency
LOx	Liquid Oxygen
LPREs	Liquid Propellant Rocket Engines
MVF	Mean Velocity Field
ONERA	Office National d'Etudes et de Recherches Aérospatiales, French Aeronautics and Space Research Center
RANS	Reynolds Averaged Navier-Stokes Simulations
ROF	Oxidizer-to-fuel ratio
RTE	Radiative Transfer Equation
SM	Spectral Model
SSM	Space Shuttle Main Engine
URANS	Unsteady Reynolds Averaged Navier-Stokes Simulations
UV	Ultra Violet D

Non-Dimensional numbers

Pr	Prandtl number
Re	Reynolds number
Sc	Schmidt number
St	Strouhal number
We	Weber number
VR	Velocity Ratio

Physical quantities

L_λ	Spectral radiance
$\boldsymbol{\tau}$	Tensor of viscous stresses
$\boldsymbol{f}$	External forces
$\boldsymbol{I}$	Unit tensor
$\boldsymbol{P}$	Tensor of viscous forces
$\boldsymbol{q}$, Q	Heat flux
$\boldsymbol{r}$	Position vector
$\boldsymbol{u}$	Specific internal energy
$\boldsymbol{V}$	Velocity vector
η_k	Kolmogorov scale
γ	Ratio of specific heats
κ	Strain
κ_λ	Absorption spectrum
λ	Wavelenght
μ	Dynamic viscosity
ν	Kinematic viscosity
ω	Angular frequency
ϕ	Phase angle
ρ	Density
σ	Surface tension
τ	Time delay
c	Speed of sound
C_p	Specific heat at constant pressure
C_v	Specific heat at constant volume
D	Diffusion coefficient
d	Diameter
e_λ	Emission spectrum
f	Frequency
f_h	Eiegenfrequency of the h^{th} mode
g_0	Standard gravity

h	Enthalpy
I	Intensity
K	Heat conductivity
k_f,k_b	Reaction rate coefficients
k_h	Wavenumber of the h^{th} Fourier component
k_{lam}	Laminar thermal conductivity
k_T	Turbulent thermal conductivity factor
l_t	Turbulent lenght sclae
$n(\boldsymbol{r})$	Continuously changing refractive index
p	Pressure
R	Gas constant
s	Entropy
T	Period
t	Time
u, v	Velocity
V	Volume
v_e	Effective exhaust velocity
I_{sp}	Specific impulse (s)
J	Momentum flux ratio
p_{cr}	Critical pressure
T_{cr}	Critical temperature

Symbols

α,β	Reaction rate coefficients
δ_{ij}	Kronecker delta
A	Amplitude
L	Lenght
M	Molecular weight
n	Number of moles
X	Molar fraction
G	Gaseous
L	Liquid
R	Reflection coefficient
Z	Impedance

Superscripts

$\hat{f}$	Real part of complex number
$\overline{f}$	Mean quantity

$\sqrt{\overline{f'^2}}$	Root mean square
$\tilde{f}$	Favre averaged, Turbulent quantity
f'	Perturbation or oscillating value

Subscripts

f	Fuel
g	Gaseous
l	Liquid
lam	Laminar
ox	Oxidizer
t	Turbulent

1 Introduction

Combustion instabilities have always represented a challenge for liquid rocket propellant engines (LPREs) . In LPREs, a great amount of energy is released during combustion and this can lead to the occurrence of coupling phenomena which may have influence on the stability of the operating conditions of the engine, since also a small percentage of energy trasnferred from the combustion process to the system may cause instability phenomena. This can in turn lead to the failure of the engine and, in some cases, of the whole mission. It is then easy to understand that in many practical cases, combustion instabilities are an undesidered phenomenon, and in particular thermoacoustic instabilities are extremely dangerous for LPREs, if not properly handled. A widely accepted classification of combustion instabilites has been made based on the frequency of the pressure oscillations observed in the system: low frequency (LF) combuston instabilities, also called chugging, and high frequency (HF) combustion instabilities. LF instabilities are generally associated to the propellants feed system and have a frequency less than 1000 Hz and have not destructive consequences for the engines. HF instabilities occur at a frequency greater than 1000 Hz and are the most dangerous and potentially damaging. Other criteria than the frequency value can be adapted to distinguish LF and HF, based for example on the Strouhal number, in which the frequency is scaled with a characteristic length of the engine, and here one can say that one is talking about LF when the Strouhal number is smaller than one, and HF instabilities when it is greater.
HF combustion instabilities are not fully understood because of the complexity and number of phenomena involved. The occurrence of the phenomenon is triggered by the coupling of pressure oscillations and unsteady energy release which derives from the combustion process.The coupling leads to an unsteady heat release rate and the phenomena close in a loop. This could lead also to unexpected high temperatures at the walls of the chamber, adding a critical point in the design of a new combustion chamber.
Due to the extreme environment which develops inside the combustion chambers at typical operating conditions in LPREs, it is difficult to investigate experimentally the HF instability phenomenon. Full scale tests are not only difficult, but also expensive, and this is the reason why in research centers experimental combustors and numerical modeling are used. The increased computational capabilities developed in the last years helped a lot in the study of this phenomenon, but there is still much to do because of the variety of processes which should be simulated and are involved in the occurrence of combustion instabilities: injection, atomization, vaporization, mixing and reaction of propellants. The detailed numerical simulation of all these processes is extremely complex and expensive, and it cannot be applied for industrial applications. Computational Fluid Dynamics (CFD) tools have been then developed through

the years to try and have a better understanding of the different phenomena. These CFD tools have anyway to be validated against experimental data in order to build effective means to improve the predictive capabilities of the codes. The focus of this work is the combustion chamber operated at DLR, named Brennkammer-H (BKH). BKH is an experimental combustors used to investigate HF instabilities and work at operating conditions representative of upper-stage rocket engines. It is equipped with optical systems and windows, which allow the recording of optical data by high-speed cameras and the observation of the flame zone during operations. The equipment of this combustors is crucial for the purposes of this work, which aims not only to study numerically the flame response during acoustic excitation, but also the comparison of images from the experiments and from CFD simulations. BKH is provided with a toothed wheel or siren, which periodically interrupts the flow through a secondary nozzle and excites the different chamber modes.

1.1 Motivation and goals

This work aims to simulate the acoustic response of a flame subject to different excitation conditions and compare and validate the results with experimental data collected by sensors and cameras. This is done by simulating the aforementioned combustion chambers' in different operating conditions and comparing the results with previous simulation results and experiments, in order to validate the models used. The validation of the models can play a crucial role in order to investigate the underlying physics of combustion instabilities and flame-acoustics interaction. The comparison between experimental data and simulation results is sometimes difficult because of the extreme environment which develops in a combustion chamber, in which a fundamental quantity which is used to investigate combustion instabilities, the heat release rate, is not directly measurable. A physical quantity which is directly observable with the use of high speed cameras is the OH* radiation produced during the combustion of liquid oxygen (LOx) and H_2. Therefore, a model for the flame and ray-tracing algorithms have been developed in order to simplify the comparison beteen two-dimensional images recorded by the cameras and three-dimensional results obtained with CFD simulations. In the next subsection, the steps used to achieve the goals described here are presented more in detail.

1.1.1 Logical flow and thesis structure

Before proceeding with the simulation of a full 3D combustion chamber, some preliminary work was needed. The first step is the simulation of a single injector domain representative of the central injector of BKH subject to a more realistic acoustic forcing profile with respect to the previous work of Beinke [15], both for longitudinal and transverse forcing. An aspect which was not investigated so far was the influence of the numerical setup on the simulation results, and this was done by changing the geometry of the domain, the mesh and the boundary

conditions for the simulation of the flame response when subject to transverse excitation in a single injector configuration. Then, a first step towards the full 3D modeling was done, simulating a BKH operating point with cold flow in order to test a new boundary condition which reproduced the behavior of the toothed wheel when interrupting the flow through the secondary nozzle of BKH. Once this boundary condition was validated and the influence of the numerical setup estimated, the necessary setup to start the full chamber simulation with excitation was ready. In order to have a tool to compare optical data from the high speed cameras and CFD results, a flame radiation model and ray-tracing algorithms producing pseudo-OH* images was developed. This tool was first tested on an existing test case by [56] and then applied to an existing steady-state solution of BKH by [15]. The same tool was then applied to a BKD test case without optical access, in which a probe collecting the radiation coming from the flame had to be also modelled. After testing the tool on these different test cases, it was then applied to the transient simulation of BKH on a region of the limit cycle where steady-state acoustic pressure and velocity fluctuations were reached, and compared with the corresponding data coming from the experiments.
Chapter 2 provides a theoretical background on the relevant topics of this work: oxygen-hydrogen combustion, fundamental equations of acoustics and combustion with a focus on the Rayleigh criterion, together with a literature overview on combustion instabilities and radiation modelling. In chapter 3, the CFD solver used for this work, the in-house DLR TAU code is described. Chapter 4 is dedicated to BKH single injector modelling. Chapter 5 introduces the toothed wheel boundary condition and its application on a cold flow BKH run. Chapter 6 is dedicated to the full chamber simulation with hot flow and acoustic excitation applying the siren boundary condition. Chapter 7 is dedicated to the tool which has been developed to produce pseudo OH* images to be compared with experimental optical data, first describing it in detail and then showing the application to BKH and BKD simulations. Chapter 8 provides conclusions and outlook for future work.

2 Theoretical and experimental background

The investigation of combustion instabilities has always been a challenge since the start of research in the field of space propulsion. They were observed for the first time in the 1930s both in liquid and solid propellant rocket engines. This chapter aims to provide the state-of-the-art knowledge of theory and experiments which are fundamental to understand the scope of this work. First, an overview of the LOx/H_2 propellant combination is presented, together with the fundamental equations describing the combustion instability phenomenon, which involve acoustics and combustion processes. Then a literature overview is given, which summarizes the research work done from different groups, both numerical and experimental. Another topic which will be considered is the modeling of OH* emission from the flame, with an introduction to the problem of modeling OH* and the strategy used to try and fill the gap of knowledge of this phenomena in cryogenic high pressure combustion. The last part of the chapter describes the experimental combustors used for the investigation of instabilities both numerically and experimentally.

2.1 Oxygen-Hydrogen Combustion

The focus of this work is on a combustion chamber operated with LOx/H_2, so an introduction on why this propellant combination is chosen and the underlying combustion reaction is needed.
There are different propellant combinations which can be used in bipropellant LPREs. The most common used oxdizers are:

- Oxygen (O_2): It is cryogenic. The evaporation temperature at ambient pressure T_{ev} is 90 K and its density is quite high ($\rho = 1140$ kg/m^3). When great quantities are needed, it should be produced close to the place of use.
- Fluorine (F_2): It is cryogenic ($T_{ev} = 85$ K) and with very high density ($\rho = 1509$ kg/m^3), it is extremely energetic and gives high performances. The main drawbacks are that it is extremely toxic, reactive and corrosive, with related toxicity of combustion products.
- Nitric acid (HNO_3): It is liquid between T_s=232 K and T_{ev}=356 K. It is highly corrosive and it is used generally mixed with other species. It has very high density ($\rho = 1549$ kg/m^3 at T = 293.15 K).
- Nitrogen tetroxide (N_2O_4): It is liquid between T_s=262 K and T_{ev}=294 K. It is the most common storable oxidizer but it requires tight housings because of its high vapor tension. Density is $\rho = 1447$ kg/m^3 at T = 293.15 K

On the other hand, fuels are:

- Hydrocarbons (CH_x): They are relatively cheap, available and easy to transport.In the USA RP-1 ($CH_{1.96}$, similar to cherosene,ρ = 800 kg/m^3) has been used for a long time (for example in the F-1 engine). One of its advantages is that it minimizes the phenomenon of fouling (formation of sticky sediments in the cooling channels). A strong research effort is now on methane (CH_4), which is cryogenic (T_{ev}=112 K), but being more dense and cheaper than hydrogen.
- Hydrogen (H_2): It is cryogenic (T_{ev}=20 K) with very low density (ρ = 70 kg/m^3). It is not easy to handle due to the very low evaporation temperature and it needs big tanks to be stored. Nevertheless, it has the advantage of having the highest specific impulse (I_{sp} above 400 s) with respect to other propellants' combinations.
- Hydrazine (N_2H_4): It can be stored and remain stable for long periods of time (also 15 years), it has a high freezing point (T_s = 275 K), T_{ev}=387 K and ρ = 1023 kg/m^3 at T = 293.15 K.
- Unsymmetrical Dymethyhydrazine, UDMH ($(CH_3)_2NNH_2$): It is an organic derivative of hydrazine with similar properties but lower freezing temperature (T_s = 216 K), T_{ev}=336 K, lower I_{sp} and ρ = 850 kg/m^3 at T = 244 K.
- Monomethylhydrazine, MMh (CH_3NHNH_2): It is an organic derivative of hydrazine but with a wider temperature range of the liquid state (T_s = 221 K, T_{ev}=361 K).
- Aerozine: Its components are 50% UDMH and 50% hydrazine.

The LOx/H_2 propellant combination presents important technical challenges due to the fact that they are both cryogenic propellants [1]. To prevent evaporation and boiling off, insulation from heat sources present in a rocket engine (e.g., exhaust and air friction during atmospheric flights) must be accomplished. In space, the rocket engine must be protected from the heat coming from sun radiation. When liquid hydrogen absorbs heat, it expands rapidly; thus, venting is necessary to prevent the tank from exploding. Metals exposed to the extreme cold of liquid hydrogen become brittle. Moreover, liquid hydrogen can leak through minute pores in welded seams. Despite all the difficulties that hydrogen can present, the great advantage that it presents is the extremely high specific impulse I_{sp}, which is one of the performance parameters used for rocket engines. The specif impulse is defined as the thrust integrated over time per unit weight-on-Earth of the propellant:

$$I_{sp} = \frac{v_e}{g_0} \tag{2.1}$$

where v_e is the effective exhaust velocity measured in m/s and g_0 is the standard gravity, 9.80665 m/s^2.

[1] gases that can be liquefied only at extremely low temperatures

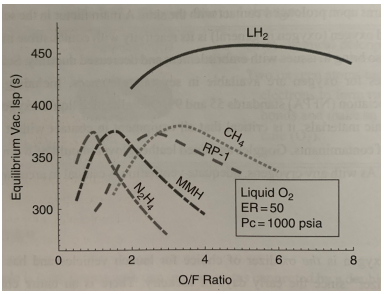

Figure 2.1: Equilibrium vacuum I_{sp} for different propellants' combination [181]

Moreover, products of the combustion reaction between oxygen and hydrogen is mostly water vapor, representing a big advantage in terms of environmental pollution. Liquid hydrogen is reacted with liquid oxygen to form water with a stoichiometric heat of reaction of 286 kj/mol:

$$2H_{2(g)} + O_{2(g)} \rightarrow 2H_2O_{(l)} + 572kJ \tag{2.2}$$

When pure hydrogen reacts with pure oxygen, the flame produced emits in the UV spectrum, being therefore invisible to the human eye. However, it results often in ice crystals in the exhaust plume with a white trail. As already mentioned, in terms of I_{sp} there is practically no competitor with this combination because of the low exhaust molecular weight and high combustion temperature. It should be mentioned however that also if the maximum I_{sp} is obtained at a mixture ratio of 4.7, the practically used mixture ratios are bewtween 5.5 and 6 because of difference in density between the fuel and the oxidizer. Figure 2.1 shows the comparison between different type of propellant combinations, where it is clear the advantage in using the hydrogen/oxygen combination.
The performances in terms of I_{sp} of liquid hydrogen, typically associated with liquid oxygen, have made hydrogen to be the choice for fueling many launch vehicles, both booster and upper stages with different engine cycles. Examples are the SSM RS-25E of the Space Shuttle which operated with a staged combustion cycle , The Vulcain engine and the HM7B of Ariane which are gas generator engines and LE-7/A of H-II Series which uses again a staged combustion cycle.

2.1.1 Supercritical conditions and injection

As already mentioned before, the evaporation temperatures of liquid oxygen and hydrogen are 90 K and 20 K, respectively, so at the ambient temperature and pressure they are in a gaseous state. To prevent the propellant from boiling-off, the tanks must be equipped with release valves to avoid explosions caused by the pressurization. Liquid hydrogen is typically used in rocket engines to cool the

combustion chamber walls, being then heated and passing from a liquid to a gaseous state, and then injected in the combustion chamber. Oxygen is typically injected in a liquid state at temperatures of about 100 K. Figure 2.2 shows a generic phase diagram.

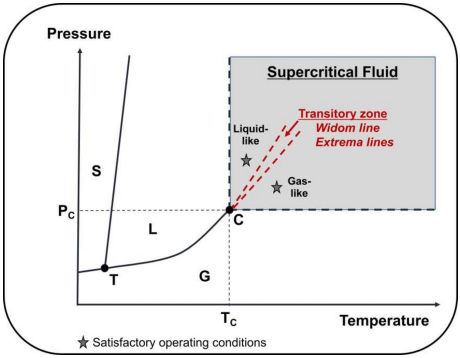

Figure 2.2: Generic phase diagram of a pure substance [146].

Phase diagrams typically plot pressure on the y-axis and temperature on the x-axis. The labels in the plot indicate the stable state of a system in equilibrium. The combinations of pressure and temperatures at which the phases can exist in equilibrium are represented by the lines. Crossing the lines in the right or left direction represent a different change of phase. Sublimation (solid to gas) and deposition (gas to solid) are represented by the S-G boundary. Melting (solid to liquid) and freezing (liquid to solid) are obtained by crossing the S-L line. Vaporization (liquid to gas) and condensation (gas to liquid) are represented by crossing the L-G boundary . In the phase diagram, two points are highlighted: the triple point and the critical point. The triple point represent the pressure and temperature combination at which the three phases (solid,liquid, vapor) coexist in thermodynamic equilibrium. The critical point is represented by a critical pressure (p_{cr}) and a critical temperature (T_{cr}) at which the liquid and gaseous phases are no more distinguishable one from another and merge together. In the region close to the critical point the characteristics of the liquid and vapor phases change dramatically and and the phases become more and more similar. At temperatures and pressures above the critical point, the substance is called supercritical fluid. A supercritical fluid has properties which are in between a liquid and a vapor phase. An important feature of a supercritical fluid is the absence of surface tension and latent heat. A supercritical fluid is also a good solvent: as the density of the fluid at constant increases, the solubility in the supercritical fluid increases. Density increases with pressure, therefore the solubility in a supercritical fluid increases with pressure. The behavior when varying the temperature is slightly different. When increasing the temperature at constant density, solubility increases.
In the proximity of the critical point, it can happen that the density drops with a

small increase of temperature, and then in this region solubility often drops with increasing temperature. This phenomenon was discussed by Oschwald et al. [132], and named "pseudo-boiling" because of the similarity with the vaporization which occurs at subcritical conditions. For the purposes of this work, we are interested in the characteristics of oxygen and hydrogen, which are summarized in Table 2.1

	Critical temperature [K]	**Critical pressure [bar]**
O_2	154,6	50,4
H_2	33,1	13

Table 2.1: Critical properties of oxygen and hydrogen

Combustion chambers of typical rocket engines are characterized by high pressures to maximize thrust and specific impulse. This translates into the fact that the chamber pressures of operating engines are typically higher that the critical pressure of one or both propellants. The SSME operated at p/p_{cr}=4.4, H-II Series had p/p_{cr}=2.40 and the Vulcain had p/p_{cr}=2.28. Figure 2.3 shows the characteristics of supercritical injection [8]. The pseudo-boiling line is also called

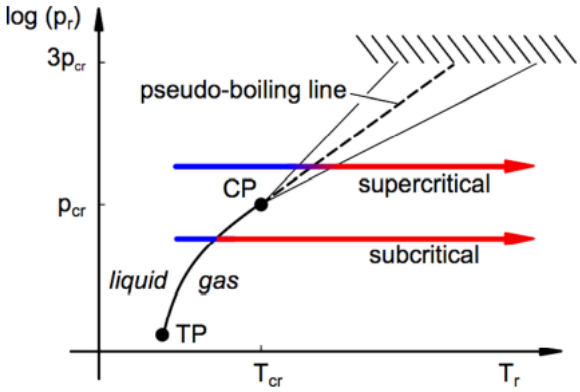

Figure 2.3: Features of supercritical injection. TP and CP indicates the triple point and critical point, respectively [8].

Widom line and it is the extension of the coexistence line in the supercritical region, separating the liquid-like and gas-like phases. In LPREs fuelled with LOx/H_2 it is possible to have transcritical injection. This term refers to a fluid in subcritical conditions which is injected in a supercritical environment. The fluid it is then rapidly heated at supercritical temperatures before combustion occurs. Looking at the values in Table 2.1, it is easy to understand that in modern LPREs, hydrogen is injected at supercritical conditions, whereas oxygen can be injected at both subcritical or supercritical conditions. In this work the considered

combustion chambers are operated at pressures above the critical pressure of the oxygen, and then oxygen experiences transcritical injection.
It is important to say that a classification based solely on the critical pressures of the components of a mixture is too simplified because the critical pressure of a mixture can exceed the one of the pure propellants [172]. An injection process can be supercritical with respect to the injected fluid and the gas could still show subcritical features in the break-up of the jet. Experimental work from Mayer [141] and Manin [136] and numerical work from Dahms [40],Qui [170] and Gaillard [63] demonstrated this phenomena. Figure 2.4 shows the difference between injection at subcritical and supercritical pressure for LOx/H_2 [9, 10]. Banuti

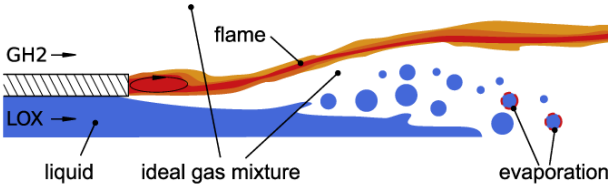

(a) Subcritical atomization.

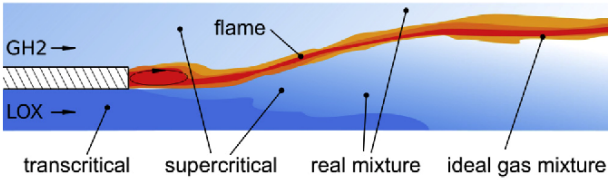

(b) Supercritical jet disintegration.

Figure 2.4: Subcritical and supercritical injection characteristics [10].

investigated the thermodynamic structure of supercritical LOx/GH_2 diffusion flames with coaxial injection at representative conditions for LPREs performing both 1D and LES simulations [10]. The real fluid effects are restricted to the region in which the LOx stream enters the chamber in a liquid state. The mixing process takes place almost completely outside of this region, where the conditions can be then compared to ideal gas conditions. Mixing of real fluids occurs in a zone which wraps the liquid oxygen, and the product which mixes with oxygen under real fluid conditions is only water. This way, the supercritical injection is similar to a subcritical flame, where a clear distinction between oxygen and hydrogen stream and the surrounding ideal gas can be made. The thermodynamic transitions which can be identified are the pseudo-boiling from a liquid to a gaseous state and then the transition to a supercritical ideal gas state outside the flame zone. This shows how important is to have an efficient chemistry model for the transcritical injection conditions, which not only allows to correctly resolve the chemistry but also to save considerably computational resources.

2.2 Fundamental equations

In this section, the equations of the physics which is relevant for this work are addressed. The acoustics of the combustion chamber is related with the combustion processes and the two phenomena close in a feedback loop and the two are closely bounded together. This underlines the importance of introducing the fundamental equations of these processes in order to better understand the physics and to put them in relation presenting at the end of the section the Rayleigh criterion, which has been the most important description about the occurrence and mechanisms of combustion instabilities. The next section presents a short overview of the main processes occurring in a rocket combustion chamber.

2.2.1 Main processes in a LPRE combustion chamber

2.2.1.1 Injection

The goal of the injection system and the combustion chamber of a LPRE is to convert the liquid propellants injected in the chamber into gaseous products at high temperatures and pressure. The gases are then expanded through the exhaust noozle, converting the thermal and potential energy into kinetic energy in order to produce thrust. Although the role of the nozzle is clearly fundamental in rocket, for the purposes of this work it will not be discussed because the nozzle doesn't play an active role in high frequency transverse combustion instabilities. The role of the nozzle is essentially setting the downstream boundary conditions on waves in the chamber depending on its position, and attenuating longitudinal instabilities [50].
The sequence of the processes occurring in a combustion chamber starts with the injection of the propellants. Injection is a fundamental process in the analysis of combustion instabilities and the design of the injectors plays a major role. The injectors configurations and operating conditions are responsible about how the propellants mix and burn in the chamber, and consequently of its static and dynamic behavior. Injection meters, distributes and atomizes propellants for efficient combustion within the chamber. Many of the two phase flow and jet atomization characteristics are still not yet fully understood and so the injection design is still a challenge in the rocket propulsion field.
Several types of injectors can be identified, but in the frame of cryogenic propellants the coaxial injectors are the most used [181]. In the LOx/H_2 engines, liquid oxygen flows through the central channel and is isolated form the outer annulus by a LOx post. The design of the LOx post is another critical aspect, because it has to isolate the flame anchoring region at the post tip from pressure waves in the combustion chamber. The stability of the anchoring region is influenced by the hydrogen injection temperature, so a hydrogen temperature ramping test is often done to check the range of temperatures over which the flame anchors without instabilities. Hulka and Hutt [105] compiled an extensive review of coaxial injectors used in LOx/H_2 rocket engines stability tests with the goal to identify the type of injector design and operating conditions which could contribute

to the onset of combustion instabilities. They found that the outer-to-inner-jet exit velocity ratio played a key role in many of the studies defining stability, and that high-velocity ratios tended to extend the engine stability range. For most of the investigated injector designs and operating conditions, a velocity ratio of about 10 was the maximum value where combustion instability occurred. Section 2.2.2.3 will explain in detail the influence of this parameter on some engine processes.

2.2.1.2 Atomization

After being injected in the chamber, the propellants' fluid streams experience break-up. When dealing with LOx/H_2 at subcritical pressures, the velocity difference between the two streams is considerable and this generates fluctuating accelerations. The onset of these accelerations triggers the Rayleigh-Taylor instability which can eventually grow and cause the peeling of the main LOx jet. This processed is referred to as primary atomization. The liquid structures produced by this process are then ejected towards the outer gas flow, experiencing a secondary break-up when the liquid surface tension cannot balance inertia forces anymore. The liquid jet is then reduced in even smaller liquid droplets, which increase the surface area of the jet and enhance a higher kinetic energy in order to increase heat exchange and mixing. However, the atomizaton process is different when dealing with supercritical or transcritical jets, where no real atomization takes place, but rather a mixing of fluids with different densities. Mayer and Tamura [140] observed that at supercritical pressure conditions, during ignition and combustion the interface between the propellants is always separated and affected by a layer of hot reacting gas, but as the pressure approaches and then overcomes the critical value, then droplets do not exist anymore and the jet shows thread-like structures that rapidly dissolve. Candel and Pons [27, 165] and Oschwald et al. [133, 156] independently demonstrated differences between subcritical and supercritical pressure conditions in cryogenic flames of fundamental quantities such as liquid core lengths, turbulent length scales and jet breakup regimes.

2.2.1.3 Vaporization

When the propellants are heated from the surrounding combustion processes and evaporate to turn into the gas state vaporization occurs. Heat is convected from the high temperature environment of the chamber. As already discussed before, supercritical conditions are slightly different from subcritical ones because the surface tension drops and no droplets are formed. Sirignano et al. [106, 225, 226] discussed and investigated droplets and spray vaporization at subcritical and supercritical pressures to study combustion and dynamic responses to oscillatory ambient conditions. Those studies established that the vaporization process can be a rate-controlling process for driving combustion instabilities.

2.2.1.4 Mixing

As the propellant are in a gaseous state they mix so that they can react and chemical reactions can take place. The mixing is achieved with convection or diffusion of the species. Convection takes place because of two combined effects:

the heterogeneity of the fluid and the forces acting on it, typically buoyancy forces. Convection is typical of impinging injectors. Diffusion is the movement of species from a zone at higher concentration to a zone with lower concentration, driven by free Gibb's energy gradients. In coaxial injectors, the forces driving the mixing are the shear stresses between the two fluid streams with different velocity and molecular and turbulent diffusion brings oxidizer and fuel in the reaction zone. The flames investigated in this work are non-premixed flames, also called diffusion flames and this is explained by the fact the mechanism driving the burning rate is diffusion. In diffusion flames, combustion takes place only at the shear layer between oxidizer and fuel. Turbulence helps the mixing of the propellants, resulting in a more efficient combustion.

2.2.1.5 Combustion

Combustion is an exothermal chemical reaction between a fuel and an oxidizer which releases energy in form of heat. In order to react, fuel and oxidizer have to be in a suitable oxidizer-to-fuel ratio (ROF) and an activation energy limit has to be overcome to trigger the reaction. An ignition system is then necessary to give the needed energy for the reaction to take place.

2.2.2 Non-dimensional numbers

In the short review of the fundamental processes related to operational combustion chamber, several key points were underlined when talking about injection ad atomization of the propellants which could trigger combustion instabilities. In this section, an overview of non-dimensional parameters which are typically used in fluid dynamics will be presented. These non-dimensional groups give the measure of the behavior of fluids under different conditions, which will be highlighted for each quantity.

2.2.2.1 Reynolds number (Re)

The Reynolds number describes the behavior of a fluid flow, indicating if it can be classified as laminar or turbulent and indicating the transition from one regime to the other. It is particularly useful when dealing with boundary layers and shear layers. The Reynolds number (Re) is defined as the ratio of the inertial forces and the viscous forces acting on a fluid which is subject to internal movement caused by different fluid velocities. The difference in the velocity of the streams generates friction, which is one of the causes of turbulent flows. On the other hand, the viscosity of the fluid inhibits turbulence. The Reynolds number weights these two phenomena and can be an indicator whether turbulence occurs or not in specific conditions.
The Reynolds number is defined as

$$Re = \frac{uL}{\nu} = \frac{\rho u L}{\mu} \tag{2.3}$$

where ρ is the density of the fluid in kg/m^3, u is the flow speed in m/s, L is a characterstic linear dimension of the element in m and ν is the kinematic viscosity

of the fluid in m/s^2, defined as ρ/μ, where μ is the dynamic viscosity in $Pa \cdot s$ or $N \cdot s/m^2$ or $kg/(m \cdot s)$. For a boundary layer over a flat plate, typically the instability arises for Re_x 5x10^5, where x is the distance from the leading edge of the flat plate and the flow velocity is the freestream velocity outside the boundary layer.
In a turbulent flow, a range of scales of the time-varying fluid motion is present and the size of the large scales of the flow, also called eddies, depend on the geometry of the flow itself. In this case, Re is an indicator which tells at what scales viscous dissipation is present. This happens when viscous forces become at least of the same order of magnitude of the inertial forces, and the energy dissipation by viscous forces can take place.

2.2.2.2 Weber number (We)

The Weber number (We) is often used in analysing fluid flows where a shear layer between two streams is present. It compares the inertial and surface tension forces of the fluid.
The Weber number is defined as

$$We = \frac{\rho u^2 L}{\sigma} \tag{2.4}$$

where ρ is the density of the fluid in kg/m^3, v is the flow speed in m/s, L is a characteristic linear dimension of the element in m (typically a diameter) and σ is the surface tension in N/m . For coaxial injectors, where two streams with different velocities are present, typically a gas and a liquid, the expression for the Weber number varies as follows.

$$We = \frac{\rho_g (u_g - u_l)^2 d_l}{\sigma} \tag{2.5}$$

The subscripts l and g indicate the liquid and gaseous streams, respectively, and d is a diameter . Farago and Chigier [52] used the Weber number to classify the atomization process depending on the morphology of the liquid jet. They found three different types of jet break-up and classified them based on different ranges of the Weber number: the Rayleigh break-up regime (We<25), membrane type break-up (25<We<100) or fiber break-up
(100<We<500).
The liquid Reynolds number has also an influence of the disintegration of the jets as Eroglu and Chigier [49] pointed out for We<300, being Re the ratio between inertial and viscous forces. Yang et al.[235] observed the effects of the momentum flux ratio and Weber number on the atomization processes of LOx/H_2 and LOx/CH_4 flames, observing that the Weber number mainly influences secondary atomization and flame angles.
In BKH, Hardi [104] observed a fiber break-up regime according to the corresponding liquid Reynolds number and Weber number, but fibers were not observed in high-speed camera images, since probably these structures vanish rapidly when a hot flame is present.

2.2.2.3 Momentum flux ratio (J)

In coaxial injectors, the injection of the propellants is different for the fuel and the oxidizer. The velocity ratio give the relative velocity of the two jets and it is defined as :

$$VR = \frac{u_f}{u_{ox}} \tag{2.6}$$

Hulka and Hutt [105] observed that in near- and supercritical injection conditions, small changes in temperature can results in important changes in density, also if the temperature is measured at the exit of the injection plane. This strongly affects the accuracy of the measurements of the velocity ratio.
The momentum flux ratio takes into account not only the relative velocity of the two streams, but also the differences in the density, being defined as :

$$J = \frac{(\rho u^2)_f}{(\rho u^2)_{ox}} \tag{2.7}$$

Engelbert et al. [48] observed that the momentum flux ratio has an impact on the breakup length of the liquid core, typically the oxidizer. Davis et al. [42, 43] derived an experimental correlation between J and the lenght of the intact core L for supercritical jets:

$$\frac{L}{d_l} = \frac{12}{J^{0.5}} \tag{2.8}$$

Young et al. [235] observed that J mostly influences the primary jet break-up of the liquid and so determines the intact core length .

2.2.2.4 The Strouhal number (St)

The Strouhal number is a dimensionless value which is extremely useful when analysing unsteady fluid flow dynamics problems. It represents the ratio of the inertial forces due to the local acceleration of the flow and the ones due to convective accelerations. In periodic flows, the Strouhal number is related to the oscillations of the flow due to the inertial forces inherent to changes in velocity by convective transport. It is defined as:

$$St = \frac{fL}{u} \tag{2.9}$$

where f is the frequency of the vortex shedding[2] in s^{-1}, L is a characteristic length (for example the hydraulic diameter) in m and u is the flow velocity in m/s. There is a correlation between St and Re and for low Re (typically in the range from 35 to 1100) [232], described by Roshko[177]:

$$St = A + \frac{B}{Re} \tag{2.10}$$

[2]Vortex shedding is an oscillating flow that takes place when a fluid past a bluff (as opposed to streamlined) body at certain velocities, depending on the size and shape of the body. In this flow, vortices are created at the back of the body and detach periodically from either side of the body forming a Von Karman vortex street, which can be generated only for a certain range of Re. The fluid flow past the object creates alternating low-pressure vortices on the downstream side of the object. The object will tend to move toward the low-pressure zone.

where A and B are curve fitting coefficients depending on the geometry of interest (for a cylinder A=0.2175 and B=-5.106). When the Reynolds number grows, the wake is deeply influenced by the underlying more complex physical phenomena and a more complex model is needed to describe the correlation between the two numbers.
Gutmark and Ho[78] showed that the interaction between the acoustics and the jets is stronger for $0.2<St<0.64$. In rocket science, St has a number or various applications in different motor types. Its importance has been investigated by Tonti [51] in the field of hydrodynamic instabilities in a finocyl grain, observing that the high St excite the onset of pressure oscillations. In a recent work, Armbruster [4] studied the variation of St for BKD , outlining the influence of the frequency of the vortex shedding in exciting the longitudinal eigenmodes of the LOx post due to orifice whistling and the possible coupling between the longitudinal modes and the first tangential mode of the chamber, which would then lead to resonance and consequently sustain combustion instabilities.

2.2.3 Acoustics

Thermoacoustic instabilities represent a major challenge when dealing with the design and development of a new combustor. They are induced by the coupling between the combustion processes and the combustion chamber acoustics. The non-linear acoustics-flame interaction causes pressure fluctuations. These pressure fluctuations can be neglected when their amplitudes are relatively small with respect to the mean pressure of the chamber, but when they reach values of the order of a fraction of the mean chamber pressure they can lead to serious consequences: the flame can propagate towards the upstream fresh gases at a speed higher than the incoming flow speed and burn part of the injection system and the chamber can be destroyed, leading to the failure of the mission itself. Therefore, the understanding of the underlying mathematics is extremely important for the study of the resonant acoustic modes of the chamber.
Most of the acoustics research for combustion instabilities focuses on linear acoustics because the initial amplitude of the perturbations is initially limited. Moreover, the characterization of the linear response can indicate if the system has a stable behaviour or not. Assuming this statement applicable to the test case investigated in this work, only linear acoustics will be considered, and relative mathematical formulation is outlined in the next sections.

2.2.3.1 Conservation equations and wave equation

In fluid dynamics, liquid and gases are considered as a continuum and the fluid motion can be described using the laws of mass, momentum and energy conservation. The conservation laws are written here in the differential form, assuming that fluid properties are continuous and that the derivative exists.

- Mass conservation:

$$\frac{\partial \rho}{\partial t} + \nabla \cdot (\rho \boldsymbol{u}) = m \tag{2.11}$$

In general we will consider situations where mass is conserved and so the source term m equals zero. In some cases however the source term can be present, for example when heat is injected in the system.

- Momentum:

$$\rho\frac{\partial \boldsymbol{u}}{\partial t} + \nabla \cdot \boldsymbol{P} + \rho \boldsymbol{u} \cdot \nabla \boldsymbol{u} = \boldsymbol{f} \tag{2.12}$$

where $\boldsymbol{P}$ is the tensor of viscous forces and $\boldsymbol{f}$ are the external forces acting on the system . The fluid stress tensor is related to the pressure p and viscous stress tensor by the following relation:

$$\boldsymbol{P} = p\boldsymbol{I} - \boldsymbol{\tau} \tag{2.13}$$

where $\boldsymbol{I}=(\delta_{ij})$ is the unit tensor and δ_{ij} is the Kronecker delta . A fluid opposes a rate of deformation rather than a deformation itself. When this relation is linear, the fluid is Newtonian and the resulting momentum conservation law is Navier-Stokes equation. Another simplification that can be introduced is the Stokes' hypothesis[3]. It gives:

$$\boldsymbol{\tau} = \mu(\nabla \boldsymbol{u} + (\nabla \boldsymbol{u})^T) - \frac{2}{3}\mu(\nabla \cdot \boldsymbol{u})\boldsymbol{I} \tag{2.14}$$

Eq. 2.14 is the constitutive equation. At high frequencies, the assumption of thermodynamic equilibrium can partially fail resulting in a dissipation due to volume changes. This is described by a relation between the volume viscosity parameter and μ which is not straightforward as observed in [224] and [160].
Considering m=0, the energy conservation law is expressed as:

- Energy:

$$\frac{\partial}{\partial t}\rho\big(e+\frac{1}{2}u^2\big)+\nabla\cdot\big(\rho\boldsymbol{u}(e+\frac{1}{2}u^2)\big) = -\nabla\cdot\boldsymbol{q}-\nabla\cdot(p\boldsymbol{u})+\nabla\cdot(\boldsymbol{\tau}\cdot\boldsymbol{u})+\boldsymbol{f}\cdot\boldsymbol{u} \tag{2.15}$$

where $u = |\boldsymbol{u}|$, e is the specific internal energy and $\boldsymbol{q}$ is the heat flux due to conduction . The linear equation for heat conduction is the Fourier's law, expressed by:

$$\boldsymbol{q} = -K\nabla T \tag{2.16}$$

where K is the heat conductivity, depending on the pressure and temperature.

Under the following assumptions:

- No combustion;
- No volume forces;
- No heat sources;

[3]The fluid is in local thermodynamic equilibrium, so that the pressure p and the thermodynamic pressure are equivalent.

- Negligible viscous forces, implying that no viscous stresses are present in the considered volume and slip wall condition is present[4];
- Linear acoustic assumption: acoustic variables (p', u', ρ') are supposed to be small with respect to reference values [5] (p_0, c_0, ρ_0);
- Isentropic variations. Under the previous assumptions, if the flow is isentropic and homogeneous at t=0, it will remain isentropic. The energy equation then is simplified and replaced by the isentropic relation :

$$s_0 = C_v ln(p/\rho^\gamma) \tag{2.17}$$

or in another form:

$$p = \rho^\gamma e^{s_0/C_v} \tag{2.18}$$

where s_0 is the entropy of the flow, which is constant under these assumptions ;

- Low-speed mean flow: $\boldsymbol{u_0}$=0.

The conservation equations (2.11), (2.12) and (2.15) then simplify as:

$$\frac{\partial \rho}{\partial t} + \nabla \cdot (\rho \boldsymbol{u}) = 0 \tag{2.19}$$

$$\rho \frac{\partial \boldsymbol{u}}{\partial t} + \rho \boldsymbol{u} \nabla \boldsymbol{u} = -\nabla p \tag{2.20}$$

$$p = \rho^\gamma e^{s_0/C_v} \tag{2.21}$$

Following the approach of Poinsot and Veynante [163], the wave equation is derived :

$$\nabla^2 p' - \frac{1}{{c_0}^2} \frac{\partial^2 p'}{\partial t^2} = 0 \tag{2.22}$$

2.2.3.2 Acoustic modes

The characterization of the acoustic behavior of a rocket combustion chamber requires the identification of the eigenfreqencies and eigenmodes of the combustion chamber volume. Solving the wave equation for complex geometries is not trivial and an analytical expression can be found only for simple geometries, such as cylindrical and rectangular domains. In general, for a statistically stationary flow, the pressure perturbation can be decomposed in a sum of orthogonal Fourier components [176]:

$$p(\boldsymbol{x}, t) = \sum_{h=-\infty}^{\infty} p_h(\boldsymbol{x}) \cos(\omega_h t - \phi_h) \tag{2.23}$$

where ω_h is the h^{th} component of the Fourier angular frequency and ϕ_h is the phase angle at t=0 . This formulation allows to describe the acoustic variables in terms of frequency instead of time and displacement. Imposing that each Fourier

[4] Only the normal component of the velocity goes to zero at the wall

[5] The reference speed is not the speed of the mean flow u_0, but the speed of sound c_0.

component satisfies independently Eq.(2.22) at all times, Eq.(2.23) can be substituted in Eq.(2.22), obtaining the Helmholtz equation:

$$(\nabla^2 + k_h^2)p_h(\boldsymbol{x}) = 0 \tag{2.24}$$

where k_h=ω_h/c_0 is the wavenumber of the h^{th} Fourier component . The eigenfrequencies of the systems can be derived as f_h=$\omega_h/2\pi$. The Helmholtz equation is a second order partial derivative equation, meaning that to solve it two boundary conditions are required for each spatial dimension.

2.2.3.3 Boundary conditions and fundamental acoustic parameters

To correctly model the physical behavior of waves in a complex geometrical domain such as rocket engines where different elements such as injectors, combustion chamber and nozzle are present, it is important to model transmission and reflection of waves. Reflection and transmission coefficient should be calculated for each boundary, where the boundary represents interfaces with medium or geometrical changes. With reflection and transmission coefficients, it is possible to describe each section of the domain in terms of a transfer function. Acoustic impedance quantifies the opposition that a system presents to the acoustic flow resulting from an acoustic pressure applied to the system expressed in Pa·s/m^3 and it is related with reflection coefficients. It is defined as:

$$Z = \frac{p'}{u'} \tag{2.25}$$

where p' and u' are acoustic pressure and velocity fluctuations, respectively . This ratio represents the acoustic resistance. More often, the specific impedance z is used, defined as:

$$z = \frac{1}{\rho_0 c_0}\frac{p'}{u'} = \frac{Z}{\rho_0 c_0} \tag{2.26}$$

The impedance of a boundary or a medium is typically frequency-dependent, so another way to express specific acoustic impedance is as the Fourier transform of acoustic resistance:

$$z(\omega) = \mathfrak{F}[r](\omega) = \frac{\mathfrak{F}[p](\omega)}{\mathfrak{F}[u](\omega)} \tag{2.27}$$

where r denotes the specific acoustic resistance. Specific acoustic resistance r [6] and specific acoustic reactance x are the real and imaginary part of the specific acoustic impedance, respectively.

$$z(\omega) = r(\omega) + ix(\omega) \tag{2.28}$$

Modeling the acoustic impedance of subsystems of LPRE is still an open challenge. In some cases, simple boundary conditions can be imposed, as open or closed ends, but more in general the modeling is still difficult. In particular, an impedance model describing nozzles and feed lines is still a research topic. It has

[6] Note that $r(\omega)$ is not the Fourier transform of the time domain specific acoustic resistance $r(t)$. $z(\omega)$ is the Fourier transform of $r(t)$.

been investigated both in experimental [17, 108–110, 134, 162, 180, 245] and numerical works [123, 184, 197–200, 234], in particular in relation to the damping effect nozzles and feed lines have on the resonant frequencies of the system. Acoustic reflection quantifies the ratio of incoming and reflected acoustic disturbance from boundaries. It is represented by the reflection coefficient R , expressed as:

$$R = \frac{A_-}{A_+} \tag{2.29}$$

where A_- and A_+ are the amplitudes of the reflected and incoming wave , respectively, and it is related to he specific impedance as:

$$R = \frac{z+1}{z-1} \tag{2.30}$$

The boundary conditions of a system can be imposed as an impedance or reflection coefficient.
Figure 2.5 shows the first tangential (1T) and first radial (1R) mode of a cylinder calculated imposing an impedance boundary condition to represent the nozzle. The cylinder can be representative of a combustion chamber volume. It can be used to perform a first analysis of the acoustic behavior of a cylindrical combustor.

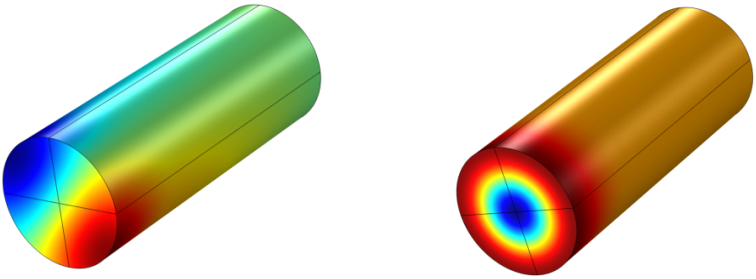

(a) 1T mode (b) 1R mode

Figure 2.5: First tangential (a) and first radial (b) mode of a cylinder calculated with an impedance boundary condition to model the nozzle.

2.2.4 Basic concepts of turbulence

The focus of this work is on turbulent diffusion flames. Here, some fundamental concepts of turbulent combustion will be given. More details about the main numerical approaches used to model turbulence in combustion will be given in Section 2.3.1. Combustion is described by the Navier-Stokes equation presented in Section 3.1. Turbulence is characterized by fluctuations of local properties and occurs for high Reynolds numbers, depending on the configuration of the system.

Local properties are usually split in an average[7] and fluctuating value:

$$f = \bar{f} + f' \tag{2.31}$$

Turbulent intensity is defined as:

$$I = \frac{\sqrt{\overline{f'^2}}}{\bar{f}} \tag{2.32}$$

where $\sqrt{\overline{f'^2}}$ represents the root mean square of the fluctuations f'.
Turbulent intensity is not sufficient to describe turbulent combustion, where turbulent energy is distributed over different length scales present in the flow field and where it must be considered which scales have enough energy to interact with the flame front. The largest length scales present in a turbulent field are the integral scales l_t , whereas the smallest are the Kolmogorov scales η_k . For each turbulent scale, a Reynolds number is defined as:

$$Re(r) = \frac{u'(r)r}{\nu} \tag{2.33}$$

where $u'(r)$ in the characteristic velocity of the motion of size r and ν is the kinematic viscosity. Typically, the largest scales of a turbulent flow are mainly controlled by inertial forces and not affected by viscous dissipation.
For homogeneous isotropic turbulence, the energy of the large scales transfers to the smaller scales by the Kolmogorov cascade [95, 119] due to the presence of non-linear velocity terms. The flux is given by the dissipation ϵ of kinetic energy k. The dissipation ϵ is estimated as:

$$\epsilon = \frac{u'^2(r)}{r/u'(r)} = \frac{u'^3(r)}{r} \tag{2.34}$$

When $Re(r)$ decreases towards 1, inertia and viscous forces go towards balance and this represents the limit where the smallest turbulence scale η_k is found in the flow field, controlled by viscosity and dissipation rate as follows:

$$\eta_k = \left(\frac{\nu^3}{\epsilon}\right)^{1/4} \tag{2.35}$$

which corresponds to Re=1. The ratio between the integral and Kolmogorov length scales represents a comparison between the largest and smaller eddies of the flow field and can be then expressed as:

$$\frac{l_t}{\eta_k} = \frac{u'^3/\epsilon}{(\nu^3/\epsilon)^{1/4}} = Re_t^{3/4} \tag{2.36}$$

where Re_t is the turbulent Reynolds number.

[7] For steady mean flow fields, the average is defined as $\bar{f}=\frac{1}{T}\int_0^t f(t)\,dt$, where T denotes the period

Another important factor in turbulent combustion is how turbulence affects the flame length by the flame strain, measuring the rate of increase of the flame front area. In fact, strain is directly related to velocity gradients in the field. Considering a first-order approximation, the strain $\kappa(r)$ induced on a flame front by an eddy of size r scales as $u'(r)/r$:

$$\kappa(r) = \frac{u'(r)}{r} = \left(\frac{\epsilon}{r^2}\right)^{1/3} \tag{2.37}$$

and the characteristic time scale τ_m of an eddy of size r is:

$$\tau_m(r) = \frac{r}{u'(r)} = \left(\frac{r^2}{\epsilon}\right)^{1/3} \tag{2.38}$$

The strain values produced by integral l_t and Komlogorov scales η_k are given by:

$$\kappa(l_t) = \frac{\epsilon}{u'^2} \approx \frac{\epsilon}{k} \tag{2.39}$$

$$\kappa(\eta_k) = \sqrt{\frac{\epsilon}{\nu}} \tag{2.40}$$

Comparing the strain induced by the eddies of the Kolmogorov scale and integral scale:

$$\frac{\kappa(\eta_k)}{\kappa(l_t)} = \sqrt{\frac{l_t u'}{\nu}} = \sqrt{Re_t} \tag{2.41}$$

from which it can be seen that although Kolmogorov scales have the smallest size and velocity and the shorter lifetime, they produce the highest stretch.
In turbulent diffusion flames, the flame length can be qualitatively estimated as a function of the Reynolds number $Re{=}ud/\nu$, where u is the initial velocity of the flow, d is the diameter of the jet and ν is the kinematic viscosity. Figure 2.6 shows the length of the flame L_f in relation to the Re. The flame length linearly

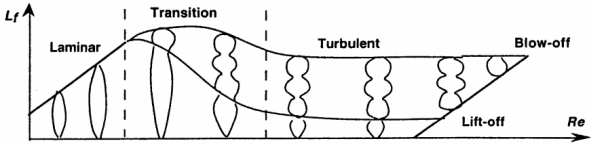

Figure 2.6: Length of a turbulent diffusion flame L_f as a function of Re [163].

increases with Re until it reaches the value which triggers the transition to turbulent regime. After the transition regime, in the turbulent phase the length of the flame remains constant independently of the value of Re. The transition point between the laminar and turbulent regime shifts closer to the injection plane and for sufficiently high injection velocities the flame is lifted from the burner and can be blown off. The flame length remains constant with the increase of injection velocity and the reaction rate per unit volume must be enhanced by turbulence. In general, combustion becomes more efficient with increasing turbulence level, unless blow-off phenomena occur.

2.2.5 The Rayleigh criterion

The Rayleigh criterion is based on the definition of acoustic energy in reacting flows:

$$e = \frac{1}{2}\rho \boldsymbol{u'}^2 + \frac{1}{2}\frac{p'}{\rho c^2} \tag{2.42}$$

Considering the wave equation for reacting flows [163]:

$$\frac{1}{\gamma p}\frac{\partial p'}{\partial t} + \nabla \cdot \boldsymbol{u'} = \frac{\gamma - 1}{\gamma p}\dot{q'}^2 \tag{2.43}$$

where γ=C_p/C_v is the ratio of specific heats and $\dot{q'}$ is the heat release rate fluctuation multiplied for p' and the equation for the acoustic velocity

$$\frac{\partial \boldsymbol{u'}}{\partial t} = -\frac{1}{\rho}\nabla p' \tag{2.44}$$

applying the scalar product by $\boldsymbol{u'}$, it gives [163]:

$$\frac{\partial e'}{\partial t} + \nabla \cdot f' = r_1 \tag{2.45}$$

with

$$r_1 = \frac{\gamma - 1}{\gamma p} p' \dot{q'}$$

and

$$f' = p' \boldsymbol{u'}$$

where r_1 is the correlation between p' and $\dot{q'}$, which is due to combustion and can represent a sink or source of the acoustic energy. The Rayleigh criterion formulated by Lord Rayleigh [174] states that when r_1 is positive, pressure and heat release rate fluctuations are in phase, the instability is amplified and r_1 is a source term. On the other hand, if r_1 is negative, pressure and heat release rate fluctuations are out of phase and the instability decreases. However, this is not sufficient to determine the stable or unstable behavior of the system because r_1 is a local parameter and depends on time and location of the measurement. There can be zones where the instability is amplified and other zones where it damped. The overall effect can be evaluated only integrating Eq.2.45 over space and time. Following the approach of Poinsot and Veynante [163] and expressing pressure, velocity and heat release rate fluctuations as harmonic fluctuations, where τ denotes the acoustic period, the final equation becomes:

$$\frac{d}{dt}\mathcal{E}' + \mathcal{F}' = \mathcal{R}_1 \tag{2.46}$$

where

$$\mathcal{E}' = \int_V E dV \quad \text{and} \quad E = \frac{1}{\tau}\int_0^\tau e' dt = \frac{1}{4\rho c^2} p_\omega p *_\omega + \frac{1}{4}\rho \boldsymbol{u}_\omega \boldsymbol{u}*_\omega \tag{2.47}$$

$$\mathcal{F}' = \int_A F \cdot \boldsymbol{n} dA \quad \text{and} \quad F = \frac{1}{\tau}\int_0^\tau f' dt = \frac{1}{\tau}\int_0^\tau p'\boldsymbol{u'} dt = \frac{1}{2}\Re(p_\omega \boldsymbol{u}*_\omega) \tag{2.48}$$

$$\mathcal{R}_1 = \int_V R dV \quad \text{and} \quad R = \frac{1}{\tau}\int_0^\tau r_1 dt = \frac{(\gamma-1)}{\tau\gamma p}\int_0^\tau p'\dot{q'} dt = \frac{(\gamma-1)}{2\gamma p}\Re(p_\omega \dot{q'}*_\omega) \tag{2.49}$$

Here $\mathcal{R}_1$ correctly represents flame/acoustic interaction: the space-averaged integral of the period-averaged value of unsteady pressure multiplied by unsteady heat release must be positive to increase the acoustic energy of the oscillation. The growth rate of the acoustic energy can be expressed assuming that the acoustic perturbations vary slowly in comparison to the acoustic time. Introducing the growth rate g and given that $gT \ll 1$, Eq.2.46 becomes:

$$g = (\mathcal{R}_1 - \mathcal{F}')/(2\mathcal{E}') \tag{2.50}$$

This form of the equation can be interpreted as a generalized Rayleigh criterion. In fact, unstable behavior is observed if g>0. Consequently:

$$\mathcal{R}_1 > \mathcal{F}' \quad \text{with} \quad \mathcal{R}_1 = \frac{\gamma-1}{\tau\gamma p}\int_V\int_0^\tau p'\dot{q'} dt dV \quad \text{and} \quad \mathcal{F}' = \frac{\gamma-1}{\tau\gamma p}\int_A\int_0^{tau} p'\boldsymbol{u'} dt dA \tag{2.51}$$

where $\mathcal{R}_1$ represent combustion source terms and $\mathcal{F}'$ represents acoustic losses at the boundaries. Figure 2.7 shows a graphical representation of the extended Rayleigh criterion. The region where gain exceeds losses, the modes corresponding to the range between f_1 and f_2 will be linearly unstable.

2.3 Combustion instabilities

When pressure and heat release rate oscillations couple and closes in a loop as stated in the Rayleigh criterion, self-sustained pressure oscillations can take place and grow uncontrolled. This phenomenon is referred to as combustion instabilities. Thermoacoustic instabilities are of particular interest for rocket engines. The perturbations that grow and modify the flow field are acoustic perturbations. The associated pressure oscillations can have well defined frequencies with amplitudes high enough to lead to the failure of the engine. There are four main physical processes which can identify the onset of thermoacoustic instabilities:

- Feedback between heat-release fluctuations with the combustion chamber acoustics;
- Coupling between the aforementioned processes;
- Strength of coupling in comparison with acoustic losses;
- Physical mechanisms behind heat-release fluctuations.

Figure 2.8 summarizes the mechanisms behind thermoacoustic instabilities.
For full-scale rocket engines, combustion instabilities are particularly dangerous. When observed, it is necessary to modify the design of the engine, since often the

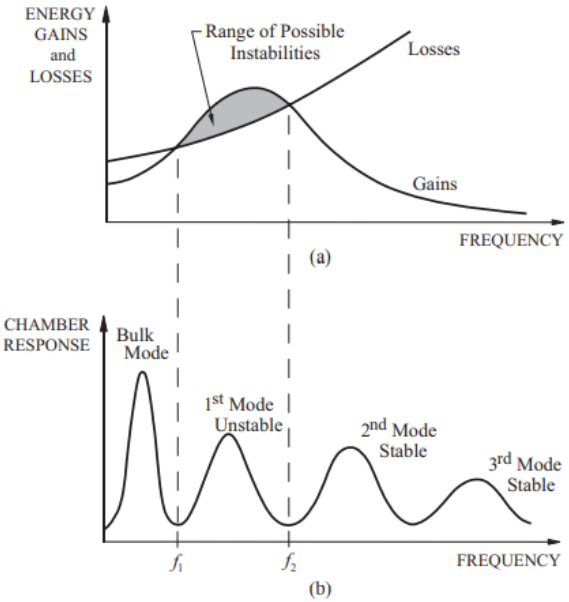

Figure 2.7: Representation of the extended Rayleigh criterion [39]

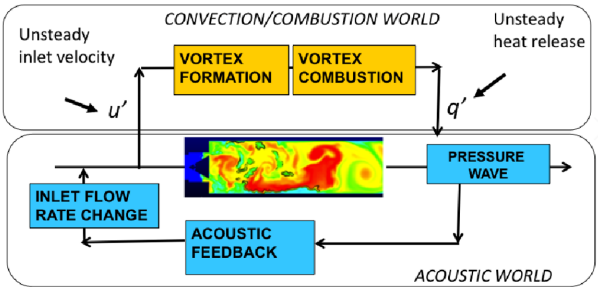

Figure 2.8: Thermoacoustic instabilities description [161].

same phenomena cannot be observed in small-scale or experimental rocket combustors. In particular, the complex geometries of real engines are not encountered in laboratory test-cases. Power density is an important parameter to consider when studying combustion instabilities and in smaller combustors or with increased power densities, it will be easier to observe their onset. High-pressure systems in particular are more difficult to study in laboratory scales. A typical example is the onset of transverse modes which are observable in real engines but

are difficult to trigger in sub-scale engines because of reduction of pressure and power densities [214]. Therefore, experimental investigations are difficult and expensive. Numerical simulations are a tool which can help to decrease the costs of the analysis and give further insights in the physics involved.
In this work the focus is on LPRE combustion instabilities, which can be essentially divided in two categories: low- and high-frequency combustion instabilities. Low frequency oscillations are often called chugging and result from the coupling between combustion processes and the feed system. They occur at frequencies below 1 kHz and less than 100 cycles per seconds [157]. Typically, the fluctuations in the feed system lead to fluctuations in the propellant flow rate. This will bring in turn a change of the chamber pressure and consequently in a response of the rate of delivery of the propellant, where the process becomes self-sustained depending on the dynamic behaviour of the components of the system. Chugging is relatively well understood and can be avoided by a greater injection pressure drop, which tends to make chamber pressure oscillations small relative to pump-delivery pressure. This requires higher pump pressure and power, and so it is not desirable to have an arbitrarily large injection pressure drop.
High frequency combustion instabilities, also called screeching, are in turn not fully understood. They are associated with one or more of the acoustic modes of the chamber. This vibrational motion would be ordinarily damped by viscous effects and carried out through the nozzle, but if the combustion process is pressure sensitive, then non uniform energy release can feed energy to the system and the oscillations will be self-sustained. In particular, when pressure oscillations exceed 5% of the mean chamber pressure and the frequency of the oscillations is higher than 1 kHz, HF instabilities are encountered. Differently from LF instabilities, HF instabilities can develop entirely within the combustion chamber and with steady inlet conditions.
In this context is important to take into account the fact that the combustion process is sensitive to pressure, temperature and velocity changes. Combustion instabilities are characterized by the fact that the transient changes of energy release are not exactly in phase with the changes of flow variables. As a first assumption, combustion processes are supposed to behave as first order dynamical systems characterized by a relaxation time, or time delay. There are several causes for the time delay: ignition of the reactants, vaporization and mixing times and chemical kinetics reaction rates, which can be described as convective time delays. Under unsteady conditions, thermodynamical variables also fluctuate, causing non-uniform conditions in space and time. Consequently, the energy release rate downstream in the chamber volume is also space and time dependent, and acts as a source of acoustic. The $n-\tau$ model developed by Crocco [37] is a one-dimensional model which relates the global heat release at time t to a time lagged acoustic velocity at a reference position:

$$\dot{q}' = nu'(t-\tau) \tag{2.52}$$

where n measures the strength of the flame response and τ measures the delay after which the flame responds to an upstream acoustic velocity fluctuation. n and

τ must include all non-acoustic phenomena, like the vortex formation generated by the acoustic velocity surge, the vortex convection and subsequent vortex combustion. n and τ are frequency dependent. In recent studies, they have been considered also amplitude dependent [158]. The n-τ model is the first example of Flame Transfer Function (FTF), which will be discussed more in detail in Section 2.3.2. If the goal is to characterize the unsteady reaction rate as a function of the acoustic field, the n-τ model is an incomplete formulation: it lacks of information about pressure perturbations and at least two locations at which acoustic velocity fluctuations is measured should be used to capture longitudinal acoustic waves.
In the next sections, a focus on the modelling on high pressure combustion and combustion instabilities will be given, together with a literature review about the state-of-the art of both modelling and experimental techniques.

2.3.1 Modelling high pressure combustion

It is still challenging to model near-critical mixing and combustion processes. Modelling a reacting high pressure flow involves the problems of chemical kinetics, subgrid scale velocity and scalar mixing interactions and highly non-linear source terms. Other challenges are the classical closure problems and problems imposed by the introduction of thermodynamic non idealities and transport anomalies[153]. Compressibility and inertial effects affect the flowfield evolution and this results in different time and space length scales for the flowfield and the thermochemical processes involved. Some scales are far too small to be properly resolved by any numerical approach. The increasing pressure brings moreover other challenges because of the inherent increase of Re, which leads to a further decrease of sub-grid scale velocity interactions and difficulties when approaching the critical conditions. Experimental studies require lot of effort, mainly because of the unfriendly environment in which the setups should be working [128, 223, 227]. Nevertheless, several works have shown a better qualitative understanding of the mechanisms involved in high pressure combustion environments [32, 80, 101, 139, 236]. Satisfying quantitative assessment is still not reached, not having validated theories, limited computational resources and numerical robustness. Anyway, the limit cases of subcritical and supercritical injection can be identified and characterized, as already seen in Section 2.1. Oefelein et al. highlighted the effect of pressure on near-critical mixing, the impact of the momentum flux ratio on the anchoring of the flame and above all the crucial role played by the density gradients and the decrease in mass flux rates, which correspond to a liquid-like behavior [153].
Numerical modelling of high-pressure combustion is still an open challenge. The Navier-Stokes system of equation is well known and resolved for low pressure systems. High-pressure systems are affected from the alteration of some physical phenomena which require more effort to be solved, regarding in particular the closure terms of the Navier-Stokes equations which require further modelling, such as the viscous stress tensor τ_{ij}, the heat flux vector Q_i, the mass flux vector of species, the reaction source terms, the internal energy and the partial molar

enthalpy of the mixture. In addition, an equation of state is required. In the next sections, the main solvers in use will be presented, underlining the pros and cons of each one and giving the motivation of the choice of the solver used in this work. In particular, three main categories of solvers are used nowadays: Direct Numerical Simulations (DNS)), Large Eddy Simulations (LES) and Reynolds Averaged Navier-Stokes (RANS).

2.3.1.1 DNS

Direct Numerical Simulations (DNS) solve the Navier-Stokes equation without introducing any turbulence modelling. Simulations using DNS have been enhanced with the introduction of massive parallel computing because of the grid resolution required by this technique. In fact, the mesh resolution requirements for DNS are stricter than the ones of LES and parallel computing has to be massively used to solve domains with grids which achieve the order of billions of points. DNS grids have to ensure that the calculations have been performed in the largest possible domain to be sure that all the large scales are resolved and that the mesh is fine enough to resolve the Kolmogorov scales and the inner structure of the flame. Thanks to this increased computational capabilities, it has been possible to simulate not only non-reacting flows but also turbulent premixed and non-premixed flames with a high level of precision [163]. However, DNS simulations are not always needed also because of a certain level of simplification which is needed to understand specific fundamental phenomenon, isolating them from the others.

2.3.1.2 LES

In LES, the smallest turbulence scales are spatially filtered whereas the largest scales, which are the ones who contain most of the energy, are directly resolved. Essentially, a low pass filter is applied to the Navier-Stokes equation system, where the scales associated with the highest frequencies are filtered out so that the largest scales of the flow are computed, whereas the smallest one are modelled. Several type of filters are employed in LES. In a general form,

$$\overline{f}(\boldsymbol{x}) = \int f(\boldsymbol{x}')F(\boldsymbol{x}-\boldsymbol{x}')d\boldsymbol{x}' \tag{2.53}$$

where F is the LES filter [163]. Typically, three types of filter are commonly used: a cut-off filter in the spectral space and a box and a Gaussian filter in physical space.
When dealing with compressible flows, a Favre filter is introduced so that

$$\overline{\rho}\tilde{f}(\boldsymbol{x}) = \int \rho f(\boldsymbol{x}')F(\boldsymbol{x}-\boldsymbol{x}')d\boldsymbol{x}'. \tag{2.54}$$

The filtered quantity $\overline{f}$ is resolved in the numerical simulation, f' is the subgrid scale part due to the unresolved flow motion.
Filtering the instantaneous Navier-Stokes equations is more complicated for LES than for RANS, because unlike in RANS, the average value of a filtered LES perturbation is not zero. This holds true also for the Favre average.

To model the Reynolds stress tensor, the most popular subgrid-scale model in LES is the Smagorinski model [206]. The Boussinesq equation gives the momentum fluxes:

$$T_{ij} - \frac{\delta_{ij}}{3} T_{kk} = -\nu_t \left(\frac{\partial \overline{u}_i}{\partial x_j} + \frac{\partial \overline{u}_j}{\partial x_i} \right) = -2\nu_t \overline{S}_{ij} \tag{2.55}$$

where T_{ij} is the Reynolds stress tensor, ν_t is the subgrid scale viscosity, S is the resolved shear stress and T_{kk} is twice the subgrid scale viscosity, representing the isotropic contribution usually absorbed in the filtered pressure.
LES simulation are more expensive than RANS simulations also because they require more strict resolution constraints. In fact, LES of a reacting flow must resolve both flow scales and flame scales. For the flow scales, a simple criterion for the resolution can be applied based on the turbulent Reynolds number. On the other hand, for the flame scales, the requirements of the mesh directly depend on the chemical model and the chemical limits depend in turn on the subgrid scale model used to describe combustion.
An alternative to the full LES modelling is using a hybrid RANS-LES approach where the advantages of both models are taken, reducing the computational costs of the simulation. The mesh with the finest resolution is used in the flame zone where LES is used. Near the walls, the condition can be relaxed and a RANS model can be used. This approach is called Detached Eddy Simulations (DES) . This approach is becoming more popular since it overcomes some of the RANS limitations giving the opportunity to study the behavior of the flow more in detail in the zone where LES is applied, with the advantage of being less expensive than a full LES approach.

2.3.1.3 RANS

The RANS equations are time-averaged Navier-Stokes equations and the starting point to write the system is the Reynolds decomposition of the flow variables in a mean and a fluctuating component. This decomposition is then inserted in the Navier-Stokes equations and then the equations are time averaged, giving the Reynolds stress tensor. The Reynolds stress tensor is the unknown term which has to be modelled to solve the equation system. This is the key point in the problem of the closure of the Navier-Stokes equations. Different models are employed for the closure, namely the zero-equation, one-equation and two-equation models. The first approach to the one-equation modelling came by Prandtl [167], putting in relation the eddy viscosity with the turbulent kinetic energy by developing a separate transport equation. Two equation models are also widely used, in particular the $k - \epsilon$ one [83]. In this model transport equations are used both for the turbulent kinetic energy and the energy dissipation rate. The weakness of these models is to rely on the eddy viscosity concept as formulated by Boussinesq [22] in which the Reynolds stress tensor is considered aligned with mean strain tensor, leading to the lack of information about streamline curvature, body forces and effects on the single components of the Reynolds stress tensor [1]. This led to the introduction of second order models as the one of Haworth and Pope [92].
As already mentioned, the RANS model can be classified as zero-equation models,

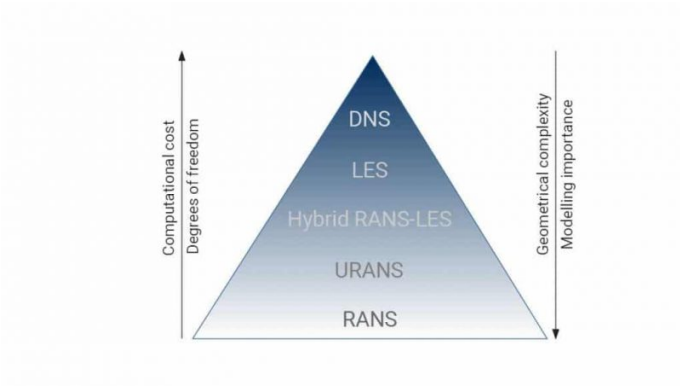

Figure 2.9: Sketch of the level of details of the different CFD solvers in terms of computational costs and modelling complexity.

one-equation model and two-equations models. The zero-equation model solves only a system of partial differential equations for the mean fields. These closures are also called mean velocity field (MVF) closures [1] . The one-equation model features an additional transport equation for the calculation of the turbulence velocity scale. The two-equations models add also a turbulence velocity length scale, usually expressed as scalar dissipation rate of turbulent kinetic energy. Another class of model are the stress-tensor models, or mean Reynolds stress closures, which consider an additional number of equations for the transport of the components of the Reynolds stress tensor τ_{ij}. When dealing with transient simulations, Unsteady Reynolds Averaged Navier-Stokes (URANS) equations are used.

2.3.1.4 Comparison of the solvers and motivation of the URANS choice.

Figure 2.9 summarizes the complexity of the different solvers in terms of modelling and computational costs. RANS approach corresponds to the lowest level of detail of the simulations. However, it is still the most popular for industrial applications because of the limited computational cost with respect to LES and DNS. If we consider an unsteady simulation looking at the local evolution of a physical variable over time, in a RANS approach the values of the variable remain constant over time, whereas for LES and DNS it will vary, showing in DNS the highest level of detail resolving the smallest scales of the variation. Figure 2.10 summarizes the properties of the three approaches in terms of energy spectrum. DNS computes all the scales of turbulence, whereas LES computes only the scales with the largest frequency content. When the cutoff frequency k_C is reached, LES models the smallest turbulence scales as described in section 2.3.1.2. The RANS approach models turbulence through the whole spectrum.

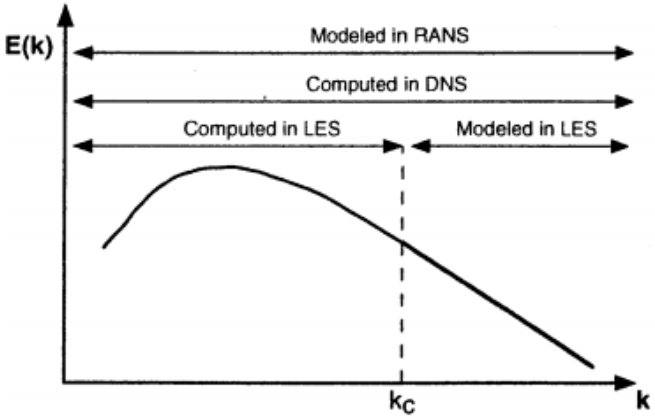

Figure 2.10: Energy spectrum as a function of the wave number in logarithmic scale [163].

In this work, RANS and URANS solvers are used because of the lower computational costs but also because of the goal to be reached. In fact, if it is intended to have information about the acoustic response of the flame to excitation without investigating in detail the small structures of the flame a URANS approach is appropriate, because the overall behavior of the flame can be simulated. In Chapters 4 and 5 it will be shown that results are in good agreement with experimental data are obtained and that the flame behavior is well reproduced. In particular, when investigating the acoustic response of the flame, the level of detail of LES and DNS can be too expensive. Once the tools used for URANS simulations are validated, which is another goal of this work, then this can further show the importance of simulations when developing new combustion chamber and be attractive also for the industry, which can then use simulations as a fundamental tool for design and evaluation of a new engine, without facing the prohibitive costs of LES and DNS, which for these reason are mainly used for scientific and research purposes.

2.3.2 Modelling combustion instabilities

Combustion instabilities modelling is a challenging topic because it involves phenomena which are highly non-linear, together with the fact that also having available experimental data is complex and difficult, so it is challenging not only to develop the models but also to validate them. A first approach is the use of CFD codes without any other reduced model, which can give further insights on several topics but need sometimes a complex post-processing to extract all the relevant fields from the numerical simulation. As already mentioned in the introductory part if this section, acoustics plays a key role in triggering combustion instabilities.

For this reason, Computational Aero-Acoustics (CAA) methods are often employed to simplify the calculations, combined with a CFD approach, in order to gain further insights in combustion instabilities.
CAA develops numerical methods to simulate acoustic waves propagation in three-dimensional regions with non-uniform mean flows when dealing with complex geometries. There are several fields of application of CAA: the first has been in aeronautics to analyze the flow around wings and planes and more in general all the features of an aircraft which are affected in some way by acoustic noise, such as jets, fans, propellers, landing gears and high-lift devices. A comparison between different numerical methods in this kind of applications can be found in the work by Manoha et al.[137]. In this work, both a linearized and non-linearized Euler system of equation is used with finite difference high order scheme on a multi-block structured grid and discontinuous Galerkin methods on unstructured grids.
In the frame of rocket engines, combustion noise is the main focus of CAA methods because it can trigger combustion instabilities [24]. Combustion noise can be classified as direct and indirect. One refers to direct combustion noise when noise is generated by heat release rate fluctuations in turbulent flows, which in turn excite the acoustic fluctuations. Direct combustion noise is then an intrinsic characteristic of turbulent flames, which should be considered as a distributed monopole source [26, 28, 103, 211]. With indirect combustion noise one refers to the generation of acoustic fluctuations due to entropy inhomogeneities in the flow field.
The unsteadiness introduced from turbulence requires it to be taken into account and this can be done coupling CFD and CAA tools. An interesting study in the field of rocket combustion chamber is the one of Schulze [192]. He performed a high frequency stability assessment of DLR thrust chamber BKD using a single injector model with a hybrid RANS/CAA approach. The procedure was able to describe the acoustic propagation in the combustion chamber including nozzle and propellant domes based of an axially distributed mean flow. The main advantage of this methodology is the flexibility of use, allowing to use relatively coarse meshes for the calculation of the acoustic field because of the separation of the acoustics and chemistry scales. The use of LEE gives a significant advantage over time domain calculations for complex acoustic analysis in the linear regime.
All these studies show that to describe the interaction between the acoustic and the flow field also cheaper and more flexible approaches are possible, overcoming the important computational costs of LES and DNS when the focus are not the finer structures of the flame but the overall flame behavior when subject to an acoustic disturbance.
Another approach to describe the behavior of the flame to give a mapping for different operating conditions is the Flame Transfer Function (FTF), or Flame Describing Function (FDF) when dealing with non-linear response of the flame. The very first FTF was introduced by Crocco [37], as already mentioned in Section 2.3 and expressed by Eq.2.52. The FTF relates the spatially integrated fluctuating heat release rate oscillations $\dot{q}'$ to an acoustic variable, usually the fluctuating

velocity u' at an upstream location of the flame, normalized with mean quantities :

$$\frac{\dot{q}'}{\overline{\dot{q}}} = FTF\frac{u'}{\overline{u}} \tag{2.56}$$

On each side of the flame only one variable is involved and so this approach requires only one measurement. The closure can be obtained using the linearized Rankine-Hugoniot jump relations for a compact flame at low Mach numbers[33, 34, 212]:

$$u'_2 = u'_1 + \left(\frac{T_2}{T_1} - 1\right)\overline{u_1}\left(\frac{\dot{q}'}{\overline{\dot{q}}} - \frac{p'_1}{\overline{p_1}}\right) \tag{2.57}$$

$$p'_2 = p'_1 - \left(\frac{T_2}{T_1} - 1\right)\rho_1\overline{u_1}^2\left(\frac{\dot{q}'}{\overline{\dot{q}}} - \frac{u'_1}{\overline{u_1}}\right) \tag{2.58}$$

The behavior of the flame usually depends on the excitation frequency, so that:

$$\frac{\dot{q}'(\omega)}{\overline{\dot{q}}} = FTF(\omega)\frac{u'(\omega)}{\overline{u}} \tag{2.59}$$

where ω denotes the excitation frequency.
Using the complex notation and expressing heat release rate and velocity fluctuations in a sinusoidal form with a real amplitude, the FTF can be expressed as:

$$FTF(\omega) = \frac{\hat{\dot{q}}(\omega)}{\hat{u}(\omega)}\frac{\overline{u}}{\overline{\dot{q}}}e^{i[\phi_{\dot{q}}(\omega) - \phi_u(\omega)]} \tag{2.60}$$

where $\hat{\dot{q}}$ and $\hat{u}$ denote the real amplitudes and ϕ are the complex phases. The amplitude and the phase of the FTF are determined by:

$$\begin{aligned} \widehat{FTF}(\omega) &= \frac{\hat{\dot{q}}(\omega)}{\hat{u}(\omega)}\frac{\overline{u}}{\overline{\dot{q}}} \\ \phi_{FTF}(\omega) &= \phi_{\dot{q}}(\omega) - \phi_u(\omega) \end{aligned} \tag{2.61}$$

Freitag [60] used the FTF approach to a generic burner and an industrial burner to study the influence of mixture fraction and pressure perturbations on the behavior of a premixed flame, noting that the mixture fraction pertubations follow the same behavior of the flame dynamics and that the influence of pressure on the flame transfer functions is limited to the pressure-dependence of the flame form and location. Heat release rate fluctuations were determined from the experimental data taking fluctuations of OH* chemiluminescence as in indicator. For premixed flames and low pressure conditions this assumption is acceptable, but it becomes highly inaccurate when dealing with high-pressure combustion, as will be explained in detail in Chapter 6. For turbulent and laminar premixed flames, FTFs have been successfully applied in many studies regarding combustion instabilities, being in good agreement with experimental data regarding the flame behavior [3, 46, 116, 150, 164, 169, 173, 189]. Schuller et al. [190] investigated the dynamics of a premixed combustion system using two approaches, both with a

FTF and FDF, putting stress on the difference and the limitations of the two approaches. As suggested by Noiray et al. [149], replacing an FTF with a FDF allows to take into account the effects of a perturbation level and to predict the limit cycle oscillation amplitude and frequencies. The FDF is derived from a set of FTF derived for a certain forcing level. The most significant limitation of the FTF is that, although it can roughly give an estimate about the stability of the system, it lacks of information about hysteresis, instability triggering level and amplitudes and frequecies of the limit cycle. The describing function methodology aims to model the combustion dynamics where the flame response to flow perturbations is nonlinear, but the resulting acoustic perturbations through the system remain in the linear range. In this case, the harmonics of higher order are filtered out by the combustor acoustics, so that the system stability is essentially governed by the fundamental frequency component. Boudy et al. [21] analysed a generic burner experimentally deriving a FDF to take into account the non-linear combustion dynamics. For limit cycles with constant amplitude, this methodology provided a quantitative estimation of the amplitude and frequency of the excitation frequency, whereas for unstable oscillations the limit cycle is not attained but the unstable mode in terms of frequency and oscillations is identified and the results are found to be in good agreement with the experimental data. The FDF approach has been refined over the years, but the methodology remains the same, giving anyway good predictions about the limit cycle oscillations and frequency shift of the flames of different combustors [19, 36, 82, 94, 120, 158, 201]. For turbulent non-premixed flames, there is not much literature available regarding the FDF application. A work by Tamanampudi et al. [215] applied a multi-mode FTF methodology together with LES simulations and a non linear Euler solver to investigate the flame response of the CVRC combustor. The agreement between the model and reference results improves with an increase of the number of modes included in the FTF. The inclusion of very high-frequency modes leads however to numerical instability and can predict the growth and behavior of combustion instability only in a weakly non-linear regime.
The main drawbacks of the FDF methods are that it can describe only harmonic limit cycles where only a dominant frequency of the thermoacoustic instabilities is present and the fact that the determination of the FDF is very expensive, since a configuration of a combustor is normally forced with harmonic signals at a large number of frequencies and amplitudes. It can be easily understood that this approach is prohibitive for industrial configurations.

2.3.3 Modelling OH* radiation

Excited hydroxyl radicals (OH*) radiation is a key quantity in the frame of the investigation high pressure combustion and combustion instabilities because it can be relatively easily measured if compared to other variables in a combustion chamber, such as temperature and heat release rate. This is mainly due to the extreme environment which develops inside a combustion chamber to which sensors and measurement tools are exposed. OH* radiation can be instead

detected using adequate optical setups. In particular for oxygen/hydrogen flames the OH* radiation has been often used to identify flame zones due to its central wavelength (310 nm) which is clearly distinguishable from black body sources, being the most distinct in the UV range. However, measuring flame radiation is not trivial. Radiation consists of essentially three components: the flame radiation, which results from high temperature combustion products and optically active gases, the radiation emitted from the walls of the chamber and the flame radiation reflected by the walls of the chamber. When the wall temperature is high or the walls are highly reflective, the radiation emitted from the walls can be comparable or even greater than flame radiation itself. Filters have then to be used to limit the collection of the radiation to the one emitted from the flame to the narrow band of the UV range.
Gaydon [65] and Mavrodineau [138] provided extensive studies of OH* radiation and spectra. One of the most used and investigated sources of OH* radiation is chemiluminescence. Chemiluminescence originates from the relaxation of electronically excited species produced during the chemical reaction in the flame and the study of light emission in the reaction zone gives information about the energy release in the flame zone.
Early experimental works used emission of radicals as an indicator of heat release rate to investigate experimental combustors and real engines [97, 168]. More recently, the effect of varying some properties of the flame (such as the flame strain rate or ROF) on chemiluminescence has been studied [64, 113, 142, 147, 207]. A considerable research effort has been made to understand if OH* radiation (also CH* for hydrocarbon flames) could be an indicator of the heat release rate of the flame, also to study combustion instabilities as was done by Hardi at DLR [86] and by Sisco at Purdue University [202]. Many studies which want to verify if a correlation between heat release rate and excited radicals produced by combustion is possible [44, 53, 59, 79, 85, 93, 99, 115, 124–126, 228, 230, 240, 242] assume that chemiluminescence takes place where the heat release rate is defined by chemical reactions, but the degree of correlation highly depends on the physical variables considered such as strain rate of the flame, propellant combinations, pressure, turbulence, equivalence ratio and degree of mixing. However, most of the studies involved low pressure and temperature environments with hydrocarbon flames.
For high pressure non-premixed O_2/H_2 flames, the only experimental work which investigates the relation between heat release and OH* radiation is the one from Burrows [25], where he used it to determine the reaction zone. This is important because at high temperatures and high pressure, the behavior of OH* radiation changes significantly. For relatively low temperatures, below 2700 K at 50 bar pressure, chemical excitation is the predominant mechanism, which produces OH* radiation. For temperatures above 2700 K, thermal excitation overcomes chemical excitation and OH* is assumed to be in thermal equilibrium with OH molecules. This is the main assumption of the Equilibrium Filtered Radiation Model (EFRM) from Fiala [56], which will be described more in detail in the next section.
Not only temperature, but also pressure has an important influence on OH* radiation, because the phenomenon of self-absorption becomes more and more

important with increasing pressures [56, 243, 244]. The term self-absorption indicates that the radiation emitted from the molecules is subject to absorption by the same molecules at ground state. Not taking this into account can lead to important errors when OH is present in high concentrations as a combustion product, as will be described in Chapter 6. Modelling these aspect becomes then crucial in the study of OH* radiation and numerical simulations play an important role to give insights in the physics of radiation, also because CFD is not limited to line-of-sight measurements, as it is when processing data from experiments. Numerical simulations can also give quantitative measurements of OH* radiation, taking into account also the radiation originating from the walls.
The starting point is solving the Radiative Transfer Equation (RTE) and the different modelling approaches solve the equation on the basis of several assumptions. If the equation is directly solved, no assumption on the thickness of the flame is needed and this approach can be considered as an absorption and emission model, with the name of optically thick flame model. The other limit case is the optically thin flame assumption, where the optical thickness of the flame tends to zero and the RTE can be simplified. This assumption is valid only if the intensity of the radiation coming from the surroundings of the flame is much lower than that of the flame itself, but it becomes wrong if the flame is attached to a hot surface or surrounded by an environment where the radiation coming from other sources is not negligible, which is typically the case of rocket flames. In the optically thin assumption approach, self-absorption is neglected. However, also if this approach is less computationally expensive, solving the RTE is still not feasible for industrial applications. An alternative approach to save computational resources is to consider the flame as emitting solid surface and use the grey medium approximation, which considers a medium in thermal equilibrium with an emissivity smaller than one and independent of the frequency. This simplification works if assuming the surface emitting on a broadband wavelength range, while it fails if the considered domain emits at only one wavelength.
This work aims to fill the gaps in modelling and visualizing OH* thermal radiation, adapting a spectral modelling program developed by Potter [166] and using a reverse ray-tracing algorithm in order to produce pseudo-OH* images starting from RANS and URANS CFD solution. This is done in a post-processing step in order to save computational time, not having to solve a separate equation for the production of OH* radicals at run time but starting from the concentration of OH molecules, assuming that they are in thermal equilibrium because the temperatures developed in rocket flames are well above 2700 K. Nevertheless, the tool takes into account both self-absorption and refraction, which are two key phenomena in the frame of high-pressure combustion when dealing with measuring OH* radiation. The algorithm and the corresponding OH* spectrum will be described and discussed in detail in Section 6.1 and 6.3.
The next sections describe the approaches used to model the OH* radiation: Detailed Chemistry (DC), Spectral Model (SM) and EFRM. Advantages and disadvantages of each approach will be discussed, giving the motivation for the choice of the model adopted in the present work.

2.3.3.1 Detailed Chemistry Radiation Model (DC)

This model considers the radiation as directly proportional to OH* concentration and directly implies the optically thin flame assumption, not providing any information about the emission and absorption spectra. This method can be applied only to CFD simulations featuring a detailed chemistry raction scheme where OH* radicals as a product of combustion as a separate species is included. This increases the computational costs, but on the other hand the post-processing of the data is extremely simple as OH* radiation is considered directly proportional to OH* concentration. The most evident advantage of this approach is that chemical excitation mechanisms can be included and non equilibrium OH* concentration can be calculated. In O_2/H_2 flames, the dominant reaction in the formation of OH* is [56, 114, 118, 159]

$$O + H + M \leftrightarrow OH^* + M \tag{2.62}$$

where M indicates the third body. This model depends essentially only on two parameters: the reactions considered to produce OH* as a separate combustion product and the thermodynamic data of OH*.

2.3.3.2 Spectral Model (SM)

The Spectral Model (SM) gives a representation of the radiation of OH* as a function of the wavelength and the emission and absorption spectra are the main outputs. The main assumption of the spectral model is local thermal equilibrium, so that rotational, vibrational, electronic and translational temperatures are equal.

Fiala [56] adapted a spectral model of the HITRAN/HITEMP database for temperatures above 3000 K to calculate emission and absorption spectra of a laminar counterflow flame. Goebel [68] examined the radiative heat transfer in a real rocket combustion chamber combining the simple radiation transfer model P-1 in combination with the Weighted Sum of Grey Gases Model (WSGGM) [208].The P-1 radiation model is described in detail by Sazhin et al. [185], considering the advantages and disadvantages. The description of the model in detail is outside the scope of this work. Here, it is sufficient to say that the P-1 model gives reliable predictions in the case of 1D plane geometry in both optically thin and optically thick media, while it overestimates the radiation heat fluxes from localized heat sources in optically thin media. Thermal radiation is modelled by the expanding the radiation intensity in terms of first order spherical harmonics. It is particularly useful for accounting for the radiative exchange between gas and particles.
The main advantage of the SM is that it can give details of the OH* spectra and resolve it at the requested wavelengths and takes self-absorption into account. On the other hand, it can be complex to implement and requests an integration procedure in order to obtain the total radiance, which is not directly given by the model.

2.3.3.3 Equilibrium Filtered Radiation Model (EFRM)

The EFRM model was developed by Fiala [56] and it is based on the assumption that OH molecules are in equilibrium with OH*, so that chemical excitation can be ignored. The advantage is that no reaction rates have to be considered and OH* does not have to be included in the chemical kinetic scheme. Assuming the gas as optically thin, self-absorption is neglected and OH* concentration is considered as directly proportional to OH concentration. The qualitative relation to describe OH* emission spectrum is

$$e_{\mathrm{OH}^*} \sim [\mathrm{OH}^*] \sim [\mathrm{OH}] \mathrm{e}^{\frac{\mathrm{hc}}{\mathrm{k_B} \lambda \mathrm{T}}}, \tag{2.63}$$

where k_B is the Boltzmann constant, λ is the dominant wavelength of the radiation and T is the temperature.
Although being computationally advantageous, the limit of this model is not to take into account self-absorption. The model has been extended to approximate self-absorption while keeping the complexity low with the EFRM-A model [57]. Nevertheless, this extension does not take into account self-absorption in the calculation of OH* spectra, but rather identifies when self-absorption is relevant and has to be considered. A SM is still necessary to describe self-absorption correctly.

2.3.4 Experimental and Numerical Test Cases

In order to study combustion instabilities, several research combustors have been developed. They are not only used to collect and analyse experimental data but also to be employed as numerical test cases for validation of numerical tools. The key feature of the experimental combustion chamber is that they can provide data about both acoustic and combustion processes which cannot be observed in real engines. This is due to the fact that in experimental combustors, instrumentation which could not be built inside a full scale engine can be instead installed in research combustors.
Experimental combustors can be divided into two main categories: self-excited and externally excited. In self-excited or naturally excited experiments combustion instabilities occur spontaneously, whereas in externally excited combustors the acoustic disturbance is triggered by an external acoustic excitation system. In the next sections the characteristics of several combustors will be described, together with the numerical work done to investigate more in detail their behavior.
The focus of this work is BKH, which has unique characteristics, being te only external excited experiment to work with $\mathrm{LOx/H_2}$ in transcritical and supercritical conditions.

2.3.4.1 BKH

BKH (Brennkammer H) is an externally excited combustor fed with $\mathrm{LOx/H_2}$ developed and operated at DLR Institute of Space Propulsion Lampoldshausen at the European Test bench P8. It features a rectangular cross section, five main coaxial injectors inserted in a cluster of secondary injectors fed with hydrogen and

a secondary nozzle. The secondary nozzle provides the external excitation, where a toothed wheel, or siren, passes over the outlet surface, periodically interrupting the flow and generating the acoustic disturbance. The velocity of the wheel determines the excitation frequency, so the response of the flame to a various set of conditions can be investigated.
Lecourt and Foucaud [127] were the first to employ a toothed wheel to interrupt the flow through nozzles and since then this approach have become the most common.
Hardi [86] conducted several experiments to study the behavior of the flames to longitudinal and transverse acoustic excitation, the breakup of the LOx core and the response of the chamber to acoustic excitation. Further experiments were done by Webster [229], focusing on the damping using a modified sector wheel to impose a discontinuous acoustic excitation, observing that the damping rates vary considerably between cold and hot runs giving a motivation to further investigate instabilities at suitable representative conditions.
BKH features tow windows for optical access. This allowed Hardi [86, 87, 89] to investigate the LOx core break-up length under transverse acoustic excitation using high-speed camera data. The LOx core length was detected manually using shadowgraph data and it was observed to retract towards the injection plane during the transverse excitation. This allowed also to observe a qualitative relation between the amplitude of the excitation and the shortening of the LOx core length. However, the line-of-sight images collected with the shadowgraph technique allowed limited insights in the flame structure, also because of the presence of turbulent structures in the instantaneous images, which imposed some difficulties in the definition of the features of the flame.
The optical access of BKH gives also the possibility to investigate OH* radiation fluctuations in BKH. Hardi at al. [86, 89] and Fdida at al. [54] investigated the flame response to transverse and longitudinal excitation using OH* radiation data to identify the flame zone and the flame behavior. It was found that during transverse mode excitation OH* radiation peaks where the pressure disturbance maximum amplitude is observed. This led to the conclusion that the transverse acoustic velocity transported the flame towards a pressure antinode, satisfying then the Rayleigh criterion and leading to sustain combustion instabilities. Also this observation were line-of-sight integrated data. Hardi et al. [87] investigated also the flame response to longitudinal excitation by visualizing OH* radiation. It resulted that the flame is not deformated during longitudinal excitation but resulted in intensity fluctuations.
For the acoustic analysis, Hardi [86] produced phase distribution maps showing regions in phase and out of phase with the acoustic disturbance. This was reached by a pixel-by-pixel cross-correlation of the optical data of intensity fluctuations and the local acoustic disturbance following the approach of Sliphorst [205].
Beinke [15] used Dynamic Mode Decomposition (DMD) taking as input the optical data to analyse the flame response to local acoustic disturbances. This was achieved by isolating the mean coherent acoustic and optical intensity fluctuations, providing a phase distribution of the local intensities for comparison. Rayleigh

indices were computed and used to produce results representative of the flame response under certain excitation conditions.
The uniqueness of the data provided by BKH make it a suitable test case for numerical studies. Beinke [15] studies BKH extensively, using RANS and URANS simulations run with the in-house DLR TAU code to investigate the acoustic response of the flame subject to longitudinal and transverse excitation. In particular, the single injector configuration was investigated giving good agreement with experimental data recovering the trends of the experiments, but with some discrepancies regarding in particular the length of the LOx core, which was underestimated. An analysis of the OH* radiation was also conducted, using both line-of-sight integration and the EFRM starting from the steady state solution of RANS calculations. The results qualitatively reproduced the OH* distribution, but did not take into account correctly the self-absorption.
Morii et al. [145] investigated the response of the dense LOx core of BKH to the 1T mode excitation with LES. The pressure in the combustion chamber was slightly overestimated because of the boundary conditions used in the simulation. Consequently, the frequency and amplitudes of the acoustic modes of the chamber differed from the experiments, and a method was developed to compare the equivalent acoustic response of the simulation to the experimental data, finding then good agreement with the experiments. The LOx core was observed to retract towards the injection plane during the 1T mode excitation, spreading and flattening along the direction perpendicular to the one of the transverse velocity. The same phenomenon was not observed during longitudinal excitation.
Horchler et al.[96] investigated flame-acoustics interaction using the DLR TAU code by performing DES simulations. In particular, the flame behavior at non-resonant and resonant transverse excitation was investigated. A numerical bombing test was conducted in order to compare the obtained eigenmodes with the Helmholtz eigenmodes. The comparison with experimental data showed an overestimation of the calculated frequencies with respect to the experimental data. As in previous research work, the transverse excitation showed to influence the flame shape by flattening and retracting the LOx core towards the injection plane.

2.3.4.2 CRC

The CRC (Common Research Chamber) is an externally excited combustion chamber developed by DLR and ONERA. It features a flat disc shape and single injector element. The CRC is combustion is fed with both LOx/H_2 and LOx/CH_4. The pressure of the chamber can reach up to 10 bar and propellants are injected radially towards the center of the chamber. The flow exit perpendicular to the injection direction, since the main nozzle is located in the center of one side of the disk. Multiple interchangeable modules are installed around the circumference of the chamber in order to host the instrumentation for measurements. One of the modules can be substituted with a secondary nozzle and the acoustic excitation system. Optical access windows are located at the sides of the chamber in order to provide data downstream from the injection. A sketch of the cross-section of the chamber is shown in Figure 2.11. In the CRC the orientation of the acoustic

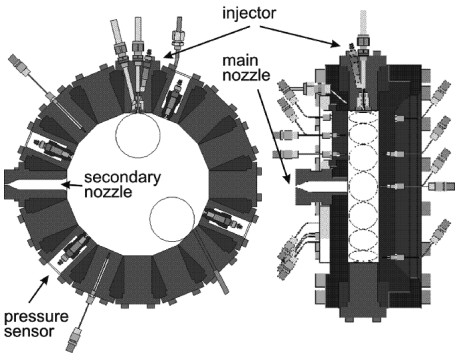

Figure 2.11: Cross section of the CRC [155]

modes can be fixed due to the presence of the secondary nozzle. Therefore, the interaction of acoustics with several chamber processes, like injection, mixing, atomization and vaporisation can be investigated. Many experimental studies have investigated the acoustic behavior of the chamber [73, 117, 154, 155, 204], identifying the main resonant modes and their effects on the flame using OH high speed camera visualization techniques. Oschwald et al.[155] analysed the effect of a mounted resonant volume on the acoustic eigenfrequencies of the coupled acoustic system. It was observed that the eigenfrequency values are systematically shifted to a lower value and additional resonance phenomena are present at frequencies which do not correspond to the originally identified eigenfrequencies. Comparing the shape of the acoustic field with images coming from the OH radiation, it was concluded that the flame response was due to pressure sensitive processes. The energy transfer from the flame to the acoustic system was examined, observing that the OH^* intensity and acoustic pressure are in phase, satisfying the Rayleigh criterion and confirming that the energy released during the combustion processes can be transferred to the acoustic field, feeding the feedback loop.

2.3.4.3 CVRC

The Continuously Variable Resonant Combustor (CVRC) is a single element cylindrical combustor operated at Purdue University [202, 203]. The combustor is fed with CH_4 or JP-8 and hydrogen peroxide (H_2O_2). H_2O_2 is fed through a catalyst bed for decomposition in order to reach representative conditions of an oxidizer-rich staged combustion. The main feature of the combustor is the variable length of the oxidizer post in order to control the frequency of the acoustic modes by changing the longitudinal modes frequencies. The combustor is provided with an optical access which allows the visualization of the flame with high speed imaging of OH* and CH* radicals. Dynamic pressure sensors are mounted in the chamber to monitor the acoustic field. Figure 2.12 shows a longitudinal cut of CVRC.
Yu et al. [237, 238] experimentally investigated high-frequency combustion

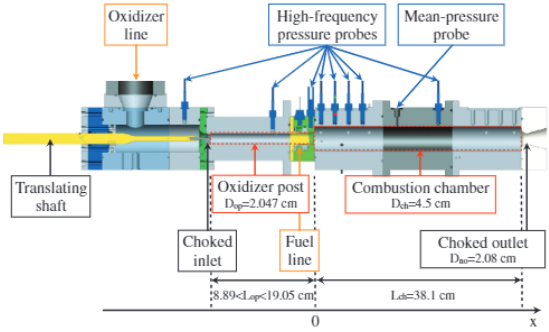

Figure 2.12: Section of CVRC [195]

instabilities changing the length of the post between stable and unstable configurations, varying the acoustic length of the tube between a quarter and half-wave resonator. They observed that when the system becomes unstable, higher harmonics appear simultaneously and instantaneously. When the system becomes stable, the harmonics disappear sequentially. The results were compared with analytical results obtained by applying LEEs, showing good agreement but also the necessity of a more accurate combustion response submodel. Sardeshmuk et al. [183] and Bedard et al. [12] observed the emission spectra of OH* and CH* chemiluminescence to assess a correlation between radiation intensity and heat release rate fluctuations. The relation was investigated taking into account the phase difference between acoustic and optical intensity fluctuations. Sardeshmuk et al. [183] observed that the quasi-steady state assumption used to model the transport of OH* chemiluminescent radicals and time resolved heat release rate is not completely adequate, whereas for CH* radicals this hypothesis is acceptable. For OH*, the optical thickness of the flame should be considered as it may affect the estimation of self-absorption. For CH*, the optical thickness should not have a negative impact on measurements. This is due to the shorter duration of CH* peak concentration with respect to OH*. Experimental results were compared with CFD simulation results, which aimed to calculate the concentration of OH* and CH* and compare the phases of chemiluminescent intensity fluctuations and heat release rate. CFD simulations recovered the experimental trend but for OH* quantitative values were overpredicted by five times. Bedard et al. [12] quantified the phase difference of line-of-sight integrated OH* and CH* intensities to the pressure signal. The experimental data were phase averaged. The pressure peak lags the CH* chemiluminescence peak of 50° in the experiments, while in the simulation the value raises to 60°. The phase angle of peak OH* chemiluminescence intensity signal lags pressure of 40° in the experiment, while in simulations the lag is reduced to 7°. This shows that neither CH* nor OH* can be used as an indicator of heat release rate at the prescribed conditions. Simulation results showed a

complex flame front and the heat release zones vary considerably in axial and radial direction. These effects cannot be observed with line-of-sight measurements. Bedard et al. [12] suggest that improvements in the simulations could be achieved by modelling transport of excited species and other chemiluminescent species such CO^*_2

and by extending the simulation domain to a 3D configuration improving also the boundary conditions. Concerning the experimental setup, the suggestion is to employ quantifiable signal measurement which include varying line-of-sight measurements for a better comparison with the emitting species, together with a deeper understanding of the optical probe geometry and opacity of the combustion gases to the emission signals.
Hardi et al. [90] used DMD techniques to CVRC optical images in order to qualitatively compare the flame response between experiments and simulations. The reconstructed images obtained were then directly compared with CFD results. The experimental data provided by CVRC make it a suitable test case for numerical simulations, using several approaches. Frezzotti et al. [62] used CVRC as a test case to extract the flame response to longitudinal acoustic excitation starting from a 2D hybrid RANS/LES apporach and to investigate numerical problems in a low order model approach using a quasi 1D eulerian approach [61]. In order to get results in agreement with experimental data, this model required a tuning of the parameters required as inputs for the model.
A recent work from Sharma et al. [196] performed a RANS simulation to assess the acoustic boundary conditions to be used as boundary conditions for the subsequent LES simulations. The intermediate oxidizer post length was chosen, corresponding to combustor acoustic modes maximum power spectral density. The results are presented in the form of peak-to-peak pressure oscillation amplitudes and power spectral density, compared then to the experimental data. Acoustic waves along with the convected flow in the reactive flow simulation were captured. The limit cycle was qualitatively and quantitatively reproduced. A clear indication of the onset of instability is reasonably well captured in dominant resonant frequencies, although showing an underestimation of peak-to-peak pressure amplitudes.
Harvazinski et al.[91] studied the interaction between hydrodynamics, acoustics and turbulent combustion in CVRC with a hybrid RANS/LES approach investigating the three different configurations of the oxidizer post. Assuming a half-wave corresponding to a closed-closed acoustic boundary condition for the combustion chamber, the tube lengths approximately correspond to quarter-, three eights, and half-wave resonators that serve to vary the phasing between the acoustic modes in the tube and the combustion chamber. A comparison between simulations and experimental data was made based on the amplitudes and spatial distribution of the modes, obtained applying DMD techniques. Looking at the pressure field, the stable and extremely unstable configurations simulation were in good agreement with the experimental data. The simulation of the trans-stable configuration showed amplitudes approximately twice the value of the unstable

configuration and matched well with the power spectra of the experiments. The simulation results were used to characterize and investigate the key features of each regime. A common feature between instabilities predicted in both the repeatable unstable regime and the bifurcated regime was an interruption in the fuel flow caused by a local high amplitude compression, resulting in a detached flame. Two types of reignition events were observed that led to high-amplitude instabilities. The reignition was coincident either with the arrival of a downstream-running compression from the post or an upstream-running compression in the combustor. The DMD analysis employed for the first longitudinal model frequency showed a good qualitative agreement for the unsteady combustion response, in particular at the unstable post length, while at the shorter post length corresponding to the stable configuration, the computational predictions indicate that the combustion response extends further downstream compared to the experimental data.
Nguyen and Sirignano [148] used Delayed Detached Eddy Simulations (DDES) with a flamelet model to gain further insights of the flame response and the physical mechanisms which lead to instabilities using an axisymmetric domain for the high-pressure highly unsteady configuration of CVRC, observing that a standing half-wavelength pressure wave was present in the combustion chamber. Pressure antinodes were located near the dump plane and at the exit of the combustion chamber, with a pressure node in the middle of the chamber. The upstream pressure antinode showed a strong coupling between the heat release rate and pressure fluctuations. An adverse pressure gradient affects the reactant streams when pressure peaks near the dump plane and the flame moves towards the injection plane. Here, combustion was dominated by premixed burning whith significant local extinctions and reignitions. As the pressure decreases through the chamber, the flame moved downwards and combustion was dominated by diffusion phenomena. Combustion dynamics were examined for the different configurations of the oxidizer post. In the semi-stable case, the flame was lifted away from the injector lip and weakly anchored at the dump plane. In the stable case, the flame moved further downstream. In both cases, there was no strong axial flame movement as previously observed in the unstable configuration of the oxidizer post. A monotonic decrease in local extinction and reignition as the flow became more stable with a decrease of pressure fluctuations was observed. However, extinction and reignition still occured in the region of the dump plane even for the stable burning. A flame index analysis identified the premixed burning regime as dominant for all of the three cases.

2.3.4.4 BKD

BKD (Brennkammer D) is a naturally excited experimental combustor used to investigate combustion instabilities. It is operated at the test bench P8 in DLR-Lampoldshausen. The chamber has a cylindrical shape and has a diameter of 80 mm. LOx/H_2 propellants are injected with 42 shear coaxial injectors and the combustor operates at chamber pressures ranging from 60 to 80 bars, providing supercritical injection conditions for oxygen and hydrogen. For the most unstable load points, BKD eigenmodes reach resonant frequencies above 10 kHz. Figure

2.13 shows a sketch of the combustor and experimental setup. Originally, BKD was

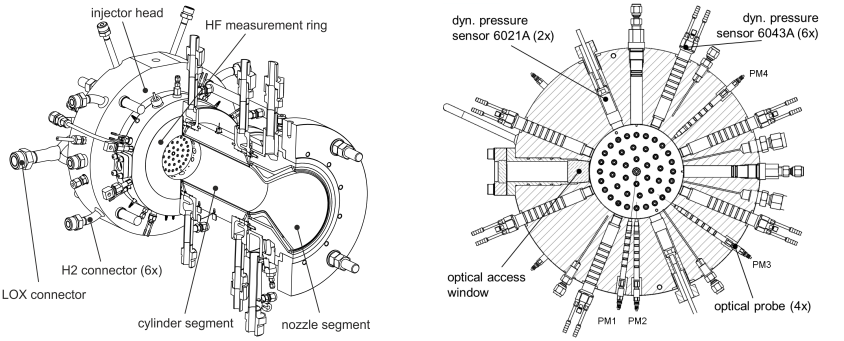

(a) BKD skecth (b) Measurement ring

Figure 2.13: BKD thrust chamber (a) and optical measurement ring (b) [7].

not designed for combustion instability investigation purposes and the diagnostic tools were limited. Gröning [75] and Gröning et al. [72, 74, 77] implemented additional instrumentation to identify and measure high frequency combustion instability phenomena, such as high-pressure sensors and optical probes. Gröning et al. [71, 74] identified the spinning tangential modes as source of the acoustic disturbances. The use of a damping cavity on the side of the chamber fixed the orientation of the acoustic modes. Gröning et al. [77] also observed that when the tangential resonant frequencies of the chamber matched the longitudinal resonant frequencies of the LOx injectors, high-frequency combustion instabilities were triggered. This led to the conclusion that high frequency injection coupling is the mechanism responsible of the onset of the instability on BKD.
The initial work performed by Gröning has been further developed by Armbruster et al. [4–7], providing not only further physical insights about the mechanisms driving instabilities in BKD, but also new measurement equipment which allows to visualize the flame and and record OH* and blue radiation in order to further study the flame dynamics. Blue radiation is characteristic of hydrogen flames, which emit in a boradband radiation spectrum with a peak of about 440 nm. While being relatively weak in cold and low-pressure flames, it can significantly contribute on the overall emission when dealing with high pressure and temperatures. The blue radiation is the most distinct radiation which can be caught from a human eye and the most popular example comes from the plume of the Space Shuttle Main Engine [56]. The new experimental instrumentation was first presented by Armbruster et al. [7] together with the results of OH* high-speed imaging. 2D flame visualization for highly representative combustion chamber conditions were possible, including chamber pressures of up to 82 bar and propellant mixture ratios up to 7. The flame dynamics was investigated for two different load points, at 50 bar and 80 bar chamber pressure respectively. The

same phenomena were observed both in OH* radiation and blue radiation images, but a highest level of detail in detecting flame dynamics features was observed in the blue radiation measurements due to the greater optical depth reached. High intensity regions were detected around the central LOx core interacting with the surrounding flames, indicating that flame-flame interaction effects cannot be neglected when modelling combustion of industrial rocket chamber configurations. BKD is extremely representative of operating conditions which are typical of upper stage rocket engines, so it is also an interesting test case for numerical works. Different approaches have been followed to analyse BKD stability behavior and the flame response to combustion dynamics. Schulze et al. [191] assessed the linear stability of four operating points by computing FTFs of the injectors subject to acoustic pressure and velocity disturbances from URANS simulation results using a real gas model. The obtained FTFs were then implemented in an acoustic solver to create the stability map of BKD.
Tonti et al. [220] investigated the flame response of a 2D axysimmetric configuration of the most unstable load point of BKD performing a URANS simulation with the in-house DLR TAU solver. The results were then interpolated on a cylindrical 3D domain in order to investigate OH* radiation emission. The numerical results showed a wrinkling of the flame surface resulting in wave-like structures in the shear layer between oxygen and hydrogen streams. To perform this study, additional modelling of the optical probe which captured the intensity of the OH* radiation signal was needed. This approach gave information about the frequency content of the signal. highlighting that the main frequency component is linked to the wake translation movement, corresponding to the excitation frequency. Turbulent structures with a higher frequency component in the shear-layer resulted in spatial scattering of the rays which alters their path through the OH rich zones modifying the overall intensity of the signal.
Urbano et al. [221, 222] ran a LES simulation of the full 3D BKD domain, including all the 42 injectors and propellant manifolds with the AVBP code. Real gas properties were taken into account by using the transport properties described by Chung et al. [35] and the Soave-Redlich-Kwong equation of state. Equilibrium chemistry for oxygen/hydrogen combustion was assumed and a β-pdf model to describe the filtered mixture fraction as the progress variable. Two load points were examined, a stable and an unstable one. The experimentally observed instabilities were not directly reproduced by LES simulations, as the two load points resulted both stable, but the instability was triggered by applying an initial transverse acoustic disturbance distribution. This allowed to show that the unstable load point resulted stable until an intial distrubance corresponding to the 8% of the initial chamber pressure was applied. It was stated that the instability was not directly detected by the LES simulation because of the mesh size, being too coarse to capture the spontaneously occurring instabilites. Urbano et al. [222] analysed the spectrum and the acoustic disturbance in the LES simulation results, showing that the first radial (1R) mode of BKD was simultanously excited and exciting the unstable behavior of the chamber. For each injection element, the Rayleigh index was computed, in order to derive a FTF which was then

implemented into an acoustic Helmholtz solver, which reproduced the 1T and 1R mode identified by the LES simulations. Experimentally, the 1R mode was identified by Gröning [76] studying the coupling between the resonant modes of the chamber and the LOx post of BKD.

3 CFD solver: the TAU code

This chapter is dedicated to the description of the in house code of DLR, TAU, with a particular focus on the features used in this work.
The TAU code is a hybrid RANS/LES compressible solver with real gas capabilities for Euler and Navier-Stokes equations. It uses a finite volume Godunov-type method on hybrid structured-unstructured grids. This makes the code capable of handling viscous and inviscid flows, complex geometries and flow regimes from low subsonic to hypersonic. TAU code is also optimized for High Parallel Computing (HPC) by grid partitioning algorithms. DLR TAU code has been validated against different flow conditions and configurations, for different applications ranging from aeronautics to hypersonics [66, 135, 193]. Schwamborn et al. [194] give a detailed overview of the code features and the successful applications both in industry and research fields.
A MAPS+ Riemann solver by Rossow [178] allows to deal with low Mach number flows and high density gradients, which are particularly challenging for a compressible flow solver. The integration is performed via an explicit third order Runge-Kutta scheme. For the unsteady computations presented in this work, a Jameson type dual stepping implicit time scheme and a one-equation Spalart-Allmaras turbulence model [210] are used. In the next sections, the governing equations of the solver will be presented, together with the chemical scheme and approach to supercritical propellants modelling and turbulence models.

3.1 Governing equations

For the simulation of BKH, the flow is treated as a reacting mixture of thermally perfect gases and one real fluid component. For each chemical species a transport equation is solved. Navier-Stokes equations for a mixture of compressible reacting gases are employed. The integral form of the equations can be written as:

$$\frac{\partial}{\partial t}\int_V \boldsymbol{U} dV + \int_A \boldsymbol{F^{inv}} \cdot \boldsymbol{n} dA = \int_A \boldsymbol{F^{visc}} \cdot \boldsymbol{n} dA + \int_V \boldsymbol{Q} dV \tag{3.1}$$

where $\boldsymbol{U}$ is the mass flux vector, which becomes the vector of conservative variables when considering thermal equlibirum conditions:

$$\boldsymbol{U} = \begin{pmatrix} \rho_s \\ \rho \boldsymbol{V}^T \\ \rho E \end{pmatrix} \tag{3.2}$$

where the subscript s denotes the chemical species. The matrix of inviscid Euler fluxes is:

$$\boldsymbol{F^{inv}} = \begin{pmatrix} \rho_s \boldsymbol{V}^T \\ \rho \boldsymbol{V}\boldsymbol{V}^T \\ \rho E \boldsymbol{V}^T \end{pmatrix} + \begin{pmatrix} 0 \\ pI_n \\ p\boldsymbol{V}^T \end{pmatrix} \tag{3.3}$$

while the viscous fluxes are represented by:

$$\boldsymbol{F^{visc}} = \begin{pmatrix} \rho D \nabla \frac{\rho_s}{\rho} \\ \boldsymbol{\tau} \\ \kappa \nabla^T T + \rho D \sum_s h_s \nabla^T \frac{\rho_s}{\rho} + (\boldsymbol{\tau}\boldsymbol{V})^T \end{pmatrix} \tag{3.4}$$

where κ is the thermal conductivity, T is the temperature, h_s is the enthalpy of the single species, $\boldsymbol{V}$ is the velocity vector, $\boldsymbol{\tau}$ is the viscous stress tensor and D is the diffusion coefficient given by :

$$D = \frac{\mu}{\rho} \frac{1}{Sc} \tag{3.5}$$

where μ represents the dynamic viscosity calculated as described by Karl and Luedeke [112] and Sc indicates the non-dimensional Schmidt number which describes the ratio between the momentum diffusivity and mass diffusivity.
The source vector describing the chemical reactions is given by:

$$\boldsymbol{Q} = \begin{pmatrix} \omega_s \\ 0 \\ \dot{q} \end{pmatrix} \tag{3.6}$$

where ω_s is the source term representing the chemical species and $\dot{q}$ is the heat release rate.
The viscous stress tensor was presented in Eq.(2.14).
The closure equation of state for the chemical species is given by:

$$p = \sum_s \rho_s R_s T \tag{3.7}$$

where R_s represents the gas constant of the species s .

3.2 Finite rate chemistry model

Hannemann [84] and Karl [111] describe the finite rate chemistry scheme used in the TAU code. The chemical reactions are described as follows:

$$\sum_s \alpha_s^r X_s \overset{k_f, k_b}{\longleftrightarrow} \sum_s \beta_s^r X_s \tag{3.8}$$

with α_s and β_s stoichiometric coefficients, X_s the species molar fractions and k_f, k_b the reaction rate coefficients.

The chemical source term ω_s present in Eq.3.6 is given by:

$$\omega_s = M_s \sum_r (\beta_s^r - \alpha_s^r) \left[k_f \prod_S (n_s)^{\alpha_s^r} - k_b \prod_S (n_s)^{\beta_s^r} \right] \tag{3.9}$$

with M_s the molecular weight of the species and n_s the number of moles, obtained as $n_s = \rho / M_s$. A modified Arrhenius law is used to determine the forward reaction rate k_f, and the backward reaction rates k_b are determined from the forward reaction rate and the equilibrium constant of the reaction. The equilibrium constant is determined from the partition function of the species taking part to the raction process and described by Hannemann [84].

3.3 Supercritical combustion

Cryogenic propellants show a different behavior with respect to ideal gases, and this should be taken into account when simulating combustion chamber processes fed with this kind of propellants [9]. Real gas effects are included in the real gas release of the DLR TAU code to take into account these effects. The two main features of the real gas implementation consist in a dedicated equation of state (EOS) for each species and a multi-fluid mixing model which determines the properties of the mixture [8, 10]. In this work, a six species seven reactions chemical scheme for oxygen-hydrogen combustion by Gaffney et al. [171] is used. This reduced mechanism model was compared to a more complex one using eight species and seventeen reactions by Jachimowski [29] and Lempke et al. [129]. When HO_2 and H_2O_2 were included in the mechanism, negligible differences were found, and so the use of the reduced chemical scheme was justified. The chemical scheme includes H_2,O_2,H,O,OH and H_2O. In the multi-fluid mixing model, an ideal gas equation of state is solved for H_2,H,O,OH and H_2O, while for O_2 a real gas equation of state is used. The real gas properties of O_2 are described by the high fidelity Soave-Redlich-Kwong equation of state [209].
The current release of the TAU code features an adaptive-tabulation of high-accuracy equation of state. Dumbser et al. [47] first introduced the idea of an adaptive tabulation based on a polynomial approach for cavitation flows. This approach was then extended to be used in the tabulation of general fluids and in viscous flows for a single component. The adaptive tabulation provides a speed up of the code of about three orders of magnitude in comparison with to the direct evaluation of EOS. Moreover, using a quadtree based approximation further reduces the tabular size. The quadtree-based approximation is very efficient as large changes in the EOS description are only present in the vicinity of the critical point and close to the liquid and vapor saturation lines. Apart from these regions, the behaviour can be well approximated by polynomials, using the cubic-type approximations for super-critical flows and the simple ideal-gas approximations for fluids far away from the critical point. Fechter et al. [55] extended the tabulation approach for the mixing description in the TAU code in the application relative to real gas mixture. The difference between the detailed EOS approach and ideal gas

estimation is tabulated, allowing to easily switch to the ideal gas approximation in the lower density regions. The use of a coarse approximation in the regions where the ideal gas assumption is acceptable describes with sufficient accuracy the behavior of the gas.
The validity of the assumption of ideal gas mixing of species properties is limited to the situation in which all the species exist as real-gas only in a pure fluid state. In supercritical oxygen-hydrogen combustion, this assumption is justified. The flame produced by a coaxial injection element in an oxygen-hydrogen liquid propellant rocket engine effectively isolates the fuel and oxidizer streams, as shown in numerical studies by Oefelein [151, 152] and experimentally observed by Oschwald et al. [156]. Mixing occurs in the hot reaction zone under ideal gas conditions, as shown in numerical studies by Bellan [18]. Simulations of counterflow 1D diffusion flames by Ribert et al. [175] and Lacaze et al. [121]. In oxygen-hydrogen combustion at supercritical pressure, all real fluid effects are limited to the LOx core, where transitions to a liquid-like to a gaseous state under pure fluid conditions occur. For the flames considered in this work then the multi-fluid mixing model is appropriate.
In the experimental combustor object of this work, other chemical species as nitrogen (N_2) and gaseous hydrogen are present. Nitrogen is used to pressure the oxidizer tank, and so liquid hydrogen injected in the chamber could be slightly contaminated by traces of N_2. Acting only in third body reactions in oxygen-hydrogen combustion, the effect on the reaction is small enough to be neglected. Gaseous hydrogen is used to purge the chamber before each test.

3.4 Turbulence models

Turbulence-combustion interaction is a fundamental phenomenon to be taken into account in the frame of rocket combustion and it is not yet fully understood. As described in Chapter 2, different computational models are used for simulations, each one modelling turbulence with different levels of accuracy, showing the importance of this investigation in numerical works. Bray [23] approached the problem from the modeller point of view, outlining the effect of turbulence and on chemical reaction rates. He observed that the effects of turbulence on combustion could be taken into account using a Probability Density Function (PDF) due to the non-uniform mixing and scalar fluctuations, whereas the effects of combustion on turbulence were not fully understood. Modelling real chemical kinetics was conducted on the basis of empirical data, so a straight experimental validation was not possible. Since the work of Bray, considerable progresses in modelling such interactions have been made, considering also the increased computational capabilities for CFD. Dahms [41] presented a turbulence-chemistry interaction model for multi-zones technique, which was applied to premixed, partially premixed and non-premixed flames. The model was built starting from fundamental theories and empirical data for turbulent scalar mixing and so it was suited for being used both in RANS and LES simulations. The turbulence-chemistry interaction model is based on the assumption of fully

turbulent developed flow, where turbulent diffusivity is much higher than molecular diffusivity. In multi-zone models, a zone represents a specific enclosure which is connected to other enclosures by specific physical variables. Multi-zones techniques are the most widely used method for engine combustion modelling.
As stated by Xiang et al. [233], with increasing Mach and Reynolds numbers in a combustor, interaction between turbulent mixing and chemical reactions intensifies significantly. Not only density and viscosity but also chemical reactions are affected by the compressibility of the flow field since it can accelerate reaction rate via increasing the collision frequency of molecules and changing the flame configuration, which in turn affects the combustion mode.
In the frame of this work performed with TAU, interaction between turbulence and combustion is implicitly included into the code adding a turbulent contribution to the laminar diffusion coefficients and thermal conductivities. Fick's law is used to model the transport of each species. D is the averaged diffusion coefficient used to model the species behavior considering the same dynamic viscosity μ and Schmidt number Sc.

$$-\rho D \frac{\rho_s}{\rho} = -\Big(\frac{\mu}{Sc}\Big)\nabla\frac{\rho_s}{\rho} \tag{3.10}$$

As stated by Beinke [15], the increase of the species diffusion velocity is led by increased turbulence. Consequently, the rate of combustion increases due to increased velocity of mixing between the species. Oxygen-hydrogen combustion is essentially an equilibrium process at the selected load points and the infinitely fast process is a reasonable assumption, so that temperature changes in unsteady conditions have a limited effect on reaction rates. The consequence is that turbulent mixing is the controlling factor of reaction rates, transporting the species in the reaction zone. The rate controlling step is captured in TAU by modelling the transport of the single species.
Thermal conductivity is also increased by turbulence. The influence on turbulence of the thermal conductivity is taken into account in TAU by adding a turbulent thermal conductivity factor k_T to the laminar thermal conductivity k_{lam}.

$$k_t = k_{lam}\frac{\mu_t}{\mu_{lam}}\frac{Pr_{lam}}{Pr_t} \tag{3.11}$$

In the former version of TAU, the ratio Pr_{lam}/Pr_t was a parameter of the model to be prescribed, while in the current version is it possible to specify only Pr_t. In this work, both approaches are used, the first for the single injector modelling, the second for the full chamber simulation. Pr_{lam}/Pr_t has an important impact on the flame length, as investigated by Beinke [15]. The comparison with the experimental data led to set this value to 2 and in this work it was assumed the same value not only because of the good agreement with the experimental data but also to give space to coherent comparison between the two studies. The main limitation of setting this value as a single parameter of the model is that it remains constant over the entire domain. This approach did not work when performing the full 3D simulation of BKH, where it had to be replaced with the Pr_t parameter and computing k_t starting from this value to avoid numerical stability problems.

TAU is a hybrid RANS/LES code, so both turbulence models to perform RANS and LES simulations are implemented. Here we will focus only on turbulence models implemented in the RANS solver, since this is the main focus of this work, in particular the one-equation Spalart-Allmaras (SA) equation and the k-ω and k-ϵ two-equation models. In particular, the choice of the Spalart-Allmaras one equation model will be justified.

3.4.1 One equation turbulence models

The Spalart-Allmaras one-equation turbulence model and its variants are implemented in TAU [216]. Here, the standard model and the Spalart-Allmaras old implementation of SA-noft2 as described from NASA [98] and reported in TAU User guide will be presented in detail, since they are the one-equation models used in this work. The presented model all assume a linear eddy viscosity model, represented by the Boussinesq equation:

$$\tau_{ij} = 2\mu_t \left(S_{ij} - \frac{1}{3}\frac{\partial u_k}{\partial x_k}\delta_{ij} \right) - \frac{2}{3}\rho k \delta_{ij} \tag{3.12}$$

where τ_{ij} is the Reynolds stress tensor, μ_t is the turbulent dynamic viscosity, δ_{ij} is the Kronecker delta, k is the thermal conductivity and S_{ij} is the shear stress. For one-equation models, the last term in generally neglected as k is not always straightforward available.
The Spalart-Allmaras turbulence model was originally developed for aerodynamic flows [210] involving wall-bounded flows and has been shown to give good results for boundary layers subject to adverse pressure gradients. It is also gaining popularity in turbomachinery applications. The one-equation model is given by [1]:

$$\begin{aligned} \frac{\partial \tilde{\nu}}{\partial t} + u_j \frac{\partial \tilde{\nu}}{\partial x_j} = c_{b1}(1 - f_{t2})\tilde{S}\tilde{\nu} - [c_{w1} f_w - \frac{c_{b1}}{\kappa^2} f_{t2}]\left(\frac{\tilde{\nu}}{d}\right)^2 + \\ + \frac{1}{\sigma}\left[\frac{\partial}{\partial x_j}\left((\nu + \tilde{\nu}) \frac{\partial \tilde{\nu}}{\partial x_j} \right) + c_{b2} \frac{\partial \tilde{\nu}}{\partial x_i} \frac{\partial \tilde{\nu}}{\partial x_i} \right] \end{aligned} \tag{3.13}$$

from which the turbulent kinematic viscosity $\tilde{\nu}$ is directly obtained.
The turbulent dynamic viscosity is given by:

$$\mu_t = \rho \tilde{\nu} f_{v1} \tag{3.14}$$

where:

$$f_{v1} = \frac{\chi^3}{\chi^3 + c_{v1}} \quad \chi = \tilde{\nu}/\nu \tag{3.15}$$

The turbulent shear stress $\tilde{S}$ is defined as:

$$\tilde{S} = \Omega + \frac{\tilde{\nu}}{\kappa^2 + d^2} f_{v2} \tag{3.16}$$

[1] Here the $\tilde{a}$ quantities denote the turbulent variables

where $\Omega = \sqrt{2W_{ij}W_{ij}}$ indicates the magnitude of the vorticity, d is the distance of the point to the nearest wall, κ=0.41 is a constant of the model and

$$f_{v2} = 1 - \frac{\chi}{1+\chi f_{v1}} \qquad f_w = g\left[\frac{1+c_{w3}^6}{g^6+c_{w3}^6}\right]^{1/6}$$
$$g = r + c_{w2}(r^6 - r) \qquad r = min\left[\frac{\tilde{\nu}}{\tilde{S}\kappa^2 d^2}, 10\right]$$
$$f_{t2} = c_{t3}exp(c_{t4}\chi^2) \quad W_{ij} = \frac{1}{2}\left(\frac{\partial u_i}{\partial x_j} - \frac{\partial u_j}{\partial x_i}\right)$$

The boundary conditions are:

$$\tilde{\nu}_{wall} = 0 \quad \tilde{\nu}_{farfield} = 3\nu_\infty : 5\nu_\infty \tag{3.17}$$

where ν_∞ indicates the freestream kinematic viscosity.
The Spalart-Allmaras turbulence model is considered as empirical, with the following values of the constants of the model:

$$c_{b1} = 0.1355 \qquad \sigma = 2/3 \qquad c_{b2} = 0.622$$
$$\kappa = 0.41 \qquad c_{w2} = 0.3 \qquad c_{w3} = 2$$
$$c_{v1} = 7.1 \qquad c_{t3} = 1.2 \qquad c_{t4} = 0.5$$
$$c_{w1} = \frac{c_{b1}}{\kappa^2} + \frac{1+c_{b2}}{\sigma}$$

Particular care has to be taken when evaluating the minimum distance d. As stated by Spalart and Allmaras in [98], "searching along grid lines or by finding the nearest wall grid point (or cell center) are incorrect, and are not the same as computing actual minimum distance to the nearest wall (in general). Using the former methods will yield grid-dependent differences in the results. [...] Improperly-calculated minimum distance functions will particularly produce incorrect results for cases in which the grid lines are not perfectly normal to the body surface, or when the nearest body does not lie in the current grid zone". Anyway, varying $\tilde{\nu}$ linearly throughout the wall regions make the SA model particularly robust from a numerical point of view. To reinforce numerical stability, some correction should be made also to $\tilde{S}$. A correction method was suggested by Allmaras et al. [2], which also prevent clipping for $\Omega \neq 0$.
A simplification of the SA model is obtained removing the f_{t2} term for suppressing turbulence in laminar regions. Consequently, the model does not result to be sensitive to $\tilde{\nu}_{farfield}$. The compressibility term is not included and the constraint on $\tilde{S}$ regards only the strict positivity condition.
The first model is used in this work for the single injector configurations, while the second is used to simulate the full chamber. A detailed discussion of the reasons why the no-f_{t2} term is used in the full chamber simulation will be discussed in Chapter 7.

3.4.2 Two equation turbulence models

In this subsection, the main two equation turbulence models implemented in TAU will be described: the Wilcox $k-\omega$ model [231] and the Menter BSL and SST model [143].
The main features of $k-\epsilon$ models were briefly described in Section 2.2.4. Wilcox [231] states that the accuracy reached by the $k-\epsilon$ models is lost when requiring drastic simplifications during the modelling process and he replaced the ϵ transport equation by a purely empirical relation for the transport of ω, which represents the specific rate of dissipation of the turbulence kinetic energy k into internal thermal energy. The ω equation can be solved without imposive particular restrictive conditions on damping or bridging procedures down to wall, which could reduce the accuracy of the model.

$$\frac{\partial(\rho k)}{\partial t}+\frac{\partial(\rho u_j k)}{\partial x_j}=\rho P-\beta^*\rho\omega k+\frac{\partial}{\partial x_j}\left[\left(\mu+\sigma_k\frac{\rho k}{\omega}\right)\frac{\partial k}{\partial x_j}\right] \tag{3.18}$$

$$\frac{\partial(\rho\omega)}{\partial t}+\frac{\partial(\rho u_j \omega)}{\partial x_j}=\frac{\alpha\omega}{k}P-\beta\rho\omega^2+\frac{\partial}{\partial x_j}\left[\left(\mu+\sigma_\omega\frac{\rho k}{\omega}\right)\frac{\partial \omega}{\partial x_j}\right] \tag{3.19}$$

where $\mu_t=\rho k/\omega$ and $P=\tau_{ij}\frac{\partial u_i}{\partial x_j}$. Eq. (3.18) and (3.19) represent the equations for turbulent kinetic energy and scalar dissipation rate, respectively. The values of the constants are:

$$\sigma_k=0.5 \quad \sigma_\omega=0.5$$
$$\beta^*=0.09 \quad \beta=3/40 \quad \alpha=5/9$$

The α coefficient was chosen to match the value of the von Karman constant of 0.408.
Thw Wilcox two-equation model is preferred in external aerodynamics because of its improved predictions when dealing with adverse pressure gradients.
Nevertheless, the solution depends on the ω value at the outer edge of a shear layer, which cannot be controlled. This has a minor importance for boundary layer calculations, while the influence of this factor on free shear layer is significant.
Several changes have been made to the Wilcox model, including for example the vorticity source term, but in TAU the original version described here is implemented.
Menter [143] demonstrated that the free-stream sensitivity of the Wilcox model is due to the lack of modelling the cross-diffusion term in the ω equation (Eq.3.19).
The correction introduced by Menter [143] consisted in blending factor F_1 which modifies Eq.(3.18) and Eq.(3.19) as follows:

$$\frac{\partial(\rho k)}{\partial t}+\frac{\partial(\rho u_j k)}{\partial x_j}=\rho P-\beta^*\rho\omega k+\frac{\partial}{\partial x_j}\left[(\mu+\sigma_k\mu_t\frac{\rho k}{\omega})\frac{\partial k}{\partial x_j}\right] \tag{3.20}$$

$$\begin{aligned}\frac{\partial(\rho\omega)}{\partial t}+\frac{\partial(\rho u_j \omega)}{\partial x_j}=\frac{\alpha}{\nu_t}P-\beta\rho\omega^2+\frac{\partial}{\partial x_j}\left[(\mu+\sigma_\omega\mu_t\frac{\rho k}{\omega})\frac{\partial k}{\partial x_j}\right]+\\ +2(1-F_1)\frac{\rho\sigma_{\omega 2}}{\omega}\frac{\partial k}{\partial x_j}\frac{\partial \omega}{\partial x_j}\end{aligned} \tag{3.21}$$

The introduction of F_1 changes the coefficient from the $k-\omega$ values near the wall to the $k-\epsilon$ values at the outer edge of the boundary layer. F_1 is a function described in a way that major changes of the coefficient takes place approximately in the middle of the boundary layer. This method is known as Menter Baseline (BSL) model and it was used as intermediate step for the development of the Menter SST model. The two models differ only for the σ_k constant, the expression of the turbulent eddy viscosity and an additional term F_2 added to the model to restrict the limits on the eddy viscosity only to the near wall region where the ratio between turbulent shear stress and specific kinetic energy is constant, additionally modifying the values of k diffusion coefficient. This modifications were based on the analysis of adverse pressure gradient flows. This model is considered as a standard model in aerodynamics, where flows of applications are particularly sensitive to separation.
In this work, the SA model was chosen due to its simplicity and robustness. It was tested over different applications with RANS and URANS simulations in TAU [15] giving reasonable agreement with the experimental data together with adjustments of other parameters of the model such as Prandtl number ratio. The two-equation models implemented in TAU for RANS and URANS are suitable for aerodynamics application and have not been validated for combustion chambers and combustion instability studies in the frame of the TAU code. Moreover, the use of the SA turbulence model can highlight the differences between the results presented in this work and previous results, showing how the results vary changing some important aspects of the simulation, as the excitation profiles applied to reproduce the flame response under acoustic disturbance, mesh and boundary conditions.

4 BKH Single Injector Modelling

The first part of this work is dedicated to the single injector modelling of the BKH experiment. Modelling the response of the flame under realistic acoustic excitation profile is crucial to gain further insight into the flame dynamics that go beyond the capacity of the experimental investigation to visualize the behavior of the flame. Experimental data are collected in BKH via an optical setup which exploits the optical access given from the windows which allow to visualize the flame, but these data are limited to the line-of-sight access to the flame zone. Another advantage is that this approach allows control of the imposed acoustic excitation which acts locally on the flame.
The single injector modelling approach has been used from different research groups both for non-reacting [69, 122, 187] and reacting flows[38, 81]. Single injector models are used when calculating FTFs to be used in reduced order modeling approaches, although often it is not possible to make a satisfying comparison with experiments due to large amount of experimental data needed for a wide range of load points (LPs).
In this chapter, the BKH experimental combustor will be presented more in detail. Then, the 1L mode excitation case will be presented: first, the numerical domain and boundary conditions employed to calculate the steady-state solution are described. Successively, the setup of the excitation profiles is presented, together with the results of the unsteady simulations and comparison with previous works and experimental data. The same approach is followed for 1T mode excitation. The last part of the chapter is dedicated to the study of the influence of the mesh and boundary conditions on the simulation, showing substantial differences above all in the calculated heat release rate, which is a key variable in the Rayleigh criterion to assess the presence of combustion instabilities. The last part presents a summary and discussion of the results.

4.1 The BKH experimental combustor

BKH is an externally excited combustion chamber developed and described in detail by Hardi [86] and test campaigns covering several load points were led by Hardi [86] and Webster [229]. Figure 4.1 shows a sketch of BKH. Figure 4.2 shows a detailed drawing of BKH where the injection plane and relevant dimensions of the chamber are displayed. Figure 4.3 shows the primary injectors configuration with the relevant dimensions.
BKH has a rectangular cross section studied to fix the orientation of the acoustic modes according to the principal dimensions of the chamber and to reproduce the acoustic configuration of an upper stage engine. The chamber is provided with optical access given by two windows on the sides of the chamber walls. The

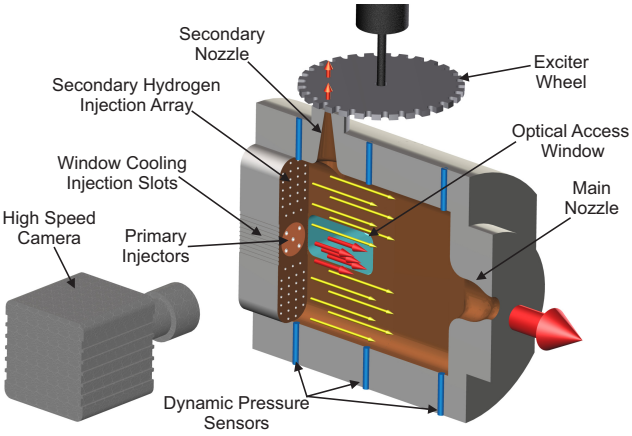

Figure 4.1: BKH [15]

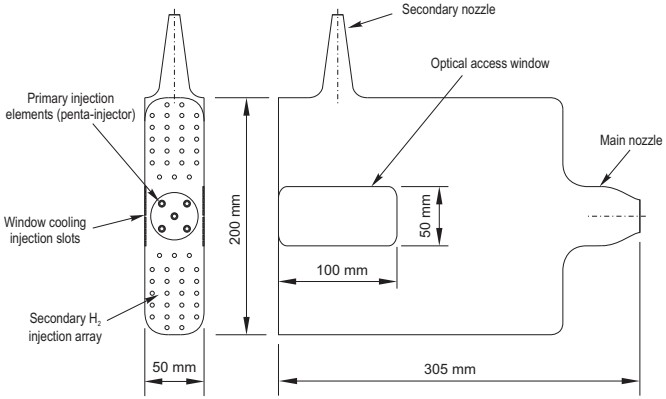

Figure 4.2: BKH section and injection plane with relevant dimensions[86]

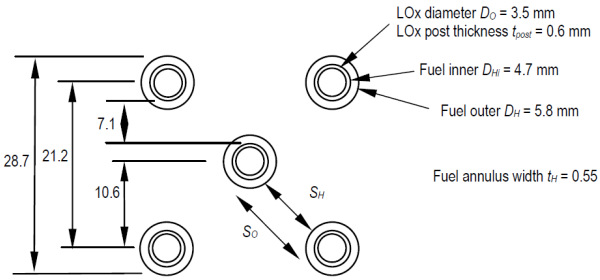

Figure 4.3: BKH section and injection plane with relevant dimensions[86]

windows are placed to capture the flame directly after the injection plane and give the possibility to have line-of-sight acess to the primary combustion zone.
Two nozzles are mounted in the chamber. The main nozzle is mounted parallel to the flow, whereas the secondary nozzle is perpendicular to the flow. The area of the secondary nozzle is about one-tenth of the area of the main nozzle, capturing about 10% of the flow. The acoustic excitation is performed periodically interrupting the flow through the secondary nozzle. A toothed wheel, or siren, passes over the secondary nozzle outlet opening and closing it. The speed of the siren determines the frequency of excitation, given the geometrical parameters of the teeth, and it is controlled by an electric motor. The disturbance propagates in the chamber as the teeth interrupt the flow through the nozzle.
The five primary coaxial injectors are hosted in the middle of the injection plane, surrounded by a cluster of 50 secondary injectors, evenly placed above and below the matrix of primary injectors. Primary injectors transport liquid oxygen as oxidizer in the inner ring and gaseous or liquid hydrogen as fuel in the outer ring of each single coaxial injector. A matrix distribution is used in order to investigate the interaction of the five flames as it is in full scale engines. The central element is surrounded by the four neighboring elements, being the most representative for investigation and shielded by the surrounding flames.
The secondary hydrogen injectors feed the chamber with gaseous hydrogen and they are employed to cool the walls and the windows from the high temperatures of the hot gases produced by the combustion process. Another important function is the prevention of flow recirculation at the top and bottom of the chamber since it would not be representative of the behavior of a full scale engine.
The window cooling system is hosted on the sides of the chamber to protect them during experiments. The cooling is performed by film cooling using hydrogen.
Diagnostic instrumentation is a key feature for all experimental combustion chambers. BKH provides a variety of instruments, ranging from dynamic pressure sensors to optical diagnostics. The key data to monitor and detect combustion instabilities are the acoustic measurements and flame response imaging as a result

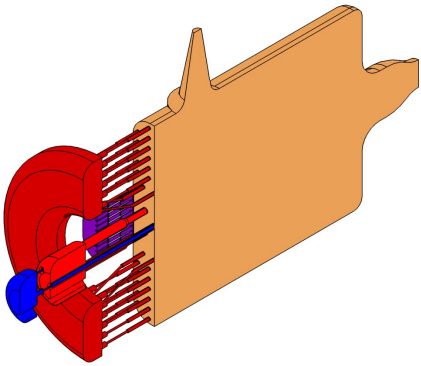

Figure 4.4: BKH cut with manifolds. Oxygen is displayed in blue, primary and secondary hydrogen in red and window cooling in purple. The chamber volume is in orange.[15]

of the acoustic forcing. BKH features dynamic pressure sensors and optical diagnostics with high sampling rates. Mass flow rates of the propellants, chamber pressure and wall temperature are monitored to control the operating points. The mass flow rates of the propellants are measured upstream of the propellants manifolds by sensors mounted at the test bench. Assuming equal distribution of propellants along the injectors and continuity between the manifold and the injection plane, the properties and mass flow rates of each propellant at the injection plane are computed. Static pressure sensors and thermocouples monitor the chamber pressure at the top of the chamber under the secondary nozzle and the wall temperature, respectively. This equipment ensures that the operating point conditions are controlled and that the structural limits of the chamber are not exceeded.
High frequency piezoelectric unsteady pressure sensors are employed to capture the acoustic disturbance produced by the BKH acoustic excitation system. The sensors are mounted on the surface at various locations on the walls and propellant manifolds. The distribution of the dynamic pressure sensors is shown in Figure 4.5. The dynamic pressure sensors are distributed in a way that the acoustic field can be reconstructed by measuring the amplitudes and phase of the disturbance at each sensor location. Where optical diagnostics is employed, sensors PCCDYN7 and PCCDYN8 are not available since they are mounted on a dummy window. The PSNDYN sensor is mounted to capture the disturbance resulting from the excitation system downstream the secondary nozzle.
Acoustic disturbances which eventually propagates in the feed lines are monitored by the sensors mounted in the propellant feed manifolds. The cooling system features no pressure sensors and so no information is available about the acoustic

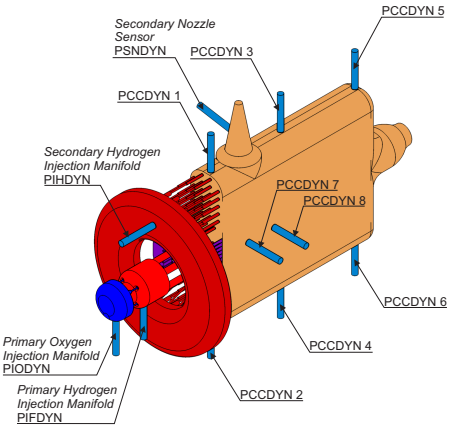

Figure 4.5: Position of dynamic pressure sensors in BKH.[15]

propagation in the window cooling system.
The sampling rate of the sensors is 100 kHz. BKH resonant modes range from 2 to 5 kHz allowing more than 20 measurements recovered within the acoustic cycle. The BKH optical access system with high-speed cameras is described more in detail in Chapter 6 when dealing with OH* radiation modeling. Figure 4.6 and 4.7 show a concept of the BKH optical diagnostic setup and a sketch of how line-of-sight measurement are displayed for an unexcited run of BKH. BKH tests are performed at test bench P8 which is a French German cryogenic test facility at the Institute of Space Propulsion in Lampoldshausen. A typical test sequence of BKH starts with purging the combustion chamber with gaseous hydrogen in order to avoid the presence of air during the test run. The propellants are then injected

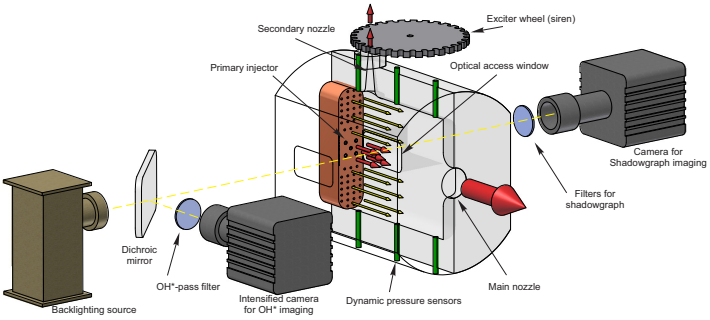

Figure 4.6: BKH optical diagnostics setup concept.[86]

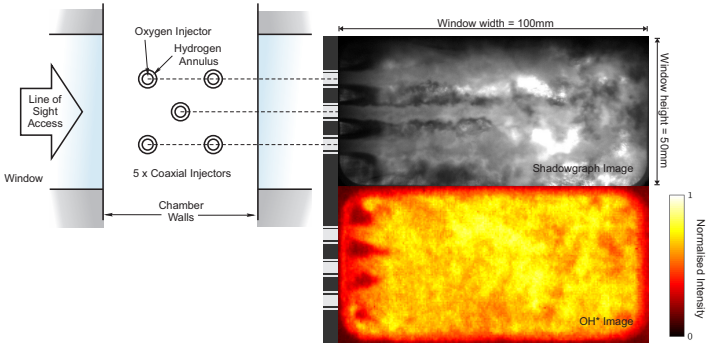

Figure 4.7: Line-of-sight optical data from a test run without acoustic excitation [86]

into the chamber with a reduced mass flow rate and ignited. Shortly after the ignition, the mass flow rates of the propellant are led to the target value of the test. The tests typically run for 40 to 45 seconds. The operating point considered in this work has a Ratio Oxidizer to Fuel (ROF) of 6 and chamber pressure (p_{cc}) of about 60 bar. This operating point is maintained for the whole test duration. The excitation system is activated before the test start and the electric motor gives the siren the speed corresponding to the specified excitation frequency of the test. Once the chamber reaches the stable operating point, the siren speed is increased to reach the excitation frequency desired for the excitation of the relevant resonant mode of the chamber. Figure 4.8 shows a spectrogram of a test run at ROF=6, p_{cc}=60 bar produced by the signal captured by PCCDYN2, placed at the bottom of the chamber as shown in Figure 4.5. The horizontal bands in the spectrum show that resonant modes of BKH are weakly excited even when no acoustic excitation is applied. This is due to combustion noise and turbulence phenomena. At 2 kHz the acoustic excitation starts, being increased linearly with a rate of 80 Hz/s to excite each of the resonant modes during the test run, appearing as diagonal lines in the spectrogram.
The raw pressure signal shows the highest amplitude of pressure oscillations during the excitation of the 1T mode. When the excitation frequency matches a resonant mode, high-speed optical cameras are triggered and register the flame dynamics when the flame is subject to acoustic disturbance.

4.2 Numerical approach

RANS and URANS simulations described in this chapter and the whole work are performed using the DLR in-house TAU code described in Chapter 3.

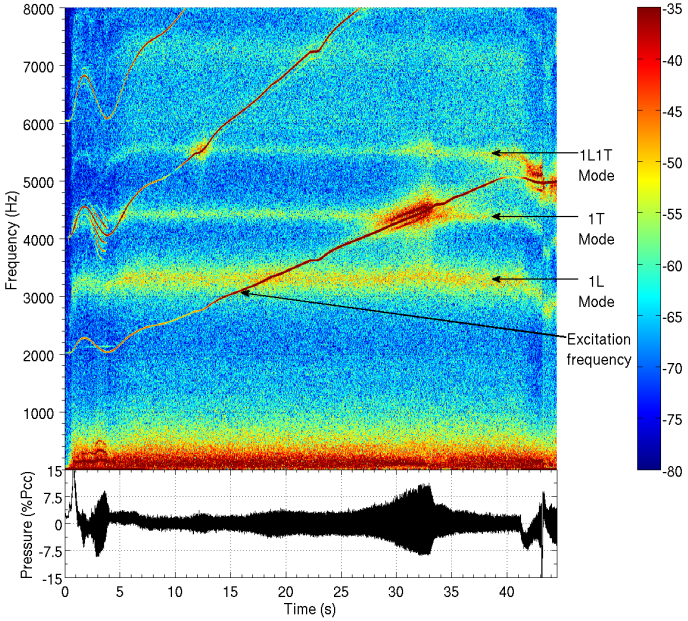

Figure 4.8: Spectrogram and pressure signal registered by PCCDYN2 during a test run at ROF=6 p_{cc}=60 bar[15]

The operating point conditions are described in Table 4.1

Property	Value	Unit
O_2 injection temperature	127	K
H_2 injection temperature	279	K
O_2 Mass flow rate	113	g/s
H_2 Mass flow rate	19	g/s
Chamber pressure	60	bar
ROF	6	-

Table 4.1: Values for the single injector configuration simulated operating point. Mass flow rates are calculated for the single element.

As a first step, a RANS simulation was performed for both the domains considered in this section, and used as starting solution for the URANS calculations where acoustic pressure and velocity excitation were applied to describe the 1L and 1T mode excitation, respectively. The excitation is applied by modulating the boundary conditions in the region representing the combustion chamber volume. The URANS simulations are used to study the response of the flame placed in the central primary injector zone of BKH.
Unsteady simulations were setup using a dual time stepping Jameson type scheme, with a physical time step of $5{\cdot}10^{-6}$ s. A Cauchy convergence criterion was used to stop the inner iterations once the convergence conditions were reached.
Figure 4.9 shows the 2D geometrical domain and the boundaries to investigate the 1L mode excitation of the single injector configuration. The 2D axisymmetric

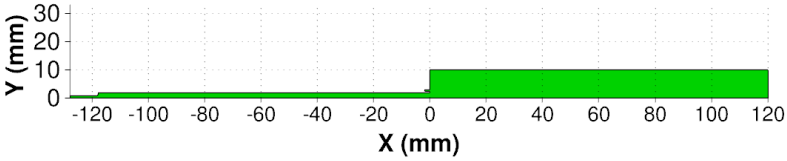

(a) Geometry

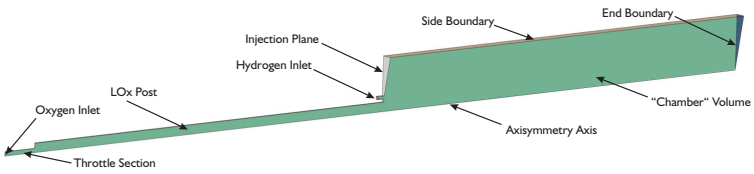

(b) Boundaries prescribed in the domain.

Figure 4.9: Domain and boundaries of the 2D axisymmetric configuration.

domain is chosen because the pressure fluctuations are imposed symmetrically with respect to the flame as it is placed in a pressure antinode and velocity node. Under this conditions, the imposed pressure excitation does not disturb the flame front at the centerline and so the 2D approximation is justified at this stage. The LOx post is included in the domain up to throttle of the manifold in order to investigate the coupling between the LOx post and the representative chamber volume. Urbano et al. [222] numerically investigated this phenomenon in LES simulations of BKD, whereas Gröning identified the LOx post coupling [77] as the triggering mechanism of self-excited instabilities in the same chamber. The throttle section is then included in this study because it accelerates the flow coming from the oxygen manifold, causing a consequent pressure drop and consequently decoupling the domain considered here from the upstream injection system.
The hydrogen post is not included since hydrogen is considered here as an ideal gas and thus it limits the applicability of the described model. This assumption leads to errors in density and specific volume 3.8%. This value increases when pressure raises and temperatures lower.
The domain has an axial extension of 120 mm, so that it extends slightly downstream the length of the optical access window and the results can be compared to experimental data. The radial dimension of 10 mm is chosen because of the peculiar configuration of BKH. In fact the central flame is surrounded by four neighboring flames and the distance between the inner and the outer flames measured at the center of each flames measures 15 mm. The 10 mm radius ensures that the representative element is contained in the domain when subject the acoustic pressure disturbance.
Mass flow rate boundary conditions are prescribed at the oxygen and hydrogen inlets. The axisymmetric boundary condition is applied to the centerline. The LOx post and hydrogen post walls, post tips and injection plane are described by an adiabatic viscous wall. An inviscid wall boundary condition is applied to the upper boundary of the domain extending from the injection plane to the end of the volume, so that no mass flow and velocity normal to the wall are present. At the outlet, a farfield boundary condition is used. The farfield boundary condition is set with density, temperature and mass fraction of the species described by the chemistry model. Equilibrium temperature, density and mass fractions are computed with the NASA software CEA [70, 239]. The farfield boundary condition is applied in order to limit the size of the domain being the outlet sufficiently downstream the flame front [11]. With the farfield boundary condition, the flux across the boundary is calculated with the difference between the internal flow state and the specified farfield state.
For URANS calculations, the farfield and inviscid wall boundary conditions are replaced with a near-field boundary conditions which are modified at each time step to impose the acoustic disturbance as described in Section 4.3. The near-field boundary condition is analogous to the farfield one and it is defined by specifying the thermodynamic state of the mixture at the surface where it is applied, imposing a property distribution at the boundaries. For the nature of the near-field boundary condition, the internal flow field follows the distribution at the

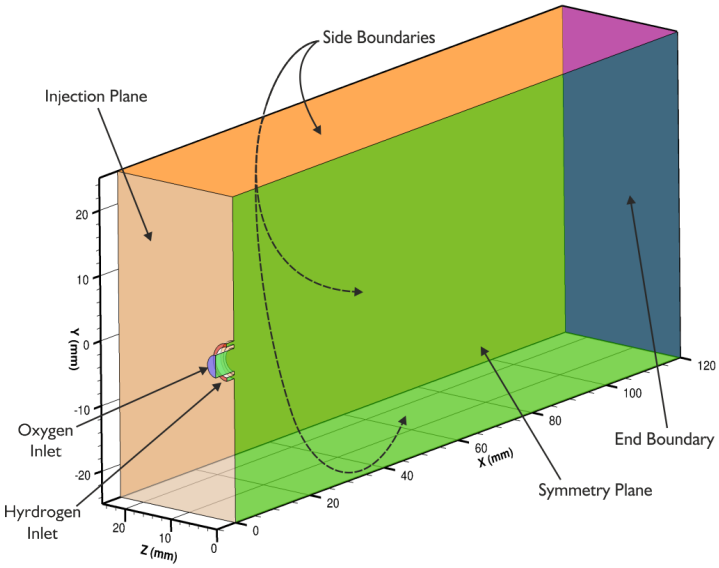

Figure 4.10: Domain of 3D single injector configuration for the investigation of the acoustic velocity disturbance [15].

boundaries, adapting at each time step. This allows to impose the acoustic fluctuation on the numerical domain.
Modeling the 1T mode excitation of the single injector configuration followed the same approach. The main difference lies in the choice of the domain. Here, a 3D rectangular domain is chosen to correctly capture the response of the flame to the transverse acoustic velocity excitation. In this case, the flame subject to transverse acoustic velocity excitation flattens and retracts towards the injection plane. The single coaxial injector is placed in a pressure node and velocity anti-node, so that the post coupling is limited. This allowed to reduce the domain not including the post into the computational domain. Figure 4.10 shows the domain geometry and characteristics. Here, for the steady state calculations both side boundaries are treated as inviscid walls and at Z = 0 and axsymmetric plane boundary condition is imposed. The rest of the boundary conditions are the same as in the 2D setup. The length of the domain is 120 mm for the same reason of the 2D configuration, while is 25 mm wide and 50 mm high. These measures are used since they are representative of the real dimensions of BKH, which contains the window cooling system and the five flames. The dimensions of the domain also allow the flame not to intersect the boundaries during the excitation process. URANS simulations are performed following the same approach described for the 2D configuration, replacing the side boundaries and the end boundary with near-field boundary

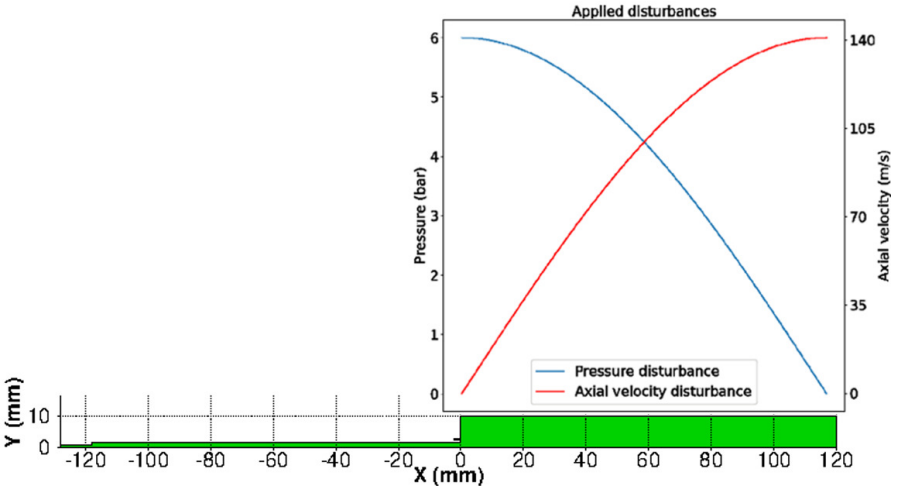

Figure 4.11: Distribution of the disturbance profiles along the 2D domain.

conditions varied at each time step to impose the acoustic velocity excitation described in Section 4.3.

4.3 Modelling excitation profiles

The acoustic disturbance is imposed over the mean pressure chamber value $\overline{p}$ as a fluctuation p' as $p{=}\overline{p}{+}p'$.
In this work, in order to apply a realistic acoustic disturbance profile, not only a constant pressure disturbance as done by Beinke [15] but also a velocity fluctuation is imposed. The logic is the same as the pressure fluctuations, so that $v{=}\overline{v}{+}v'$ where $\overline{v}$ represents the mean velocity field and v' the imposed fluctuation. As described by Tonti et al., excitation profiles are imposed as:

$$p' = Ae^{i\omega t} \tag{4.1}$$

$$v' = \frac{i}{\rho\omega}\nabla\hat{p}e^{i\omega t} \tag{4.2}$$

where $\hat{p}$ is the real part of the pressure fluctuation signal and $\omega{=}2\pi f$.
The velocity fluctuation starts about 1/4 after the beginning of the acoustic cycle, describing the behavior as observed in the experiment, due to delayed response of the flame to the traveling velocity disturbance triggered at the peak of the acoustic pressure perturbation signal. The distribution of the pressure and axial velocity disturbance along the 2D domain is shown in Figure 4.11. Assuming isentropic expansion and compression of the gaseous mixture, the near-field

boundary condition is applied at each time step to impose the desired acoustic disturbance by specifying temperature, density, velocity and composition of the mixture. The starting steady-state solution gives the values of the gas constant and specific heats of the mixture.
The near-field boundary condition is built as follows. First the pressure at the boundaries is specified. Then, the corresponding density is calculated using the isentropic law for ideal gases. Successively, the ideal gas equation of state is used to specify the temperature and the steady-state solution mixture composition is assumed, which corresponds to the equilibrium composition where the combustion product are mostly hydrogen and water vapor, with the mass fraction of each species kept constant during the cycles.
This method has the advantage to be computationally cheap, but has some limitations, as explained by Tonti et al. [218]. The mass injected in the domain across the boundary has a specified mixture with properties given by the near-field boundary condition imposed. Here the near-field boundary species distribution is adapted from the steady-state solution, so the mass entering in the domain has the same mixture composition as the steady-state solution, this meaning that an a-priori approximation of the flow outside the boundary is used. The flow entering in the domain during the pressure peak of the acoustic cycle is therefore not the same as the one leaving the domain during the low pressure phase of the acoustic cycle because gradients across the boundary are present. That is the reason why the single injector configuration is more representative of a single injection element isolated in a chamber full of combustion products.
The 1T mode excitation is simulated by modeling the transverse acoustic velocity excitation of the flame. The perturbation is prescribed as a function of the height of the chamber and the required amplitude of the pressure fluctuation at the wall, as described in Beinke [15]:

$$p' = \left|p'_{wall}\right| sin\left(\frac{y\pi}{H}\right) e^{i\omega t} \tag{4.3}$$

To match the desired pressure, the transverse acoustic velocity disturbance is imposed as follows:

$$\begin{aligned} v' &= \frac{i}{\rho\omega}\nabla\hat{P}e^{i\omega t} = \\ &= \frac{i}{\rho\omega}\nabla\left(\left|p'_{wall}\right| sin\left(\frac{y\pi}{H}\right)\right)e^{i\omega t} \end{aligned} \tag{4.4}$$

which becomes

$$v' = \frac{|p'_{wall}|}{2\rho f H} cos\left(\frac{y\pi}{H}\right) e^{i(\omega t+\pi/2)} \tag{4.5}$$

where H =200 mm, $\rho = 2.71\ kg/m^3$ is the value of the density for the equilibrium mixture and f is the frequency of the imposed excitation.
The mesh used in the first part of this chapter is the same used by Beinke for both the 1L and 1T mode excitation [15]. The last part of the chapter is dedicated to the study of the effect of the mesh and boundary conditions of the results and

then the mesh is described in detail there. For the sake of comprehension, here only the main details of the mesh are given.
The fully unstructured mesh of the 2D domain consists in approximately 160 k nodes with prismatic and tetrahedral elements, with a minimum size of 0.03 mm in the shear layer which gradually increases to a maximum size of 0.5 mm downstream at the end of the domain. The mesh is refined in the reaction zone in order to correctly capture the shear layer where the ignition of the flame and the combustion reaction takes place, between the oxidizer and fuel streams.
The fully unstructured mesh used for the 3D 1T mode simulation consists of 590 k nodes, with a minimum element size of 0.08 mm in the shear layer which gradually reach 2 mm downstream of the flame. A stretching factor of 1.2 is is used to progressively decrease the size of the tetrahedral and prismatic elements used in the mesh.
These values for both configurations were chosen after a mesh convergence study which did not affect in a significant way the LOx core length and the flame distribution across the computational domain.

4.4 Steady state results

The starting solution for the simulations of the 1L and 1T mode excitation is in both cases a converged steady state solution. Here, the steady state fields for both configurations are briefly described highlighting the main features of the steady state fields.

4.4.1 2D steady-state field

Figure 4.12 shows the pressure distribution along the domain in the steady-state solution. The pressure in the chamber has a value of 60.7 bar as prescribed by the farfield boundary condition. A pressure drop along the throttle and the first part of the LOx post of about 20% can be noticed, between x = -127 mm and x = 112 mm. This correctly reproduces the pressure drop which typically verifies when the flow decelerates by the variation of the surface from a narrower to a wider volume. Downstream x = -112 mm the pressure rises again and then tends to the same value as in the representative chamber volume. Figure 4.13 show the distribution of density, temperature, OH mass fraction and heat release, respectively. The density distribution shows the length of the intact LOx core extending for about 64 mm downstream the injection plane. The combustion zone is indicated by the OH mass fraction distribution, which surrounds the LOx core. The temperature field is characterized by a small recirculation zone with relatively cold hydrogen which extends until the upper boundary of the chamber volume near the corner of the domain. Downstream of the flame front, the temperature is uniform corresponding to the adiabatic flame temperature calculated by CEA and imposed as a farfield boundary condition. The dissociation of water produced the peculiar shape of the heat release distribution shown in Figure 4.13d. This phenomenon occurs essentially in the hottest region of the flame. The maximum heat release is

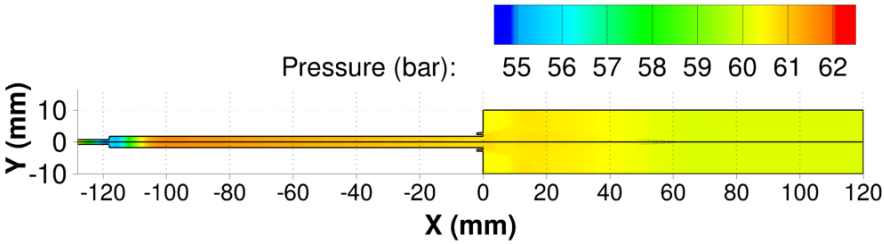

Figure 4.12: Steady-state pressure field in the 2D domain.

observed in the combustion zone in the shear layer between the LOx and H_2 streams in a region close to the injection plane. Heat release is negligible downstream the combustion region because chemical equilibrium is reached. Looking at the OH mass fraction and heat release rate close to the injection plane, the relation between the combustion zone identified via the OH mass fraction distribution and the maximum values of the heat release can be seen. This is shown in Figure 4.14. The flame is anchored to the tip of the LOx post between the inlets of the oxygen and hydrogen streams. The color bar of the heat release has been adjusted to highlight the values of the distribution.

4.4.2 3D steady state field

The 3D steady state field presents essentially the same flow field distribution of the 2D configuration, as stated also by Beinke [15]. Figure4.15 shows the density, OH mass fraction and temperature field. The values are shown for the center plane at Z=0. The LOx core length measured at the isosurface $\rho = 100$ kg/m^3 results in about 65 mm, slightly longer than in the 2D case. However, varying the turbulent Schmidt number from 0.3 to 0.2, the LOx core length increases from 65 to about 70 mm, as shown in Figure 4.16.
The influence of the turbulent Schmidt number on flow fields and flames it is still an open research topic, since there is still no agreement on which value has to be set when running a CFD simulation and often best fitting values are used. Hwang et al. [102] investigated the effect of varying the turbulent Schmidt number in a LES simulation of a LOx/GH_2 single injector rocket combustor, the ONERA RCM-3. The turbulent Schmidt number was varied over a range of 0.2 to 0.8. The best agreement with the experimental data from OH emission was found for $Sc_t = 0.4$ and 0.5 when comparing the inner flame surface size and the oxygen jet contour distribution. In flows where the density varies both in longitudinal and transverse direction, the Sc_t varies with the level of stratification of the flow and affects mostly mass diffusivity so that with a lower Sc_t an increase of mass diffusivity is observed. In this study, a Sc_t of 0.3 will be kept despite the better

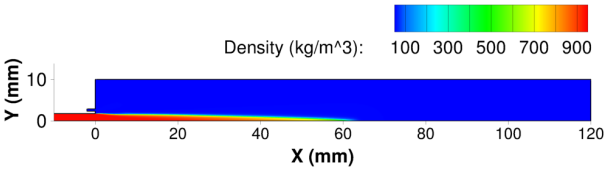

(a) Density

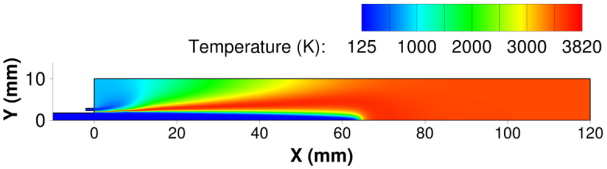

(b) Temperature

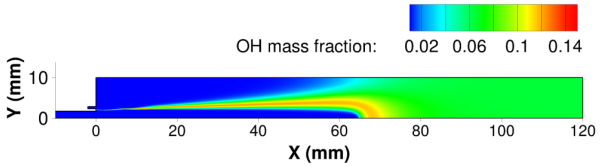

(c) OH mass fraction

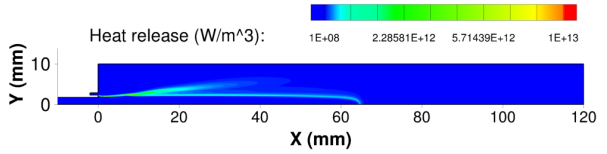

(d) Heat release

Figure 4.13: Steady-state distribution of density (a), temperature (b), OH mass fraction (c) and heat release (d) in the 2D domain.

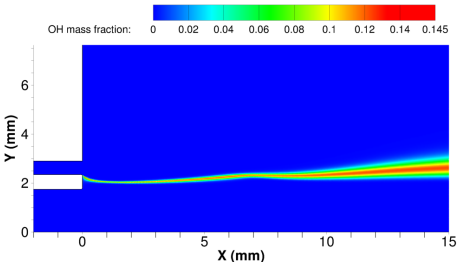

(a) OH mass fraction

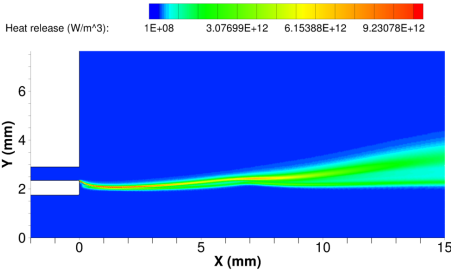

(b) Heat release rate

Figure 4.14: OH mass fraction (a) and heat release rate (b) closeup.

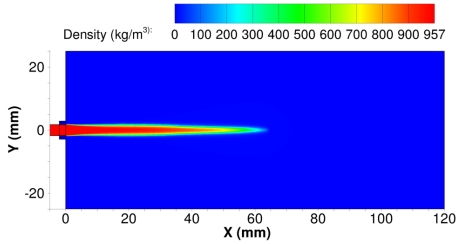

(a) Density

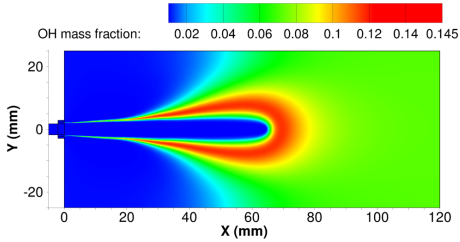

(b) OH mass fraction

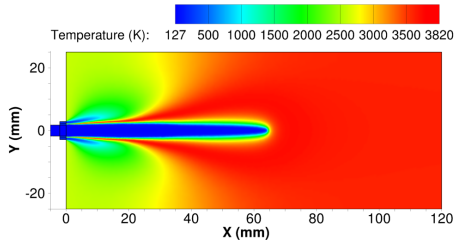

(c) Temperature

Figure 4.15: Density (a), and OH mass fraction (b) and temperature (c) distribution in the 3D axisymmetric configuration.

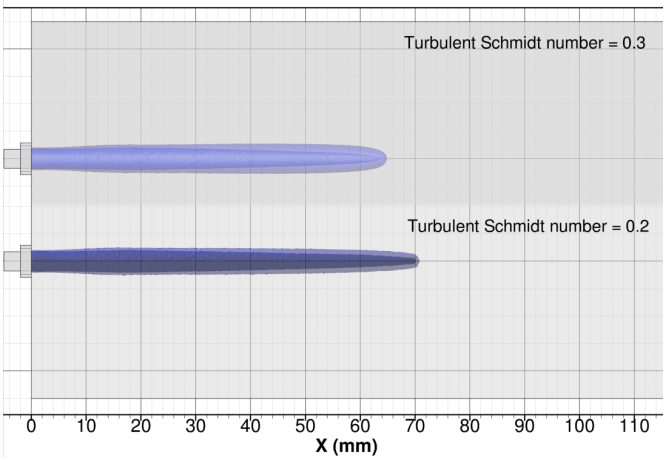

Figure 4.16: Isodensity surfaces at ρ =100 kg/m^3 and ρ = 10 kg/m^3 for Sc_t =0.2 and Sc_t =0.3

agreement of $Sc_t = 0.2$ with the experimental data in order to have a more direct comparison with the former work by Beinke [15]. In future work, variable turbulent Schmidt and Prandtl number calculations should be foreseen, in order to let the values adapt with the changes of the flow field in time-varying simulations.

4.5 1L mode excitation results

In this section, the response of the flame subject to 1L mode excitation of the flame is investigated, considering a matrix of exciting conditions which provides further insights into the flame response. In fact, BKH geometry is optimized to study the response of the flame to the 1T mode excitation. The amplitude of the longitudinal mode reached in the experiments is about 3% of p_{cc}. Here, higher amplitude disturbances are investigated to different frequencies. The range of frequencies is chosen because it resulted to be of particular interest for BKH. The resonant frequency of the chamber of the 1L mode is 3300 Hz, while the post shows from experimental data a 1L mode frequency of 3400 Hz. In this work, the purpose is to investigate the response of the chamber to acoustic pressure disturbances of different amplitudes ranging from off-resonance conditions (3200 Hz) to resonant frequencies of the chamber (3300 Hz) and of the LOx post (3400 Hz). It can be considered as a first step towards a FTF for BKH, mapping the flame response to several acoustic pressure disturbance profiles. Figure 4.17 shows the pressure signals for the 3 bar amplitude of the acoustic pressure excitation for f=3400 Hz for the entire physical time of the simulation. Figure 4.18 shows the same pressure signal once the steady state fluctuations are reached.

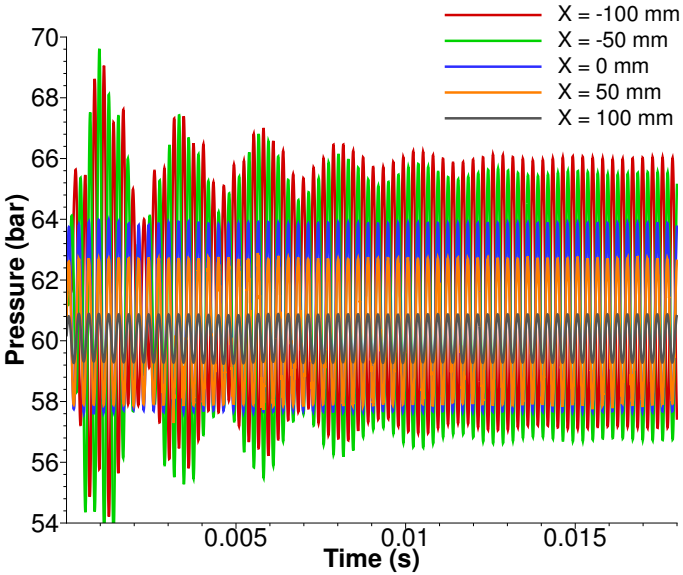

Figure 4.17: Pressure signal in the chamber axis at different locations for the entire calculation time at f=3400 Hz.

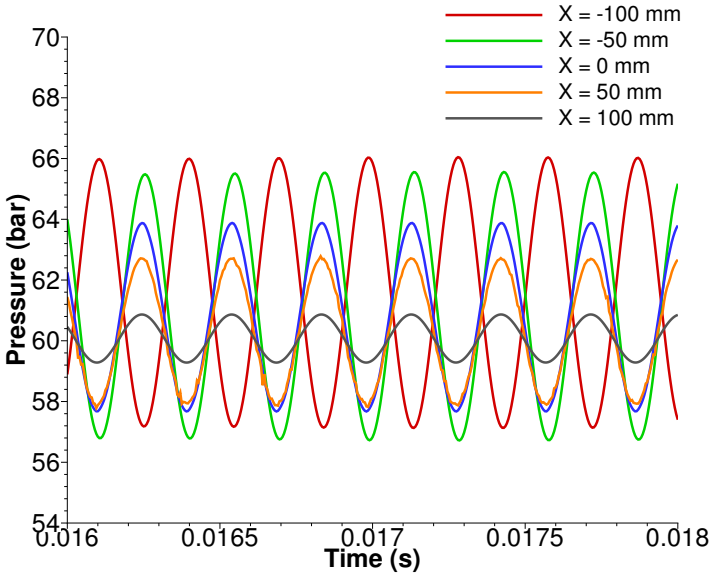

Figure 4.18: Pressure signal in the chamber axis at different locations for 3 bar amplitude at steady-state fluctuations for f=3400 Hz.

	Axial coordinate	Frequency (Hz)		
		3200	**3300**	**3400**
1.5 bar	X = -100 mm	+4.2%	+5.0%	+5.7%
	X = -50 mm	+3.0%	+4.4%	+5.4%
3 bar	X = -100 mm	+6.9%	+8.2%	+8.7%
	X = -50 mm	+5.3%	+7.2%	+7.8%
4.5 bar	X = -100 mm	+9.75%	+10.7%	+12.4%
	X = -50 mm	+7.6%	+9.1%	+11.5%
6 bar	X = -100 mm	+13.3%	+14.3%	+17.3%
	X = - 50 mm	+10.7%	+12.9%	+15.5%

Table 4.2: Deviation from the mean p_{cc} at X = -100 mm and X = -50 mm inside the LOx post at steady-state fluctuations for the different amplitudes and frequencies of the applied disturbance.

The signals profiles for the different configurations are similar to each other. Amplitude and frequencies change with the prescribed boundary conditions, but the general behavior can be described as follows. Figure 4.17 shows that for the first 2 ms of the excitation, the response of the LOx post at X < 0 is stronger than the imposed disturbance, indicating the internal resonance of the post. In off-resonance conditions at 3200 Hz, the difference in the amplitude oscillations between X = -100 mm and X = -50 mm is higher than in the two resonant cases once the steady state oscillations are reached. In particular, the amplitude of the oscillations at the injection plane at X = 0 mm is comparable with the one measured at X = -50 mm, showing only a slight time delay of about $1{\cdot}10^{-4}$ s and amplitude reduction of 1.2% of the mean peak-to-peak amplitude. For all the three excitation frequencies, the signal in the LOx post at X = -100 mm is out of phase with the other signals, indicating a resonance of the LOx post. At 3300 Hz, where the resonant mode of the chamber is matched, spurious oscillations can be identified at the pressure peak of each cycle at X = 50 mm, which coincides with the tip of the flame. This spurious pressure oscillations are caused by the axisymmetry boundary condition imposed as all the signals are taken on the axis, as will be shown in Section 4.7.3.1. The same behavior, although attenuated can be seen for the 3400 Hz frequency. When the resonant modes of the chamber and the post are matched, the amplitude of the pressure oscillation grows at X = -100 mm and X = -50 mm, overcoming the amplitude of the imposed disturbance and indicating a resonant conditions which increases the amplitude of the pressure oscillations. Table 4.2 quantifies the difference of the signals in the post at the two locations with respect to the mean p_{cc}. The deviation from the mean pressure signals increases regularly with increasing amplitude for the corresponding frequency, with a difference of about 3% for each of the axial locations, respectively.

Another important parameter for the study of combustion instabilities is the heat

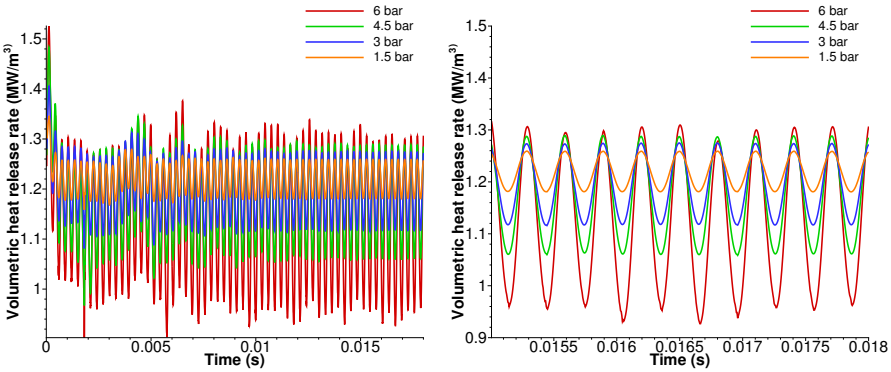

(a) Whole signal (b) Steady-state fluctuations

Figure 4.19: Volumetric integrated heat release rate at different amplitudes for 3300 Hz excitation frequency.

	$\overline{Q}$(MW/m^3)			
	3200 Hz	**3300 Hz**	**3400 Hz**	**Amplitude (%)[1]**
1.5 bar	1.2196	1.2198	1.2182	6.5
3 bar	1.1952	1.1953	1.1978	12.5
4.5 bar	1.1646	1.1723	1.1718	18.3
6 bar	1.1253	1.1297	1.1296	29.2

Table 4.3: Mean volumetric heat release at steady state fluctuations.

release rate. Different levels of heat release rate are reached at different excitation level. Figure 4.19 shows the evolution of the volume integrated heat release rate over time for 3300 Hz, which is the resonant frequency of the chamber, for all the four disturbance amplitudes.
For the different excitation amplitudes, the heat release rate fluctuations vary over time until reaching steady state fluctuations. After an overshoot when starting the excitation for all the four cases, the volumetric heat release rate tend to stabilize and reach the limit cycle. It can be seen from Figure 4.19 that the steady state fluctuations are reached around different mean values of the volumetric heat release rate, with this value which decreases as the excitation amplitude increases. At the same time, the amplitude of the fluctuations around the mean value becomes higher as the acoustic disturbance level increases.
Table 4.3 summarizes the mean value of the volumetric heat release rate signal $\overline{Q}$ for the different amplitudes of the signals at the different frequencies.

[1]Mean volumetric heat release at steady-state fluctuations and amplitude of the heat

	$\mathbf{Q}_{gain}/\mathbf{P}_{gain}$		
	3200 Hz	**3300 Hz**	**3400 Hz**
1.5 bar	1.36	1.38	1.39
3 bar	1.39	1.38	1.35
4.5 bar	1.42	1.38	1.35
6 bar	1.65	1.56	1.55

Table 4.4: Ratio between gain of volumetric heat release rate and pressure signals.

$\overline{Q}$ decreases with increasing amplitude of the disturbance for constant frequency values. The highest values are reached when the excitation frequency matches the resonant chamber mode, maintaining the same trend as pressure amplitude fluctuations increase. This explains also the differences in the ratios between the gain of the fluctuating heat release rate and pressure signals shown in Table 4.4. The ratio is calculated as follows: once steady-state fluctuations are reached, pressure and heat release rate fluctuations around the mean value are calculated.

$$\begin{aligned} p' &= p_{tot} - \overline{p} \\ q' &= q_{tot} - \overline{Q} \end{aligned} \tag{4.6}$$

where p_{tot} and q_{tot} indicate the whole signal and $\overline{p}$ and $\overline{Q}$ represent the mean values. Then, the root mean square of the fluctuations are calculated.

$$\begin{aligned} p'_{rms} &= \sqrt{(p')^2} \\ q'_{rms} &= \sqrt{(q')^2} \end{aligned} \tag{4.7}$$

The gain of the signals is then derived.

$$\begin{aligned} P_{gain} &= \frac{p'_{rms}}{\overline{p}} \\ Q_{gain} &= \frac{q'_{rms}}{\overline{Q}} \end{aligned} \tag{4.8}$$

and finally the ratio Q_{gain}/P_{gain} is obtained.
Table 4.4 shows that the ratio between heat release rate gain and pressure gain decreases with increasing frequency for each amplitude of the pressure disturbance, as was also shown by Noiray et al. [149]. For the same frequency, the ratio varies between different levels of pressure amplitude fluctuations, showing the highest ratio for 6 bar amplitude disturbance.
Figure 4.20 and Figure 4.21 show the deformation of the LOx core at phase = π for 1.5, 3, 4.5 and 6 bar at steady-state fluctuations for the minimum and the maximum excitation frequency.

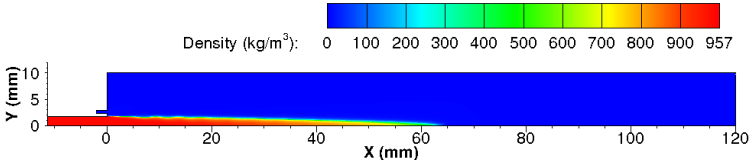

(a) 1.5 bar

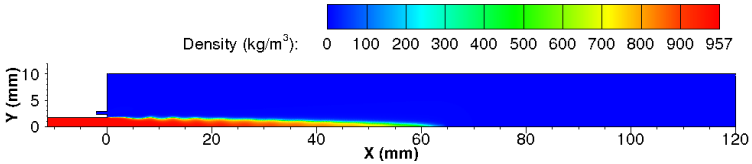

(b) 3 bar

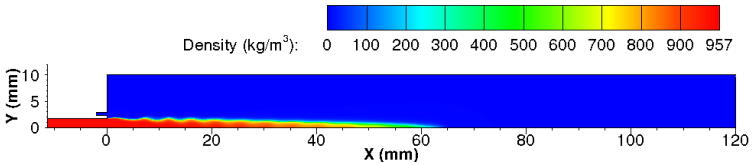

(c) 4.5 bar

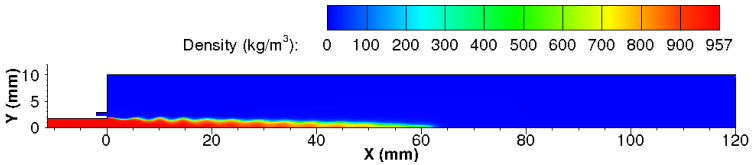

(d) 6 bar

Figure 4.20: Density distribution in the chamber volume for different amplitudes at 3200 Hz.

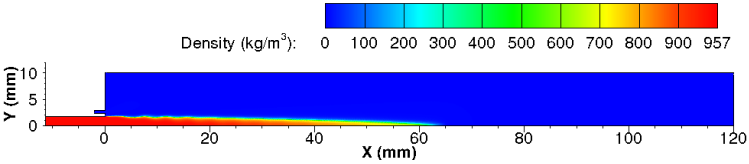

(a) 1.5 bar

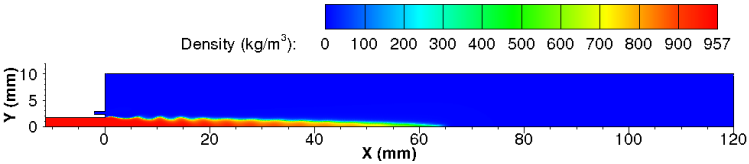

(b) 3 bar

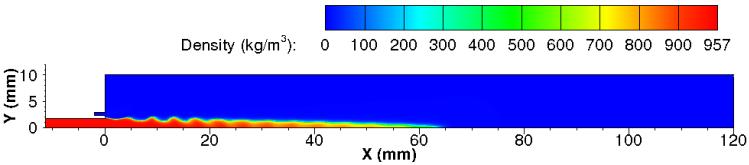

(c) 4.5 bar

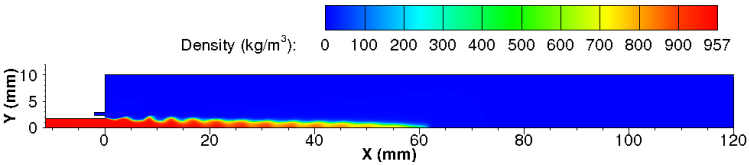

(d) 6 bar

Figure 4.21: Density distribution in the chamber volume for different amplitudes at 3400 Hz.

Pressure amplitudes (bar)	Excitation frequency (Hz)		
	3200	3300	3400
1.5	+0.97%	+1.16%	+1.37%
3	+1.52%	+2.03%	+2.62%
4.5	+1.15%	+1.90%	+ 1.46%
6	+4.5%	+ 3.28%	+4.35%

Table 4.5: Mean difference between the length of the LOx core at steady state and for the different excitation conditions

The length of the LOx core, defined as the distance in which the dense LOx core remains intact through the chamber, is slightly affected by the level of the excitation, resulting in a slight stretch of the LOx core downstream. This happens at the lowest part of the cycle, corresponding to the lower pressure condition. With increasing amplitude of the perturbation the flame shows a stronger wrinkling, presenting wave-like structures at the shear layer between the oxygen and hydrogen streams as shown in Figure 4.20. The strongest fluctuations are visible slightly downstream the injection plane. The amplitude of the ripples decreases as the LOx core density decreases and penetrates into the chamber volume. Increasing the frequency of the excitation increases the amplitude of the wave-like structures with respect to the unperturbed field, as can be seen in the comparison between Figure 4.20 and Figure 4.21. Table 4.5 shows the percentage variations of the length of the LOx core with respect to the value of the steady-state configuration. A delay in the response of the LOx core to the disturbance should anyway be considered, in a way that taking the values at the pressure peak and trough are not necessarily the maximum and minimum values of the LOx core length.
For the 4.5 bar and 6 bar cases, it can be seen that for the resonant frequency of the chamber (3300 Hz), the variation of the length of the LOx core is lower than for the other two examined frequencies. It is interesting to notice that in those cases, the LOx core is slightly wider than in the cases at lower pressure amplitudes. Moreover, before steady-state fluctuations are reached, a disruption of the LOx core occurs for the 4.5 and 6 bar amplitudes of the pressure disturbance occurs. When the minimum (negative) value of the axial velocity is reached, the LOx core breaks up, forming a bubble which travels downstream and it is consumed before reaching the end of the domain. When the amplitude of the imposed disturbances is lower, this phenomenon is not observed and the LOx core remains intact. On the other hand, axial velocity disturbance seems not to have any impact of this phenomenon. Comparing the amplitude of the ripples at the shear layer with previous simulations from Beinke [15], which imposed a uniform pressure disturbance, no difference is shown and then it can be concluded that the impact of the axial velocity on the amplitude of the wave-like structures is negligible.

release rate fluctuations around the steady-state value

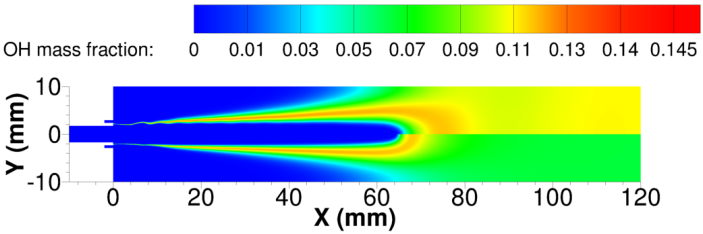

Figure 4.22: Comparison of OH mass fraction distribution at 6 bar 3200 Hz excitation (top) and steady state solution (bottom)

The axial velocity disturbance has instead a visible impact of the OH mass fraction distribution. Figure 4.22 shows the comparison between the steady-state solution and the 6 bar 3200 Hz excitation frequency. This example has been chosen because of the values of the stretch of the LOx core displayed in Table 4.5, being the case where the greatest difference in the LOx core length with respect to the steady-state length is observed. The color scale was adjusted to put stress on the differences in the distribution.

The OH mass fraction distribution indicates the location of the flame. The length of the flame is altered by the imposed disturbance, resulting in a stretching of 5%. The farfield boundary condition imposed at the end boundary as described in Section 4.3 together with the imposed acoustic velocity disturbance produces the difference in the distribution between the steady state solution and the transient solution. The flux is in fact forced from the end boundary, meaning that it acts to push gas with a different OH mass fraction inside the flow field, thus causing the discrepancy.

For the evaluation of the effect of the axial velocity disturbance on the flame length, a comparison with previous results of Beinke [15] is necessary, since in this simulation no axial velocity disturbance was included. Figure 4.23 shows the comparison of the 3 bar 3400 Hz excitation frequency which was run also by Beinke [15].

The axial velocity distribution has an impact on the flame length. When applying a uniform pressure disturbance, the flame results to be longer and more stretched. In fact, not only the length but also the volume in which the flame is contained results to be thinner. Measuring the difference at the tip of the LOx core, the solution without axial velocity forcing results to be 3.3% longer than with axial velocity disturbance measured at the same phase π of the signal. For the 1.5, 4.5 and 6 bar the difference results to be about 2.1%.

A comparison of the axial distribution of some relevant quantities at the maximum and minimum pressure amplitude of an acoustic cycle between the uniform pressure disturbance and the realistic acoustic distribution gives further insights into the differences between the two approaches. Figure 4.24 shows both

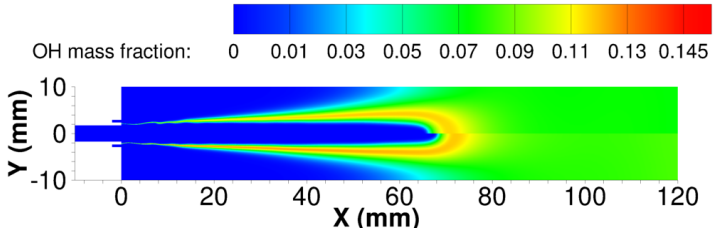

Figure 4.23: Comparison of OH mass fraction distribution at 3 bar 3400 Hz excitation with representative pressure disturbance including axial velocity (top) and with uniform pressure disturbance (bottom) [15]

approaches at a pressure maximum and Figure 4.25 shows the two distributions at a pressure minimum.

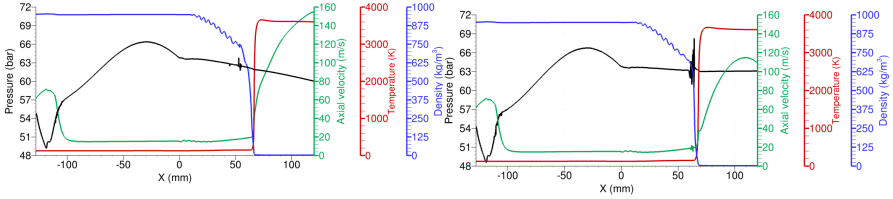

(a) With axial velocity forcing

(b) Without axial velocity forcing

Figure 4.24: Distribution of properties along the axis at the maximum of acoustic pressure oscillation amplitudes at 3 bar 3400 Hz.

In both cases, the profile of the axial velocity shows visible differences. In particular, the value of the axial velocity remains constant for the cases without axial velocity forcing, whereas in the case where the forcing is present the value fluctuates between 124 and 160 m/s. This has an impact on the density distribution, which decreases more smoothly at the tip of the flame. The temperature distribution does not show any difference between the two cases. The pressure distribution along the axis shows less spurious oscillations in the case with axial velocity forcing, mainly due to the different version of the TAU code used for the simulations. Moreover, the value at the end of the domain results to be higher than in the case without axial velocity forcing due to the different pressure distribution applied in this work and described in Section 4.3. In the case of constant pressure disturbance imposed, the value at the end of the domain coincides with the maximum and minimum value of the amplitude of the oscillation imposed, respectively. When the realistic distribution is imposed, the

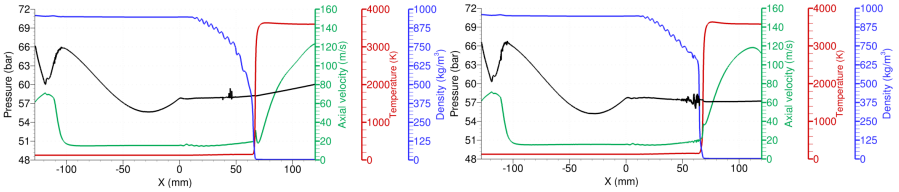

(a) With axial velocity forcing (b) Without axial velocity forcing

Figure 4.25: Distribution of properties along the axis at the minimum of acoustic pressure oscillation amplitudes at 3 bar 3400 Hz.

value at the end of the computational domain remains constant and coincides with the value of the mean chamber pressure obtained with the steady-state solution and being more representative of the experimental data. Comparing the axial distribution of the different values helps to explain and show how the flame is affected from the different excitation profiles imposed, in particular the effects on the length which is displayed by the density behavior. Density reaches the minimum values at the location where the intact LOx core is not present anymore and only combustion products are present in the domain. At about the same location along the axis, the temperature suddenly raises as the combustion reaction is completed.
Spurious pressure oscillations are less evident in the results of this work.. This raised some questions about how the numerical setup of the simulation could affect this aspect and this is the motivation to investigate the influence of the geometry and boundary conditions on the simulation results. This will be discussed in Section 4.7.

4.5.1 Comparison with experimental data

Reconstructed DMD images from Beinke [15] are used here for comparison with the 1.5 bar amplitude of the perturbation. This choice is justified by the observation in BKH experiment, where for the 1L mode excitation a maximum of 3% fluctuations about the mean pressure of the chamber are captured by the experimental setup.

From the comparison, it can be seen that the amplitude of the ripples is comparable with the experimental data for the same length and height of the domain, although the intensity in the experimental images are normalized. Different phase definition is used for the reconstruction of the acoustic modes with respect to the numerical simulation results. Taking this difference into account, the position, relative amplitude and spacing between the waves match with the experimental data.

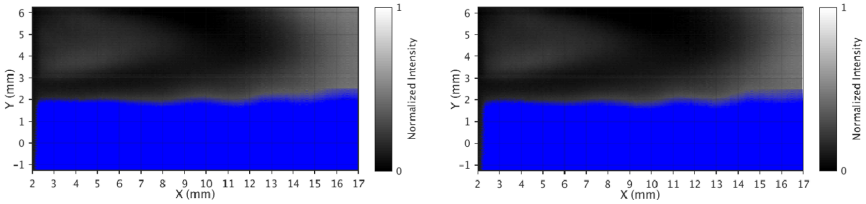

(a) Phase 0 (b) Phase π

Figure 4.26: Reconstructed DMD images at different phases of the acoustic cycle. LOx core in blue [15].

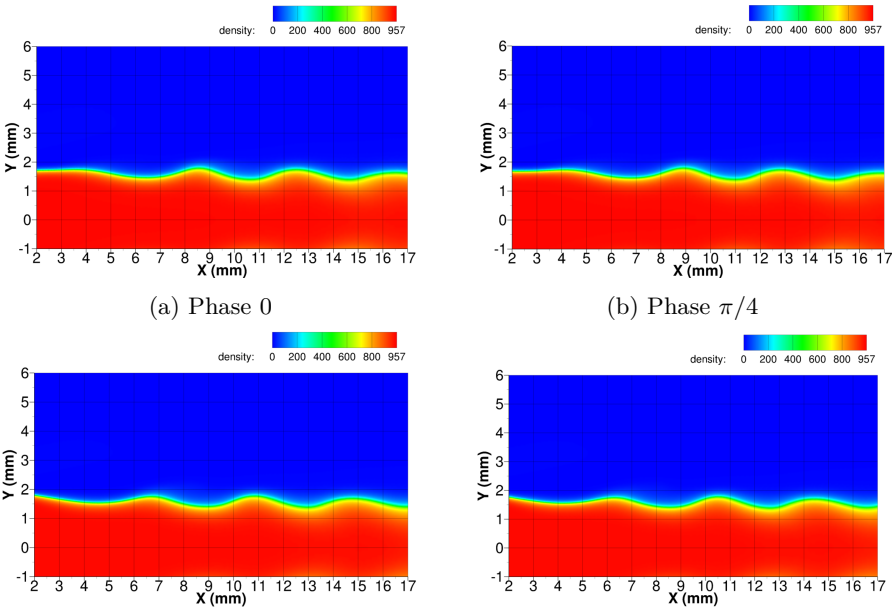

(a) Phase 0 (b) Phase $\pi/4$

(c) Phase $5/4\pi$ (d) Phase π

Figure 4.27: Density distribution at the same location of the shadowgraph images at different phases of the acoustic cycle for 1.5 bar pressure excitation amplitude.

4.6 1T mode excitation

The 1T mode excitation was run in this work to compare the results produced with different version of the TAU code This is the reason why only one value for the amplitude of the transverse velocity excitation was chosen for comparison with previous results from Beinke [15]. Here, the amplitude of the disturbance corresponding to 1.25% of the mean pressure chamber was chosen, the frequency of the excitation was set at 4400 Hz as results from the experimental data for this operating conditions in BKH. The pressure at the top and bottom of the chamber present out of phase fluctuations, reproducing the structure of the 1T mode, while the pressure along the centerline remains constant. The centerline of the considered domain shows on the other hand a maximum peak of the transverse velocity as the pressure gradient and the imposed velocity disturbance produce the desired profile of the transverse excitation. Figure 4.28 shows the length of the LOx core displaying density isosurfaces at $\rho = 100$ kg/m^3 and 10 kg/m^3 after ten acoustic cycles.

A detailed analysis of the 1T mode single injector configuration excitation varying the amplitude of pressure oscillations is provided by Beinke [15] and it is outside the scope of this work. In order to further discuss the influence of the numerical setup, an overview of the results is however needed. Figure 4.29 and 4.30 show the pressure profiles at various locations together with the transverse velocity measured at the centerline when a steady-state behavior is reached and the integrated heat release rate over time.

As it is shown in Figure 4.29, the pressure at the centerline is not perturbed by the excitation, whereas a 1T mode behavior is reproduced looking at the top and bottom wall, where the two pressure signals are out of phase.
Details about the simulation of the 1T mode for the single injector configuration under different excitation conditions can be found in Beinke [15]. However, a few comments about the behavior of the LOx core are needed. The transverse acoustic forcing causes both the transport and deformation of the LOx core, causing the flattening and the retraction of the core towards the injection plane. As shown by Beinke [15], when the intensity of the fluctuations increases, the LOx core results to be shorter and flatter. The retraction is caused by the fact that the flattening of the LOx core make its consumption more rapid than the surrounding hydrogen stream. The stabilization of the LOx core is reached after several acoustic cycles while it is still flattened and transported by the acoustic velocity.
High volumetric heat release rate is observed when oxygen is deflected into the high velocity hydrogen stream. The frequency of the heat release rate fluctuations has double the frequency of the imposed acoustic disturbance and it fluctuates twice per acoustic cycle, with a phase shift of $\pi/4$ with respect to the pressure fluctuations both at the top and bottom of the numerical domain, matching the behavior observed for the 1L mode excitation.

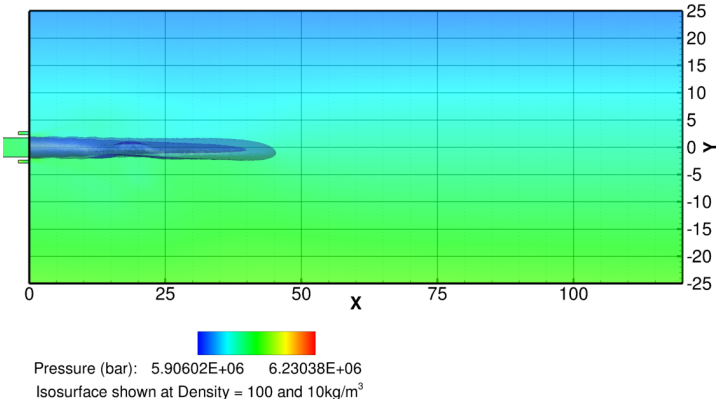

(a) XY plane

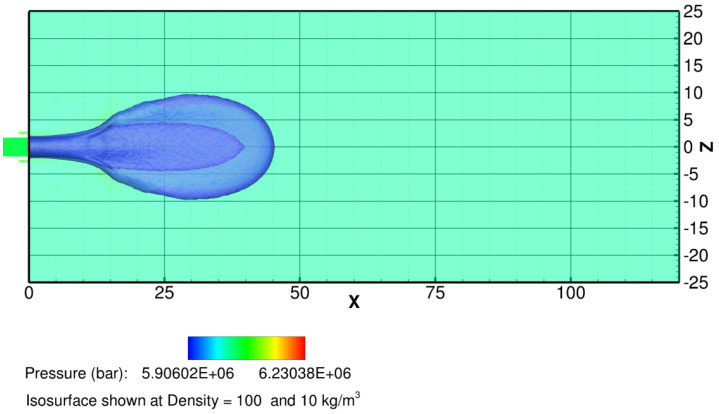

(b) XZ plane

Figure 4.28: Density isosurfaces at 10 and 100 kg/m^3 after ten acoustic cycles

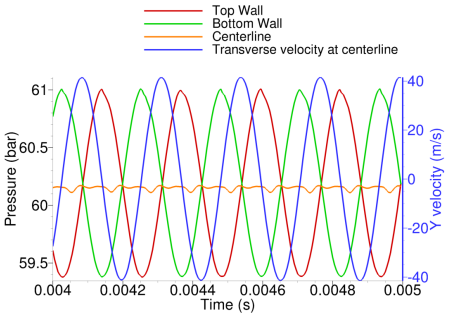

Figure 4.29: Pressure and transverse velocity profiles at various locations over time at steady-state fluctuations.

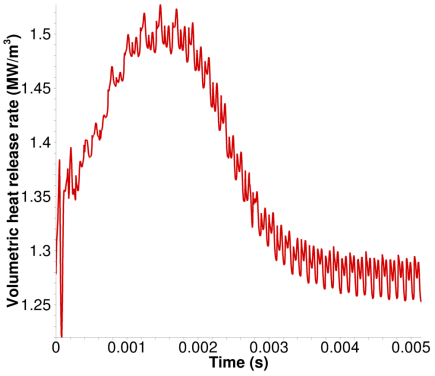

Figure 4.30: Integrated heat release rate for the 1T mode excitation.

4.7 Influence of the numerical setup

In this section, the influence of the numerical setup on the simulation results is investigated, namely the geometry and mesh used for the simulations. The necessity of this study comes from the results shown in Section 4.5. Figure 4.18, 4.24 and 4.25 show some spurious pressure oscillations at the tip of the flame along the axisymmetry axis. This raised the question if the numerical setup, and in particular the axisymmetry boundary condition used for both the 1L and 1T mode excitation could have an important influence on the results. In the next sections, the configurations used for this investigation are presented, highlighting the differences with the previously shown configurations and comparing the results for both the 1L and 1T mode excitation.

4.7.1 Numerical setup: domain and mesh

The boundary conditions for both the 1L and 1T mode excitation were kept the same, except for the axisymmetry boundary conditions which was removed to use 3D configurations for the single injector modelling. Figure 4.31 shows the two geometries used for the 1L and 1T mode excitation investigations for the influence of the boundary conditions on the results.

For the 1L mode investigation, two different 3D mesh setups were used, a fully unstructured and a hybrid mesh. For the 1T mode investigation, the steady-state solution was calculated both with a hybrid and a fully unstructured mesh, whereas the excitation results were calculated only on the full box unstructured mesh. This was done because in particular for the 1T mode excitation, a particular stress was placed only on the influence of the axisymmetry boundary condition used. Figure 4.32 shows the hybrid mesh configurations used for the simulations.

For the pressure excitation simulation, the fully unstructured mesh has 0.8M nodes, whereas the hybrid configuration has 0.7M nodes. Two hexahedral blocks are used in the structured/unstructured mesh, one in the LOx post and one in the flame zone. The two blocks are connected with an unstructured zone with the same mesh density as the 2D configuration. This was done in order to achieve a good resolution of the shear layer and to save computational resources due to the lower number of nodes provided by the hybrid configuration. The hybrid mesh for the velocity excitation consists of 1.0M nodes and the structured blocks configuration is shown in Figure 4.32b. The radius of the blocks is progressively increased since at the end of the flame a high resolution as in the flame zone is not necessary and this helps saving computational time. The resolution in the flame zone is higher, with a length of the structured cell of 0.4 mm near the injection plane which progressively decreases in order to arrive at the same final dimension of the cell provided in the axisymmetric configuration. The other mesh used for the investigation is the fully unstructured mesh, which is identical to the half domain mesh but mirrored about the axsymmetry axis, consisting of 1.2M nodes.

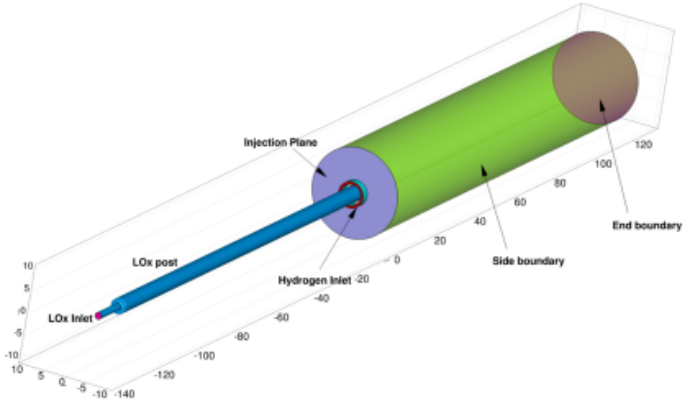

(a) 1L domain

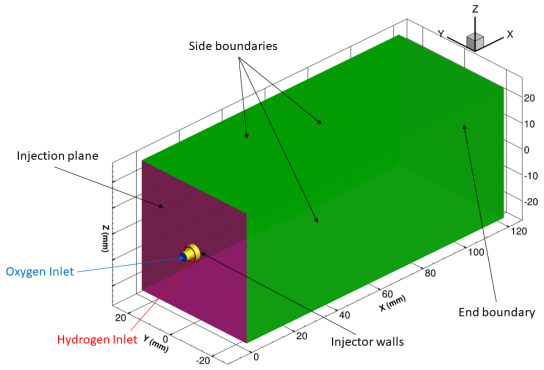

(b) 1T domain

Figure 4.31: 3D domain for 1L mode (a) and 1T mode (b) simulation.

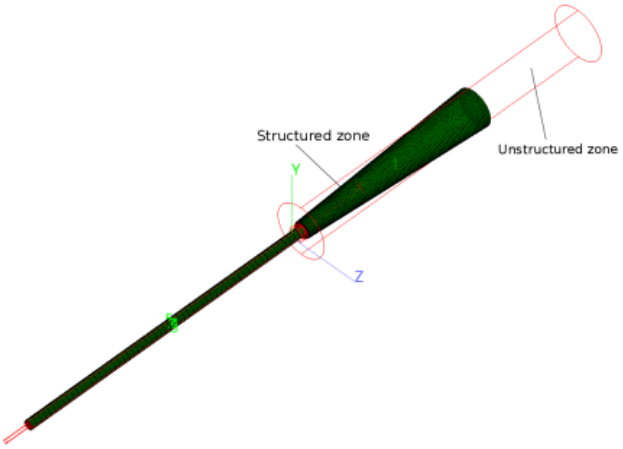

(a) 1L domain

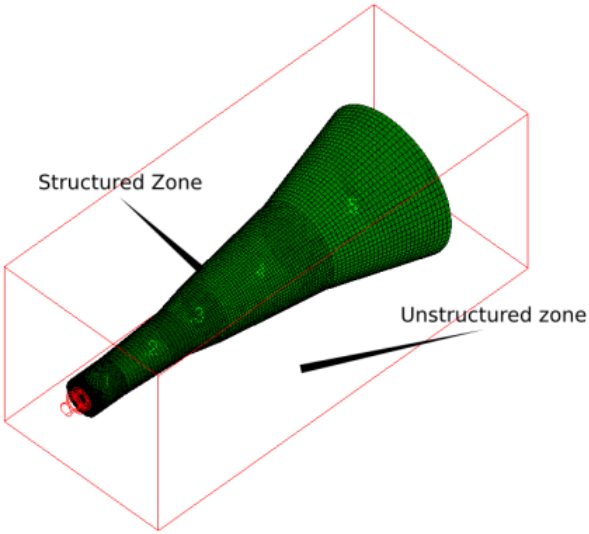

(b) 1T domain

Figure 4.32: Hybrid meshes for 1L mode (a) and 1T mode (b) simulation.

	2D	3D hybrid	3D unstructured
LOx core length at $\rho = 10$ kg/m^3 (mm)	≈64	≈60	≈56
LOx core length at $\rho = 100$ kg/m^3 (mm)	≈62	≈56	≈53
L/D	≈18	≈16	≈15

Table 4.6: LOx core length measured at different densities and L/D ratio for the cylindrical configuration.

4.7.2 Steady state results

The influence of the numerical setup can be seen already when comparing data such as the length of the LOx core between the different configurations. In particular, when comparing the pressure excitation configuration, the difference between the 2D and 3D geometries is evident. Figure 4.33 shows the LOx core length for $\rho = 10$ and 100 kg/m^3. The 2D results are interpolated on a 3D domain to make it comparable with the new 3D geometries. The isosurfaces are shown at the centerplane.
Table 4.6 summarizes the results shown in Figure 4.33. L denotes the jet length, whereas D indicates the diameter of the core measured at the injection plane. The 2D configuration features the longest and thinnest core, as indicated by the L/D ratio. The shortest core is the one obtained with the 3D fully unstructured mesh, whereas the hybrid mesh shows a slightly longer LOx core. This is due to the different geometry of the elements used for the mesh. The hybrid mesh in fact has hexahedral elements in the structured zone and the fully unstructured mesh presents tetrahedral elements in the same zone, which corresponds to the zone containing the flame. The tetrahedral elements are particularly suited for complex geometries, but they have the drawback to introduce distortion in the mesh when the shape function is integrated with Gauss points. This does not happen with hexahedral elements since they feature a central symmetry. Anyway, the global solution accuracy for Euler equations should remain second order because the possible loss in accuracy can occur at the boundaries of the cell and the first order error terms tends to cancel each other when averaged over several elements. In viscous regions, second order derivatives play a significant role and canceling of first order truncation error could not occur. In this case, it will be necessary to maintain central symmetry of the control volumes in boundary layer regions when solving the Navier-Stokes equations [182]. This means that when dealing with strong gradients, as in shear layers and boundary layers, it is better to use hexahedral elements. This is shown in particular in Figure 4.34, where the shear layer between the oxidizer and fuel stream is displayed for the three meshes downstream of the injection plane. Although the number of nodes being less than in the fully unstructured meshes, the resolution of the shear layer is not affected and a smoother transition to the fully developed flame is observed.
Another aspect which has to be mentioned is the spread of the flame in the transverse direction. The flame results to be slightly wider for the 3D geometries, since in this case there is the possibility for the flux to spread laterally. This

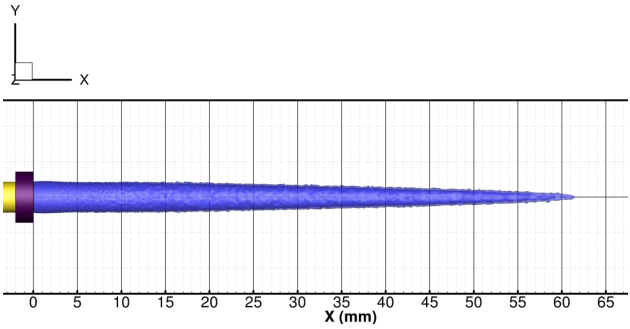

(a) 2D domain

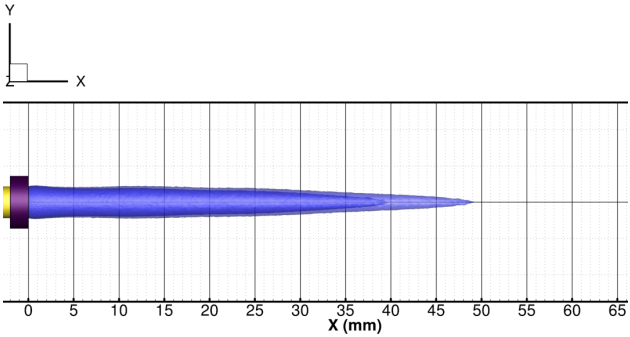

(b) Unstructured 3D domain

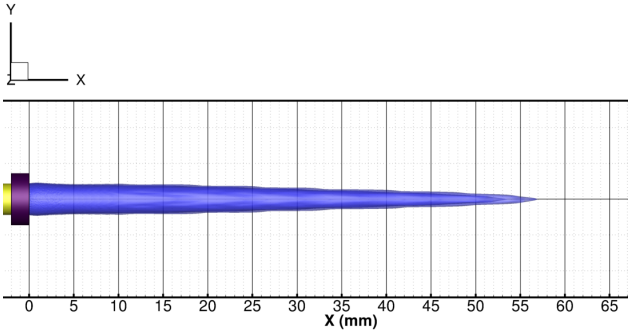

(c) Hybrid 3D domain

Figure 4.33: Density isosurfaces at ρ= 10 and 100 kg/m^3. The 2D solution is interpolated on a 3D domain to make the results immediately comparable.

underlines the fact that also geometric effects, and not only mesh configurations, have an influence on the topology of the solution. This is also true when dealing with turbulence: mixing and diffusion are never purely 2D phenomena, so 3D models take into account diffusion phenomena by the transport terms of turbulence equations.

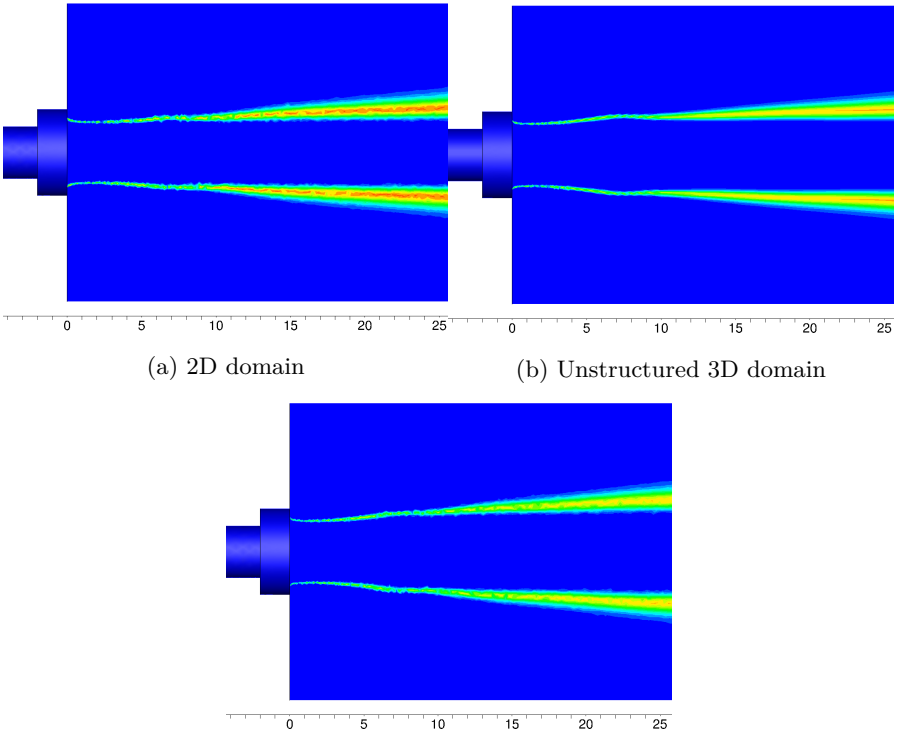

(a) 2D domain

(b) Unstructured 3D domain

(c) Hybrid 3D domain

Figure 4.34: Shear layer close up for the three meshes downstream of the injection plane. OH mass fraction is used to identify the shear layer zone.

The same considerations can be done when comparing the transverse velocity excitation configurations. Figure 4.35 shows the comparison between the density isosurfaces of the half domain, the fully unstructured mirrored domain and the full domain with the hybrid mesh and Table 4.7 summarizes the main features of the three jets. The hybrid mesh configuration shows a slightly longer LOx core, as a consequence of the same considerations done for the cylindrical geometry. No substantial difference is observed between the half domain and full 3D

unstructured domain for the steady-state solution in terms of LOx core length. In the next section, the results of the unsteady simulation both for the 1L and 1T simulation will be presented, together with a comparison of the most relevant quantities to underline the importance of the geometrical difference in terms of study of the acoustic response of the flame.

	Half domain	**3D hybrid**	**3D unstructured**
LOx core length at $\rho = 10$ kg/m^3 (mm)	≈65	≈70	≈65
LOx core length at $\rho = 100$ kg/m^3 (mm)	≈63	≈68	≈63
L/D	≈18.5	≈20	≈18.5

Table 4.7: LOx core length measured at different densities and L/D ratio for the box configuration.

4.7.3 Excitation results

In this section, the comparison of the results of the different configurations when applying the 1L and 1T excitation profiles is shown. For the 1L excitations, two different frequencies are considered, 3200 Hz and 3400 Hz. For the 3200 Hz frequencies, the calculations have been performed for the 2D configuration, the hybrid and the unstructured mesh, while for the 3400 Hz only the 2D and 3D fully unstructured configurations are shown. For the 1T configuration, the excitation frequency is 4400 Hz. Both excitation profiles feature an amplitude of the pressure oscillations of 1.8% of the mean pressure of the chamber.
In Section 4.5 the evolution of the pressure signal in time and the pressure field were described, showing spurious pressure oscillations along the axisymmetric axis. Here, a comparison of the pressure signal evolution in time along the axis at the tip of the flame is made, comparing the signals of the three configurations at 3200 Hz for the 2D geometry, the 3D hybrid mesh and the fully unstructured grid. The time step used for the unsteady simulation of the 3D cases is the same as the one used in the 2D simulations. The goal of the comparison is to understand the origin of the spurious pressure oscillations and understand why they are present in the 2D and axisymmetric simulations, whereas they do not appear when using a 3D geometry.

4.7.3.1 1L mode excitation

In this section, an excitation profile is imposed on the steady state solution of the full 3D configurations and compared with the results of the 2D simulations presented in Section 4.5. Figure 4.36 shows the signal measured at the tip of the flame, which corresponds to x=50 mm, on the location of the symmetry axis for the 2D configuration, y = 0 and z = 0 mm for the 3D geometries. The amplitude of the signal is reproduced for the three configurations and does not vary with respect to the imposed amplitude. However, the spurious pressure oscillations which are present in the 2D configuration are not present in the 3D cases, both with hybrid and unstructured mesh.

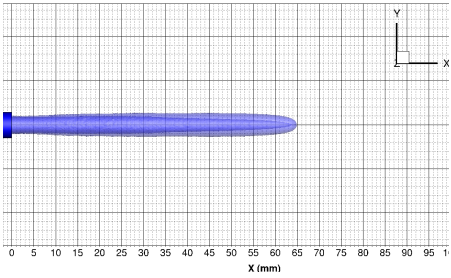

(a) Half box

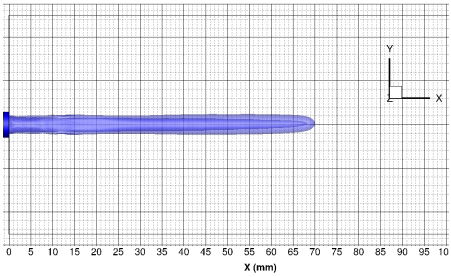

(b) Full box hybrid mesh

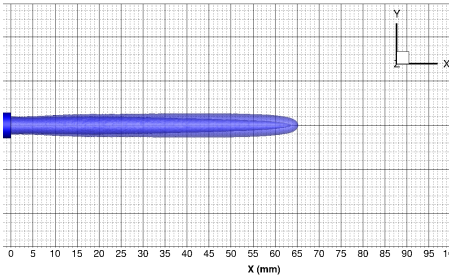

(c) Full Box unstructured mesh

Figure 4.35: Density isosurfaces at ρ= 10 and 100 kg/m^3 for the box configuration.

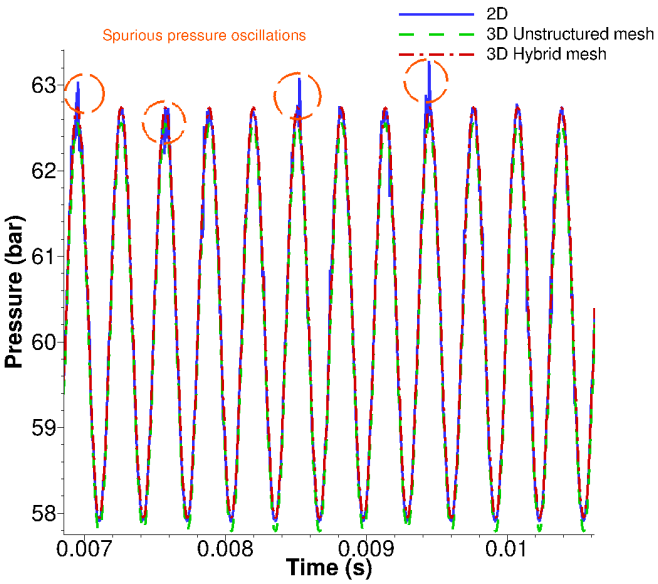

Figure 4.36: Pressure signal at steady-state fluctuations for the three configurations at the tip of the flame, x=50 mm (Amplitude 3 bar, frequency 3200 Hz).

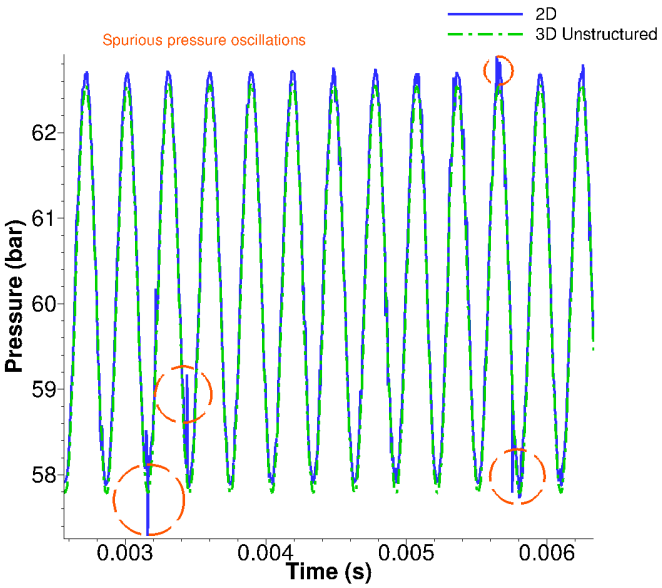

Figure 4.37: Pressure signal at steady-state fluctuations for the 2D and 3D unstructured configuration at the tip of the flame, x=50 mm (Amplitude 3 bar, frequency 3400 Hz).

Figure 4.37 shows the comparison of the pressure signal over time for an amplitude of the oscillations of 3 bar at a frequency of 3400 Hz for the 2D and the 3D unstructured configuration at the same location of the signal plotted in Figure 4.36. Also here, it can be seen that spurious pressure oscillations are present on the symmetry axis for the 2D simulation. This gives an indication of the fact that the axisymmetry boundary condition is the main cause of the spurious numerical pressure oscillations observed on the axis at the tip of the flame.

The BKH flame presents a typical behavior when subject to the 1L mode excitation with the occurrence of wave-like structures on the flame surface. Figure 4.38 shows the density field after 10 ms, when steady-state fluctuations are reached, corresponding to 16 acoustic cycles at 3200 Hz. The black lines delimiting the different regions are isolines used to compare the regions with different density. The 2D configuration features the longest LOx core with a penetration inside the chamber of $\approx$ 65 mm. The 3D geometries present a shorter LOx core, where the hybrid configuration measures about 62 mm and the unstructured configuration about 58 mm. The hybrid mesh captures the phenomenon of the formation of the ripples, although the shear layer is smoother than in the 2D geometry due to the numerical damping given by the hexahedral block. The unstructured mesh

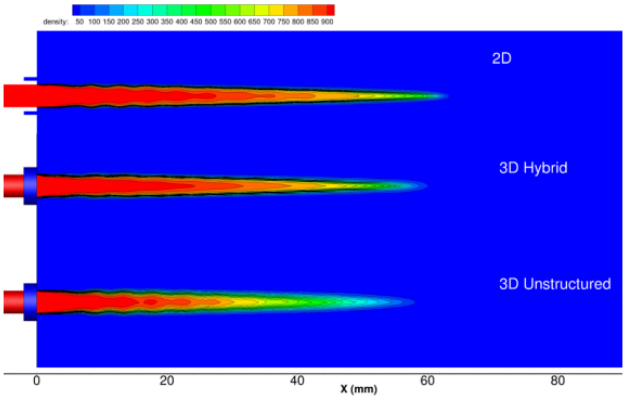

Figure 4.38: Comparison of the density field after 16 acoustic cycles for the three configurations.

	2D	3D hybrid	3D unstructured
Difference of mean value [1]	+17.4%	+3.4%	+3.5%
Relative at steady state fluctuations (peak-to-peak)	reference	+6%	+6%

[1] Compared to initial steady state solution.

Table 4.8: Heat relase rate fluctuations at p'=3 bar f=3200 Hz.

features a considerably shorter LOx core, presenting the detachment of pockets of oxygen inside the core itself, clearly visible at x = 18 mm.

Heat release rate is a key variable in the study of high frequency combustion instabilities and thus the correct prediction of this value in CFD simulation has a fundamental importance, considering also that heat release rate is not experimentally measurable. In this work, the comparison of the volumetric heat release rate from the different configurations is made in order to assess how the setup of the simulations can influence the values of this key variable.
Figure 4.39 shows the steady-state fluctuations of the integrated heat release rate for 3 bar amplitude at the frequency of 3200 Hz and the results are summarized in Table 4.8.

At steady-state fluctuations, both the 3D solutions shows an amplitude of the heat release rate fluctuations considerably higher than in the 2D case. This can be explained again by the use of the axisymmetric boundary condition. The axisymmetric boundary condition in TAU is implemented as a first order boundary condition, whereas the solver implements a second order spatial reconstruction. A first order upwind scheme uses one upstream point for the

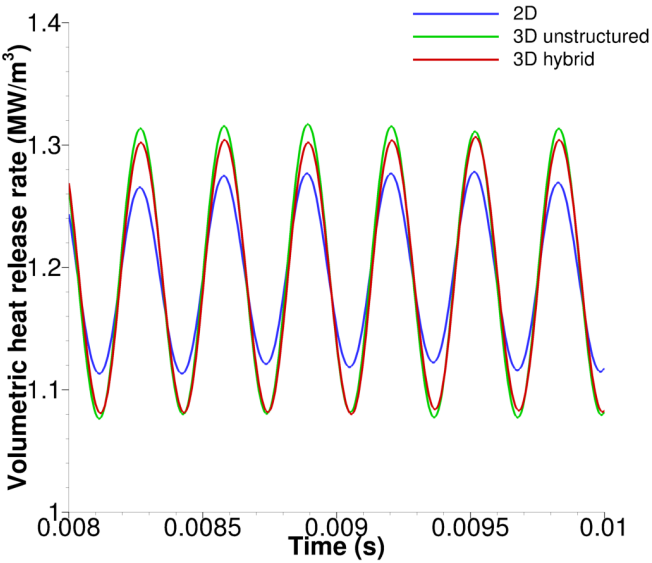

Figure 4.39: Comparison of the volumetric heat release rate for three different configurations at steady-state fluctuations.

computations, assuming the face values being identical to the cell values. A second order upwind scheme uses two upstream points and Taylor series are used to evaluate the values at the cell interface from the solution obtained at cell centroid, resulting in higher accuracy, as shown by Tonti et al. [217]. This difference is relevant when calculating values which have to be integrated over a volume, and can lead to an underestimation of the integrated heat release rate.
The same behavior can be seen also for higher frequencies as for f=3400 Hz, where the difference between steady-state fluctuations of the 2D configuration and both 3D configurations still presents a difference of 6%. This is an indication that there is a systematic discrepancy,due to the use of the axisymmetric boundary condition.

4.7.3.2 1T mode excitation

The same approach used in Section 4.7.3.1 is employed to study the influence of the geometry and boundary conditions for the transverse excitation.
When subject to transverse velocity excitation, the flame features a typical behavior: it flattens, spreading laterally, and retracts towards the injection plane. In this case, only the comparison between the half box and the full box both with fully unstructured mesh was made, in order to focus on the effect that the axisymmetric boundary condition has and isolating it from mesh effects.
Figure 4.40 shows the comparison of the density isosurfaces for the half and the full domain. The shape and the length are comparable at ρ=10 kg/m^3, while the full domain configuration shows a shorter core at ρ=100 kg/m^3. In the full domain configuration the core looks slightly wider, and the shape of the density isosurface at ρ=100 kg/m^3 is rounder than in the half domain. The effect of the axisymmetric boundary condition can be seen in this difference of shape in the inner part of the core, which is smoother.

The most important difference between the configurations can be seen in the integrated variables, as shown in Figure 4.41 and 4.42.

Looking at Figure 4.41, the behavior of the two curves is similar in the first 1 ms. After that, the two curves starts to shows different slopes, where the full domain results to reach the peak concentration shortly before the half domain, although the peak value is the same, corresponding to 5.25x10^{-5}. Then, the curves assume here a different behavior: the one representing the full domain tends to stabilize shortly after towards a value of 4.83x10^{-5}, whereas the half domain tends to the value of 4.74x10^{-5}, showing still a decrease towards slightly lower values and with a linear decrease. The full domain shows instead a parabolic decrease. This underlines once again the difference which exists between the axisymmetric boundary condition and the full domain.
Another important aspect which was already discussed for the cylindrical configuration in Section 4.7.3.1 is the difference in the volumetric heat release rate. Figure 4.42 shows the two signals over time for the full and the half domain during the entire simulation (a) and at steady-state fluctuations reached (b). Also here, the difference in the values is considerable. Table 4.9 summarizes the values shown in Figure 4.42.

The volumetric heat release rate fluctuations results to be higher in the full domain

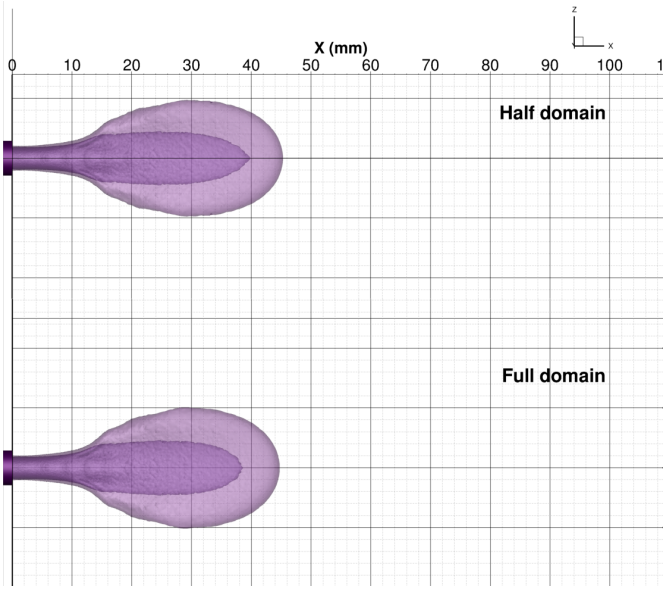

Figure 4.40: Comparison of density isosurfaces at ρ=100 and 10 kg/m^3 after ten acoustic cycles.

	Half domain	**Full domain**
Difference of mean value [1]	+1%	+6.2%
Relative at steady state fluctuations (peak-to-peak)	reference	+3%

[1] Compared to initial steady state solution.

Table 4.9: Heat release rate fluctuations for the half and full domain during 1T mode excitation.

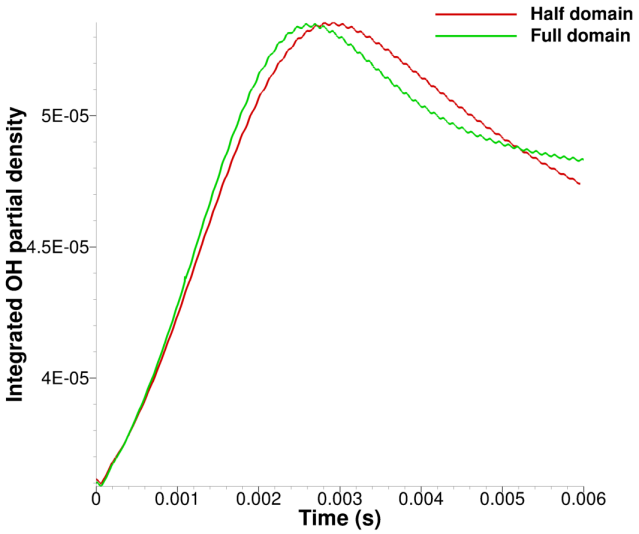

Figure 4.41: OH partial density integrated over the domain for the half and the full domain.

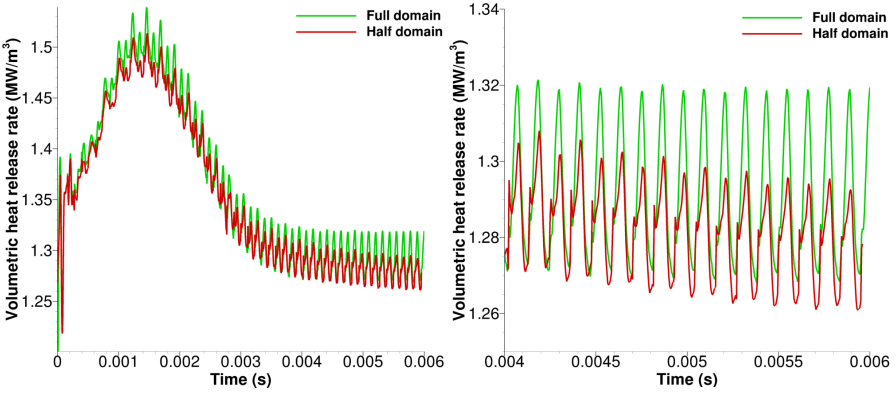

(a) Entire signal (b) Steady state fluctuations

Figure 4.42: Volumetric heat release rate for the half and the full domain.

both in terms of mean value and at steady-state fluctuations reached. At steady state, the shape of the signal is essentially the same, whereas at the time where the maximum heat is released, the full domain captures more peaks than the half box. Here, is fundamental to mention that for the full domain all the boundary conditions are kept the same, except for the elimination of the axisymmetric boundary condition. This was removed by simply mirroring the geometry and taking the same mesh of the half domain. This means that the different values obtained for the two simulations are to be charged to the use of the axisymmetric boundary condition.

4.8 Summary

This chapter presented single injector simulations representative of the central injector of the BKH combustor in order to investigate different phenomena taking place when different excitation conditions are applied. Starting from a simple and relatively inexpensive 2D axisymmetric computation, the acoustic response of the BKH element subject to pressure excitation was studied, building a matrix of excitation conditions ranging from off-resonance to resonant conditions for the LOx post and the chamber. Here, together with a pressure excitation, also an axial velocity forcing is considered in order to build more realistic acoustic excitation conditions. With increasing frequency and amplitude of the applied excitation, the wave-like structures of the shear layer become more pronounced and the wavelength shorter. With increasing amplitude of the oscillations, the LOx core tends to stretch.
Beinke [15] conducted the same analysis for the 1T mode excitation, which corresponds to a velocity excitation, using an axisymmetric domain although three dimensional to capture the spanwise spreading of the LOx core, which is characteristic for this kind of excitation system. Here, the calculations are shortly presented for an amplitude of the disturbance corresponding to 1.25% of the mean pressure chamber with a new version of TAU, as an introduction for the next section.
In fact, some spurious pressure oscillations along the symmetry axis and plane for 2D and 3D simulations, respectively, are observed the tip of the flame, and the cause of this spurious oscillations had to be investigated. This led to a change of the setup of the simulations, in particular removing the axisymmetric boundary condition. In the 1L mode excitation case, the use of a hybrid mesh and a revolution of the domain of 360° around the x-axis led to the suppression of these spurious oscillations, identifying the cause in the symmetry boundary conditions. Moreover, a quantitative difference in the volumetric heat release rate was shown: the axisymmetric boundary condition leads to an underprediction of the peak and mean values. This is particularly important when investigating high frequency combustion instabilities, where the heat release rate is a key quantity as underlined by the Rayleigh criterion.
The same behavior was observed when studying the 1T mode excitation, here only considering the mirroring of the domain, without changing the mesh but only

doubling it. Also here, the integrated quantities such as OH partial density and heat release rate showed a quite different behavior, leading to the conclusion that the axisymmetric boundary condition should be avoided not only in TAU, but more in general when the implemented boundary conditions in the code have numerical schemes with different numerical orders with respect to the numerical scheme used to solve the field, in order not to have an underestimation of the key values when studying instabilities in a rocket combustor.

5 BKH Cold Flow Modelling

The experiment presented in this chapter aims to investigate how the external excitation system of BKH can be effectively modelled. Chapter 4 investigated the behavior of the flame in a single injector configuration when subject to an imposed pressure and velocity profile, defined mathematically and substituting precise values at each time step of the simulation. Here, the purpose is to model the secondary nozzle excitation system in order to get closer to a realistic excitation profile which takes into account not only the pressure disturbance but also the geometric details of the toothed wheel. In this case, it is worth to spend some words about the different acoustic excitation systems which produce the acoustic disturbance which in turn propagates inside the combustion chamber.
Experimental combustors which use an external acoustic excitation system are typically stable, and the external excitation system is used to study the effects of the disturbance at different operating conditions for the combustion processes. In cold flow tests, combustion is not present and the acoustic excitation can be produced with electronic actuators. Cheroudi et al. [30, 31] studied nitrogen jets at sub- and supercritical pressure conditions under acoustic excitation using a piezo-siren acoustic excitation system. Anyway, the disturbance produced by a system consisting of a nozzle and a siren wheel has not been studied in detail yet. The purpose of this kind of systems is to produce a smooth sinusoidal signal, but this is in contrast to what is observed in the experiments. Limited experimental data have been collected to describe the flow field near a nozzle and siren wheel system and further analysis of experimental data requires understanding of the acoustic disturbance perturbing the study element. Furthermore, the disturbance applied to simulated flames should be representative of that in the experiment in order to recover a realistic flame response. Therefore, determining the actual amplitude and profile of the disturbance is quite critical.
Here, a new boundary condition representing the siren which interrupts the flow through the secondary nozzle is employed on a cold flow test case from BKH. The experimental data will be shortly presented in the next section, followed by the numerical setup of the simulation. Then, the numerical results will be shown, together with a comparison with previous numerical simulations which used a different approach and with experimental data.

5.1 Experimental data and numerical setup

Figure 5.1 shows the spectrogram of a cold flow check of BKH, where the dynamic pressure signal is recorded by a sensor placed at the bottom wall of the combustion chamber at the opposite location with respect to the secondary nozzle. The horizontal bands in the spectrogram indicate the resonant modes of the

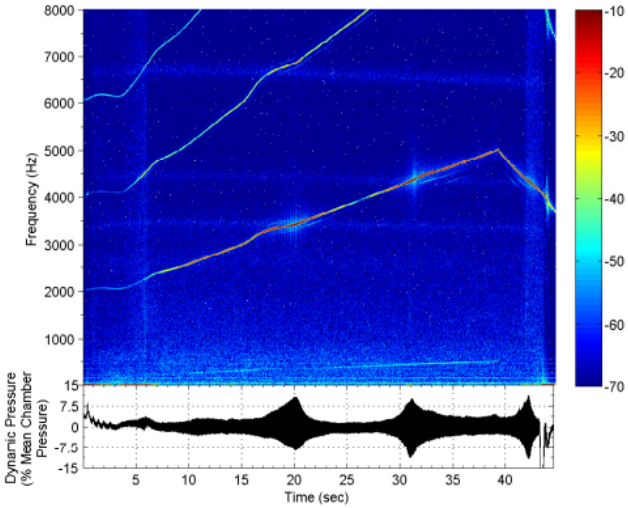

Figure 5.1: Spectrogram of dynamic pressure data from BKH cold flow test and dynamic pressure data.

chamber, which are weakly excited during the test. The 1T mode excitation frequency is about 3400 Hz.

The amplitude of the acoustic disturbance increases when its frequencies match the resonant modes of the chamber. At 20 sec, the 1T mode of the chamber is excited. Overtones are also visible, indicating that the profile of the excitation is not perfectly sinusoidal and produces disturbances at certain frequencies. This is shown in Figure 5.2, which represent the dynamic pressure signal recorded at the secondary nozzle sensor position.

From the recorded data, it can be seen that the signal is highly non-linear. The profile is steep and it also does not oscillate symmetrically around zero. The high pressure part of the cycle looks smoother than the lower part, which presents a secondary peak. This secondary peak indicates the first overtone of the excitation frequency.

The experimental data provided are the basis for the setup of the numerical simulation. The goal of the analysis was to implement and validate the siren boundary condition, which is an extension of the exit pressure outflow boundary condition already implemented in TAU. In order to investigate the results produced with the application of the new boundary condition, a simplified, BKH-like geometry was used, with a configuration which features a single dummy injector but with equivalent mass flow of gaseous hydrogen as in the experimental setup. A symmetry boundary condition could be used here, since combustion is

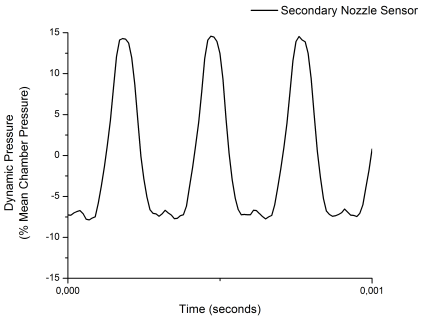

Figure 5.2: Dynamic pressure oscillations at secondary nozzle location from experimental data during 1T mode excitation.

not present and no effects on the calculation of heat release rate, relevant when combustion phenomena take place, have to be taken into account. Moreover, this allows to exploit the vertical symmetry of BKH reducing the computational costs. The mesh is fully unstructured, with 93 K nodes. Both the main and the secondary nozzle are cut at the throat since the flow is choked. Figure 5.3 shows the geometry and mesh used to perform the calculations, Table 5.1 summarizes the operating conditions.

Property	**Value**	**Unit**
Hydrogen Temperature	295	K
Chamber pressure	30	bar
Hydrogen mass flow rate	1.3	kg/s

Table 5.1: Operating conditions for the cold flow load point.

First, a steady state solution was calculated, with both exit pressures at the nozzles outlet set to ambient conditions. Then, once a steady flow field was reached, the siren excitation was applied.
The siren boundary condition specifies the geometrical details of the toothed wheel, namely length of the teeth and gaps, and the velocity of the siren, which in this case is set to be in the x direction. These two physical quantities specify the frequency of the excitation as f[Hz]=u [m/s]/($gap + block$)[m]. The length of the siren gap and block are set to be the same, corresponding to be 0.01 m and the velocity is set to 72.3 m/s to match the experimental frequency of the 1T mode. The signal is set as sinusoidal, but the specification of the geometric details of the siren (gap and block length of the teeth) and the specification of velocity of the toothed wheel allow to reproduce the passage of the toothed wheel on the nozzle outlet. This represents a step forward with respect to the previous approach

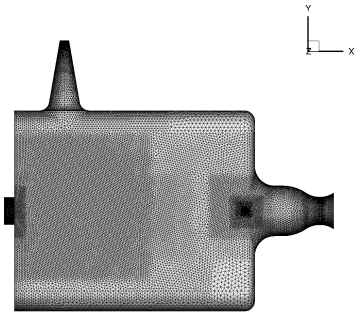

Figure 5.3: Simplified BKH geometry used for preliminary testing of the siren boundary condition.

followed by Beinke [13, 14], where two different excitation profiles were used. One represented a open-closed condition, the other one was a purely sinusoidal signal which did not take into account the geometrical specification of the teeth of the siren nor the velocity of the wheel itself.
Initially, a time step of $5.0\text{x}10^{-6}$ s for the transient simulation was set, leading to an under-resolved signal which did not capture the pressure oscillations with satisfactory accuracy. The time step size has been then changed to $5.0\text{x}10^{-7}$ s.
In the next section, numerical results are presented and compared both with experimental data and previous numerical results.

5.2 Numerical results

The previous numerical results used for comparison is the open-closed boundary condition from Beinke [13, 14]. The motivation for this choice is the better agreement with the experimental data with respect to the sinusoidal boundary condition. The limit cycle was reached in this case after 3 ms. The numerical setup used in this work led to a longer physical time until the limit cycle was reached, 7 ms. Figure 5.4 shows the pressure signals extracted at the top and bottom wall sensors for the whole calculation (a) and when steady state fluctuations are reached (b).
The typical 1T mode behavior is retrieved by the simulation. The top and bottom wall pressure signals are out of phase. The signal taken at the top wall sensor shows slightly lower amplitudes with respect to the bottom wall pressure signal, with a peak-to-peak value of the oscillations of 10% of the mean chamber pressure, whereas the bottom wall sensor registers a peak-to-peak amplitude of 12.5%.
Figure 5.5 shows the comparison of the dynamic pressure recorded at the top and bottom wall sensors for the experimental data, the previous open-closed boundary condition and the new boundary condition at steady state fluctuations. The signal

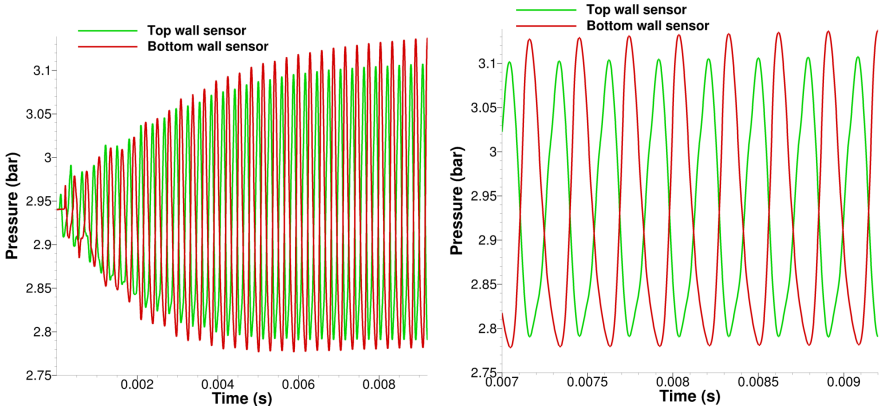

(a) Whole signal

(b) Steady state fluctuations

Figure 5.4: Pressure signal at the top and bottom wall sensors during 1T mode excitation.

extracted from experimental data is dynamic pressure, expressed in percentage of the mean chamber pressure. For the comparison with numerical results, this physical variable has been chosen.

It can be seen that the new boundary condition recovers the signal shape and amplitude better than the open/closed boundary condition previously employed by Beinke [13]. In particular, the largest error can be observed in the upper part of the dynamic pressure oscillations for the bottom wall sensors, where the discrepancy of the experimental and numerical data reaches the 24% for the PCCDYN2, placed at x=7.0 mm and y=-100.0 mm. For the top wall sensors, the largest discrepancy is observed for PCCDYN5 at x=230.0 mm and y=100 mm, where the maximum value is 44% higher than in the experiment. These discrepancies can be explained by the simplified configuration employed for the simulation. The setup used does not include all the injection elements, and all the hydrogen is injected though a single dummy injector with an equivalent mass flow. These can lead to a different distribution of the hydrogen through the chamber, leading to different values in particular in the zones which are far from the injection plane, which are the zones where the sensors which register a higher discrepancy are placed. The general trend however, shows a better agreement of the the data produced by the new boundary condition in terms of shape and amplitude for the sensors which are closer to the injection plane.

The same comparison can be made with data from the secondary nozzle sensor. Figure 5.6 shows the comparison of the dynamic pressure recorded at the secondary nozzle sensor for the experimental data, the open/closed boundary condition and the new boundary condition.

Also here, the new boundary condition shows a discrepancy in the amplitude of

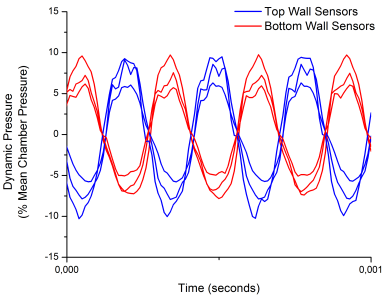

(a) Experimental data

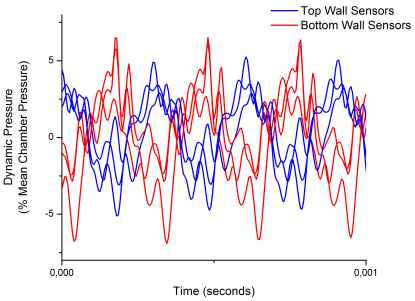

(b) Open/closed boundary condition

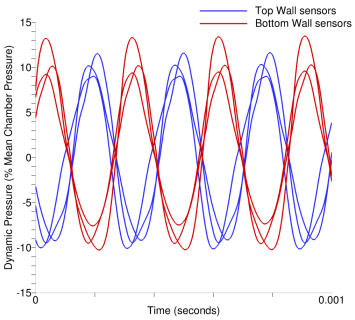

(c) New boundary condition

Figure 5.5: Comparison of dynamic pressure signals at top and bottom wall sensors.

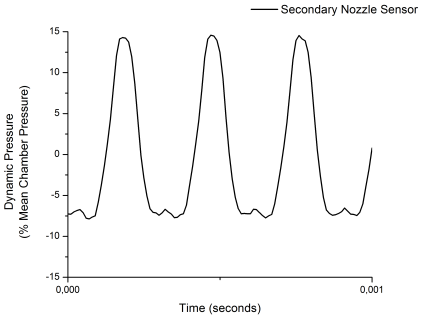

(a) Experimental data

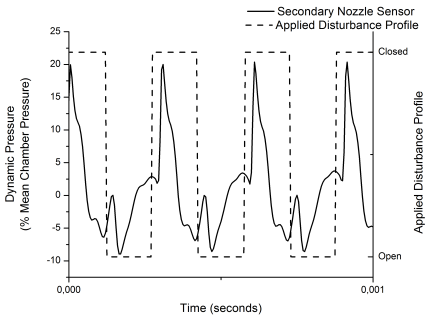

(b) Open/closed boundary condition

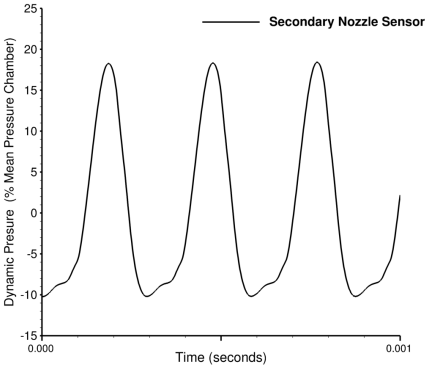

(c) New boundary condition

Figure 5.6: Comparison of dynamic pressure signals at secondary nozzle sensor.

the signal which results to be 20% higher than in the experiment. However, the shape is well recovered, showing also a small peak comparable to the one shown in the experimental data at the bottom part of cycle. The open/closed boundary condition, on the other hand, shows a discrepancy both in the amplitude, with an overprediction of about 30%, and in the shape of the signal. The open/closed boundary condition shows sharp peaks both at the top and bottom of the cycle, with a steep profile of the disturbance. Also the small peak shown in the experimental data is not well recovered from the open/closed boundary condition, which shows a sharper and higher peak which is not present in the new boundary condition simulation. The distribution of the dynamic pressure field at the maximum and minimum phase of the acoustic cycle is shown in Figure 5.7. The typical 1T mode pressure distribution is shown in the figure, with the nodal line along the axial coordinate if the domain. The maximum and minimum pressure alternates at the top and bottom of the chamber, showing a structure which matches well the experimental data. The discrepancy in the amplitude of the signal can be due to the fact that in the numerical simulation, no space between the siren and the nozzle exit is considered, whereas the experimental setup features a gap which ranges from 0.05 and 0.1 mm depending on the test case considered. This means that there is not a part of the flow which exits the secondary nozzle and no pressure losses are taken into account, resulting then in higher pressure recorded from the sensor.

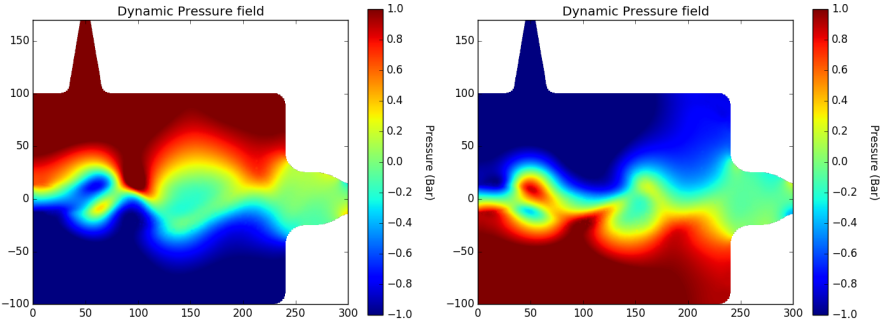

(a) 90° (b) 270°

Figure 5.7: Normalized dynamic pressure distribution at different phases of the cycle.

Figure 5.8 and 5.9 show the Fast Fourier Transform of a sample of 2 ms of the dynamic pressure signal for the bottom wall sensor and the secondary nozzle sensor.
It can be seen that the frequency of the signal is well recovered both by the open/closed boundary condition and the new boundary condition. The excitation profile is also well recovered, especially in terms of relative amplitude of the peaks. In particular, Figure 5.9 shows that the new boundary condition recovers the

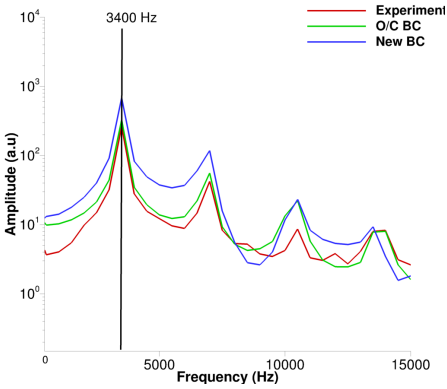

Figure 5.8: FFT of the dynamic pressure signal of the bottom wall sensor.

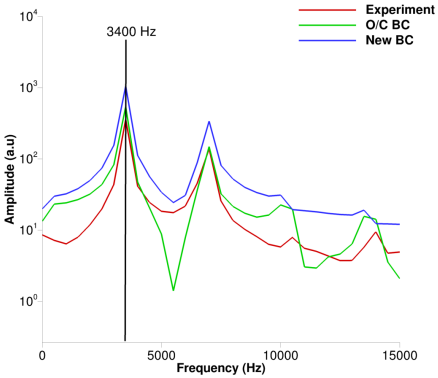

Figure 5.9: FFT of the dynamic pressure signal of the secondary nozzle sensor.

shape of the signal better than the open/closed boundary condition, despite the amplitude of the signal results higher. At frequencies about 7 kHz, the relative amplitude of the peaks is exactly matched by the new boundary condition, with overtones which are also correctly captured. A noticeable difference can be seen on the other hand on the open/closed boundary condition, where the shape of signal significantly deviates from the reference experimental data, resulting also here in a higher amplitude of the signal and in a different shape at higher frequencies.
As already stated by Beinke [13], the second peak in the pressure signal recorded at the secondary nozzle sensor location corresponds to the peak the pressure signal of Figure 5.7 (a). When the pressure applied at the secondary nozzle exit plane is low compared to the chamber pressure and when the transition from subsonic to sonic flow takes place, this behavior is expected. The new boundary condition reproduces this phenomenon and gives better quantitative and qualitative results with respect to the open/closed boundary condition.
In this case, the pressure for the cold flow experiment is about 30 bar with a critical pressure of gaseous hydrogen which corresponds to approximately 15.8 bar. The pressure at the exit of the secondary nozzle is atmospheric. When part of secondary nozzle is not closed by the passage of the teeth of the siren, the flow experiences the transition to sonic. When the flow is instead interrupted by the teeth, the pressure rises again and the flow becomes subsonic. The pressure rise at the secondary nozzle sensor location is reasonably explained by the transition of the flow from subsonic to sonic. The new boundary condition features a smoother profile of the excitation because the incomplete closure of the secondary nozzle exit is taken into account. The discrepancies in the amplitude of the signal and the FFT are reasonably due to the differences in the setup of the simulation, such as the use of a single dummy injector and the contact between the toothed wheel and the exit of the secondary nozzle outlet, where the distance between the siren and the outlet boundary is not taken into account.

5.3 Summary

To accurately reproduce the excitation system of the BKH combustor, a new boundary condition which simulates the passage of the toothed wheel on the secondary nozzle exit area was implemented in TAU code. For validation purposes, the simulation has been run for a cold flow check of BKH where only gaseous hydrogen was injected with a chamber pressure of 30 bar. The domain used for the simulation is symmetric with respect to centerplane and a dummy injector with an equivalent mass flow was employed to simplify the domain.
The excitation system provided by the toothed wheel intended to produce a sinusoidal disturbance, but the experimental data showed that the produced excitation profile does not produce a smooth signal and excited also overtones, producing a steep profile. A secondary pressure rise also occurs, due to the transition of the flow from subsonic to sonic conditions in the nozzle throat for part of the excitation period. Even if the pressure disturbance produced is not perfectly sinusoidal, the wall mounted sensors record a pressure signal which is

comparable to a well established 1T mode distribution.
Here, a comparison with experimental and a previously implemented boundary condition was made. The boundary condition which in the past was in better agreement with the experimental data was an open/closed boundary condition, where the secondary nozzle was alternatively opened and closed to simulate the passage of the siren. The new boundary condition applies a sinusoidal profile where also the geometrical details of the siren are taken into account. The results show a better agreement of the new boundary condition with respect to the open/closed one with experimental data. In particular, the secondary pressure rise in the signal captured by the sensor placed at the secondary nozzle location is well reproduced, showing a comparable oscillation in terms of amplitude and shape. The excitation frequency is also correctly captured, showing a relative amplitude of the peaks which is comparable with the one shown in the experiments. Also the overtones at higher frequencies results to be captured by the new boundary condition, whereas the open/closed one did not manage to recover the profile with the same precision at higher frequencies.

6 OH* Radiation Modelling and Ray-tracing

The comparison between experimental data and numerical simulations has always been challenging when dealing with rocket combustion chambers, due to the unfriendly environment developing inside the engines. Extremely high temperatures and pressures are involved, and collecting experimental data is extremely challenging. Numerical simulations are a tool which can be used to get more insights in the physical processes occurring inside the combustion chamber, but these results have to be validated against experiments.
A physical quantity which is relatively easy to compare is the OH* radiation produced during the combustion processes. In the experiments, the intensity of OH* radiation can be recorded by high-speed cameras or optical probes. Developing a numerical tool which enhances the comparison of OH* radiation between experiments and numerical results becomes then crucial. In order to do that, a proper OH* radiation model has to be used, depending on the propellants combination and the operating conditions of the engines.
The first part of this chapter gives an overview of the OH* radiation for high pressure LOX/H_2 flames and the challenges which the experimental and numerical work presents, describing the spectrum and discussing the relevant physical phenomena which can have an influence on the radiation itself. Then, the Spectral Model (SM) approach is discussed and the choice of this modelling strategy is justified. The next step is the description of the ray-tracing algorithm developed to capture the intensity of the OH* radiation originating from the flame and the application of the model to a representative BKH test case.

6.1 OH* radiation spectrum

In LOx/H_2 flames, OH* radiation is the most distinct spectral peak in the UV range. The central wavelength is 310 nm, and it is deeply in the UV, so that the background radiation has no influence on the measurement. Moreover, OH is a species which is present in all the combustion reactions of fuels containing hydrogen, with well known physical properties. An extensive review on OH* radiation in flames is provided by Gaydon [65] and Mavrodineau [138]. OH* not only has a rotational-vibrational spectrum in the infrared, but also a UV part, which is dominant and has a band-head of 306.4 nm. It originates from the transition from the first electronically excited state and the ground state, denoted with $A^2\Sigma^+$ and $X^2\Pi_i$, respectively. When considering the light as a stream of photons, it can be stated that the transition between the excited state and the ground state releases an amount of energy corresponding to the difference of

energy between the two states ΔE_{j-i}, which in turn corresponds to the energy released by the photon $E_{photon} = h\nu = (hc)/\lambda$. where h is the Planck's constant, ν the frequency, c the speed of light and λ the wavelength. In gaseous flames, only single molecules typically interact with the radiation. The probability of the transition to occur is represented by the Einstein coefficient $A_{i\to j}$ [144]. The pure emission spectrum (which does not include self-absorption) is then given by the Einstein coefficient and the number distribution of OH* molecules. When thermal equilibrium is reached, the number density[1] of the molecular states is defined by the equilibrium temperature. Figure 6.1 shows an example of OH* emission spectrum.

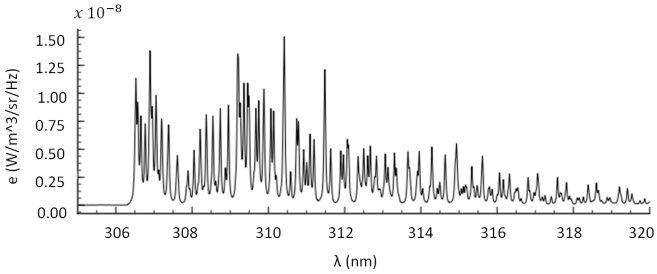

Figure 6.1: OH* emission spectrum at p=62 bar and T=3000 K [107]

On the other hand, there is the inverse phenomenon, which is the absorption of the photon by the ground state OH, which increases the energy content of the molecule. As for the emission, also this phenomenon can take place only if the probability of the inverse transition is sufficiently high, and so also an absorption spectrum is provided. It is important to remark that absorption and emission occur at the same wavelength, reducing the actual amount of emitted radiance when OH is present in high concentrations. This last observation states then that the overall spectrum of the flames is normally not only a function of the emission, but also of the absorption. The radiation emitted from excited molecules is subject to the absorption by the same molecules which are present in the ground state. This process is known as self-absorption. Self-absorption may be defined as the attenuation of radiation by the sample emitting the radiation. This absorbed radiation does not reach the detector and, if appreciable, counting efficiencies can be markedly reduced. Taking self-absorption into account is fundamental to model correctly the radiation of flames where OH is present as a combustion product in high concentrations. Generally, for radiation coming from radicals at low concentrations such as CH or C_2, self-absorption can be neglected. This is not valid for molecules with high concentrations in flames, such as the infrared radiation from H_2O and CO_2. Previous studies underlined that self-absorption affects the flame radiation considerably with increasing pressure [56, 243, 244].

[1]The number density (symbol: n or ρN) is an intensive quantity used to describe the degree of concentration of countable objects (particles, molecules etc.) in physical space

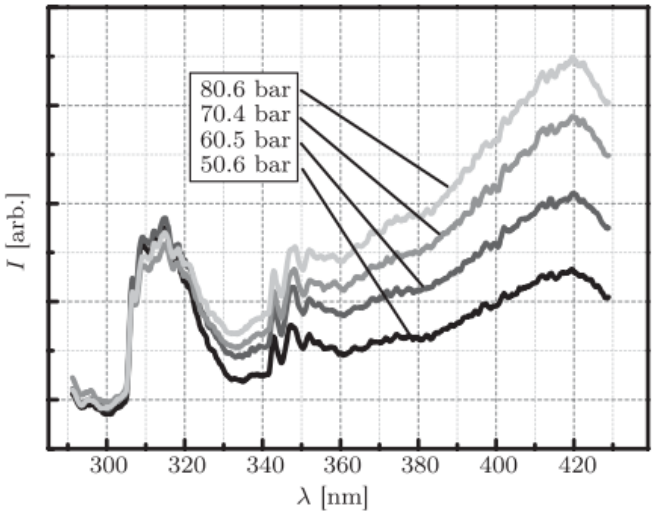

Figure 6.2: Flame emission spectra of BKD for different pressure levels. The impact of self-absorption becomes more important with increasing pressure [58].

Figure 6.2 shows the impact of self-absorption at increasing pressure levels in BKD. When the chamber pressure increases, the intensity of the radiation increases in turn for the blue radiation, which is about 420 nm for the LOx/H_2 flames. This happens because the radiance of the blue radiation increases with the square of pressure. On the other hand, the intensity of OH* radiation emitted by a flame is linearly proportional to the pressure and varies exponentially with temperature. In LOx/H_2 flames, the mole fraction of OH is considerable and significantly attenuates OH* radiation. This effect becomes more important with increasing pressure. Self-absorption reduces the emitted radiation, as can be seen in Figure 6.2 at the wavelength of 310 nm.

The hydroxyl radical represents a particular case indeed: in hydrocarbons combustion, its molar fraction is negligible and then so is self-absorption, in particular for flames at low temperatures and pressures. Nevertheless, when dealing with hydrogen/oxygen combustion, OH can reach up to 15% in the reaction zone and self-absorption has a strong impact on the spectrum. Figure 6.3 shows the difference between the pure emission spectrum, and the spectrum obtained including self-absorption [56].

In most practical situations, a completely resolved spectrum cannot be obtained, and optical filters are used in order to reduce the range of wavelength captured by the detector to a narrower band. The filter is typically centered around the dominant emission wavelength of the spectrum, which has the value of 308.501 nm

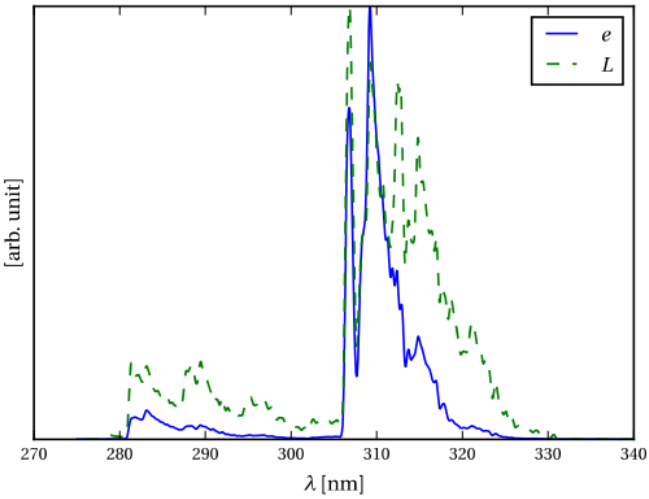

Figure 6.3: Spectrum of pure OH at T = 3000 K and p = 1 bar. The pure emission spectrum (e) and radiance spectrum (L) which takes into account self-absorption are compared [56].

for OH*. The use of filters has the advantage to facilitate the measurements, but the measurements are in turn sensitive to the filter transmittance, which has then to be taken into account to correctly simulate the spectrum, and quantum efficiency of the detectors.

6.1.1 Excitation mechanisms

The excitation mechanism is the key process which allows to investigate the origin of the radiation and how the chemical steady-state concentration of the excited molecule M* is reached. The emissivity of a volume element is described as:

$$e_{\mathrm{M}^*} \sim [\mathrm{M}^*] \tag{6.1}$$

where M* indicates the sub-species of the ground species M.
The excited species are typically produced by one of the following reactions:

- Thermal collision:

$$\mathrm{M} + \mathrm{Q} \underset{\mathrm{k_Q}}{\overset{\mathrm{k_{th}}}{\rightleftharpoons}} \mathrm{M}^* + \mathrm{Q} \tag{6.2}$$

  where Q is a generic molecule, k_{th} is the reaction rate of the thermal excitation and k_Q is the reaction rate for the quenching, which is often referred to as the reverse reaction of thermal excitation.

- Absorption of photon:

$$\mathrm{M} + h\nu \rightleftharpoons \mathrm{M}^* \tag{6.3}$$

- Chemical reaction of species A and B producing M^*:

$$\mathrm{A} + \mathrm{B} \underset{\mathrm{k_{diss}}}{\overset{\mathrm{k_{ch}}}{\rightleftharpoons}} \mathrm{M}^* \tag{6.4}$$

  where k_{ch} is the reaction rate constant and k_{diss} corresponds to the reaction rate of the dissociation process. The reaction can also take place in presence of a third reactant:

$$\mathrm{A} + \mathrm{B} + \mathrm{Q} \underset{\mathrm{k_{diss}}}{\overset{\mathrm{k_{ch}}}{\rightleftharpoons}} \mathrm{M}^* + \mathrm{Q} \tag{6.5}$$

The steady-state concentration of the molecule M^* can be derived from a detailed balance and considering infinite time for the processes. Generally, the absorption and dissociation are neglected since the excitation due to these processes is much lower than the one due to chemical or thermal excitation.
If thermal excitation overcomes chemical excitation, M^* is in thermal equilibrium with its ground state molecule M. Its concentration is a function of the temperature and ground state concentration. This typically happens at temperatures above 2700 K. For relatively cold flames (temperatures below 2500 K), the radiation coming from excited molecules is much larger than thermal radiation. In this case, the resulting radiation is chemiluminescence. When modelling chemiluminescence, absorption and thermal excitation are often neglected, and the radiation is mainly due to the rate constant of the reaction and the concentration of the reactants. When chemical excitation is predominant, M^* is not electronically thermalized with respect to the ground state molecule M.
In particular, for OH* chemiluminescence of hydrogen flames, the dominant reactions is:

$$\mathrm{O} + \mathrm{H} + \mathrm{Q} \longleftrightarrow \mathrm{OH}^* + Q \tag{6.6}$$

6.2 BKH optical diagnostics

Optical diagnostic setups are used to visualize the flame during experimental test sequences. OH* and shadowgraph images are recorded using a high-speed camera as shown in the sketch of the BKH optical diagnostic system in Figure 6.4. Simultaneous recording is allowed by a dichroic mirror placed at 45° with respect to the optical axis. This angle is set because ultra-violet light can be reflected without interrupting the optical path between the back-lighting source and shadowgraph imaging of the camera. Hardi described in detail the optical setup used during BKH experiments [86]. Line-of-sight access to the primary injection region is provided by the quartz optical windows placed at the side walls of BKH. A sketch of line-of-sight access during a BKH test run is shown in Figure 6.5. The windows are placed in a position where they can capture the flames and one side is aligned with the injection plane to have a view of the jets directly downstream the injection plane. The BKH injectors are configured in a matrix

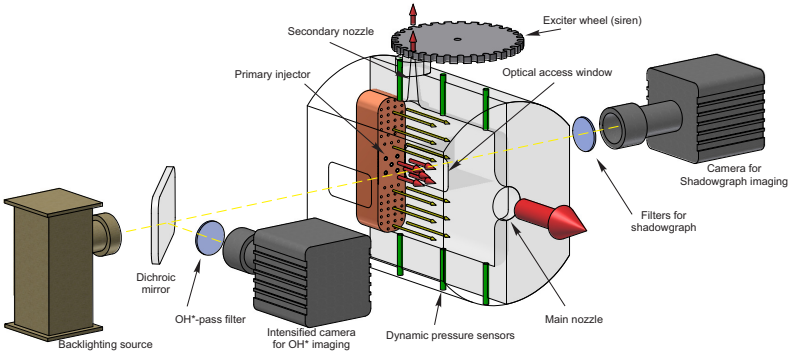

Figure 6.4: BKH optical diagnostics setup [15].

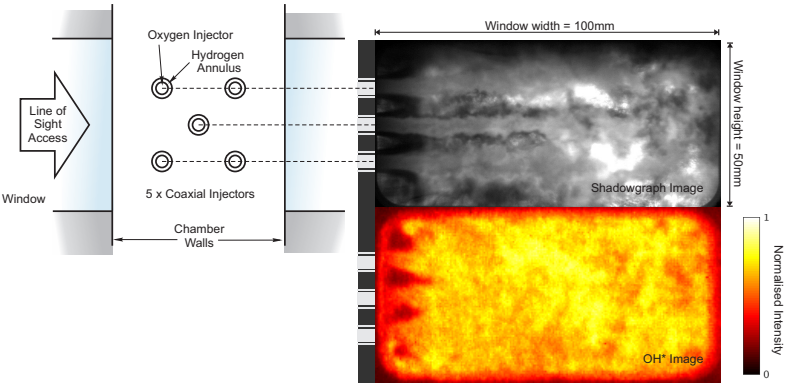

Figure 6.5: Line-of-sight access and images recorded during a BKH test without acoustic excitation [15].

pattern, so line-of-sight optical access can only capture the middle injector and outer lower and upper injector directly. In BKH experimental images then, the three injectors appear as vertically spaced oxygen streams and flames.
Shadowgraph imaging is a process which records images of the flames based on the light passing through media with different refraction indices. This diffracts the light and then visualization of density gradients through the media is possible. When using a back-lighting source the light diffracted by the changes in the refractive index where density gradients are present in the flow field does not reach the other side of the chamber and the shadow cast as light is diffracted producing the shadowgraph images.
To record shadowgraph images in BKH, a Photron FASTCAM SA5 is used. On the opposite side of BKH to the camera a back-lighting source is placed and used to illuminate the flame zone. An additional optical filter before reaching the high-speed camera is employed in order to block the combustion light emitted by the flame which has not to be captured and allowing the light emitted from the back-lighting source to be correctly captured. The filter has a peak of 314.5 nm and FWHM of 4 nm. Regions with high density gradients are then displayed in the images, such as the LOx core exiting the shear coaxial injectors which propagates downstream the injection plane.
To capture OH* images during BKH experiments, a Photron FASTCAM APX-i^2 was employed. An optical filter was placed in front of the camera to filter the radiation at wavelengths corresponding to the range of interest for OH* emission, with a wavelength pass-band of 305±5 nm centered on the OH* wavelength.

6.3 The SMART algorithm

In this section, the algorithm developed in the frame of this work is presented. This algorithm, named SMART (Spectral Model and Ray-Tracing), aims to produce pseudo-OH* images which can be compared with the experimental data coming from high-speed cameras and optical probes. SMART takes into account both self-absorption and refraction phenomena, representing a step forward towards the modelling of complex phenomena which occur during flame radiation processes.
The considered range of wavelengths goes from 305 to 320 nm in order to account for self-absorption phenomena for OH molecules, but this range can be easily modified by changing the settings in the radiation model part of the algorithm. Although including self-absorption and refraction, other phenomena which can be neglected are not considered: diffraction, scattering, dispersion and black-body radiation from walls are not included in the model. Diffraction is a phenomenon which should be taken into account when dealing with subcritical flames because the surface tension produces liquid droplets when the jet disintegrates. However, for the nature of the rocket flames considered in this work, surface tension is negligible.
The algorithm takes as input data a CFD solution stored in the nodes of the grid and treats the data as a quasi-continuum with a inverse distance interpolation

method based on nearest neighbours.
The first step is the pre-processing of the solution, where the refractive index n for each node of the input data is calculated. The Gladstone-Dale relation [67] gives an estimation of the refractive index as:

$$n(T,p) = 1 + \rho(T,p) \cdot k \tag{6.7}$$

where T refers to the temperature, p to the pressure, ρ to the density and k is the Gladstone-Dale coefficient. For fluid mixtures with different species, the representative Gladstone-Dale coefficient $\overline{k}$ is employed:

$$\overline{k} = \sum k_i \cdot x_i \tag{6.8}$$

with i the species and x_i the molar fraction of the species at the evaluated point.
The definition of the points at which the rays are expected to enter is the first step to obtain the pseudo-OH* images. The two vectors needed are the position vector $\boldsymbol{r}$=$[r_x,r_y,r_z]^T$ and the vector corresponding to the opposite direction of the light that would enter the detector $\boldsymbol{T}$=$[T_x,T_y,T_z]^T$. The eikonal equation which describes the electromagnetic wave propagation on a path s is then integrated, assuming geometrical optics in a scalar field of continuously changing refractive index $n(\boldsymbol{r})$, following the approach of Born and Wolf [20] :

$$\frac{\mathrm{d}}{\mathrm{d}s}\left[n(\mathbf{r})\frac{\mathrm{d}\mathbf{r}}{\mathrm{d}s}\right] = \nabla n(\mathbf{r}) \tag{6.9}$$

Equation 6.9 is then split into two first order differential equations and solved with an explicit Runge-Kutta method of order 5 [45]:

$$\frac{\mathrm{d}\mathbf{r}}{\mathrm{d}s} = \frac{\mathbf{T}}{n(\mathbf{r})} \tag{6.10}$$

$$\frac{\mathrm{d}\mathbf{T}}{\mathrm{d}s} = \nabla n(\mathbf{r}) \tag{6.11}$$

An initial condition vector y_0 is required by the solver, described as:

$$y_0 = \begin{bmatrix} \mathbf{r}|_{s=0} \\ \frac{\mathbf{T}}{n}\big|_{s=0} \end{bmatrix} = \begin{bmatrix} r_x|_{s=0} \\ r_y|_{s=0} \\ r_z|_{s=0} \\ T_x/n|_{s=0} \\ T_y/n|_{s=0} \\ T_z/n|_{s=0} \end{bmatrix} \tag{6.12}$$

As the calculated position vector is outside of the defined geometry boundaries the solvers stops. The solution is given as a set of vectors $[\mathbf{r}(s=0)\ldots\mathbf{r}(s=s_{\mathrm{end}})]^{\mathsf{T}}$ representing the point on the ray.
The nearest neighbour interpolation routine then interpolates the thermodynamic properties (T,p, and the mass fractions $X = [w_{H_2}, w_{H_2O}, w_{O_2}, w_{OH}]$) at the chosen

point along the ray. H and O mass fractions are neglected as they are close to zero. These properties are the inputs for the routine which determines the emission and absorption spectrum e_λ and κ_λ for the respective points.
OH* is not calculated at run time as a separate species in the CFD solution. The assumption is that OH* is in thermal equilibrium with OH, so that OH* can be calculated in a post-proecssing step. The necessary inputs are OH mass fraction, temperature T and pressure p. The mass fraction w_i of the i species are given to accurately simulate the chemical kinetics in the combustion chamber. The spectral modelling by Potter [166] is used and adapted for the purpose of simulating OH* radiation in SMART. In particular, the assumption made for the calculation of emission and absorption spectra is the thermal equilibrium, which states that translational, vibrational, rotational and electronic temperature are the same:

$$T = T_{trans} = T_{vib} = T_{rot} = T_{el} \tag{6.13}$$

The simulated transition is only the transition $A^2\Sigma^+ \rightarrow X^2\Pi$ and the returned emission and absorption spectra are calculated for the wavelenghts range of 305-320 nm. Following the approach of Stützer and Oschwald [213], the transition band $\nu = 0$, $\Delta\nu$=0 is chosen. Higher order transitions presented a too low signal-to-noise ratio, so only experimental data for this first order transition were collected. The spectra can be calculated for a set number of equidistant spectral points [166]. The main transition is from the first electronically excited state to the ground state but the model includes a number of fine rotational-vibrational transitions between the two electronic states. It also includes the effects of collisional broadening and Doppler broadening. The Einstein coefficients and spectroscopic constants are based on references [100, 130, 131, 179].
Figure 6.6 shows a sketch of the ray tracing algorithm. The ray path starts on a point on the window, passes through the jets and reaches the chamber walls. On its path, emission and absorption spectra along the ray are calculated. When the ray reaches the chamber walls, the integration of the coefficient to obtain the intensity starts, ending at the window [219].
Emission and absorption spectra e_λ and k_λ are calculated for the chosen points along the ray path. The Radiative Transfer Equation 6.14 (RTE) is solved, starting from the physical origin point of the ray and ending at the detector position for each wavelength:

$$\frac{\mathrm{d}L_\lambda}{\mathrm{d}s} = e_\lambda(s) - \kappa_\lambda(s) \cdot L_\lambda(s) \tag{6.14}$$

where L_λ is the spectral radiance. In order to make the results comparable with the experimental data, the spectral radiance is multiplied by the transmittance of the OH* pass filter used in the experiments $\tau_{\lambda,filter}$.

$$L_{\lambda,\mathrm{filtered}}(s) = L_\lambda(s) \cdot \tau_{\lambda,\mathrm{filter}} \tag{6.15}$$

Finally, the total filtered radiance $L_{filtered}(s)$ is obtained by integrating the spectral filtered radiance over the range of wavelengths of interest, in this case 305-320 nm.

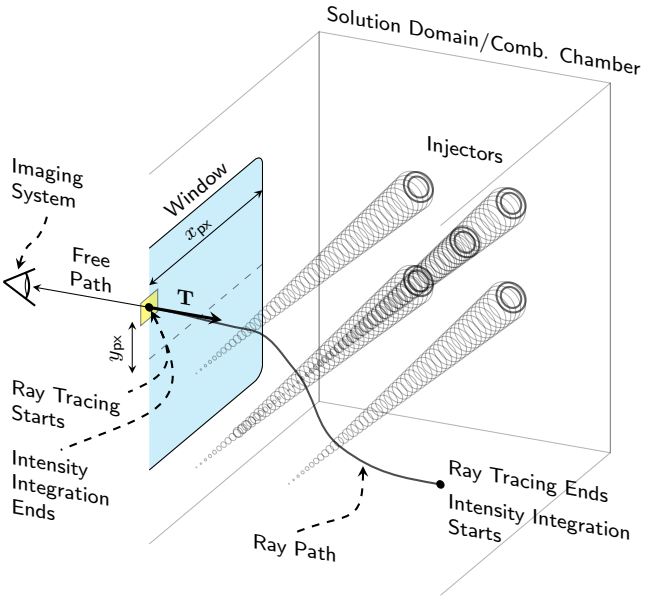

Figure 6.6: Sketch of the ray tracing algorithm. [219].

$$L_{\text{filtered}}(s) = \int_{305nm}^{320nm} L_{\lambda,\text{filtered}}(s)\mathrm{d}\lambda \tag{6.16}$$

The total radiance is then obtained for each point along the ray path. Only the radiance at the end of the ray path is relevant to obtain pseudo-OH* radiation images because it is the only one collected by the detector. The assumption of equal sensitivity, quantum efficiency and area is made for the outgoing rays.

6.4 Application to the BKH combustor

Before applying the algorithm to this test case, a previous validation was conducted by Tonti et al. [219] based on a simpler test case by Fiala [56], where a counterflow laminar gas-gas flame was considered. In this section, SMART is applied to a CFD solution of BKH by Beinke [15].
Domain, mesh and operating point used for the simulation are described in detail by Beinke [15] and here they are briefly summarized.
The domain is symmetric with respect to the x-y plane as shown in Figure 6.7. The mesh is fully unstructured and refined in the flame zone, with about 2.6 Mio nodes. The operating conditions are summarized in Table 6.1.

Table 6.1: Operating conditions

Chamber pressure	60.7 bar
Oxygen temperature	127 K
Main hydrogen temperature	279 K
Secondary hydrogen temperature	278 K
Window cooling hydrogen	281 K
Oxygen mass flow rate ($\dot{m_{LOx}}$)	565 g/s
Primary hydrogen mass flow rate ($\dot{m_H}$)	95 g/s
Secondary hydrogen mass flow rate ($\dot{m_{H_2}}$)	933 g/s
Window cooling mass flow rate ($\dot{m_{WC}}$)	260 g/s
ROF	6

Figure 6.8 shows the relevant results of the CFD simulation which are used as input for the algorithm
In this application of SMART, only the rays which exit the chamber perpendicular to the window are considered, since they are the ones captured by the high-speed camera. The assumption of parallel rays is acceptable because of the large distance between the camera and the window, since the solid angel of each pixel is negligible.
Figure 6.9 shows how refraction impacts the rays. The color of the rays indicates the integrated total radiance and the thickness gives information about the area

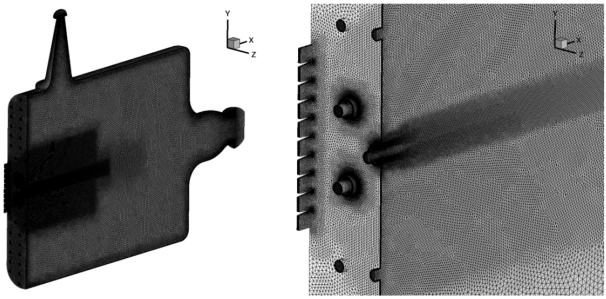

Figure 6.7: Mesh and domain used for the application of SMART [15]

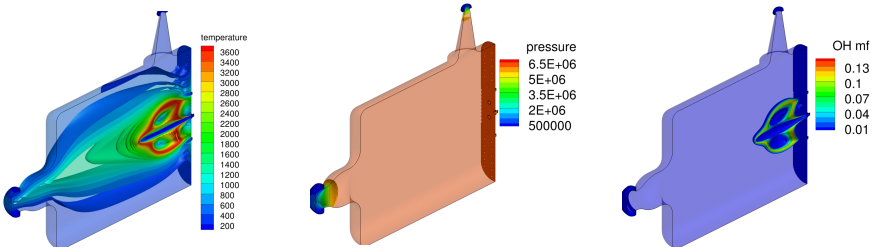

(a) Temperature (b) Pressure (c) OH mass fraction

Figure 6.8: Temperature (a), pressure (b) and OH mass fraction distribution (c) in BKH. The load point refers to 60 bar chamber pressure and ROF 6 [15]. These distributions are used as an input for the ray tracing algorithm which generates the pseudo-OH* images

where larger emission occurs. Where density gradients are present, the rays are bent. When the rays pass through the OH-rich reacting shear layer to the other side of the core, they are attenuated. It can be also noticed that the total radiance of a ray changes significantly only when the ray is refracted passing tangentially through the shear layer where OH* is present. The model however does not take into account diffraction, scattering or internal refraction inside the LOx core.

Figure 6.10 shows the comparison between the experimental data, the previous 1D integration of OH* radiation performed by Beinke [15] and the application of the SMART algorithm to the same CFD solution. The plots refer to the intensity of the signal.

An important thing which has to be noticed is that the main difference between the results from CFD simulation and the experimental data is that the OH distribution does not extend until the end of the window at x = 100 mm, but ends slightly downstream the injection plane. This is an indication of the fact that in

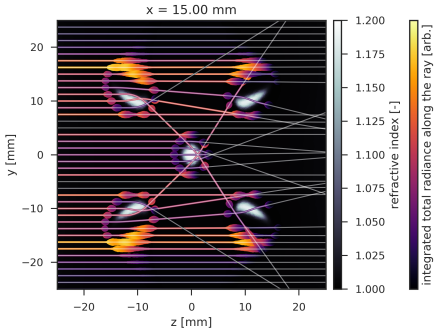

(a) x = 15 mm

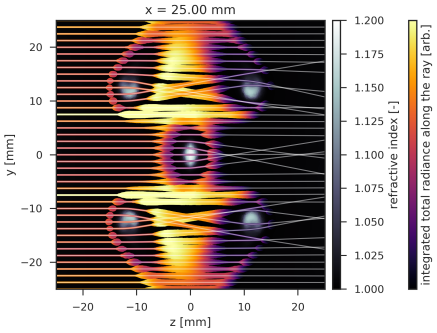

(b) x = 25 mm

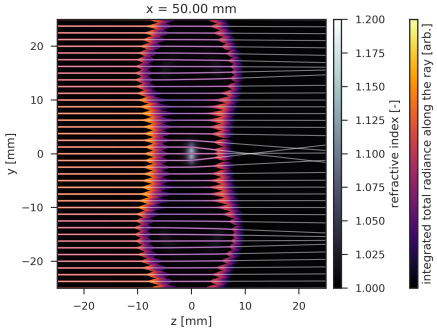

(c) x = 50 mm

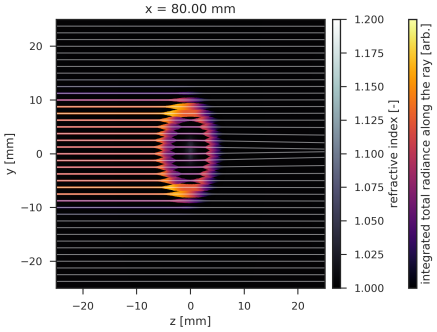

(d) x = 80 mm

Figure 6.9: Ray path visualization through refractive index gradient. The gradients correspond to the increase in the LOx jet density at different locations.

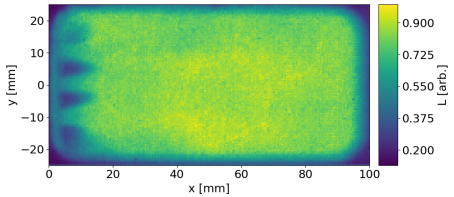

(a) Time averaged OH* radiation from experiments

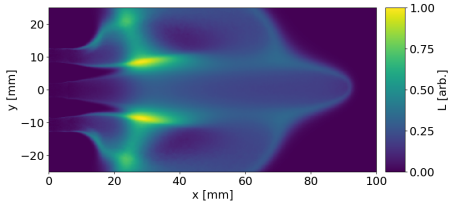

(b) Line-of-sight integrated OH* radiation

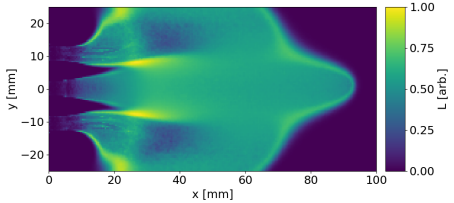

(c) SMART

Figure 6.10: Comparison between the time averaged OH* radiation measurements (a), the LOS integrated image [15] (b) and the image obtained with SMART (c). [219]

the simulation oxygen is too rapidly consumed, leading to a shorter flame zone which reflects on the distribution of OH inside the chamber. Another element which can have an influence is that the transport of OH* is not modelled and this holds true because OH* are considered as a subset of the OH ground state molecules. OH* molecules are not modeled in a detailed chemistry scheme. The absence of modelling the transport of OH* could lead to an underestimation of radiation close to the end of the window at x = 100 mm. Comparing Figure 6.10b and 6.10c, an overall difference in the intensity of the radiation is clear. Without taking into account self-absorption and refraction, the intensity of the radiation is lower in all the domain. In both images, however, the largest intensity of the total radiance occurs in the shear layer where the jet interacts and in the outer parts of the jets, where combustion takes place and the temperature results to be higher than in other regions of the flame, at x = 25 mm. The region slightly downstream the injection plane is better resolved when SMART is applied, showing a difference in the radiance intensity also in the zones inside the jets, between x= 10 mm and x = 15 mm.
An interesting aspect which has to be considered is that SMART takes currently into account self-absorption and that emission is now spectrally resolved being not considered as the transition at a specific wavelength. The integrated spectral radiance L_λ is also multiplied for the spectral transmittance of the filter $\tau_{\lambda,filter}$, which attenuates the spectral radiance values according to their wavelength. Moreover, a fully three dimensional ray tracing allows the visualization of high density regions of the LOx cores according to the physical mechanisms of refraction [219].
In order to have further insights into emission zones under rocket combustor chambers operating conditions, several physical parameters along a chosen ray path are displayed in Figure 6.11. The regions where thermal excitation occurs are marked with red boxes. They coincide with the zones of OH* presence.

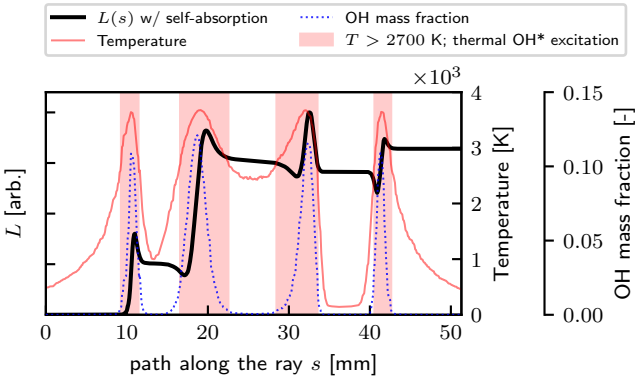

Figure 6.11: Integrated radiance along the ray path.

The high temperature and the presence of OH molecules are the main reasons of increased flame emission. Temperature drops between 10 and 16 mm and 34 and 38.5 mm along the ray path, indicating the regions where the ray passes through the LOx jet. The four emission zones are highlighted in red and the emission along the ray path shows a fluctuating behavior where thermal excitation occurs, with a slight spatial delay with respect to the temperature and OH mass fraction profile. Stating where the total radiance changes is difficult because radiance values are obtained integrating the contributions of spectral radiance at different wavelengths, when Equation 6.14 is solved. The terms of the equation show that when absorption overcomes emission, then the spectral radiance must be high as well as the absorption coefficients. This leads to the consequence that self-absorption has an important effect when dealing with rocket combustion chambers operating conditions and has an important impact on flame emission. The integrated radiance has to be obtained first for each wavelength line-by-line, because self-absorption has a larger effect at wavelengths where emissivity is high and relatively small where emissivity is low [219]. Figure 6.12 shows the difference in the solution when including self-absorption in the calculations both along the single ray path and in terms of relative difference in the whole solution field. Neglecting self-absorption would give a total radiance 15 times greater than when self-absorption is considered for rays which pass through multiple flames before reaching the detector.
Another important aspect of SMART is the inclusion of refraction phenomena and their effect on the results. The relative difference in radiance on a pixel-by-pixel basis between the fully ray-traced image and the 1D integrated image is shown in Figure 6.13. The values are normalised to the pixel values of the 1D integrated image.
The largest difference can be observed between x=0 mm and x=20 mm. This is the zone just downstream the injection plane, where the jets interact, and where the recirculation zones are present. These zones present the largest density gradients, and so considering refraction becomes particularly important in order to correctly model radiation at these locations, where a liquid-gas interface is present. This allows to have a more correct comparison between the pseudo-OH* images produced by the algorithm and the experimental data.

6.5 Summary

A method for comparing CFD results and optical measurement of filtered radiation from high pressure oxygen hydrogen flames was developed. Pseudo-OH* images are generated from the CFD simulation solutions. The SMART post-processing routine which produces the images first performs reverse ray-tracing from each pixel of the image, sampling the thermodynamic properties along the path and modelling the emission and absorption spectra for wavelengths between 305 and 320 nm. Then the spectral radiance along the ray is obtained by solving the radiative transfer equation line-by-line. Finally, the spectral radiance is integrated to obtain the total radiance [219].

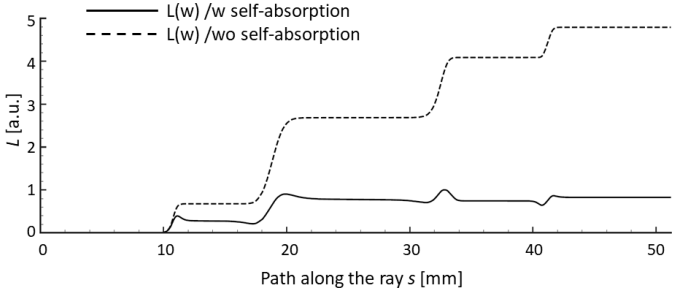

(a) Radiance along the ray path with and without self-absorption

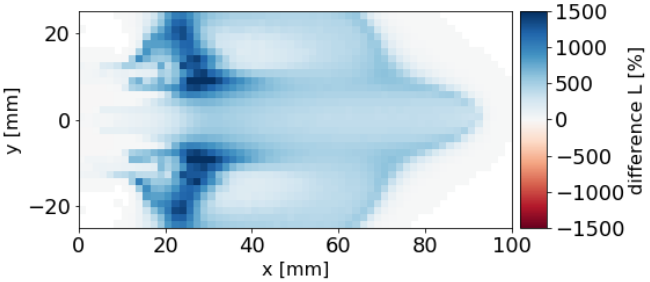

(b) Relative difference of total radiance neglecting self-absorption

Figure 6.12: Difference in total radiance prediction with and without self-absorption

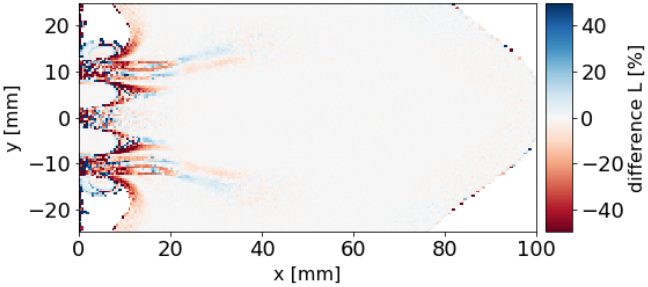

Figure 6.13: Relative difference in simulated total radiance between fully ray traced and 1D integrated image.

Two main phenomena which have previously not been taken into account for cryogenic flames are included in this work, self-absorption and refraction. In previous works, neglecting self-absorption, the total radiance is overpredicted by a factor of 15 in the multi-flame rocket combustor test case considered here. The use of ray-tracing, which models the refraction of the light as it passes through the chamber, has a significant effect, especially for rays interacting with the LOx jet, as refraction in these zones can be very high. Comparing the experimental images with the ones produced by the current method, the difference is still significant but lies in the ability of the CFD solver to predict the distribution of OH* partial density in the field of view of the combustor. Comparing LOS integrated images with fully ray-traced ones, the absolute difference in radiance reaches about 20% of the normalized image radiance range. In regions where rays encounter the LOx jets, rays gathering radiance by passing through multiple flames are shown to be just as bright as those passing through only one, due to self-absorption.
SMART takes into account two very important phenomena contributing to the flame radiance, which are refraction and self-absorption. This allows to reduce the overprediction of the flame radiation for a more accurate relative intensity distribution in a pseudo-OH* image. The comparison with experimental data is improved, allowing better validation of CFD models using experimental data from flame visualization. However, the analysis also indicated that for better validation of OH* flame visualization between experiments and CFD, a chemiluminescence model should be considered in the CFD simulations in the future.

7 BKH Full chamber analysis

This chapter presents the CFD simulation results of the full 3D geometry of the BKH combustion chamber and the subsequent acoustic analysis performed with the commercial software COMSOL Multiphysics - Acoustic Module in order to calculate the eigenfrequencies of the main resonant modes of the chamber.
As already mentioned previously in this work, HF combustion instabilities are a phenomenon which can be potentially destructive for LPREs. Extensive experimental testing can identify the frequencies of the most dangerous resonant modes, but the costs of this operation are prohibitive. Then, developing numerical tools which can identify the resonant modes and correctly calculate their eigenfrequencies becomes a crucial aspect in the design of a LPRE.
With the development of High Performance Computing (HPC), different numerical tools can be used ranging from Finite Element Methods (FEM) to Large Eddy Simulations (LES) and in some cases even Direct Numerical Simulations (DNS). With the help of these advancements in numerical simulations, modelling of transcritical flows has been significantly improved and high-pressure LPREs stability can now be investigated [16, 186, 188, 222].
Also a flame response function together with an acoustic solver can be used to identify the main resonant frequencies of the combustion chamber [195, 241], but this approach needs two fundamental inputs. A baseline flow field is needed, depending on the solver used for the acoustic analysis. The Helmholtz solver requires the speed of sound field and the Linearized Euler Equation (LEE) solver takes the mean velocity field. The other fundamental element needed is a model for the flame response to perturbations describing the complex interaction between heat release rate and acoustic pressure fluctuations, as a time lag model. The baseline flow can be otained with relatively unexpensive calculations, wheres the flame response model cannot to be obtained easily from theoretical considerations. The drawback is then that in this approach the accurate determination of a flame response function is fundamental to obtain a stability map of the engine and obtain this function is not trivial.
In this chapter a steady-state solution of the BKH combustor is presented, comparing it with previous numerical simulations and underlining the main differences and improvements both in the setup and results. A comparison with experimental data is also performed and the ray-tracing algorithm presented in Chapter 6 is applied to the OH distribution in the zone corresponding to the window which provides optical access to the flame in the combustion chamber. Then, an acoustic analysis of this solution is performed using the LNS solver of the commercial software COMSOL Multiphyiscs.
Modal analysis of the BKH combustor was already perfomed by Hardi et al. with a FEM acoustic solver in ANSYS to calculate the acoustic modes, but it did not consider the variation of the acoustic properties inside the chamber volume. The

distribution of the relevant acoustic variables was considered constant inside the chamber volume and estimated with CEA [86, 88]. An improvement was introduced by Beinke [15] implementing the RANS solution in a COMSOL Helmholtz solver, taking into account the speed of sound and density distribution inside the chamber. Nevertheless, the Helmholtz solver suffers of an important limitation: it cannot take into account the background flow, forcing the introduction of some simplifications in the acoustic boundary conditions, which can affect the results and lead to important discrepancies in the calculation of the resonant frequencies. This gave the motivation to conduct the analysis with a LNS solver, which can take into account the background flow and remove some simplifications introduced with the Helmholtz solver.
The next section describes in detail the domain, mesh and boundary conditions used for the RANS simulation with a focus on the differences with the previous setup by Beinke [15]. Then, results of the CFD simulation are presented and a comparison with former simulations and experimental data is given, applying also SMART. The acoustic analysis is then described with the calculation of the resonant modes starting from the CFD solution presented in Section 7.2 and compared with the experimental data from Hardi [86].

7.1 Numerical setup

BKH can operate at a various range of pressures and ROF. The current work focuses on one specific point which corresponds to a chamber pressure of 60 bar and ROF of 6. This choice was made to be able to compare the results with the former calculations of Beinke [15], which conducted the simulations for the same load point, and because these operating conditions are the ones representing the highest chamber pressure reached during BKH experiments. The operating pressure is greater than the critical pressure of both hydrogen and oxygen. LOx is injected at a subcritical temperature and supercritical pressure. Once it is injected in the chamber, LOx experiences the transition from sub-critical to supercritical before mixing with other species in the chamber, resulting then in a trans-critical injection.
ROF 6 was chosen because it is the highest value reached in BKH tests and because it is the most representative value for upper stage rocket engines. Moreover, plenty of experimental data are available for this load point, representing then an optimal choice for validation.
Table 7.1 summarizes the operating conditions of the selected test case. The values are slightly corrected with respect to the values presented by Beinke [15] since there were some slight calibration errors in the experimental setup. Oxygen mass flow rate has been corrected using online measurements of nitrogen concentration. Nitrogen is used to pressurise the supply tank, and a small amount (around 1-3%) mixes with the oxygen which eventually reaches the specimen. The correction results in a small reduction in the stated value of oxygen mass flow rate. Secondary hydrogen mass flow rate has been corrected for a systematic calibration offset in the flowmeter. Data from many campaigns reveals a consistent

overestimation of flow rate, which have been corrected for the present work. The oxygen mass flow rate is set now to 565 g/s instead of 566 g/s and the secondary hydrogen mass flow rate is not correctly set at 899 g/s, whereas before the value was set to 933 g/s. Temperature and pressure of the propellants are measured in the domes and the chamber pressure is recorded by a static pressure sensor located at the top wall of the chamber. Mass flow rates of the propellant are measured with mass flow sensors. Table 7.2 lists the calculated values for the main inputs of the RANS simulation.
The values listed in Table 7.2 are the values set as input for the RANS calculation together with the temperatures measured in the experiments. They refer to individual elements mass flow rates, assuming a equal distribution of the considered propellant among the correspondent elements.
The domain used for the simulation is shown in Figure 7.1.

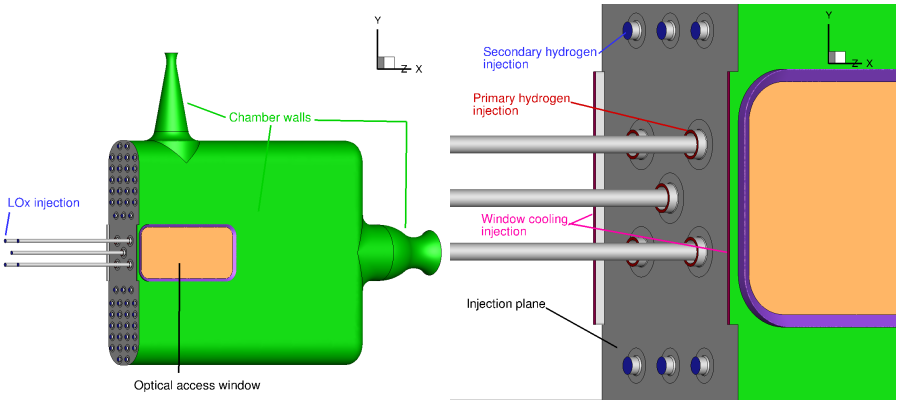

(a) Full chamber

(b) Injection detail

Figure 7.1: BKH geometry used for the RANS simulation.

With respect to the simulation by Beinke [15] here the domain is full 3D. The choice is justified by the analysis conducted in Chapter 4, where evidence of the fact that the axisymmetric boundary condition affect the results in terms of heat release rate, giving an underestimation of this variable which is particularly important when investigating HF instabilities. Moreover, here the LOx injectors are included in their full length up to the throttle section of the injectors. The hydrogen post is cut at a length of 2 mm upstream the injection plane. The injection system of the window cooling was simplified, not describing in details the injection slots but maintaining the correspondent mass flow rate value. On the other hand, the window frame features the geometrical details of the real BKH combustor. The main and secondary nozzle are modelled with a divergent section for the outlet which exhausts directly into the atmosphere, setting the outlet pressure at 1 bar. This way, when setting up an unsteady simulation with the

Measured Values		**Value**	**Unit**	**Uncertainty**
Combustion Chamber Pressure	P_{CC}	60.7	bar	±1%
Oxygen				
Mass flow rate	$\dot{m}_O$	565	g/s	±3%
Dome Temperature	T_O	127	K	±1.25 K
Dome Pressure	P_O	80.9	bar	±1%
Primary Hydrogen				
Mass flow rate	$\dot{m}_H$	95	g/s	±3%
Dome Temperature	T_H	279	K	±1.25 K
Dome Pressure	P_H	69.7	bar	±1%
Secondary Hydrogen				
Mass flow rate	$\dot{m}_{H2}$	899	g/s	±3%
Dome Temperature	T_{H2}	278	K	±1.25 K
Dome Pressure	P_{H2}	94.9	bar	±1%
Window Cooling Hydrogen				
Mass flow rate	$\dot{m}_{WC}$	260	g/s	±3 %
Dome Temperature	T_{WC}	281	K	±1.25 K
Dome Pressure	P_{WC}	86.3	bar	±1%

Table 7.1: Experimental data for the considered load point.

Calculated Values		**Value**	**Unit**	**Uncertainty**
Oxygen				
Mass flow rate	$\dot{m}_O$	113	g/s	±3%
Primary Hydrogen				
Mass flow rate	$\dot{m}_H$	19	g/s	±3%
Secondary Hydrogen				
Mass flow rate	$\dot{m}_{H2}$	18	g/s	±3%
Window Cooling Hydrogen				
Mass flow rate	$\dot{m}_{WC}$	130	g/s	±3 %

Table 7.2: Calculated values for the considered load point

activation of the toothed wheel, it will be possible to cut the divergent part of the secondary nozzle and take then mean pressure at the outlet surface, which will represent the pressure set from the system.
The boundary conditions used also differ from the ones used by Beinke [15], in particular at the inlet of the injection elements. In the current work, all the injectors are modelled with a mass flow boundary condition, specifying the mass flow rate and temperature in order to match the experimental data given in Table 7.1, whereas Beinke used Dirichlet boundary conditions at the primary and secondary hydrogen injectors and for the window cooling, specifying temperature, density and velocity. All the walls are specified as viscous adiabatic walls.

7.1.1 Mesh

The mesh used in this work is a hybrid structured/unstructured mesh. The oxygen and hydrogen post walls are described with hexahedral elements. The flame zone features a structured block starting from 2 mm downstream the injection plane until 90 mm. A truncated cone surrounding the structured block extends until 110 mm downstream the injection plane providing a further refinement of the mesh. Figure 7.2 shows the complete mesh and a detail of the mesh at the injection at z = 0. The remaining zones where filled with unstructured tetrahedra.
The size of the elements was adapted using a number of geometrical sources according to the zone of the chamber which had to be simulated. The zones where large gradients are expected were refined with respect to the zones where no particularly relevant physical phenomena take place. The most refined zones are in particular the post tip where the flame anchors and the flame zone where large gradients are expected as where combustion takes place.
The mesh has ∼25 Mio nodes. The hexahedral block is discretized with 180 points in the axial direction, 290 points in the vertical direction and 220 points for the width. The minimum dimension of the nodes inside the block is 0.1 mm downstream the injection plane, where the block encounters a source of tetrahedral elements which starts from the injection plane and extends until 2 mm downstream for the five injectors. The cylinder surrounding the block has a minimum element dimension of 0.4 mm starting from the injection plane, arriving at 0.8 mm at x = 110 mm, after the full length of the window.
The stretching ratio used for the tetrahedral elements is set to 2 since in regions far from the flame zone a high resolution of the flow field is not necessary. The mesh is then refined in the main and secondary nozzle region. The boundary layer element start with a size of 0.001 mm at the wall location, with 15 layers and a stretching ratio of 1.3 which allows slightly bigger elements just slightly far away from the wall.
A mesh independence study was conducted and the choice of this dimension results from a progressive refinement of specific zones such as the flame zone and the linking zone between the injection plane and the block containing the flames. The residuals of the density and the length of the LOx core were considered as parameters to check the mesh independence. Increasing the number of points did

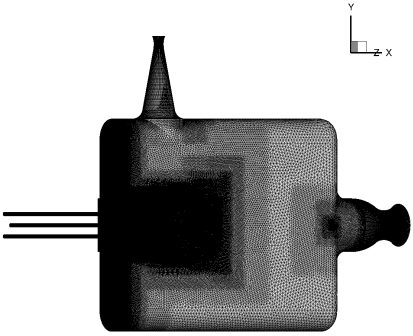

(a) Full chamber

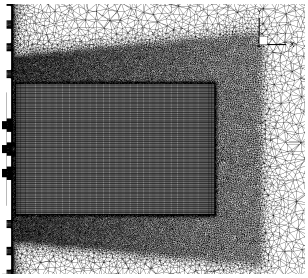

(b) Injection detail

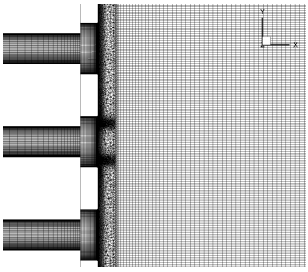

(c) Injection detail

Figure 7.2: Mesh of the steady state chamber model.

not lead to any changes in the LOx core length.

7.2 Numerical results

The RANS simulation results presented in this work are obtained using the DLR TAU code described in Chapter 3. The simulation was run exploiting the real gas capability of TAU. The solution is obtained initialising the environment inside the chamber with the relevant physical variables obtained by CEA considering an equilibrium fluid. Adiabatic flame temperature, mass fractions of the species and density are set as initial conditions for the simulation inside the whole domain. They were computed giving as an input to CEA the experimental chamber pressure and ROF. The calculations were then started by imposing as boundary conditions the values described in Table 7.2 and the correspondent measured static temperatures.
The steady state solution converged after 220k iterations. The simulation was run on the HPC CARA, running on 20 cores with a DDR4 processor.
CFL number was set to 1.2. The turbulence parameters were set as follows: the Spalart-Allmaras one equation turbulence model was chosen, the Schmidt number for Fick's and turbulent diffusion have a value of 0.3, as well as the turbulent Prandtl number. The setup here is different from the setup of Beinke [15], in particular regarding the turbulent Prandtl number. The Schmdit number for Fick's and turbulent diffusion were chosen because they provide results which are in good agreement with experimental data in particular for the length of the LOx core.
In the previous version of TAU code in fact, it was not possible to define a turbulent and laminar Prandtl number separately, obliging the user to directly set the ratio between laminar and turbulent Prandtl number, which was set to 2 by Beinke [15] after conducting an analysis and a comparison with experimental data in particular in terms of the LOx core length. The Spalart-Allmaras turbulence model was selected due to its robustness and ease of implementation, showing also in previous works a good agreement with experimental data.
In the next section, an overview of the flow field and flame zone is given, comparing the numerical results of this work with previous numerical results by Beinke [15] and with experimental data.

7.2.1 Flow field

Density, temperature and OH mass fraction distributions are shown in Figure 7.3 as they would be seen from the optical access window. The purpose of showing the fields in such a way is justified from the fact that BKH experimental images are registered having access to the optical window. Moreover, this domain will be the one considered when running SMART for comparison with the optical data and the fields shown here are the relevant fields which have to be given as an input for the algorithm.

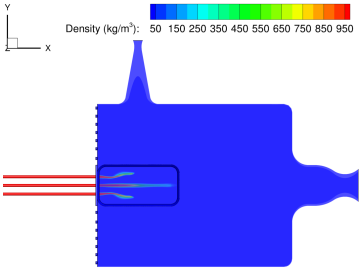

(a) Density

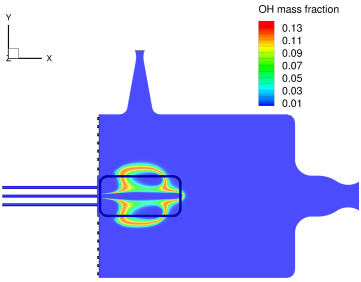

(b) OH mass fraction

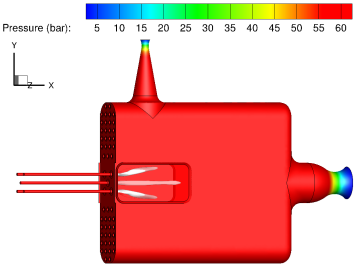

(c) Pressure and density isosurfaces at ρ=50 kg/m^3

Figure 7.3: Density (a), OH mass fraction (b) and pressure field (c) at steady state.

The mean chamber pressure resulting from the simulation is 59.7 bar, being in the uncertainty range of the experimental data and resulting to be lower than the mean pressure obtained by Beinke [15] (62.3 bar), which was slightly higher than the experimental value. The reason could lie in the different geometry used for the simulation, in the different mesh and in the inclusion of a longer part of the LOx post. A small pressure drop occurs in fact along the injectors, which influences the final value of the mean chamber pressure. Moreover, also the geometry of the nozzles is quite different: at the throat, where the flow is choked in this work we obtain the value directly from the simulation, not imposing it at the throat.
Looking at the density isosurfaces, they indicated the length of LOx core. The center jet results to be longer than the surrounding jets, being shielded from the outer environment. The four surrounding jets are shorter and are deflected with respect to the central axis of the chamber. Figure 7.4 shows the heat release rate distribution together with OH mass fraction isosurface which allows to identify the flame zone which will be taken into account when applying SMART.

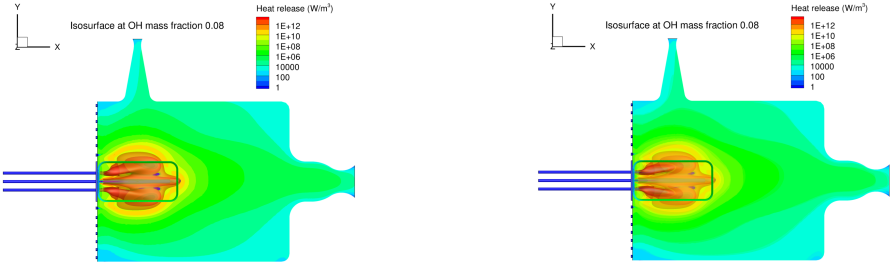

(a) Centerplane (b) Outer view

Figure 7.4: Heat release field and OH isosurfaces inside the BKH chamber at centerplane and outer plane.

The general aspects of the structure of the flow field have already been discussed by Beinke [15]. Here, a comparison of the results using the different setups are presented and discussed. Figure 7.5 shows the comparison of the density field as seen from the window frame in terms of isosurfaces at $\rho = 10$ kg/m^3 of the current simulation and the previous simulation by Beinke [15].
The length and the shape of the LOx core are different in the two simulations. The new simulation shows a LOx core which extends further downstream the end of the window, whereas the previous one reaches a lenght of about 90mm at cutoff density. A difference is noticeable also in the shape of the outer flames. The LOx cores result to be thinner in the new simulation, whereas the previous simulation result to have a thicker LOx core with a deflection of the outer jets further downstream.
Figure 7.6 shows the comparison of OH mass fraction distribution inside the chamber for the two simulations. Also here it can be seen that both the shape and length of the OH mass fraction distribution is quite different in the two

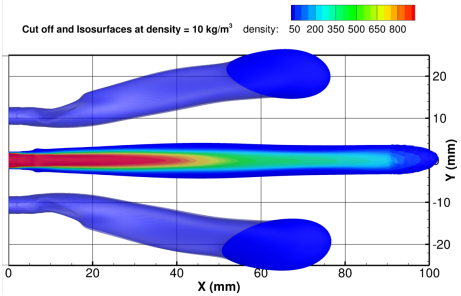

(a) New simulation

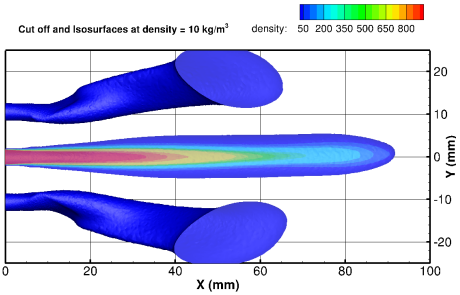

(b) Previous simulation [15]

Figure 7.5: Comparison of the density field as seen from the window between the new simulation and the previous simulation by Beinke [15].

simulations. In particular, the new simulation shows a longer and wider distribution. The two outer flames are visible in both simulations, but the intensity inside the fields changes considerably, showing that the new simulation has a higher concentration of OH in the middle of the distribution.

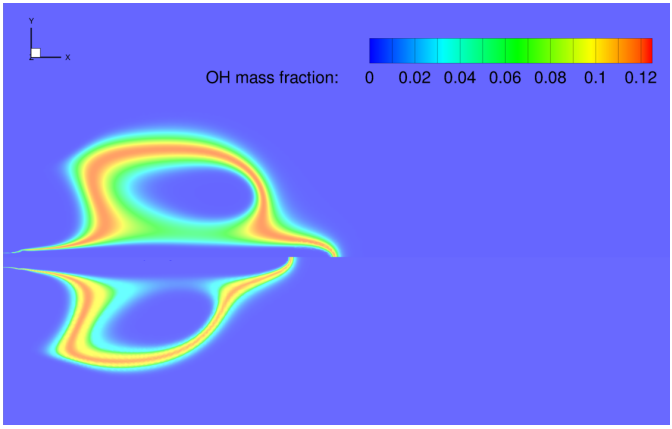

Figure 7.6: Comparison of the OH mass fraction distribution between the new setup (top) and the simulation by Beinke (bottom) [15]

Figure 7.7 shows the temperature field and OH mass fraction isosurface at 0.08 with the value chosen to have a consistent comparison with the results by Beinke [15]. This is the starting point of the application of SMART since it shows the OH mass fraction and temperature distribution in the flame zone.
With respect to the previous simulation of Beinke, temperature and OH mass fraction fields results to be different, in particular they result to be longer and wider, covering a bigger area of the window zone. Temperature results to be higher in the area near the window. As explained in Chapter 6, the thermal excitation overcomes the chemical excitation when temperature is above 2700 K. This gives already an idea of the fact that the thermally excited OH* will be visible in the zones where temperature exceeds 2700 K, giving different results with respect to previous simulations. Figure 7.8 shows a comparison of the application of SMART between the simulation presented here, the previous results and the experimental data.
The results of the application of SMART on the new simulation are compared with the experimental OH* time averaged image and the application of SMART on the simulation by Beinke [15]. It is evident that the OH* radiance distribution now extends towards the end of the window. The radiance emitted from the two lobes now extends until x=80 mm with a increase of $\simeq$33% with respect to the previous simulation. The central part of the jet extends over the end of the window and also the with is more extended than in old CFD results. The radiation of the zone downstream the injectors up to x = 10 mm is less visible

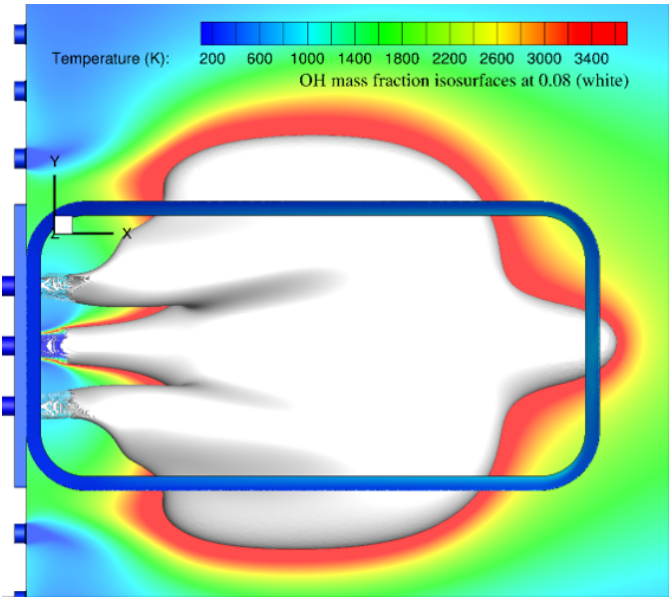

Figure 7.7: Temperature distribution and OH mass fraction isosurface.

than in the previous simulation. This can be due to the fact that in the previous simulation the domain is axisymmetric, whereas the new simulation features all the five jets and also the other jets which are not visible from the window give their contribution, resulting in a lower emitted radiance. Since the camera parameters are linear when getting OH* intensity, the same behavior has been used to get the images from the CFD. An overall improvement is observable in the new CFD solution, altough the experimental data are not completely matched. This is due to the fact that chemiluminescence is not included in SMART, which is a post-processing tool which takes into account only OH* thermal radiation. Figure 7.9 shows the comparison between the image obtained applying SMART and and 1D integrated image. Also here, the same behavior described in Chapter 6 can be observed. The 1D integration sums the mass of OH along the Z direction. The assumption of optically thin flame is used, where self-absorption is not taken into account. This leads to an underestimation of the integrated total radiance whereas the SMART image shows results comparable with experimental results as shown in Figure 7.8. This underlines the fact that it is crucial to take into account the optical path of the rays as done with the ray-tracing algorithm.

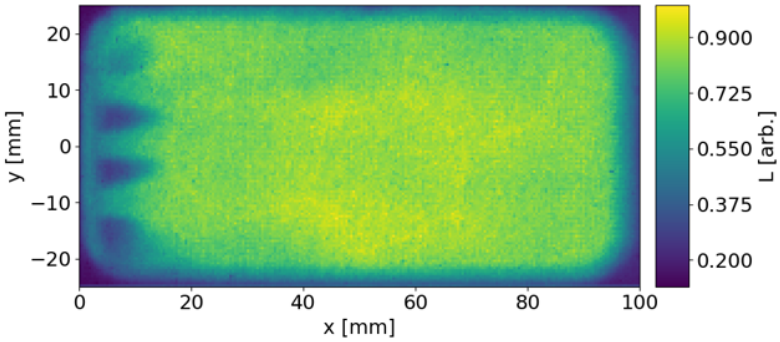

(a) Experimental image

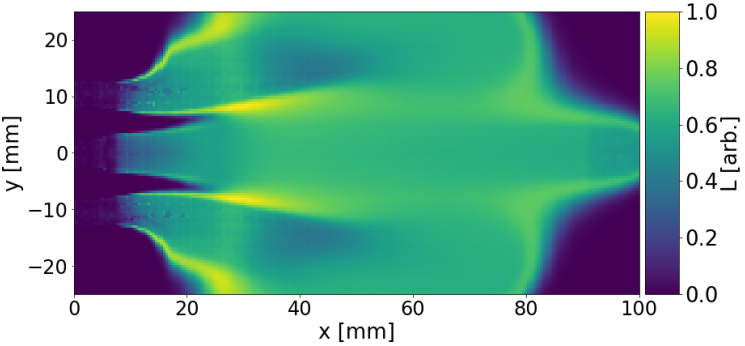

(b) New solution

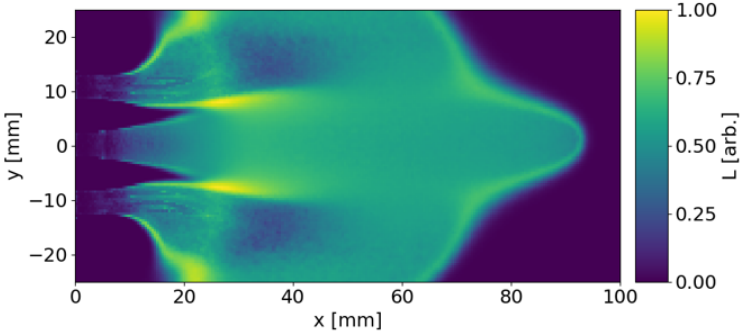

(c) Previous simulation

Figure 7.8: Comparison of experimental data and the application of SMART on the new solution and previous simulation by Beinke [15].

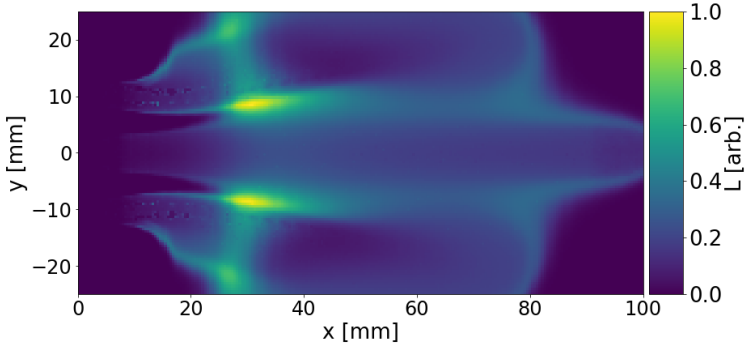

(a) 1D integrated

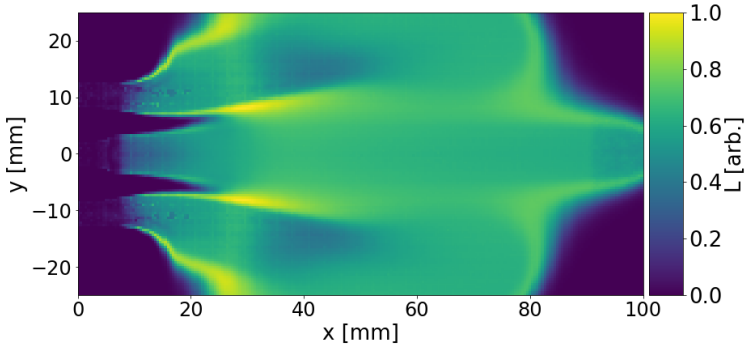

(b) Fully ray traced

Figure 7.9: Comparison of the 1D integrated radiance and the SMART image.

7.2.2 Acoustic analysis

The results of the CFD solution described in Section 7.2.1 are used to conduct an acoustic analysis to evaluate the eigenmodes and eigenfrequencies of BKH for the described operating point. The main purpose is to develop a numerical approach which allows to use the frequencies of the correspondent modes to setup the transient simulation, without using the experimental data, in order to develop a predictive tool to study the transient regime of the combustor when subject to excitation. Here, a combined approach using CFD results and the Linearized Navier-Stokes (LNS) solver of the COMSOL Multiphysics commercial software is used.
The steps described here are the first approach using the LNS solver. Several tries were done in the past with the LEE solver of COMSOL, experiencing however several numerical stability problems which are now overcome with the use of LNS. This is also a step forward with respect to the previously used Helmholtz solver, which assumed a certain number of simplifications. First of all, the Helmholtz solver does not take into account the mean background flow, which is instead present in the analysis with the LNS solver. This implies that the divergent section of the main nozzle had to be replaced with a proper impedance boundary condition and the flow through the main nozzle had to be described in a simplified manner. Moreover, the LNS solver takes into account also variables which are important when dealing with combustion chambers such as dynamic viscosity, thermal conductivity and specific heat at constant pressure.
This study is performed at first by averaging the results of the CFD solutions at given cross-sections. In zones where higher gradients are present, the number of cross-section taken into account for the analysis is higher than in the zones where little gradients are observed. In this way, a 1D variation of the cross-sectional averaged quantities is obtained. This approach has been followed because it is relatively unexpensive compared with a full 3D simulation in terms of computational costs and can be easily used also for full scale industrial engines. The solution field was sliced at relevant parametric locations in order to obtain a 1D variation of radially-averaged quantities, taking into account the configuration of the thermodynamic field. Depending on the axial gradients of the field, different slicing refinement regions were taken into account. To identify the flame zone, OH mass fraction was considered as a marker. A spacing of 1 mm was the considered in the flame zone, 5 mm in the remaining volume of the chamber and 3 mm in the main nozzle region. Where strong gradients are presents, further refinement regions were considered. Figure 7.10 shows the speed of sound distribution at the centerplane together with the regions where further refinement of the slicing was needed.
The next step was to extract area-averaged quantities from the CFD data. This was made by using the IntegrateVariables filter in Paraview, which returns the integrated variables and the area of the slices. Dividing the integrated variables by the area of the slices, area-averaged values are then obtained. Note that the dynamic viscosity, thermal conductivity, and specific heat at constant pressure were not explicitly computed by the CFD, but still required as input for the

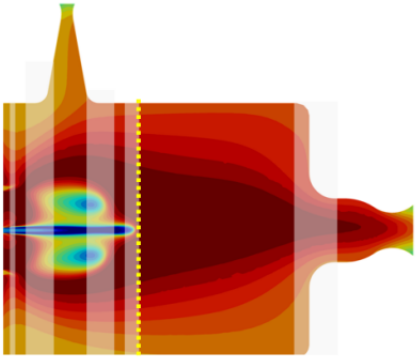

Figure 7.10: Speed of sound distribution at the centerplane. The regions with further refinement are highlighted.

material in COMSOL. The latter was then retrieved by taking their mass fraction average quantities based on the mass fractions computed by the CFD for the O, O_2, H_2O, H_2 and H species. Figure 7.11 shows the variation of the species calculated with Python's thermolibrary.

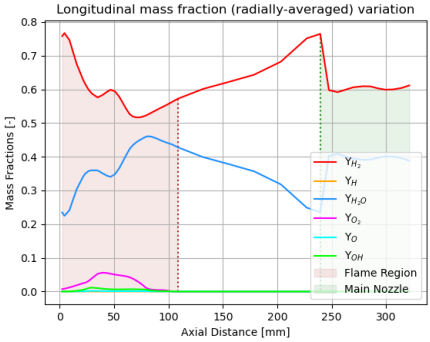

Figure 7.11: Variation of the mass fractions of the species along the domain.

Figure 7.12 shows the radial average of the relevant variables needed as an input for the LNS analysis. In particular, for the background flow are pressure, temperature and velocity and for the fluid properties density, dynamic viscosity, bulk viscosity, thermal conductivity, specific heat at constant pressure, speed of sound and specific heat ratio are needed.
The domain used for the acoustic simulation is simplified with respect to the CFD solution. Only the chamber volume is considered, cutting the injectors up to the

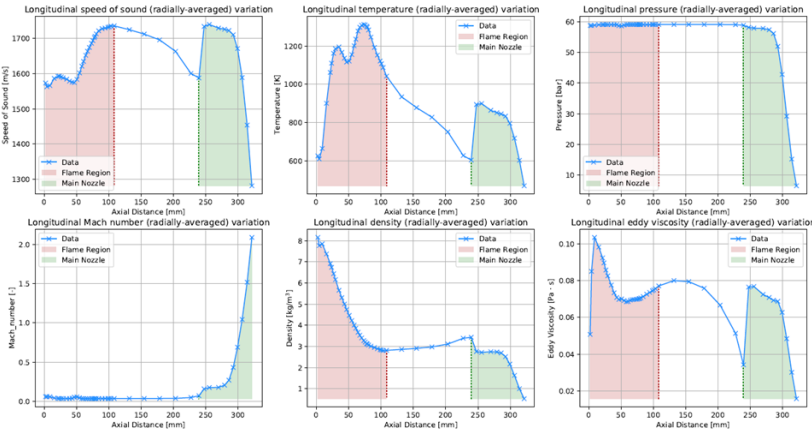

Figure 7.12: Radial average of the needed properties.

injection plane. Figure 7.13 shows the geometry and mesh used for the acoustic simulation. The mesh consists of 227.5k nodes, considerably less than the ∼25 Mio nodes of the CFD simulation.

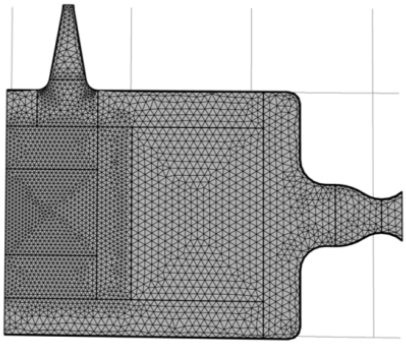

Figure 7.13: Domain and mesh used in the acoustic solver.

The injection plane and the nozzles are represented as hard wall boundary, namely acoustically closed boundary conditions. Since the radial-average method employed does not account for off-longitudinal-axis variations of the fluid properties, interpolating the various averages of the slices does provide any information about the flow in the secondary nozzle. Thus, since via this employed method no sonic throat is automatically achieved, the secondary nozzle was truncated at its throat.

The results of the acoustic simulation are shown in Figure 7.14 and summarized in Table 7.3. The values of the experimental data are given by Hardi [86].
Beinke [15] also conducted an acoustic analysis of the CFD results of his simulation using the COMSOL Helmholtz solver. The boundaries of the domain were all treated as sound hard walls and since the main and secondary nozzle are chocked, also for them a hard wall treatment could be used. The injectors were described with a real impedances, representing a partially reflecting boundary condition obtained from density and speed of sound value at the inlet of each injector. Table 7.4 summarizes the results.

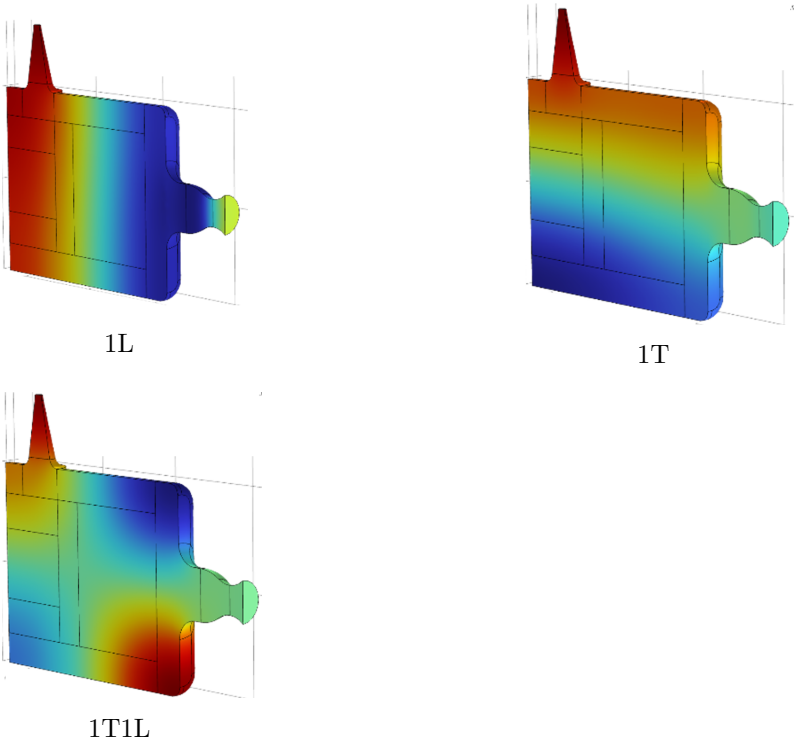

Figure 7.14: Mode shapes

Comparing the results of Table 7.3 and Table 7.4, a slightly better agreement with the experimental data can be observed for the Helmholtz solver for the 1T and 1L mode. Differences in the setup of the simulation have anyway to be considered. The Helmholtz solver does not consider a background flow in the domain, so that the velocity field is not given as an input of the simulation. Here, an impedance condition at the injection was considered whereas in the LNS solver this simplification was not introduced.

Mode	Calculated frequency LNS (Hz)	Experimental freqeuncy (Hz)	Error (%)
1L	3558.5	3250	8.7
1T	4076.3	4350	6.2
1T1L	5494.0	5450	0.8

Table 7.3: Results of the acoustic analysis LNS

Mode	Calculated frequency Helmholtz (Hz)	Experimental freqeuncy (Hz)	Error (%)
1L	3272	3250	0.7
1T	4433	4350	2.1
1T1L	5318	5450	2.4

Table 7.4: Results of the acoustic analysis Helmholtz by Beinke [15]

Considering the number of simplifications introduced in the model, the LNS solver gives frequencies which are higher than the experimental data but still with reasonable values. The effects of the sonic throat in the secondary nozzle were not taken into account due to the radial average interpolation used for this simplified approach. The solver could not determine directly the acoustic boundary condition at the throat and so the ideal close condition was used, determining already a source of discrepancy the modelling BKH. The effect of the closed boundary condition can be investigated when imposing an impedance boundary condition at the exit of the secondary nozzle derived from density and speed of sound values of the CFD solution. Figure 7.15 shows that the use of the characteristic impedance pushes the antinode slightly lower into the convergent part of the secondary nozzle and this in turn reflects on the effective height of the chamber where the acoustic wave is free to oscillate. The frequency of the 1T mode then raises to 4124.5 Hz, reducing the error to 5.2%.
The other aspect which can have an influence on the results is the fact that the injection part was cut for the analysis. This has an impact in particular on the estimation of the 1L mode frequency. Hardi [86] showed in the experiments that the longitudinal modes travel also in the injection elements and the presence of the injectors' posts play an important role when determining the resonant frequencies of the chamber. Another source of error could come from the averaging method used to determine the radial average profiles, which affects the accuracy of the calculation of the longitudinal modes.
On the other hand, the T1L1 mode is predicted with very high accuracy. Looking at the shape of the mode, it is only confined at the corners of the chamber and it is the one least affected by changes in nozzle boundary conditions.

7.3 Summary

A simulation of the steady state field of the BKH combustor was performed. A different approach was used from previous simulations. The most important

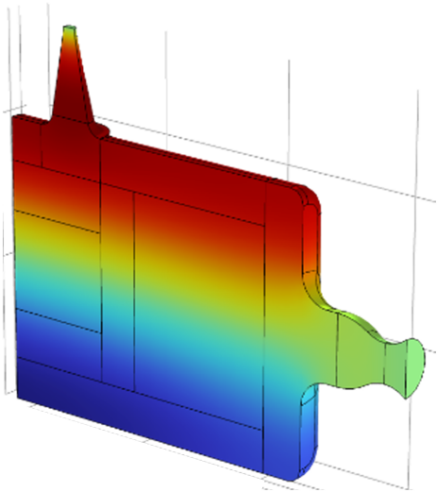

Figure 7.15: 1T mode with impedance boundary condition at the secondary nozzle.

differences are in the geometry and mesh and in the setup of the diffusion terms of the simulation and the Prandtl number. Here, the geometry is full 3D with the LOx injector length considered until the throttle section and the mesh is hybrid, with a structured block capturing the flame zone.
The main difference with the previous setup is in the LOx core length. The LOx core results to be longer than in the previous simulations, reaching almost the end of the window. Also the OH mass fraction and temperature distribution result to be different, having an impact on the simulated total radiance emitted by the flame when applying the SMART tool on the CFD solution. The results are now in better agreement with the experimental data, not reaching anyway the full area of the window. This can be due to the fact that chemiluminesence is not taken into account by SMART, since the OH* should be calculated at runtime by a dedicated chemistry model to cover also the zones where chemical excitation dominates over thermal excitation, namely where the temperature is below 2700 K.
Then, an acoustic analysis of the solution was performed to calculate the eigenfrequencies of the main resonant modes of the chamber. The acoustic module of the commercial software COMSOL Multiphysics was employed using a LNS solver. The LNS solver allows to take into account several physical values which could be not considered when employing the Helmholtz solver as in previous work. The main difference is that the background flow is now included in the simulation, as well as other important quantities describing the fluid as density, dynamic viscosity, bulk viscosity, thermal conductivity, specific heat at constant pressure, speed of sound and specific heat ratio. It was chosen to first conduct the analysis

in a simple and relatively computationally unexpensive way, considering the 1D radial average of the variables of interest and cutting the injectors up to the injection plane. The results of the simulation in terms of eigenfrequencies show a higher discrepancy than the previous Helmholtz results. This is due to the simplifications introduced in the setup. The analysis of the boundary condition at the secondary nozzle showed an improvement in the calculation of the 1T mode when using an impedance boundary condition rather than a sound hard wall. This is a first step towards a more complete analysis where the results of the CFD simulation will be interpolated directly onto the acoustic solver mesh, but it was needed since in the past several numerical stability problems were encountered when using the LEE solver. This demonstrates the fact that the LNS approach can be used to have an estimation of the main resonant modes of the chamber, leading towards a full numerical approach in the calculation of the resonant frequencies. The frequencies of the main resonant modes could then be used to impose the excitation frequency of the unsteady simulation, without using the experimental data and going towards a predictive tool for the investigation of high frequency combustion instabilities.

8 Conclusions and Outlook

The investigation of high frequency combustion instabilities in a rocket combustion chamber is fundamental for liquid propellant rocket engines, since they are the most dangerous and can lead to the failure not only of the engine, but of the entire mission. The flame response to combustion instabilities is one of the most important aspects for their prediction. Knowing the flame response can help avoiding the onset of the instabilities.
The BKH is an experimental combustor with operating conditions which are representative of an upper stage engine. It features five shear coaxial injectors fed with liquid oxygen and hydrogen, both gaseous or liquid and a secondary nozzle which is opened and closed by a toothed wheel. The toothed wheel periodically interrupts the flow through the nozzle, producing the acoustic perturbation which in turn acts on the flame dynamics. This work analysed experimental data and compared them with the numerical results in order to develop a numerical modelling methodology to investigate the flame dynamics and combustion instabilities.
A first analysis was made to identify the flame response to the 1L mode excitation under a matrix of test cases, from off-resonance conditions to the injector resonance and finally chamber resonance, at different amplitudes and different frequencies for a single injector configuration. The in-house DLR TAU code was used for all the CFD simulations run in this work with real-gas modelling capability. The results were compared both with experimental data and previous numerical simulations.
Here, the modelling of the acoustic disturbance was improved with the respect to previous work, not using a uniform pressure disturbance but a disturbance which varies along the axis and takes into account the coupling with the acoustic velocity. The results showed a shorter flame with respect to previous simulations for all the matrix of excitation conditions, showing that more realistic excitation conditions give different results both in terms of the length of the flame and in the pressure distribution along the axis of the configuration.
However, spurious pressure oscillations were visible along the axis. Heat release rate is a key quantity when investigating combustion instabilities. The accurate evaluation of the heat release rate becomes crucial. Removing the axisymmetric boundary condition allowed to remove the spurious pressure oscillations along the symmetry axis for the longitudinal excitation and symmetry plane for the transverse excitation and led to a higher amplitude of the heat release rate oscillations, showing that care should be taken when setting up a simulation.
The second part of this thesis was focused on the implementation of a realistic boundary condition which could represent the passage of the toothed wheel on the secondary nozzle exit plane. The investigation was conducted using a rather simple model of BKH using a cold flow test as a benchmark to investigate the

response to the 1T mode excitation. Here, since no combustion occurs, an axisymmetric domain could be used simplifying also the geometry of the injection elements. A dummy injector was used, with an equivalent hydrogen mass flow which included all the present injection elements, from the main injectors to the window cooling. The results of the simulation were then compared with previous numerical simulations which used a simple open-closed boundary condition to trigger the excitation and with experimental data. It was observed that the frequency of the excitation produced by the siren boundary condition matched the experimental data. The amplitude of the signal was slightly over estimated but the shape was well recovered, including capturing accurately also the overtones of the signal. This demonstrated that the new boundary condition implemented in the code works and can be used also for other transient simulations.
The next part of the thesis addressed the development of a tool which can allow the comparison of optical data recorded from high-speed cameras and CFD results. This tool is called SMART (Spectral Modelling and Ray-Tracing algorithm). It is used in a post-processing step and it allows to estimate the OH* thermal radiation from the OH mass fraction calculated in the CFD simulation. The SMART algorithm takes into account both self-absorption and refraction and it allows to have a comparison including key physical features of the radiation. The algorithm was first run on a previous RANS simulation for validation purposes. When comparing the results of OH* radiation with experimental data, it is clearly visible that SMART better matches the experimental data in terms of radiation emitted from OH*. Although the results are qualitatively comparable with the experimental data, a satisfying quantitative comparison is still not reached. This can be due to the fact that chemiluminescence is not taken into account and in the zones with a temperature lower than 2700 K, chemiluminescence overcomes thermal excitation.
The last part of this work is focused on a RANS simulation of BKH changing the geometry, mesh an boundary conditions with respect to previous works, applying the SMART algorithm to the steady state solution and investigating the acoustic behavior of the chamber with a LNS acoustic solver.
The results were compared with experimental data and previous simulations. A better agreement with experiments in terms of LOx core length with respect to previous work was found in the steady-state solution. This can be due to the different mesh used, where the flame region is contained in a structured block. The use of the hybrid mesh leads to both accurate solutions and better convergence for the numerical solution methods. Also when applying SMART, the results of the OH* radiance now almost fill the whole window, leading to a better agreement with experimental results. This is due to the fact that the flame is now longer and so thermally excited OH* calculated from OH extend further downstream.
The acoustic analysis was conducted using the acoustic module of the commercial software COMSOL Multiphysics employing the LNS solver. This is a step forward with respect to the use of the Helmholtz solver, which does not take into account a mean background flow and requires impedance boundary condition to describe the behavior of the nozzles. Here, a simplified approach was used to identify the main

resonant modes of the chamber. 1D radially averaged quantities were extracted from the CFD simulations and interpolated on a simpler domain to be imported in COMSOL. The results are comparable with the experimental data, although a discrepancy is still present. This can be due to the interpolation method but also to the fact that the injectors for the acoustic simulation where cut up to the injection plane, leading to a higher discrepancy for the 1L mode frequency values due to the fact that the reduction of the length of the domain implies that the acoustic waves have less space to travel.
Future work should address improving the acoustic analysis by importing CFD results directly in the acoustic solver and overcoming the limitations of the interpolation. This will lead to higher computational costs but it expected to produce results which are more accurate and can be used to setup an unsteady simulation of BKH. The simulation of the 1T mode excitation of BKH under representative operating conditions with siren excitation is the next step which should be done, together with a previous acoustic analysis of the full chamber to impose the frequency of the excitation directly from the numerical simulations.
A further development of SMART should take into account chemiluminescence and be extended to calculate the spectra of CH* in order to be able to use the algorithm also for LOx/methane flames not only in BKH but also for other combustion chambers with different geometries.

Appendix

Application of SMART to a LES simulation

The SMART algorithm is a flexible tool and with small modifications of some code lines can be applied to different simulations.
Here the results of the application of SMART to a LES simulation of BKH. The format of the output files is different from the TAU files, but the algorithm can still be applied modifying the format of the input files required.

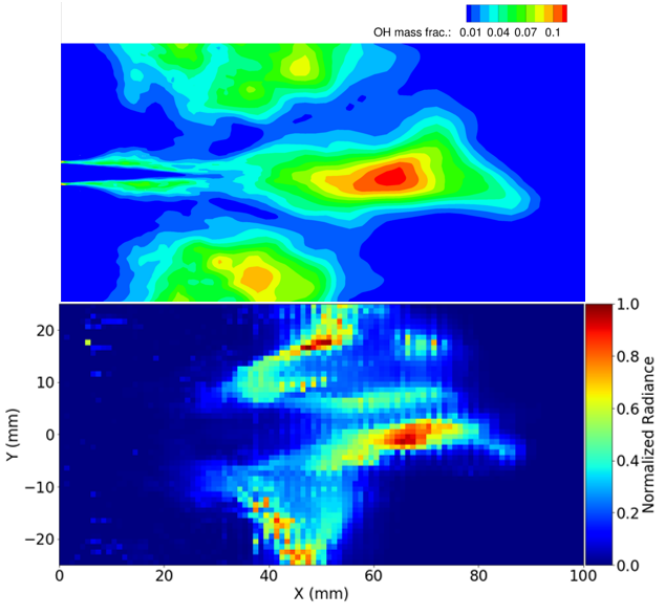

Comparison of the OH mass fraction distribution in the window region of the LES simulation and the application of SMART in the same area.

Application of SMART to BKD

In order to apply the SMART algorithm to the REST HF-9 Test case, which is BKD, it was necessary to model the optical probe which detected the OH* radiation emitted from the flame.

The view angle of the probe is determined by the rays that reach the circular boundary of the fiber-optics face. The probe is approximated to an observation cone with a vertex representing a sink for radiation, indicated with B. The probe surface is assumed to be non-reflective. The total radiation reaching the probe is then obtained by:

$$\phi(B) = \int_0^\infty \int_\Omega \tau_{\nu,OH} I_\nu(B, \vec{u}) \left| \vec{u} \cdot \vec{n_B} \right| d\Omega d\nu$$

where τ_ν, $\vec{u}$, $\vec{n_B}$ and Ω are the probe's transmissivity function of the wavenumber ν, the radiation direction vector, the normal unit vector of the surface at point B (considered as the probe's pointing vector) and the solid angle given by the observation cone, respectively. I_ν represents the integrated total radiance.

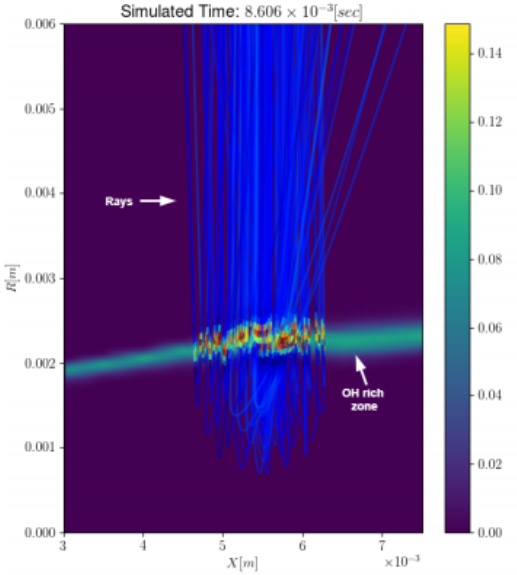

(a) α=0

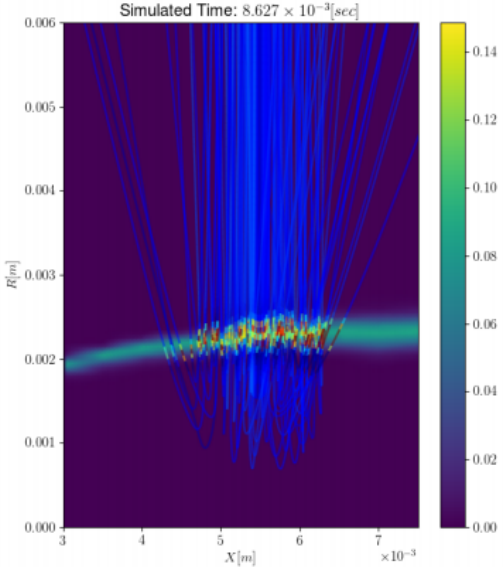

(b) α=π/2

OH mass fraction distribution and ray paths at different phase angles of the cycle

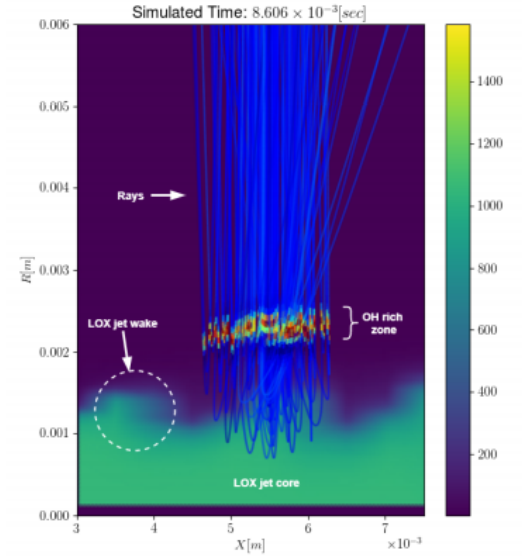

(a) α=0

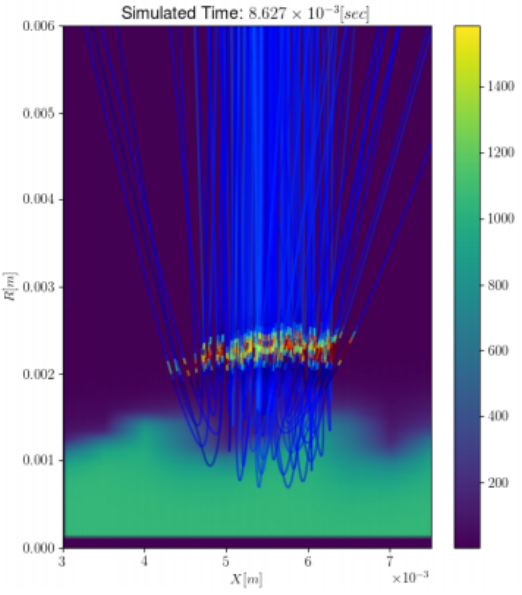

(b) α=π/2

Density distribution and ray paths at different phase angles of the cycle

List of Publications

Journal Articles

- J.S. Hardi, T. Traudt, C. Bombardieri, M. Börner, S.K. Beinke, W. Armbruster, N. Blanco, F. Tonti, D. Suslov, B. Dally, M. Oschwald **Combustion dynamics in cryogenic rocket engines: Research programme at DLR Lampoldshausen**. – *Acta Astronautica, Vol. 147, pp. 251-258, 2018*
- F. Tonti, J. Perovšek, J.Z. Usandivaras, S. Karl, J. Hardi, Y. Morii, M. Oschwald **Obtaining pseudo-OH* radiation images from CFD solutions of transcritical flames** – *Combustion and Flame, Vol. 233, 111614*

Conference Papers

- F.Tonti, S. Karl, S. Beinke, J. Hardi, M. Oschwald **Numerical Modelling of Acoustic Excitation of High Frequency Combustion Instabilities in an Experimental Combustor**. – *Space Propulsion Conference*, May 14-18, 2018, Sevilla, Spain
- F. Tonti, J.S. Hardi, S. Karl, M. Oschwald **, Unsteady Modeling of LOX/GH2 Flame Response to Longitudinal Chamber Mode Forcing**. – *Joint Propulsion Conference, AIAA Propulsion and Energy Forum*, 2018, Cincinnati, OH
- F. Tonti, J. Hardi, T. Horchler, S. Fechter, M. Oschwald **Influence of numerical model setup on the response of acoustically forced LOX/H2 flames**. – *8th European Conference for Aeronautics and Space Sciences, (EUCASS)*, July 1-4, 2019, Madrid, Spain
- F. Tonti, L. Trotta, J. Hardi, M. Oschwald **Acoustic characterization of an experimental combustor using a combined approach with RANS simulation and an acoustic LNS solver**. – *2nd International Conference on Flight Vehicles, Aerothermodynamics and Re-entry missions & Engineering*, June 19-23, 2022, Heilbronn, Germany.
- F. Tonti, J. Zapata Usandivaras, J. Perovšek, S.Karl, J.Hardi, M.Oschwald **REST HF-9 Test Case: Numerical reproduction of OH* radiation measurements of unsteady supercritical LOx/H2 combustion**. – *9th European Conference for Aeronautics and Space Sciences (EUCASS)*, June 27- July 1, 2022, Lille, France

Bibliography

[1] G. Alfonsi. Reynolds-Averaged Navier-Stokes Equations for Turbulence Modeling. *Applied Mechanics Reviews - APPL MECH REV*, 62, 2009. doi: 10.1115/1.3124648.

[2] S. Allmaras, F. Johnson, and P. Spalart. Modifications and clarifications for the implementation of the Spalart-Allmaras turbulence model. *Seventh International Conference on Computational Fluid Dynamics (ICCFD7)*, pp. 1–11, 2012.

[3] A. Andreini, B. Facchini, A. Giusti, and F. Turrini. Assessment of Flame Transfer Function Formulations for the Thermoacoustic Analysis of Lean Burn Aero-engine Combustors. *Energy Procedia*, 45, pp. 1422–1431, 2014. doi: 10.1016/j.egypro.2014.01.149.

[4] W. Armbruster, J. Hardi, and M. Oschwald. Impact of shear-coaxial injector hydrodynamics on high-frequency combustion instabilities in a representative cryogenic rocket engine. *International Journal of Spray and Combustion Dynamics*, 14, 2022. doi: 10.1177/17568277221093848.

[5] W. Armbruster, J. S. Hardi, Y. Miene, D. Suslov, et al. Damping device to reduce the risk of injection-coupled combustion instabilities in liquid propellant rocket engines. *Acta Astronautica*, 169, pp. 170–179, 2020. issn: 0094-5765. doi: https://doi.org/10.1016/j.actaastro.2019.11.040.

[6] W. Armbruster, J. S. Hardi, and M. Oschwald. Flame-acoustic response measurements in a high-pressure, 42-injector, cryogenic rocket thrust chamber. *Proceedings of the Combustion Institute*, 38(4), pp. 5963–5970, 2021. issn: 1540-7489. doi: https://doi.org/10.1016/j.proci.2020.05.020.

[7] W. Armbruster, J. S. Hardi, D. Suslov, and M. Oschwald. Injector-Driven Flame Dynamics in a High-Pressure Multi-Element Oxygen–Hydrogen Rocket Thrust Chamber. *Journal of Propulsion and Power*, 35(3), pp. 632–644, 2019. doi: 10.2514/1.B37406.

[8] D. Banuti and K. Hannemann. The absence of a dense potential core in supercritical injection: A thermal break-up mechanism. *Phys. Fluids*, 28(035103), 2016.

[9] D. Banuti, M. Raju, P. Ma, M. Ihme, et al. Seven questions about supercritical fluids - towards a new fluid state diagram. In: *55th AIAA Aerospace Sciences Meeting*. Jan. 2017. doi: 10.2514/6.2017-1106.

[10] D. T. Banuti, P. C. Ma, J.-P. Hickey, and M. Ihme. Thermodynamic structure of supercritical LOX–GH2 diffusion flames. *Combustion and Flame*, 196, pp. 364–376, 2018. doi: https://doi.org/10.1016/j.combustflame.2018.06.016.

[11] A. Bayliss and E. Turkel. Far field boundary conditions for compressible flows. *Journal of Computational Physics*, 48(2), pp. 182–199, 1982. issn: 0021-9991. doi: https://doi.org/10.1016/0021-9991(82)90046-8.

[12] M. J. Bedard, T. L. Fuller, S. Sardeshmukh, and W. E. Anderson. Chemiluminescence as a diagnostic in studying combustion instability in a practical combustor. *Combustion and Flame*, 213, pp. 211–225, 2020. doi: https://doi.org/10.1016/j.combustflame.2019.11.039.

[13] S. Beinke, J. Hardi, M. Oschwald, and B. Dally. Modelling Acoustic Excitation of High Frequency Combustion Instability Experiments. In: *5th European Conference for Aeronautics and Space Sciences EUCASS 2013*. Jan. 2013. isbn: 978-84-941531-0-5.

[14] S. Beinke, M. Oschwald, and B. Dally. Modelling Acoustic Excitation for the Simulation of Combustion Instability Experiments. In: *18th Australasian Fluid Mechanics Conference*. Jan. 2012.

[15] S. K. Beinke. *Analysis of flame response to acoustic forcing in a rocket combustor*. PhD thesis, University of Adelaide, Australia, 2017.

[16] S. K. Beinke, J. S. Hardi, D. T. Banuti, S. Karl, et al. Experimental and numerical study of transcritical oxygen-hydrogen rocket flame response to transverse acoustic excitation. *Proceedings of the Combustion Institute*, 38(4), pp. 5979–5986, 2021. doi: https://doi.org/10.1016/j.proci.2020.05.027.

[17] W. A. Bell, B. R. Daniel, and B. T. Zinn. Experimental and theoretical determination of the admittances of a family of nozzles subjected to axial instabilities. *Journal of Sound and Vibration*, 30, pp. 179–190, 1973.

[18] J. Bellan. Theory,modeling and analysis of turbulent supercritical mixing. *Combustion Science and Technology*, 178(1-3), pp. 253–281, 2006. doi: 10.1080/00102200500292241.

[19] A. Bigongiari and M. Heckl. Analysis of the interaction of thermoacoustic modes with a Green's function approach. *International Journal of Spray and Combustion Dynamics*, 10, pp. 326–336, 2018. doi: 10.1177/1756827718809570.

[20] M. Born and E. Wolf. *Principles of Optics: Electromagnetic Theory of Propagation, Interference and Diffraction of Light (7th Edition)*. 7th. Cambridge University Press, 1999. Chap. 4.

[21] F. Boudy, T. Schuller, D. Durox, and S. Candel. The Flame Describing Function (FDF) unified framework for combustion instability analysis: progress and limitations. *Int.I Summer School and Workshop on Non-Normal and NonlinearEffects in Aero- and Thermoacoustics*, 2013.

[22] J. Boussinesq. *Théorie de l'écoulement tourbillonnant et tumultueux des liquides dans les lits rectilignes a grande section*. Gauthier-Villars et fils, 1897.

[23] K. Bray. The interaction between turbulence and combustion. *Symposium (International) on Combustion*, 17(1), Seventeenth Symposium (International) on Combustion, pp. 223–233, 1979. doi: https://doi.org/10.1016/S0082-0784(79)80024-7.

[24] V. S. Burnley and F. E. C. Culick. Influence of Random Excitations on Acoustic Instabilities in Combustion Chambers. *AIAA Journal*, 38(8), pp. 1403–1410, 2000. doi: 10.2514/2.1116.

[25] M. C. Burrows. Radiation processes related to oxygen-hydrogen combustion at high pressures. *Symposium (International) on Combustion*, 10(1), Tenth Symposium (International) on Combustion, pp. 207–215, 1965. doi: https://doi.org/10.1016/S0082-0784(65)80165-5.

[26] S. Candel, D. Durox, S. Ducruix, A.-L. Birbaud, et al. Flame Dynamics and Combustion Noise: Progress and Challenges. *International Journal of Aeroacoustics*, 8(1), pp. 1–56, 2009. doi: 10.1260/147547209786234984.

[27] S. Candel, M. Juniper, G. Singla, P. Scouflaire, et al. Structure and dynamics of cryogenic flames at supercritical pressure. *Combustion Science and Technology*, 178, pp. 161–192, 2006. doi: 10.1080/00102200500292530.

[28] S. Candel, D. Durox, and T. Schuller. "Flame Interactions as a Source of Noise and Combustion Instabilities". In: *10th AIAA/CEAS Aeroacoustics Conference*. 2004. doi: 10.2514/6.2004-2928.

[29] J. Casimir J. *An analytical study of the hydrogen-air reaction mechanism with application to scramjet combustion*. Tech. rep. NASA Langley Research Center Hampton, VA, United States, 1988.

[30] B. Chehroudi and D. Talley. Interaction of acoustic waves with a cryogenic nitrogen jet at sub- and supercritical pressures. In: *40th AIAA Aerospace Sciences Meeting & Exhibit*. doi: 10.2514/6.2002-342.

[31] B. Chehroudi, D. Davis, and D. Talley. *Initial Results from a Cryogenic Coaxial Injector in an Acoustic Field*. Tech. rep. Jan. 2002, p. 9.

[32] B. Chehroudi, D. Talley, W. Mayer, R. Branam, et al. Understanding Injection Into High Pressure Supercritical Environments. P. 37, 2003.

[33] B.-T. Chu. On the Generazion of Pressure Waves at a Plane Flame Front. In: *4th International Symposium on Combustion*. 1952.

[34] B.-T. Chu. *Mechanism of Generation of Pressure Waves at Flame Fronts*. Tech. rep. National Advisory Comittee for Aeronautics, The John Hopkins University, 1956.

[35] T. H. Chung, M. Ajlan, L. L. Lee, and K. E. Starling. Generalized multiparameter correlation for nonpolar and polar fluid transport properties. *Industrial & Engineering Chemistry Research*, 27, pp. 671–679, 1988.

[36] B. Ćosić, J. P. Moeck, and C. O. Paschereit. Prediction of Pressure Amplitudes of Self-Excited Thermoacoustic Instabilities for a Partially Premixed Swirl-Flame. In: vol. Volume 1A: Combustion, Fuels and Emissions. Turbo Expo: Power for Land, Sea, and Air. June 2013. doi: 10.1115/GT2013-94160.

[37] L. CROCCO. Aspects of Combustion Stability in Liquid Propellant Rocket Motors Part I: Fundamentals. Low Frequency Instability With Monopropellants. *Journal of the American Rocket Society*, 21(6), pp. 163–178, 1951. doi: 10.2514/8.4393.

[38] B. Cuenot and T. Schmitt. Large Eddy Simulation of transcritical and supercriticalflows. In: *ERCOFTAC Bulletin 124*. 2020.

[39] F. E. Culick. *Unsteady Motions in Combustion Chambers for Propulsion Systems*. NATO Research and Technology Organization., 2006.

[40] R. N. Dahms and J. C. Oefelein. Atomization and Dense-Fluid Breakup Regimes in Liquid Rocket Engines. *Journal of Propulsion and Power*, 31(5), pp. 1221–1231, 2015.

[41] R. N. U. Dahms. Progress toward a turbulence-chemistry interaction model for multi-zone techniques. In: *Conference: Proposed for presentation at the Advanced Engine Combustion Review Meeting held January 31 - February 1, 2019 in Knoxville, TN*. 2019.

[42] D. Davis, B. Chehroudi, and I. Sorenson. "Measurements in an Acoustically Driven Coaxial Jet Under Supercritical Conditions". In: *43rd AIAA Aerospace Sciences Meeting and Exhibit*. Reno, 2005. doi: 10.2514/6.2005-736.

[43] D. W. Davis and B. Chehroudi. Measurements in an Acoustically Driven Coaxial Jet under Sub-, Near-, and Supercritical Conditions. *Journal of Propulsion and Power*, 23(2), pp. 364–374, 2007. doi: 10.2514/1.19340.

[44] N. Doan and N. Swaminathan. Analysis of Markers for Combustion Mode and Heat Release in MILD Combustion Using DNS Data. *Combustion Science and Technology*, 191(5-6), pp. 1059–1078, 2019. doi: 10.1080/00102202.2019.1610746.

[45] J. R. Dormand and P. J. Prince. A family of embedded Runge-Kutta formulae. *Journal of computational and applied mathematics*, 6(1), pp. 19–26, 1980.

[46] F. Duchaine, F. Boudy, D. Durox, and T. Poinsot. Sensitivity analysis of transfer functions of laminar flames. *Combustion and Flame*, 158, pp. 2384–2394, 2011. doi: 10.1016/j.combustflame.2011.05.013.

[47] M. Dumbser, U. Iben, and C.-D. Munz. Efficient implementation of high order unstructured WENO schemes for cavitating flows. *Computers Fluids*, 86, pp. 141–168, 2013. doi: 10.1016/j.compfluid.2013.07.011.

[48] C. Engelbert, Y. Hardalupas, J. H. Whitelaw, and B. E. Launder. Breakup phenomena in coaxial airblast atomizers. *Proceedings of the Royal Society of London. Series A: Mathematical and Physical Sciences*, 451(1941), pp. 189–229, 1995. doi: 10.1098/rspa.1995.0123.

[49] H. Eroglu and N. Chigier. WAVE CHARACTERISTICS OF LIQUID JETS FROM AIRBLAST COAXIAL ATOMIZERS. *Atomization and Sprays*, 1(4), pp. 349–366, 1991. issn: 1044-5110.

[50] F.E.C.Culick and V.Yang. "Overview of Combustion Instabilities in Liquid-Propellant Rocket Engines". In: Liquid Rocket Engine Combustion Instability, 1995, pp. 3–37.

[51] F.Tonti. *Studio dei fenomeni aero-acustici nei propulsori a propellente solido*. MA thesis, Università degli studi di Roma "La Sapienza", 2016.

[52] Z. Farago and N. Chigier. Morphological Classification of Disintegration of Round Liquid Jets in a Coaxial Air Stream. *"Atomization and Sprays"*, 2, 1992. doi: 10.1615/AtomizSpr.v2.i2.50.

[53] S. Farhat, W. Ng, and Y. Zhang. Chemiluminescent emission measurement of a diffusion flame jet in a loudspeaker induced standing wave. *Fuel*, 84(14), pp. 1760–1767, 2005. issn: 0016-2361. doi: https://doi.org/10.1016/j.fuel.2005.03.020.

[54] N. Fdida, J. S. Hardi, H. Kawashima, B. D. I. Knapp, et al. Flame response to high-frequency oscillations in a cryogenic oxygen/hydrogen rocket combustor. *Progress in Propulsion Physics Volume 11*, 2019.

[55] S. Fechter, S. Karl, V. Hannemann, and K. Hannemann. "Simulation of LOx/GH2 single coaxial injector at high pressure conditions". In: *53rd AIAA/SAE/ASEE Joint Propulsion Conference*. 2017. doi: 10.2514/6.2017-4765.

[56] T. Fiala. *Radiation from high pressure hydrogen-oxygen flames and its use in assessing rocket combustion instability*. PhD thesis, Technische Universität München, 2015.

[57] T. Fiala and T. Sattelmayer. Assessment of existing and new modeling strategies for the simulation of OH* radiation in high-temperature flames. *CEAS Space Journal*, 8(1), pp. 47–58, 2016. doi: 10.1007/s12567-015-0107-z.

[58] T. Fiala, T. Sattelmayer, S. Gröning, J. Hardi, et al. Comparison Between Excited Hydroxyl Radical and Blue Radiation from Hydrogen Rocket Combustion. *J. Propuls. Power*, 33(2), pp. 490–500, 2017. doi: 10.2514/1.B36280.

[59] E. Freitag, H. Konle, M. Lauer, C. Hirsch, et al. *Pressure Influence on the Flame Transfer Function of a Premixed Swirling Flame*. May 2006. doi: 10.1115/GT2006-90540.

[60] E. Freitag. *On the Measurement and Modelling of Flame Transfer Functions at Elevated Pressure*. PhD thesis, Technische Universität München, 2009.

[61] M. Frezzotti, S. D'Alessandro, B. Favini, and F. Nasuti. Numerical issues in modeling combustion instability by quasi-1D Euler equations. *International Journal of Spray and Combustion Dynamics*, 9, p. 175682771771101, 2017. doi: 10.1177/1756827717711015.

[62] M. Frezzotti, F. Nasuti, C. Huang, C. Merkle, et al. Determination of heat release response function from 2D hybrid RANS-LES data for the CVRC combustor. 2015. doi: 10.2514/6.2015-3841.

[63] P. Gaillard, V. Giovangigli, and L. Matuszewski. A diffuse interface Lox/hydrogen transcritical flame model. *Combustion Theory and Modelling*, 20(3), pp. 486–520, 2016. doi: 10.1080/13647830.2016.1150518.

[64] T. García-Armingol and J. Ballester. Influence of fuel composition on chemiluminescence emission in premixed flames of CH4/CO2/H2/CO blends. *International Journal of Hydrogen Energy*, 39(35), pp. 20255–20265, 2014. issn: 0360-3199. doi: https://doi.org/10.1016/j.ijhydene.2014.10.039.

[65] A. G. Gaydon. *The Spectroscopy of Flames*. Springer, 1974.

[66] T. Gerhold, M. Galle, O. Friedrich, J. Evans, et al. "Calculation of complex three-dimensional configurations employing the DLR-tau-code". In: *35th Aerospace Sciences Meeting and Exhibit*. doi: 10.2514/6.1997-167.

[67] J. H. Gladstone and T. P. Dale. XIV. Researches on the refraction, dispersion, and sensitiveness of liquids. *Philosophical Transactions of the Royal Society of London*, 153, pp. 317–343, 1863. doi: 10.1098/rstl.1863.0014.

[68] F. Goebel, B. Kniesner, M. Frey, O. Knab, et al. Radiative heat transfer analysis in modern rocket combustion chambers. *CEAS Space Journal*, 6, pp. 79–98, 2014.

[69] M. Gonzalez-Flesca, T. Schmitt, S. Ducruix, and S. Candel. Large eddy simulations of a transcritical round jet submitted to transverse acoustic modulation. *Physics of Fluids*, 28(5), p. 055106, 2016. doi: 10.1063/1.4948586.

[70] S. D. Gordon and B. J. Mcbride. Computer program for calculation of complex chemical equilibrium compositions. In: *NASA Reference Publication 1311*. 1996.

[71] S. Gröning, M. Oschwald, and T. Sattelmayer. Einfluss einer Kavität auf das Druckfeld der ersten Tangentialen Mode einer Raketenbrennkammer unter repräsentativen Bedingungen. In: *Deutscher Luf- und Raumfahrt Kongress (DLRK)*. Sept. 2013.

[72] S. Gröning, M. Oschwald, and T. Sattelmayer. Selbst erregte tangentiale Moden in einer Raketenbrennkammer unter repräsentativen Bedingungen. In: *61. Deutscher Luft- und Raumfahrtkongress 2012*. 2012. URL: https://elib.dlr.de/77862/.

[73] S. Gröning, M. Sliphorst, B. Knapp, and M. Oschwald. Acoustic Mode Identification in the CRC. In: *9th REST Scientific Workshop*. Jan. 2010.

[74] S. Gröning, D. Suslov, M. Oschwald, and T. Sattelmayer. Stability Behaviour of a Cylindrical Rocket Engine Combustion Chamber Operated with Liquid Hydrogen and Liquid Oxygen. In: *5th European Conference for Aeronautics and Space Sciences EUCASS 2013*. Jan. 2013. ISBN: 978-84-941531-0-5.

[75] S. Gröning. *Untersuchung selbsterregter Verbrennungsinstabilitäten in einer Raketenbrennkammer*. PhD thesis, RWTH Aachen University, 2017.

[76] S. Gröning. *Untersuchung selbsterregter Verbrennungsinstabilitäten in einer Raketenbrennkammer*. PhD thesis, RWTH Aachen, 2017.

[77] S. Gröning, J. S. Hardi, D. Suslov, and M. Oschwald. Injector-Driven Combustion Instabilities in a Hydrogen/Oxygen Rocket Combustor. *Journal of Propulsion and Power*, 32(3), pp. 560–573, 2016. DOI: 10.2514/1.B35768.

[78] E. Gutmark and C. .-. Ho. Preferred modes and the spreading rates of jets. *Physics of Fluids*, 26(10), pp. 2932–2938, 1983. DOI: 10.1063/1.864058.

[79] L. Haber, U. Vandsburger, W. Saunders, and V. Khanna. An Experimental Examination of the Relationship between Chemiluminescent Light Emissions and Heat-release Rate Under Non-Adiabatic Conditions. P. 8, 2001. DOI: 10.1115/2000-GT-0121.

[80] M. HABIBALLAH, M. ORAIN, F. GRISCH, L. VINGERT, et al. EXPERIMENTAL STUDIES OF HIGH-PRESSURE CRYOGENIC FLAMES ON THE MASCOTTE FACILITY. *Combustion Science and Technology*, 178(1-3), pp. 101–128, 2006. DOI: 10.1080/00102200500294486.

[81] L. Hakim, T. Schmitt, S. Ducruix, and S. Candel. Dynamics of a transcritical coaxial flame under a high-frequency transverse acoustic forcing: Influence of the modulation frequency on the flame response. *Combustion and Flame*, 162, 2015. doi: 10.1016/j.combustflame.2015.05.022.

[82] X. Han, J. Li, and A. S. Morgans. Prediction of combustion instability limit cycle oscillations by combining flame describing function simulations with a thermoacoustic network model. *Combustion and Flame*, 162(10), pp. 3632–3647, 2015. issn: 0010-2180. doi: https://doi.org/10.1016/j.combustflame.2015.06.020.

[83] K. Hanjalić and B. E. Launder. A Reynolds stress model of turbulence and its application to thin shear flows. *Journal of Fluid Mechanics*, 52(4), pp. 609–638, 1972. doi: 10.1017/S002211207200268X.

[84] V. Hannemann. *Numerische Simulation von Stoß-Stoß-Wechselwirkungen unter Berücksichtigung von chemischen und thermischen Nichtgleichgewichtseffekten: 23 Tabellen.* DLR/FB-97/07. DLR, Abt. Operative Planung, 1997. url: https://books.google.de/books?id=j9FhHQAACAAJ.

[85] Y. Hardalupas and M. Orain. Local measurements of the time-dependent heat release rate and equivalence ratio using chemiluminescent emission from a flame. *Combustion and Flame*, 139(3), pp. 188–207, 2004. issn: 0010-2180. doi: https://doi.org/10.1016/j.combustflame.2004.08.003.

[86] J. Hardi. *Experimental investigation of high frequency combustion instability in cryogenic oxygen-hydrogen rocket engines.* PhD thesis, University of Adelaide, 2012.

[87] J. Hardi, M. Oschwald, and B. Dally. Flame response to acoustic excitation in a rectangular rocket combustor with LOx/H2 propellants. *CEAS Space Journal*, Vol. 2, 2011. doi: 10.1007/s12567-011-0020-z.

[88] J. S. Hardi, M. Oschwald, and B. Dally. Acoustic characterisation of a rectangular rocket combustor with liquid oxygen and hydrogen propellants. *Proceedings of the Institution of Mechanical Engineers, Part G: Journal of Aerospace Engineering*, 227(3), pp. 436–446, 2013. doi: 10.1177/0954410012437511.

[89] J. S. Hardi, H. C. G. Martinez, M. Oschwald, and B. B. Dally. LOx Jet Atomization Under Transverse Acoustic Oscillations. *Journal of Propulsion and Power*, 30(2), pp. 337–349, 2014. doi: 10.2514/1.B34979.

[90] J. S. Hardi, W. Zach Hallum, C. Huang, and W. E. Anderson. Approaches for Comparing Numerical Simulation of Combustion Instability and Flame Imaging. *Journal of Propulsion and Power*, 32(2), pp. 279–294, 2016. doi: 10.2514/1.B35780.

[91] M. E. Harvazinski, C. Huang, V. Sankaran, T. W. Feldman, et al. Coupling between hydrodynamics, acoustics, and heat release in a self-excited unstable combustor. *Physics of Fluids*, 27(4), p. 045102, 2015. doi: 10.1063/1.4916673.

[92] D. C. Haworth and S. B. Pope. A generalized Langevin model for turbulent flows. *The Physics of Fluids*, 29(2), pp. 387–405, 1986. doi: 10.1063/1.865723.

[93] L. He, Q. Guo, Y. Gong, F. Wang, et al. Investigation of OH* chemiluminescence and heat release in laminar methane–oxygen co-flow diffusion flames. *Combustion and Flame*, 201, pp. 12–22, 2019. issn: 0010-2180. doi: https://doi.org/10.1016/j.combustflame.2018.12.009.

[94] M. Heckl. A New Perspective on the Flame Describing Function of a Matrix Flame. *International Journal of Spray and Combustion Dynamics*, 7, pp. 91–112, 2015. doi: 10.1260/1756-8277.7.2.91.

[95] J. Hinze. *Turbulence*. McGraw-Hill, 1975.

[96] T. Horchler, S. Fechter, and J. Hardi. Numerical Investigation of Flame-Acoustic Interaction at Resonant and Non-Resonant Conditions in a Model Combustion Chamber. In: *Symposium on Thermoacoustics in Combustion: Industry meets Academia (SoTiC 2021)*. Sept. 2021.

[97] B. Hornstein, C. Budnik, and W. Courtney. RESEARCH STUDY OF LIGHT EMISSION CAUSED BY PRESSURE FLUCTUATIONS IN ROCKET ENGINES. In: 1965.

[98] *https://turbmodels.larc.nasa.gov/spalart.html*.

[99] Y. Hu, J. Tan, L. Lv, and X. Li. Investigations on quantitative measurement of heat release rate using chemiluminescence in premixed methane-air flames. *Acta Astronautica*, 2019.

[100] K. Huber and G. Herzberg. *Molecular spectra and molecular structure - 4. Constants of Dynamic Molecules*. Vol. 4. Van Nostrand Reinhold New York, 1979.

[101] J. Hutt and J. Cramer. "Advanced rocket injector development at the Marshall Space Flight Center". In: *Space Programs and Technologies Conference*. 1996. doi: 10.2514/6.1996-4266.

[102] W.-S. Hwang, W. Han, K. Y. Huh, J. Kim, et al. Numerical Simulation of a GH2/LOx Single Injector Combustor and the Effect of the Turbulent Schmidt Number. *Energies*, 13(24), 2020. ISSN: 1996-1073. DOI: 10.3390/en13246616.

[103] M. Ihme. Combustion and Engine-Core Noise. *Annual Review of Fluid Mechanics*, 49(1), pp. 277–310, 2017. DOI: 10.1146/annurev-fluid-122414-034542.

[104] J.Hardi. *Experimental investigation of high frequency combustion instability in cryogenic oxygen-hydrogen rocket engines.* PhD thesis, The University of Adelaide, 2012.

[105] J.Hulka and J.J.Hutt. "Instability Phenomena in Liquid Oxygen/Hydrogen Propellant Rocket Engines". In: vol. 169. Liquid Rocket Engine Combustion Instability, 1995.

[106] J.P.Delplanque and W.A.Sirignano. Transcritical Vaporization and Combustion of LOX Droplet Arrays in a Convective Environment. *Combustion Science and Technology*, 105(4-6), pp. 327–344, 1995.

[107] J.Perovšek. *Ray Tracing and Spectral Modeling of Excited Hydroxyl Radiation from Cryogenic Flames in Rocket Combustion Chambers.* MA thesis, LuleåUniversity of Technology, Department of Computer Science, Electrical and Space Engineering, 2018.

[108] B. Janardan and T. L. Zinn. CR-159542 MEASUREMENTS OF ADMITTANCES AND CHARACTERISTIC COMBUSTION TIMES OF REACTIVE GASEOUS PROPELLANT COAXIAL INJECTORS by ". In: 2011.

[109] B. A. Janardan, B. R. Daniel, W. A. Bell, and B. T. Zinn. Measurements of Reactive Gaseous Rocket Injector Admittances. *Combustion Science and Technology*, 20, pp. 185–193, 1979.

[110] B. A. Janardan, B. R. Daniel, and B. T. Zinn. Characteristics of response factors of coaxial gaseous rocket injectors. In: 1975.

[111] S. Karl. *Numerical Investigation of a Generic Scramjet Configuration.* PhD thesis, Technische Universität Dresden, May 2011.

[112] S. Karl and H. Luedeke. Application of the DLR Tau code to predict acoustic damping rates in generic combustion chamber configurations. In: Jan. 2012.

[113] T. Kathrotia, U. Riedel, A. Seipel, K. Moshammer, et al. Experimental and numerical study of chemiluminescent species in low-pressure flames. *Applied Physics B*, 107(3), pp. 571–584, 2012. ISSN: 1432-0649. DOI: 10.1007/s00340-012-5002-0.

[114] T. Kathrotia, M. Fikri, M. Bozkurt, M. Hartmann, et al. Study of the H + O + M reaction forming Oj: Kinetics of OH chemiluminescence in hydrogen combustion systems. *Combustion and Flame*, 157, pp. 1261–1273, 2010.

[115] T. Kathrotia, U. Riedel, and J. Warnatz. A Numerical Study on the Relation of OH*, CH*, and C2* Chemiluminescence and Heat Release in Premixed Methane Flames. In: Jan. 2009.

[116] K. T. Kim, H. J. Lee, J. G. Lee, B. D. Quay, et al. Flame Transfer Function Measurement and Instability Frequency Prediction Using a Thermoacoustic Model. In: *Turbo Expo: Power for Land, Sea and Air*. Vol. Volume 2: Combustion, Fuels and Emissions. 2009.

[117] B. Knapp and M. Oschwald. High Speed Visualization of Flame Response in a LOX/H2 Combustion Chamber During External Excitation. In: *12th International Symposium on Flow Visualization*. Sept. 2006.

[118] T. Koike and K. Morinaga. Further Studies of the Rate Constant for Chemical Excitation of OH in Shock Waves. *Bulletin of the Chemical Society of Japan*, 55(1), pp. 52–54, 1982. DOI: 10.1246/bcsj.55.52.

[119] A. N. Kolmogorov. The local structure of turbulence in incompressible viscous fluid for very large Reynolds numbers. *Proceedings of the Royal Society of London. Series A: Mathematical and Physical Sciences*, 434, pp. 13–9, 1991.

[120] H. Krediet, C. Beck, W. Krebs, S. Schimek, et al. Identification of the Flame Describing Function of a Premixed Swirl Flame from LES. *Combustion Science and Technology - COMBUST SCI TECHNOL*, 184, pp. 888–900, 2012. DOI: 10.1080/00102202.2012.663981.

[121] G. Lacaze and J. Oefelein. A non-premixed combustion model based on flame structure analysis at supercritical pressures. *Combustion and Flame*, 159, pp. 2087–2103, 2012. DOI: 10.1016/j.combustflame.2012.02.003.

[122] C. Lagarza-Cortés, J. Ramírez-Cruz, M. Salinas-Vázquez, W. Vicente-Rodríguez, et al. Large-eddy simulation of transcritical and supercritical jets immersed in a quiescent environment. *Physics of Fluids*, 31(2), p. 025104, 2019. doi: 10.1063/1.5054797.

[123] N. Lamarque and T. Poinsot. Boundary Conditions for Acoustic Eigenmodes Computation in Gas turbine Combustion Chambers. *AIAA Journal*, 46(9), pp. 2282–2292, 2008. doi: 10.2514/1.35388.

[124] M. Lauer and T. Sattelmayer. *On the Adequacy of Chemiluminescence as a Measure for Heat Release in Turbulent Flames With Mixture Gradients*. June 2009. doi: 10.1115/GT2009-59631.

[125] M. Lauer, M. Zellhuber, T. Sattelmayer, and C. J. Aul. Determination of the Heat Release Distribution in Turbulent Flames by a Model Based Correction of OH* Chemiluminescence. *Journal of Engineering for Gas Turbines and Power*, 133(12), 121501, 2011. issn: 0742-4795. doi: 10.1115/1.4004124.

[126] M. R. W. Lauer. *Determination of the Heat Release Distribution inTurbulent Flames by Chemiluminescence Imaging*. PhD thesis, Technische Universität München, 2011.

[127] R. LECOURT and R. FOUCAUD. "Experiments on stability of liquid propellant rocket motors". In: *23rd Joint Propulsion Conference*. 1987. doi: 10.2514/6.1987-1772.

[128] T. Lee, W. G. Bessler, H. Kronemayer, C. Schulz, et al. Quantitative temperature measurements in high-pressure flames with multiline NO-LIF thermometry. *Appl. Opt.*, 44(31), pp. 6718–6728, 2005. doi: 10.1364/AO.44.006718.

[129] M. Lempke, P. Gerlinger, and M. Aigner. Assumed PDF Modeling in Rocket Combustor Simulations. In: *Progress in Propulsion Pyhisics*. Vol. 4. Mar. 2013. doi: 10.1051/eucass/201304569.

[130] *LIFBASE*. https://www.sri.com/engage/products-solutions/lifbase. Accessed 21 July 2018.

[131] J. Luque and D. R. Crosley. Transition Probabilities in the $A2\Sigma^+$ - X2 Π_i Electronic System of OH. *The Journal of chemical physics*, 109(2), pp. 439–448, 1998.

[132] M.Oschwald and A.Schik. Supercritical nitrogen free jet investigated by spontaneous raman scattering. *Experiments in fluids*(, 27), pp. 497–506, 1999.

[133] M.Oschwald and M. Micci. SPREADING ANGLE AND CENTERLINE VARIATION OF DENSITY OF SUPERCRITICAL NITROGEN JETS. *Atomization and Sprays*, 12(1-3), pp. 91–106, 2002. ISSN: 1044-5110.

[134] M.Salikuddin and P.Mungur. Acoustic Radiation Impedance of Duct-Nozzle System. *Journal of Sound and Vibration*, 86(4), pp. 497–522, 1983.

[135] A. Mack and V. Hannemann. Validation of the Unstructured DLR-TAU-Code for Hypersonic Flows. In: June 2002. DOI: 10.2514/6.2002-3111.

[136] J. Manin, M. Bardi, L. Pickett, R. Dahms, et al. Microscopic investigation of the atomization and mixing processes of diesel sprays injected into high pressure and temperature environments. *Fuel*, 134, pp. 531–543, 2014.

[137] E. Manoha, S. Redonnet, and S. Caro. "Computational Aeroacoustics". In: Encyclopedia of Aerospace Engineering, Dec. 2010. ISBN: 9780470686652. DOI: 10.1002/9780470686652.eae344.

[138] R. Mavrodineau and H. Boiteaux. *Flame Spectroscopy*. Wiley, 1965.

[139] W. Mayer, A. Schik, and M. Schaffler. Injection and Mixing Processes in High Pressure Liquid Oxygen/Gaseous Hydrogen Rocket Combustors. *Journal of Propulsion and Power*, 16, pp. 823–828, 2000.

[140] W. Mayer and H. Tamura. Propellant injection in a liquid oxygen/gaseous hydrogen rocket engine. *Journal of Propulsion and Power*, 12(6), pp. 1137–1147, 1996. DOI: 10.2514/3.24154.

[141] W. O. H. Mayer, A. H. A. Schik, B. Vielle, C. Chauveau, et al. Atomization and Breakup of Cryogenic Propellants Under High-Pressure Subcritical and Supercritical Conditions. *Journal of Propulsion and Power*, 1998.

[142] S. Meng, S. Wu, and M. Zhang. Numerical and experimental study of flow structure and heat release distribution in a stratified swirl flame with high-speed PIV and OH* measurements. *AIP Advances*, 11(7), p. 075311, 2021. DOI: 10.1063/5.0056312.

[143] F. R. Menter. Two-equation eddy-viscosity turbulence models for engineering applications. *AIAA Journal*, 32, pp. 1598–1605, 1994.

[144] M. Modest. *Radiative Heat Transfer*. 3rd. Elsevier, Amsterdam, 2013.

[145] Y. Morii, S. Beinke, J. Hardi, T. Shimizu, et al. Dense core response to forced acoustic fields in oxygen-hydrogen rocket flames. *Propulsion and Power Research*, 9, 2020. doi: 10.1016/j.jppr.2020.06.001.

[146] A. Mouahid, P. Boivin, S. Diaw, and E. Badens. Widom and extrema lines as criteria for optimizing operating conditions in supercritical processes. *The Journal of Supercritical Fluids*, 186, p. 105587, 2022. issn: 0896-8446. doi: https://doi.org/10.1016/j.supflu.2022.105587.

[147] H. N. Najm, P. H. Paul, C. J. Mueller, and P. S. Wyckoff. On the Adequacy of Certain Experimental Observables as Measurements of Flame Burning Rate. *Combustion and Flame*, 113(3), pp. 312–332, 1998. issn: 0010-2180. doi: https://doi.org/10.1016/S0010-2180(97)00209-5.

[148] T. M. Nguyen and W. A. Sirignano. The impacts of three flamelet burning regimes in nonlinear combustion dynamics. *Combustion and Flame*, 195, Special Commemorative Issue: Professor Chung King (Ed) Law 70th Birthday, pp. 170–182, 2018. issn: 0010-2180. doi: https://doi.org/10.1016/j.combustflame.2018.03.031.

[149] N. NOIRAY, D. DUROX, T. SCHULLER, and S. CANDEL. A unified framework for nonlinear combustion instability analysis based on the flame describing function. *Journal of Fluid Mechanics*, 615, pp. 139–167, 2008. doi: 10.1017/S0022112008003613.

[150] H. T. Nygård and N. A. Worth. Flame Transfer Functions and Dynamics of a Closely Confined Premixed Bluff Body Stabilized Flame With Swirl. *Journal of Engineering for Gas Turbines and Power*, 143(4), 041011, 2021. issn: 0742-4795. doi: 10.1115/1.4049513.

[151] J. Oefelein. Mixing and Combustion of cryogenic oxygen-hydrogen shear-coaxial jet flames at supercritical pressure. *Combustion Science and Technology*, 178, pp. 229–252, 2006. doi: 10.1080/00102200500325322.

[152] J. C. Oefelein. Thermophysical characteristics of shear-coaxial LOX–H2 flames at supercritical pressure. *Proceedings of the Combustion Institute*, 30(2), pp. 2929–2937, 2005. issn: 1540-7489. doi: https://doi.org/10.1016/j.proci.2004.08.212.

[153] J. C. Oefelein and V. Yang. Modeling High-Pressure Mixing and Combustion Processes in Liquid Rocket Engines. *Journal of Propulsion and Power*, 14(5), pp. 843–857, 1998. doi: 10.2514/2.5349.

[154] M. Oschwald and B. Knapp. "Investigation of Combustion Chamber Acoustics and its Interaction with LOX/H2 Spray Flames". In: vol. 1. Sept. 2009, pp. 205–223. ISBN: 978-2-7598-0411-5. DOI: 10.1051/eucass/200901205.

[155] M. Oschwald, B. Knapp, M. Sliphorst, and M. Marpert. Combustion Chamber Acoustics and its Interaction with LOX/H2- and LOX/CH4-Spray Flames. In: *26th International Symposium on Space Technology and Science (ISTS)*. Vol. 7. Dec. 2009. DOI: 10.2322/tstj.7.Pa_97.

[156] M. Oschwald, J. Smith, R. Branam, J. Hussong, et al. Injection of fluids into supercritical environment. *Combustion Science and Technology*, 178, pp. 49–100, 2006.

[157] P.Hill and C.Peterson. *Mechanics and Thermodynamics of Propulsion*. Pearson, 1992.

[158] P. Palies, D. Durox, T.Schuller, and S.Candel. Nonlinear combustion instability analysis based on the flame describing function applied to turbulent premixed swirling flames. *Combustion and Flame*, 2011.

[159] E. Petersen, M. Kopp, N. Donato, and F. Güthe. Assessment of Current Chemiluminescence Kinetics Models at Engine Conditions. *Journal of Engineering for Gas Turbines and Power*, 134(5), 051501, 2012. ISSN: 0742-4795. DOI: 10.1115/1.4004735.

[160] A. Pierce. *Acoustics: An Introduction to Its Physical Principles and Applications*. Vol. 34. June 1989. ISBN: 0883186128. DOI: 10.1063/1.2914388.

[161] T. Poinsot. Simulation methodologies and open questions for acoustic combustion instability studies. In: 2013.

[162] T. Poinsot, S. Candel, and E. I. Esposito. Experimental determination of the reflection coefficient of a premixed flame in a duct. *Journal of Sound and Vibration*, 107, pp. 265–278, 1986.

[163] T. Poinsot and D. P. Veynante. Theoretical and numerical combustion. In: 2001.

[164] W. Polifke and C. Lawn. On the low-frequency limit of flame transfer functions. *Combustion and Flame*, 151, pp. 437–451, 2007. DOI: 10.1016/j.combustflame.2007.07.005.

[165] L. Pons, N. Darabiha, S. Candel, G. Ribert, et al. Mass transfer and combustion in transcritical non-premixed counterflows. *Combustion Theory and Modelling*, 13, pp. 57–81, 2009.

[166] D. Potter. *Modelling radiating shock layers for atmosferic entry at Earth and Mars*. PhD thesis, School of Mechanical and Mining Engineering, University of Queensland, 2011.

[167] L. Prandtl. *Über ein neues Formelsystem für die ausgebildete Turbulenz*. Nachrichten der Akademie der Wissenschaften zu Göttingen, Mathematisch-Physikalische Klasse. Vandenhoeck & Ruprecht, 1945. URL: https://books.google.de/books?id=JByAPwAACAAJ.

[168] R. Price, I. Hurle, and T. Sugden. Optical studies of the generation of noise in turbulent flames. *Symposium (International) on Combustion*, 12(1), pp. 1093–1102, 1969. ISSN: 0082-0784. DOI: https://doi.org/10.1016/S0082-0784(69)80487-X.

[169] Y. Pyo, D. Kim, S.-K. Kim, and D. Cha. Numerical investigation on combustion instability modeling in a lean premixed gas turbine combustor combining finite element analysis with local flame transfer function. *Journal of Mechanical Science and Technology*, 33, 2019. DOI: 10.1007/s12206-019-1048-9.

[170] L. Qiu and R. D. Reitz. An investigation of thermodynamic states during high-pressure fuel injection using equilibrium thermodynamics. *International Journal of Multiphase Flow*, 72, pp. 24–38, 2015.

[171] J. R. GAFFNEY, J. WHITE, S. GIRIMAJI, and J. DRUMMOND. "Modeling turbulent/chemistry interactions using assumed pdf methods". In: *28th Joint Propulsion Conference and Exhibit*. AIAA, 1992. DOI: 10.2514/6.1992-3638.

[172] R.C.Reid, J.M.Prausnitz, and B.E.Poling. *The properties of gases and liquids*. Ed. by M. Hill. 4th edition. 1987.

[173] V. K. Rani and S. L. Rani. Development of a comprehensive flame transfer function and its application to predict combustion instabilities in a dump combustor. *Combustion Science and Technology*, 190(8), pp. 1313–1353, 2018. DOI: 10.1080/00102202.2018.1440215.

[174] J. W. S. B. Rayleigh. The Theory of Sound. *Nature*, 1878.

[175] G. Ribert, N. Zong, V. Yang, L. Pons, et al. Counterflow diffusion flames of general fluids:Oxygen/hydrogen mixtures. *Combustion and Flame*, 2008.

[176] A. Rona. The Acoustic Resonance of Rectangular and Cylindrical Cavities. *Journal of Algorithms Computational Technology*, 1, 2007. DOI: 10.1260/174830107782424110.

[177] A. Roshko. On the development of turbulent wakes from vortex streets. In: *National Advisory Comittee for Aeronautics*. 1953.

[178] C.-C. Rossow. Extension of a Compressible Code Toward the Incompressible Limit. *AIAA Journal*, 41(12), pp. 2379–2386, 2003. doi: 10.2514/2.6863.

[179] B. Ruscic, A. F. Wagner, L. B. Harding, R. L. Asher, et al. On the Enthalpy of Formation of Hydroxyl Radical and Gas-Phase Bond Dissociation Energies of Water and Hydroxyl. *The Journal of Physical Chemistry A*, 106(11), pp. 2727–2747, 2002. doi: 10.1021/jp013909s.

[180] S. Ryoo, J. Kim, H. Kim, H. Moon, et al. An Experimental Study on Nozzle Damping Characteristics for Combustion Instability Suppression. In: 2017.

[181] S.D.Heister, W.E.Anderson, T. Purpoint, and R.J.Cassady. *Rocket Propulsion*. Ed. by C. U. Press. 2018.

[182] I. Sadrehaghighi. *Mesh Generation in CFD*. Jan. 2020.

[183] S. Sardeshmukh, M. Bedard, and W. Anderson. The use of OH* and CH* as heat release markers in combustion dynamics. *International Journal of Spray and Combustion Dynamics*, 9, pp. 409–423, 2017. doi: 10.1177/1756827717718483.

[184] T. Sattelmayer, R. Kathan, S. Köglmeier, R. Kaess, et al. Validation of Transverse Instability Damping Computations for Rocket Engines. *Journal of Propulsion and Power*, 31, pp. 1–11, 2015. doi: 10.2514/1.B35536.

[185] S. Sazhin, E. Sazhina, O. Faltsi-Saravelou, and P. Wild. The P-1 model for thermal radiation transfer: Advantages and limitations. *Fuel*, 75, pp. 289–294, 1996. doi: 10.1016/0016-2361(95)00269-3.

[186] T. Schmitt, Y. Méry, M. Boileau, and S. Candel. Large-Eddy Simulation of oxygen/methane flames under transcritical conditions. *Proceedings of the Combustion Institute*, 33(1), pp. 1383–1390, 2011. issn: 1540-7489. doi: https://doi.org/10.1016/j.proci.2010.07.036.

[187] T. Schmitt, J. Rodriguez, I. A. Leyva, and S. Candel. Experiments and numerical simulation of mixing under supercritical conditions. *Physics of Fluids*, 24(5), p. 055104, 2012. doi: 10.1063/1.3701374.

[188] T. Schmitt, L. Hakim, M. Boileau, G. Staffelbach, et al. Large-Eddy Simulation of a multiple injector cryogenic combustor under transcritical conditions and large amplitude high frequency modulations. In: May 2014.

[189] T. Schuller, D. Durox, and S. Candel. A unified model for the prediction of laminar flame transfer functions: comparisons between conical and V-flame dynamics. *Combustion and Flame*, 134(1), pp. 21–34, 2003. ISSN: 0010-2180. DOI: https://doi.org/10.1016/S0010-2180(03)00042-7.

[190] T. Schuller, T. Poinsot, and S. Candel. Dynamics and control of premixed combustion systems based on flame transfer and describing functions. *Journal of Fluid Mechanics*, 894, 2020. DOI: 10.1017/jfm.2020.239.

[191] M. Schulze and T. Sattelmayer. Linear stability assessment of a cryogenic rocket engine. *International Journal of Spray and Combustion Dynamics*, 9, p. 175682771769528, 2017. DOI: 10.1177/1756827717695281.

[192] M. Schulze. *Linear Stability Assessment of Cryogenic Rocket Engines*. PhD thesis, Technische Universität München, 2016.

[193] D. Schwamborn, T. Gerhold, and V. Hannemann. "On the Validation of the DLR-TAU Code". In: *New Results in Numerical and Experimental Fluid Mechanics II: Contributions to the 11th AG STAB/DGLR Symposium Berlin, Germany 1998*. Ed. by W. Nitsche, H.-J. Heinemann, and R. Hilbig. Vieweg+Teubner Verlag, Wiesbaden, 1999, pp. 426–433. ISBN: 978-3-663-10901-3. DOI: 10.1007/978-3-663-10901-3_55.

[194] D. Schwamborn, T. Gerhold, and R. Heinrich. The DLR TAU-code: Recent applications in research and industry. In: Jan. 2006.

[195] L. Selle, R. Blouquin, M. Théron, L.-H. Dorey, et al. Prediction and Analysis of Combustion Instabilities in a Model Rocket Engine. *Journal of Propulsion and Power*, 30, pp. 978–990, 2014. DOI: 10.2514/1.B35146.

[196] A. Sharma, A. De, and S. S. Kumar. Analysis of Self-Excited Combustion Instability in a Sub-scale Rocket Engine Using Large Eddy Simulation. In: *Proceedings of the 26thNational and 4th International ISHMT-ASTFE Heat and Mass Transfer Conference*. Dec. 2021.

[197] T. Shimizu, D. Hori, and Y. Daimon. Acoustic structure and damping estimation of a cylindrical rocket chamber during oscillation. In: July 2012. ISBN: 978-1-60086-935-8. DOI: 10.2514/6.2012-4206.

[198] T. Shimizu, D. Hori, S. Yoshida, S. Tachibana, et al. On acoustic damping of a cylindrical chamber in resonant modes. *Fluid Dynamics Research*, 44, p. 045506, 2012.

[199] R. Sigman and B. Zinn. "Theoretical determination of nozzle admittances using a finite element approach". In: *18th Aerospace Sciences Meeting*. 1980. doi: 10.2514/6.1980-85.

[200] R. Sigman and B. T. Zinn. A finite element approach for predicting nozzle admittances. *Journal of Sound and Vibration*, 88, pp. 117–131, 1983.

[201] C. Silva, N. Franck, T. Schuller, D. Durox, et al. Combining a Helmholtz solver with the flame describing function to assess combustion instability in a premixed swirled combustor. *Combustion and Flame*, 160, pp. 1743–1754, 2013. doi: 10.1016/j.combustflame.2013.03.020.

[202] J. Sisco. *Measurement and analysis of an unstable model rocket combustor*. PhD thesis, Purdue University, 2007.

[203] J. Sisco, R. Smith, V. Sankaran, and W. Anderson. "Examination of Mode Shapes in an Unstable Model Rocket Combustor". In: *42nd AIAA/ASME/SAE/ASEE Joint Propulsion Conference Exhibit*. 2006. doi: 10.2514/6.2006-4525.

[204] M. Sliphorst, B. Knapp, S. Gröning, and M. Oschwald. Combustion Instability-Coupling Mechanisms Between Liquid Oxygen/Methane Spray Flames and Acoustics. *Journal of Propulsion and Power*, 28, 2012. doi: 10.2514/1.B34339.

[205] M. Sliphorst. *High Frequency Combustion Instabilities of LOx/CH4 Spray Flames in Rocket Engine Combustion Chambers*. PhD thesis, Technische Universität Delft, Jan. 2011.

[206] J. SMAGORINSKY. Genral circulation experiments with the primitive equations. *Monthly Weather Review*, 91(3), pp. 99–164, 1963.

[207] G. Smith, J. Luque, C. Park, J. Jeffries, et al. Low pressure flame determinations of rate constants for OH(A) and CH(A) chemiluminescence. *Combustion and Flame*, 131, pp. 59–69, 2002. doi: 10.1016/S0010-2180(02)00399-1.

[208] T. F. Smith, Z. F. Shen, and J. N. Friedman. Evaluation of Coefficients for the Weighted Sum of Gray Gases Model. *Journal of Heat Transfer*, 104(4), pp. 602–608, 1982. issn: 0022-1481. doi: 10.1115/1.3245174.

[209] G. Soave. Equilibrium constants from a modified Redlich-Kwong equation of state. *Chemical Engineering Science*, 27(6), pp. 1197–1203, 1972. ISSN: 0009-2509. DOI: https://doi.org/10.1016/0009-2509(72)80096-4.

[210] P. SPALART and S. ALLMARAS. "A one-equation turbulence model for aerodynamic flows". In: *30th Aerospace Sciences Meeting and Exhibit*. DOI: 10.2514/6.1992-439.

[211] W. C. Strahle. Combustion noise. *Progress in Energy and Combustion Science*, 4(3), pp. 157–176, 1978. ISSN: 0360-1285.

[212] L. Strobio Chen, S. Bomberg, and W. Polifke. Propagation and Generation of Acoustic and Entropy Waves Across a Moving Flame Front. *Combustion and Flame*, 166, pp. 170–180, 2016. DOI: 10.1016/j.combustflame.2016.01.015.

[213] R. Stützer and M.Oschwald. The Hyperfine Structure of the OH* Emission Spectrum and its Benefits for Combustion Analysis. *Proceedings of of the 8th European Conference for Aeronautics and Space Sciences EUCASS*, 2019.

[214] T.Poinsot. Prediction and control of combustion instabilities in real engines. In: *Proceedings of the Combustion Institute*. Vol. vol. 36. 1. 2017, pp. 1–28.

[215] G. M. R. Tamanampudi, S. Sardeshmukh, W. Anderson, and C. Huang. Combustion instability modeling using multi-mode flame transfer functions and a nonlinear Euler solver. *International Journal of Spray and Combustion Dynamics*, 12, p. 1756827720950320, 2020. DOI: 10.1177/1756827720950320.

[216] *TAU User Guide*.

[217] F. Tonti, J. Hardi, T. Horchler, S. Fechter, et al. Influence of numerical model setup on the response of acoustically forced LOx/H2 flames. In: *8TH EUROPEAN CONFERENCE FOR AERONAUTICS AND AEROSPACE SCIENCES (EUCASS)*. 2019.

[218] F. Tonti, J. Hardi, S. Karl, and M. Oschwald. "Unsteady Modelling of LOx/GH2 Flame Response to Longitudinal Chamber Mode Forcing". In: *AIAA 2018 Joint Propulsion Conference*. DOI: 10.2514/6.2018-4949.

[219] F. Tonti, J. Perovšek, J. Z. Usandivaras, S. Karl, et al. Obtaining pseudo-OH* radiation images from CFD solutions of transcritical flames. *Combustion and Flame*, 233, p. 111614, 2021. ISSN: 0010-2180. DOI: https://doi.org/10.1016/j.combustflame.2021.111614.

[220] F. Tonti, J. Zapata Usandivaras, J. Perovšek, S. Karl, et al. Numerical reproduction of OH* radiation measurements of unsteady supercritical LOx/H2 combustion. In: *Symposium on Thermoacoustic in Combustion: Industry meets Academia (SoTic)*. 2021.

[221] A. Urbano, Q. Douasbin, L. Selle, G. Staffelbach, et al. Study of flame response to transverse acoustic modes from the LES of a 42-injector rocket engine. *Proceedings of the Combustion Institute*, 36(2), pp. 2633–2639, 2017. ISSN: 1540-7489. DOI: https://doi.org/10.1016/j.proci.2016.06.042.

[222] A. Urbano, L. Selle, G. Staffelbach, B. Cuenot, et al. Exploration of combustion instability triggering using Large Eddy Simulation of a multiple injector liquid rocket engine. *Combustion and Flame*, 169, pp. 129–140, 2016. ISSN: 0010-2180. DOI: https://doi.org/10.1016/j.combustflame.2016.03.020.

[223] A. Vaidyanathan, J. Gustavsson, and C. Segal. Oxygen/Hydrogen–Planar-Laser-Induced Fluorescence Measurements and Accuracy Investigation in High-Pressure Combustion. *Journal of Propulsion and Power - J PROPUL POWER*, 25, pp. 864–874, 2009. DOI: 10.2514/1.39013.

[224] W. G. Vincenti and C. H. Kruger. *Introduction to physical gas dynamics*. 1965.

[225] S. W.A., D. J.P., C. C.H., and B. R. "Fundamental Mechanisms of Combustion Instabilities: Liquid-Propellant Droplet Vaporization: A Rate-Controlling Process for Combustion Instability". In: *Liquid Rocket Engine Combustion Instability*. 1995, pp. 307–343.

[226] W.Sirignano. Recent Advances in Spray Combustion Theory. In: vol. 24. Jan. 2006. ISBN: 978-1-62410-039-0. DOI: 10.2514/6.2006-1522.

[227] Y. Wang and W. D. Kulatilaka. Spectroscopic investigation of high-pressure femtosecond two-photon laser-induced fluorescence of carbon monoxide up to 20bar. *Appl. Opt.*, 58(10), pp. C23–C29, 2019. DOI: 10.1364/AO.58.000C23.

[228] H. Wäsle, A. Winkler, M. Lauer, and T. Sattelmeyer. Combustion noise modelling using chemiluminescence data as indicator for the heat release distribution. In: *European Combustion Meeting*. 2007.

[229] S. C. L. Webster. *Analysis of Pressure Dynamics, Forced Excitation and Damping in a High Pressure LOX/H2 Combustor*. PhD thesis, RWTH Aachen University, 2016.

[230] M. Wierman, N. Nugent, and W. Anderson. Combustion response of a LOX/LCH4 element to transverse instabilities. In: July 2011. isbn: 978-1-60086-949-5. doi: 10.2514/6.2011-5549.

[231] D. C. Wilcox. Reassessment of the scale-determining equation for advanced turbulence models. *AIAA Journal*, 26, pp. 1299–1310, 1988.

[232] C. Williamson and R. A. Measurements of base pressure in the wake of a cylinder at low Reynolds numbers. *Zeitschrift fur Flugwissenschaften und Weltraumforschung*, 14(1-2), pp. 38–46, 1990.

[233] Z. Xiang, S. Yang, S. Xie, J. Li, et al. Turbulence–chemistry interaction models with finite-rate chemistry and compressibility correction for simulation of supersonic turbulent combustion. *Engineering Applications of Computational Fluid Mechanics*, 14(1), pp. 1546–1561, 2020. doi: 10.1080/19942060.2020.1842248.

[234] W. Mu-xin, L. Pei-jin, Y. Wen-jing, and W. Xiang-geng. Nozzle Admittance and Damping Analysis Using the LEE Method. *International Journal of Turbo & Jet-Engines*, 34, pp. 33–41, 2015.

[235] B. Yang, F.Cuoco, and M.Oschwald. Atomization and Flames in LOX-H2 and LOX-CH4 Spray Combustion. *Journal of Propulsion and Power*, 234(4), pp. 763–771, 2007.

[236] M. Yao, J.-P. Hickey, P. Ma, and M. Ihme. Molecular diffusion and phase stability in high-pressure combustion. *Combustion and Flame*, 210, pp. 302–314, 2019. doi: 10.1016/j.combustflame.2019.08.036.

[237] Y. Yu, L. O'Hara, J. Sisco, and W. Anderson. Experimental Study of High-Frequency Combustion Instability in a Continuously Variable Resonance Combustor (CVRC). In: *47th AIAA Aerospace Sciences Meeting including The New Horizons Forum and Aerospace Exposition*. 2009. doi: 10.2514/6.2009-234.

[238] Y. C. Yu, J. C. Sisco, S. Rosen, A. Madhav, et al. Spontaneous Longitudinal Combustion Instability in a Continuously-Variable Resonance Combustor. *Journal of Propulsion and Power*, 28(5), pp. 876–887, 2012. doi: 10.2514/1.B34308.

[239] M. Zehe, S. Gordon, and B. McBride. CAP: A Computer Code for Generating Tabular Thermodynamic Functions from NASA Lewis Coefficients. *NTRS - Nasa Technical Reports Server*, 2002.

[240] F. Zhang, T. Zirwes, P. Habisreuther, and H. Bockhorn. A DNS Analysis of the Correlation of Heat Release Rate with Chemiluminescence Emissions in Turbulent Combustion. *High Performance Computing in Science and Engineering '16*, 2016.

[241] D. Zhao and Y. Guan. Characterizing modal exponential growth behaviors of self-excited transverse and longitudinal thermoacoustic instabilities. *Physics of Fluids*, 34(2), p. 024109, 2022. doi: 10.1063/5.0082617.

[242] H. Zhu, C. Hu, Q. Guo, Y. Gong, et al. Investigation on chemiluminescence and structure characteristics in CH4/O2 diffusion flames. *Experimental Thermal and Fluid Science*, 102, pp. 595–602, 2019. issn: 0894-1777. doi: https://doi.org/10.1016/j.expthermflusci.2018.10.017.

[243] X. L. Zhu, J. P. Gore, A. N. Karpetis, and R. S. Barlow. The effects of self-absorption of radiation on an opposed flow partially premixed flame. *Combustion and Flame*, 129, pp. 342–345, 2002.

[244] X. Zhu and J. Gore. Radiation effects on combustion and pollutant emissions of high-pressure opposed flow methane/air diffusion flames. *Combustion and Flame*, 141(1), pp. 118–130, 2005. issn: 0010-2180. doi: https://doi.org/10.1016/j.combustflame.2004.12.012.

[245] B. T. Zinn, W. A. Bell, B. R. Daniel, and A. J. Smith. Experimental determination of three-dimensional liquid rocket nozzle admittances. *AIAA Journal*, 11, pp. 267–272, 1973.